

**Automated microfluidic device development for metabolism, nutrient uptake,  
and hormone secretion analyses of primary endocrine tissues**

by

Xiangpeng Li

A dissertation submitted to the Graduate Faculty of  
Auburn University  
in partial fulfillment of the  
requirements for the Degree of  
Doctor of Philosophy

Auburn, Alabama

August 5, 2017

Keywords: Microfluidics, Analytical Chemistry, Lab-on-a-chip, Diabetes, Obesity,  
Adipocytes

Copyright 2017 by Xiangpeng Li

Approved by

Christopher J. Easley, Chair, Knowles Associate Professor of Chemistry and Biochemistry

Wei Zhan, Associate Professor of Chemistry and Biochemistry

Bradley L. Merner, James E. Land Assistant Professor of Chemistry and Biochemistry

Mark L. Adams, Assistant Professor of Electrical and Computer Engineering

Guanqun (Vivian) Cao, Assistant Professor of Mathematics and Statistics

## Abstract

Pancreatic islets secrete the dominant endocrine hormone, insulin, which controls the metabolic function of nearly all other organ systems. Additionally, adipose tissue (fat) is now understood to be a complex, multicellular endocrine organ with profound systemic effects, which also alters the function of many other organs. Although there has been renewed interest in insulin secretion and adipose tissue dynamics in response to meals high in refined carbohydrate and sugars, using standard approaches, we unfortunately have a limited view of the temporal relationships between glucose, insulin, and adipose function. Microfluidic technology offers novel features that can meet these needs. This dissertation work focuses on the development of automated microfluidic methods to aid in understanding metabolism, nutrient uptake, and hormone secretion of primary endocrine tissues.

In Chapter 2, a digitally controllable, 16-channel microfluidic input/output multiplexer ( $\mu$ MUX) was developed for mimicking the circulation in the endocrine system. 3D-printed templates were designed to sculpt devices, creating millimeter scale reservoirs and confinement chambers to interface endocrine tissues to the channels. Dynamic insulin secretion profiles and fatty acid uptake/release were monitored in real-time on the  $\mu$ MUX, and quantitative measurement of proteins at attomole levels was achieved. This system has also revealed novel temporal information on insulin-dependent fatty acid transport machinery.

The development of a real time fluorescence assay for monitoring of fatty acid uptake is discussed in Chapter 3. This assay was designed based on the natural binding of fatty acid to serum albumin. Quencher labeled bovine serum albumin was shown to mask the background fluorescence of Bodipy labeled fatty acid analogues and allow for homogeneous real-time measurement of fatty acid uptake by cells or tissues with minimal background fluorescence. The insulin-induced fatty acid uptake in adipose tissue explants was studied in the

$\mu$ MUX device using this assay. A synthesized CD-36/SR-B2 inhibitor has shown significant inhibition on the insulin effect on fatty acid uptake rate.

An automated, droplet forming microfluidic system (PumpDrop) is introduced in Chapter 4 for continuous, high temporal resolution, on-chip secreted protein quantification. The PumpDrop system integrated precise peristaltic pumping, homogeneous immunoassay, lock-in droplet detection, and on-chip assay incubation with droplet storage channels. As a proof of concept, dynamic insulin secretion profiles from single islets of Langerhans was achieved at high temporal resolution using only an optical readout. This system should be directly translatable to other cells or tissues for secretome dynamic studies.

Chapter 5 highlights a study of protein coatings at aqueous-in-oil droplet surfaces. A biotinylated perfluorocarbon-surfactant was synthesized for microfluidic droplet formation, and the biotin moiety was shown to recruit streptavidin molecules to the aqueous-oil interface. This proof-of-concept paves the way for the development of interface binding based homogeneous bioassays within droplets, which could further improve the discrimination between signal and background in immunoassays.

The final Chapter reviews the research contribution of this dissertation, and provides an outlook into future research stemming from these topics.

## Acknowledgments

Pursuing a PhD is tough. I would not be able to achieve it without the help of countless people over the past 5 years.

Firstly, I would like to express my sincere thanks to my advisor, Dr. Christopher Easley for his invaluable assistance, guidance and encouragement throughout my PhD studies at Auburn. Your intelligence, enthusiasm, and hard working placed an example I hope to match some day. I also feel very luck to join your research group where I can freely test my ideas and pursuit my goals.

Next, I would like to give my sincere appreciation to Dr. Wei Zhan, Dr. Bradley Merner, Dr. Mark Adams, Dr. Guanqun Cao and Dr. Pengyu Chen for serving on my committee and university reader. Thank you for your generous guidance, suggestions and kindly supports. I also would like thank Dr. Michael Miller, Dr. Michael Meadows, Dr. Melissa Boersma, Mrs. Allison Bird for your training and assistance in the area of confocal microscope, NMR, MS, and flow cytometry, respectively.

Many thanks go to Dr. Rik Blumenthal, Dr. Jimmy Mills, Dr. Stewart Schneller, Dr. Curtis Shannon, Dr. Vincent Ortiz, Dr. Vince Cammarata, Dr. Anne Gorden, Dr. Steven Mansoorabadi, Dr. Ash Abebe, Dr. Philippe Gaillard, and Dr. Peng Zeng. From your courses, I learned not only the knowledges, but also your intelligence and rigorous scientific attitude. Special thanks also go to my awesome lab mates, Dr. Joonyul Kim, Dr. Will Ashby, Dr. Jiaming Hu, Dr. Leah Godwin, Dr. Kennon Deal, Dr. Cheryl Colquhoun, Dr. Jessica Brooks, Dr. Adriana Avila, Jean Negou, Mani Somasundaram, Juan Hu, Mark Holtan, Katarena Ford, Gebriel Hagos, Niamat Khuda, Hui Jin and Nan Shi. Thank you for the fun and support. Good luck to all of you!

Finally, and most importantly, I must thank my family: my wife Suyun and my parents for

their constant support and unconditional love, and my kids, Andrew and Ally for so many happy time.

*Dedicated to*  
*Suyun, Andrew, Ally, and My Parents*  
*for their support and love!*

## Table of Contents

Abstract . . . . .	ii
Acknowledgments . . . . .	iv
List of Figures . . . . .	xi
List of Tables . . . . .	xviii
1 Introduction . . . . .	1
1.1 Obesity, Diabetes, and Related Diseases . . . . .	1
1.1.1 Diabetes . . . . .	1
1.1.2 Obesity . . . . .	8
1.1.3 New methodology for endocrine tissues study? . . . . .	13
1.2 Introduction to Microfluidics . . . . .	14
1.2.1 Microfluidics . . . . .	14
1.2.2 Polydimethylsiloxane (PDMS) based microfluidics . . . . .	21
1.2.3 Active microfluidic systems using pneumatic valving . . . . .	27
1.2.4 Droplet based microfluidic systems . . . . .	34
1.2.5 Microfluidic methods for adipocyte study . . . . .	46
1.3 Concluding Remarks . . . . .	55
2 Development of automated microfluidic systems for endocrine tissue analyses . .	57
2.1 Introduction . . . . .	57
2.2 Experimental Methods . . . . .	58
2.2.1 General materials . . . . .	58
2.2.2 Microfluidic device master wafer fabrication . . . . .	60
2.2.3 3D-printed interface templates for tissue culture regions . . . . .	61
2.2.4 Microdevice fabrication . . . . .	61

2.2.5	Control interface . . . . .	63
2.2.6	Solution level sensing . . . . .	64
2.2.7	Time and channel programs . . . . .	65
2.2.8	$\mu$ MUX device characterization . . . . .	65
2.2.9	Extraction of primary islets and adipose explants . . . . .	70
2.2.10	Islet secretion sampling and insulin quantification . . . . .	72
2.2.11	Fatty acid uptake analysis . . . . .	73
2.3	Result and Discussion . . . . .	73
2.3.1	$\mu$ MUX device design . . . . .	73
2.3.2	System Automation . . . . .	74
2.3.3	$\mu$ MUX device optimization . . . . .	79
2.3.4	Temporal Sampling Mode: Dynamic Islet Function . . . . .	81
2.3.5	Temporal Stimulation Mode: Dynamic Adipose Tissue Function . . . . .	83
2.4	Conclusions . . . . .	87
3	Dynamic nutrient exchange in murine adipose tissue . . . . .	88
3.1	Introduction . . . . .	88
3.2	Experimental . . . . .	91
3.2.1	General materials and reagents . . . . .	91
3.2.2	Synthesis of BSA-Quencher . . . . .	92
3.2.3	CD-36 inhibitor synthesis . . . . .	92
3.2.4	Adipocyte explant extraction and culture . . . . .	93
3.2.5	Microfluidic device fabrication and operation . . . . .	94
3.2.6	Fluorescent explant imaging . . . . .	95
3.3	Result and Discussion . . . . .	97
3.3.1	BSA-Quencher design and synthesis . . . . .	97
3.3.2	Fluorescence imaging for real time fatty acid uptake measurement . . . . .	98
3.3.3	CD36 Inhibitor and its effect on fatty acid uptake . . . . .	101

3.4	Conclusions . . . . .	104
4	Automated droplet microfluidic system for high resolution measurement . . . . .	106
4.1	Introduction . . . . .	106
4.2	Materials and Methods . . . . .	108
4.3	Results and Discussion . . . . .	119
4.4	Conclusions . . . . .	134
5	Controlled protein coatings at aqueous-in-oil droplet surfaces . . . . .	136
5.1	Introduction . . . . .	136
5.2	Experimental and methods . . . . .	138
5.2.1	Materials . . . . .	138
5.2.2	Kry-Biotin surfactant synthesis . . . . .	138
5.2.3	Microfluidic device fabrication and droplet formation . . . . .	139
5.3	Result and Discussion . . . . .	141
5.3.1	Biotinylated surfactant synthesis . . . . .	141
5.3.2	Microfluidic device design and droplet formation . . . . .	142
5.3.3	Surface interaction simulation . . . . .	143
5.3.4	Interfacial streptavidin/biotin interactions . . . . .	146
5.4	Conclusions . . . . .	148
6	Conclusion and Future Directions . . . . .	150
6.1	Conclusions . . . . .	150
6.1.1	Automated microfluidic systems . . . . .	150
6.1.2	Bioassay development . . . . .	151
6.2	Future Directions . . . . .	151
6.2.1	Automated endocrine tissue culture and on-chip detection system . . . . .	151
6.2.2	More sensitive droplet assays for dynamic tissue secretion study . . . . .	152
6.2.3	Improve the temporal resolution of droplet based analog assay . . . . .	152
6.2.4	Better understanding of adipocytes fatty acid uptake . . . . .	153

6.2.5	Closing Remarks . . . . .	154
	Bibliography . . . . .	156
	Appendices . . . . .	183
A	The effects affecting glycohemoglobin level . . . . .	184
A.1	Introduction . . . . .	184
A.2	Method and Analysis . . . . .	185
A.2.1	Data . . . . .	185
A.2.2	Define dummy variables . . . . .	186
A.2.3	Multiple linear regression (Full model) . . . . .	187
A.2.4	Model selection (Backward) . . . . .	189
A.2.5	Model selection (Stepwise) . . . . .	189
A.2.6	Model selection (Best subset) . . . . .	189
A.3	Explanation, conclusion, and discussion . . . . .	190
A.4	Conclusion . . . . .	191
A.5	SAS code . . . . .	192
B	Spectra . . . . .	195
B.1	CD36 inhibitor spectrum . . . . .	195
B.2	Kry-Biotin spectrum . . . . .	195
C	LabVIEW Codes . . . . .	201
C.1	LabVIEW application for $\mu$ MUX device . . . . .	201
C.2	LabVIEW application for PumpDrop device . . . . .	201
D	Copyright Permissions . . . . .	221

## List of Figures

1.1	WHO Diabetes Trends . . . . .	2
1.2	The pancreas is a mixed exocrine and endocrine organ . . . . .	3
1.3	Crosstalk between pancreatic $\beta$ cells and other organs . . . . .	5
1.4	Simplified schematics of insulin secretion from $\beta$ cell . . . . .	6
1.5	WHO Obesity Trends . . . . .	8
1.6	Chronic inflammation in adipose tissue triggers insulin resistance . . . . .	12
1.7	Example of microfluidic devices. . . . .	15
1.8	Laminar flow . . . . .	16
1.9	Microfluidic cell trapping. . . . .	18
1.10	Biological dynamic processes time scale. . . . .	19
1.11	Lung-on-a-chip microdevice . . . . .	20
1.12	Growth of publications related to microfluidics. . . . .	22
1.13	PDMS. . . . .	23
1.14	Soft lithography for micropatterned PDMS. . . . .	24
1.15	The analog of Moores Law for nanofluidic systems. . . . .	27

1.16 PDMS based elastomeric microvalves. . . . .	28
1.17 Peristaltic pumping and rotary mixer. . . . .	29
1.18 Microfluidic multiplexer. . . . .	31
1.19 Seive valve. . . . .	32
1.20 Droplet formation. . . . .	35
1.21 Biocompatible surfactants. . . . .	38
1.22 Droplet sorting. . . . .	39
1.23 Picoinjection and droplet merger. . . . .	40
1.24 Droplet count using a 3D particle counter. . . . .	43
1.25 Block diagram of typical lock-in detection system and microfluidic $\mu$ Chopper. . . . .	44
1.26 Examples of adipose studies on microfluidic devices. . . . .	51
2.1 $\mu$ MUX device design . . . . .	59
2.2 Cross-section of a $\mu$ MUX fluidic channel . . . . .	60
2.3 Fabrication procedure of $\mu$ MUX devices including 3D-templated reservoir molding. . . . .	62
2.4 Automated solution level sensing. . . . .	64
2.5 $\mu$ MUX system automation. . . . .	66
2.6 Automation data for dynamic insulin secretion . . . . .	67
2.7 $\mu$ MUX device characterization and optimization. . . . .	68

2.8	Islet mimics for solution exchange experiments. . . . .	69
2.9	Buffer bottle for collecting islet secretion samples. . . . .	71
2.10	Images of pancreatic islets on a $\mu$ MUX device. . . . .	72
2.11	Schematic of the $\mu$ MUX channel design at higher resolution. . . . .	75
2.12	First-generation “full/empty” sensor . . . . .	77
2.13	Cross-sections of multiple devices with varying depths of tissue culture regions. . . . .	79
2.14	3D-printed template for tissue culture interfaces . . . . .	80
2.15	Temporal sampling mode of the $\mu$ MUX. . . . .	82
2.16	Temporal stimulation and imaging mode of the $\mu$ MUX . . . . .	85
2.17	Dynamic fatty acid uptake with 2 treatments . . . . .	86
3.1	Cartoon Representation of BSA-Q Assay Mechanism . . . . .	90
3.2	Absorption and emission of BSA-Q and Bodipy fatty acids . . . . .	96
3.3	Bodipy fatty acid titration with BSA-Q . . . . .	97
3.4	Example time lapse fluorescent imaging of adipose explants. . . . .	99
3.5	Fatty acid transport through cells . . . . .	100
3.6	Dynamic fatty acid uptake by adipose tissue . . . . .	102
3.7	CD36 inhibitor synthesis . . . . .	102
3.8	Dynamic fatty acid uptake by adipose tissue after inhibitor treatments . . . . .	103

3.9	Inhibitor effects on fatty acid uptake . . . . .	104
4.1	PumpDrop Chip Design . . . . .	109
4.2	The cross section of microfluidic channels . . . . .	111
4.3	Fabrication procedure of PumpDrop devices . . . . .	113
4.4	Flow chart for PumpDrop chip automation . . . . .	114
4.5	Peristaltic pumping induced chaotic mixing . . . . .	117
4.6	Enlarged PumpDrop channel layout with fluidic channel description . . . . .	120
4.7	PumpDrop control channel description and pumping test . . . . .	122
4.8	Droplets pack up within channels . . . . .	123
4.9	Previous version of PumpDrop Channel layout. . . . .	123
4.10	Droplet formation steps . . . . .	125
4.11	Droplet formation with various parameters . . . . .	126
4.12	PumpDrop device characterization . . . . .	126
4.13	Cross-section of the islet trapping region . . . . .	128
4.14	Example of bottom view of single islet in the trapping chamber . . . . .	129
4.15	Insulin diffusion test . . . . .	129
4.16	Insulin concentration measurement within droplets . . . . .	131
4.17	Example of droplet insulin assay data analysis . . . . .	132

4.18	Insulin secretion from three different single islets . . . . .	135
5.1	Schematics of biotin-STV interaction on the aqueous-oil interface of droplet . . .	137
5.2	Schematics for Kry-Biotin synthesis . . . . .	138
5.3	TwoOil chip design schematics and image . . . . .	140
5.4	Droplets made with Kry-Biotin and PicoSurf 1 surfactant . . . . .	142
5.5	Confocal z-scanning fluorescent images a droplet . . . . .	143
5.6	Streptavidin distribution within droplets simulation . . . . .	146
5.7	Fluorescent images of droplets with various concentration of STV-AF 488 . . . .	146
5.8	Fluorescent intensity of the droplet centers and edges . . . . .	147
5.9	Confocal microscope scanning model . . . . .	148
6.1	Microfluidic device design for more sensitive droplet assays . . . . .	153
A.1	Glycoation of Protein . . . . .	185
A.2	Stepwise model parameter estimate . . . . .	188
A.3	Mellow's Cp . . . . .	190
B.1	Mass Spectrum of CD36 Inhibitor . . . . .	196
B.2	<sup>1</sup> H-NMR Spectrum of CD36 Inhibitor . . . . .	197
B.3	<sup>13</sup> C-NMR Spectrum of CD36 Inhibitor . . . . .	198
B.4	Mass Spectrum of Kry-Biotin . . . . .	199

B.5	Mass Spectrum of Kry-Biotin after one month storage at 4 °C . . . . .	200
C.1	Front panel of $\mu$ MUX control app . . . . .	202
C.2	Block diagram of $\mu$ MUX control app . . . . .	202
C.3	Block diagram of $\mu$ MUX control app (step 1 A) . . . . .	203
C.4	Block diagram of $\mu$ MUX control app (step 1 B) . . . . .	203
C.5	Block diagram of $\mu$ MUX control app (step 2 A) . . . . .	204
C.6	Block diagram of $\mu$ MUX control app (step 2 B) . . . . .	204
C.7	Block diagram of $\mu$ MUX control app (step 2 C) . . . . .	205
C.8	Block diagram of $\mu$ MUX control app (step 2 D) . . . . .	205
C.9	Block diagram of $\mu$ MUX control app (step 2 E) . . . . .	206
C.10	Block diagram of $\mu$ MUX control app (step 2 F) . . . . .	206
C.11	Front panel of PumpDrop app . . . . .	207
C.12	Block diagram of PumpDrop app . . . . .	207
C.13	Block diagram of for PumpDrop app (Characterization mode) . . . . .	208
C.14	Block diagram of PumpDrop app (Close all valves) . . . . .	208
C.15	Block diagram of PumpDrop app (Droplet generation) . . . . .	209
C.16	Block diagram of PumpDrop app (Load oil) . . . . .	209
C.17	Block diagram of PumpDrop app (Load probes) . . . . .	210

C.18 Block diagram of PumpDrop app (Load reference) . . . . .	210
C.19 Block diagram of PumpDrop app (Load sample) . . . . .	211
C.20 Block diagram of PumpDrop app (Manual control) . . . . .	211
C.21 Block diagram of PumpDrop app (Islet mimic) . . . . .	212
C.22 SubVI front panel (Calculate pumping step for droplet formation mode) . . . . .	212
C.23 SubVI block diagram (Calculate pumping step for droplet formation) . . . . .	213
C.24 SubVI front panel (5 step pump) . . . . .	214
C.25 SubVI block diagram (5 step pump) . . . . .	214
C.26 SubVI front panel (15 DIO channel control) . . . . .	215
C.27 SubVI block panel (15 DIO channel control) . . . . .	216
C.28 SubVI front panel (Assign pumping steps) . . . . .	216
C.29 SubVI block diagram (Assign pumping steps) . . . . .	217
C.30 SubVI front panel (Count droplets) . . . . .	217
C.31 SubVI block diagram (Count droplets) . . . . .	218
C.32 SubVI front panel (Load cell channel for islet mimicking) . . . . .	218
C.33 SubVI block diagram (Load cell channel for islet mimicking) . . . . .	219
C.34 SubVI front panel (Incubation for islet mimicking) . . . . .	219
C.35 SubVI block diagram (Incubation for islet mimicking) . . . . .	220

## List of Tables

1	List of abbreviations . . . . .	xix
1.1	Islet cell types, hormones, and functions. . . . .	4
1.2	Adipokines . . . . .	11
1.3	Batokines . . . . .	12
1.4	Adipocytes and adipose tissues studies on microfluidic systems . . . . .	48
A.1	List of variables . . . . .	186
A.2	Full model parameter estimates . . . . .	187
A.3	Backward elimination parameter estimates . . . . .	189

Table 1: List of abbreviations

<b>ADP</b>	Adenosine diphosphate	<b>ID</b>	inner diameter
<b>ATP</b>	Adenosine triphosphate	<b>K<sub>a</sub></b>	association constant
<b>BAT</b>	Brown adipose tissue	<b>LED</b>	Light-emitting diode
<b>BHQ</b>	Black hole quencher	<b>LGLI</b>	low-glucose-low-insulin
<b>BMI</b>	Body Mass index	<b>LOC</b>	Lab-on-a-chip
<b>BSA</b>	Bovine serum albumin	<b>LOD</b>	limit of detection
<b>BSA-Q</b>	Bovine serum albumin-Black hole quencher based fatty acid uptake assay	<b>MITOMI</b>	Mechanically induced trapping of molecular interactions
<b>CAD</b>	computer-aided design	<b>NGS</b>	Next-generation DNA sequencing methods
<b>CCD</b>	charge-coupled device	<b>OD</b>	outer diameter
<b>DAQ</b>	Data acquisition	<b>PBS</b>	Phosphate buffered saline
<b>DCC</b>	dicyclohexylcarbodiimide	<b>PCR</b>	Polymerase chain reaction
<b>DIC</b>	Differential interference contrast	<b>PDMS</b>	Polydimethylsiloxane
<b>DNA</b>	Deoxyribonucleic acid	<b>PFPE</b>	Perfluoropolyether
<b>FFA</b>	Free fatty acid	<b>pH</b>	potential of hydrogen
<b>FFA*</b>	fluorescence labeled fatty acid	<b>PLA</b>	Proximate ligation assay, or polyactic acid
<b>FITC</b>	Fluorescein isothiocyanate	<b>RNA</b>	ribonucleic acid
<b>FRET</b>	Foster resonance energy transfer	<b>ROI</b>	Region of interest
<b>GDP</b>	Guanosine diphosphate	<b>STV</b>	Streptavidin
<b>GFP</b>	green fluorescent protein	<b>TCA</b>	tricarboxylic acid cycle
<b>GLUT</b>	Glucose transporter	<b>UCP1</b>	Mitochondrial brown fat uncoupling protein 1
<b>GTP</b>	Guanosine triphosphate	<b>UV</b>	UltraViolet
<b>HEPES</b>	4-(2-Hydroxyethyl)piperazine-1-ethanesulfonic acid	<b>WAT</b>	White adipose tissue
<b>HGHI</b>	high-glucose-high-insulin	<b>WHO</b>	World health organization
<b>IC3D</b>	Integrated comprehensive droplet in a 3-dimensional way	<b>μMUX</b>	microfluidic input/output multiplexer

## Chapter 1

### Introduction

#### 1.1 Obesity, Diabetes, and Related Diseases

The increasing epidemics of obesity, diabetes and metabolic syndrome represent a serious problem to the health of the global population (Figure 1.1 and Figure 1.5). The World Health Organization (WHO) estimated that in 2012, a total of 3.7 million deaths were directly caused by diabetes and another 2.2 million deaths were related to high blood glucose[1].

##### 1.1.1 Diabetes

Diabetes is a chronic disease in which the body does not properly process food for use as energy, which occurs either when the pancreas does not produce enough insulin or the body cannot effectively use the insulin. High blood glucose level, hyperglycaemia, is a common effect of diabetes and over time leads to severe damage to the heart, blood vessels, eyes, kidneys, and nerves[2].

There are mainly two types of diabetes. Type 1, previously known as juvenile diabetes, is characterized by deficient insulin secretion, which is a result of loss of the insulin producing  $\beta$ -cells by autoimmune attack from the immune system. Although currently incurable and patients depend on lifelong insulin injections, novel approaches to insulin treatment have been developed or are in development, including insulin pumps, continuous glucose monitoring and hybrid closed-loop systems[4]. Islets transplantation[5], stem cell treatment for  $\beta$ -cells regeneration[6] and combined immunotherapies[7] are promising as future therapies. Type 2 diabetes, which results from the body's ineffective use of insulin, is the most common

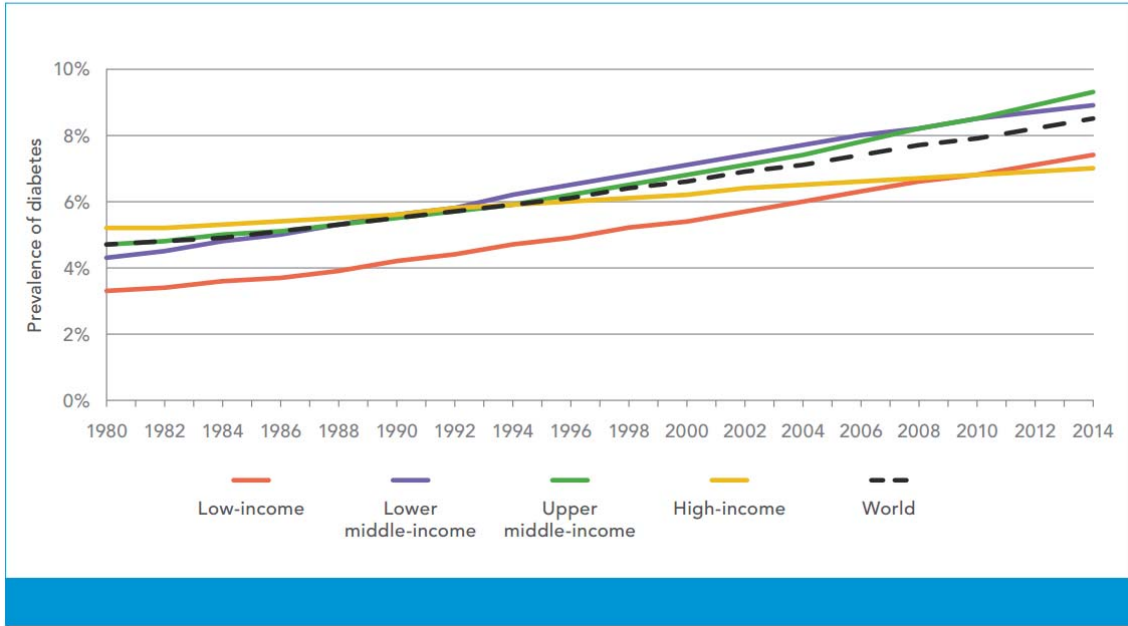


Figure 1.1: Trends in prevalence of diabetes, 1980-2014, by income group [3].

type of diabetes (90% to 95% of diagnosed cases of diabetes) and is largely the result of obesity and physical inactivity[1]. Although no cure has yet been found for the disease, several approaches are used to control the symptoms, such as lifestyle modifications, treatment of obesity, oral hypoglycemic agents, and insulin sensitizers like metformin, alpha glucosidase inhibitors like thiazolidinediones, or insulin[8].

## The pancreas and the islets of Langerhans

The pancreas is an elongated organ nestled behind the stomach and adjacent to the duodenum. It is a mixed exocrine and endocrine gland (Figure 1.2) that controls many homeostatic functions. The exocrine cells make the majority of the organ and supply the gut with digestive enzymes to break down the food. The clusters formed with endocrine cells, or islets of Langerhans, are scattered throughout the tissue of the pancreas.

The islets are composed of four different endocrine cells ( $\alpha$ ,  $\beta$ ,  $\delta$ , and pancreatic-polypeptide-producing (PP) cells), each of which secret characteristic hormones in response to metabolic

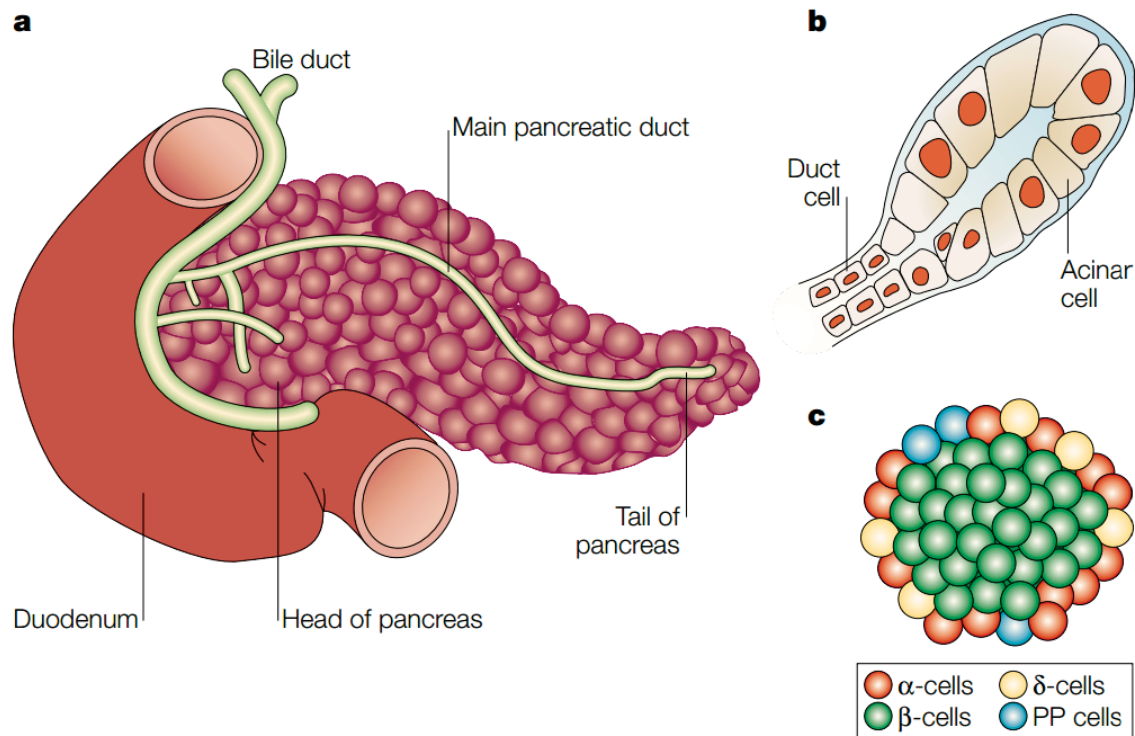


Figure 1.2: The pancreas is a mixed exocrine and endocrine organ

a. The mature pancreas is adjacent to the duodenum. b. Digestive enzymes are secreted from acinar cells and subsequently transported to the intestine via the pancreatic ductal system. c. The endocrine pancreas consists of four hormone-producing cell types:  $\alpha$ ,  $\beta$ ,  $\delta$  and PP cells.  $\alpha$  cells (red) secrete glucagon and make up 15-20% of the endocrine pancreas.  $\beta$  cells (green) secrete insulin and make up 60-80% of the endocrine pancreas.  $\delta$  cells (yellow) secrete somatostatin and make up 5-10% of the endocrine pancreas, whereas PP cells (blue) secrete pancreatic polypeptide and make up less than 2% of the endocrine pancreas. This figure is reprinted with permission from ref [9] ©2002, Nature Publishing Group.

Cell types	Hormones	Functions
$\alpha$	Glucagon	Stimulates hepatic glycogenolysis and gluconeogenesis, as well as exert effects on lipid metabolism, energy balance, body adipose tissue mass and food intake [10]
$\beta$	Insulin	Maintains normal blood glucose levels by facilitating cellular glucoseuptake, regulating carbohydrate, lipid and protein metabolism and promoting cell division and growth through its mitogenic effects.[11]
$\delta$	Somatostatin	Broad inhibitory effects on the secretion of hormones such as growth hormone, insulin and glucagon [12]
PP	Pancreatic polypeptide	Feedback inhibitor of pancreatic secretion after a meal [13]

Table 1.1: Islet cell types, hormones, and functions.

changes, as well as other cells including vascular cells, resident immune cells, neurons, and glial cells. The functions and hormones secreted by these cells are summarized in table 1.1.  $\beta$  Cells secrete one of the more dominant endocrine hormones, insulin; defects in either secretory mechanisms or peripheral tissue responses to insulin are primary causes and/or symptoms of diabetes.

### Insulin secretion from $\beta$ cells

Blood glucose levels are regulated by the hormones insulin and glucagon within a narrow normal range. After a meal, the nutrients, especially glucose, taken up by the digestive system increase the insulin secretion from pancreatic  $\beta$  cells. Then, insulin acts to decrease blood glucose by stimulating the uptake of glucose into skeletal muscles and adipose tissues, where glucose is transformed and stored as glycogen and triglycerides respectively. Insulin also suppresses hepatic glucose production through gluconeogenesis (Figure 1.3).

An elevated blood glucose level is the major induction factor of insulin secretion from  $\beta$  cells.  $\beta$  cells uptake glucose through glucose transporter 2 (GLUT2) . The metabolism of glucose through glycolysis and the tricarboxylic acid cycle produces ATP. The increased

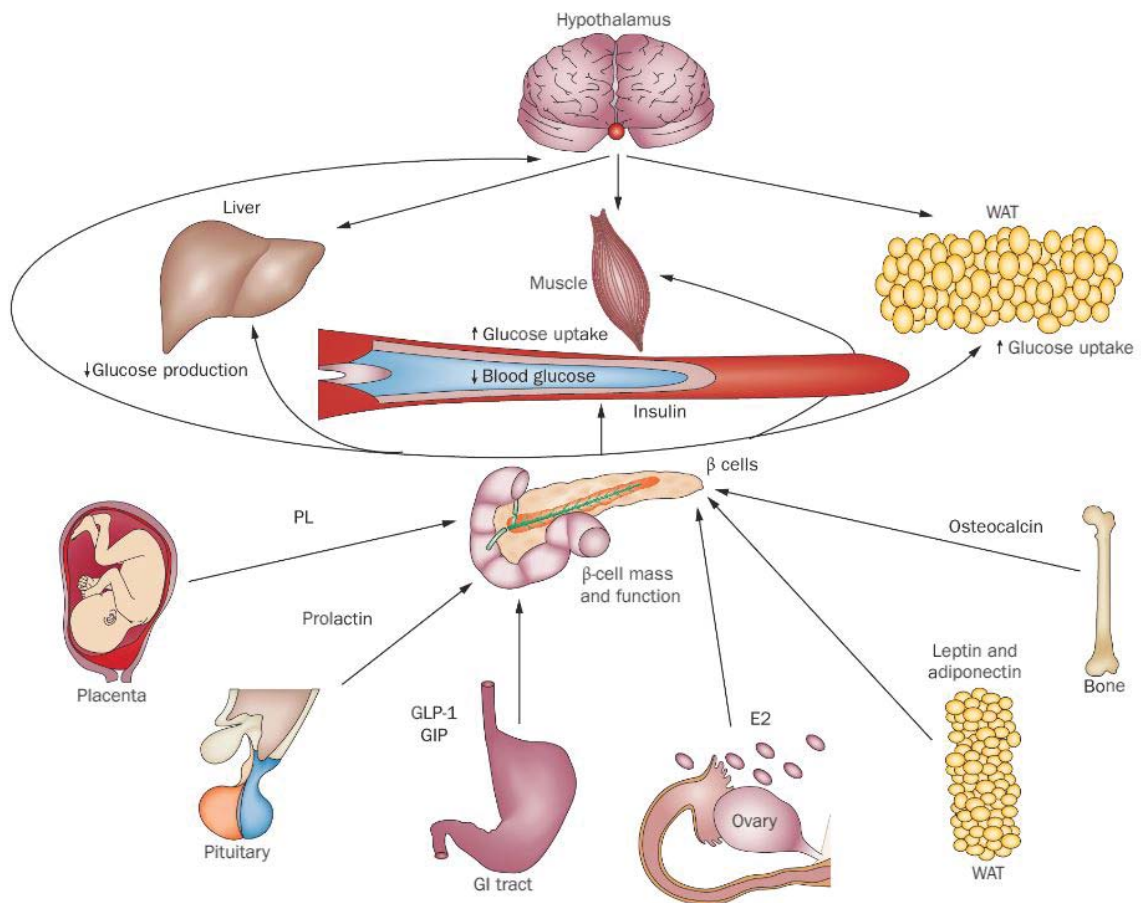


Figure 1.3: Crosstalk between pancreatic  $\beta$  cells and other organs in the regulation of glucose homeostasis.

Pancreatic  $\beta$  cells are critical to maintain glucose homeostasis. This figure is reprinted with permission from ref [14] ©2012, Nature Publishing Group.

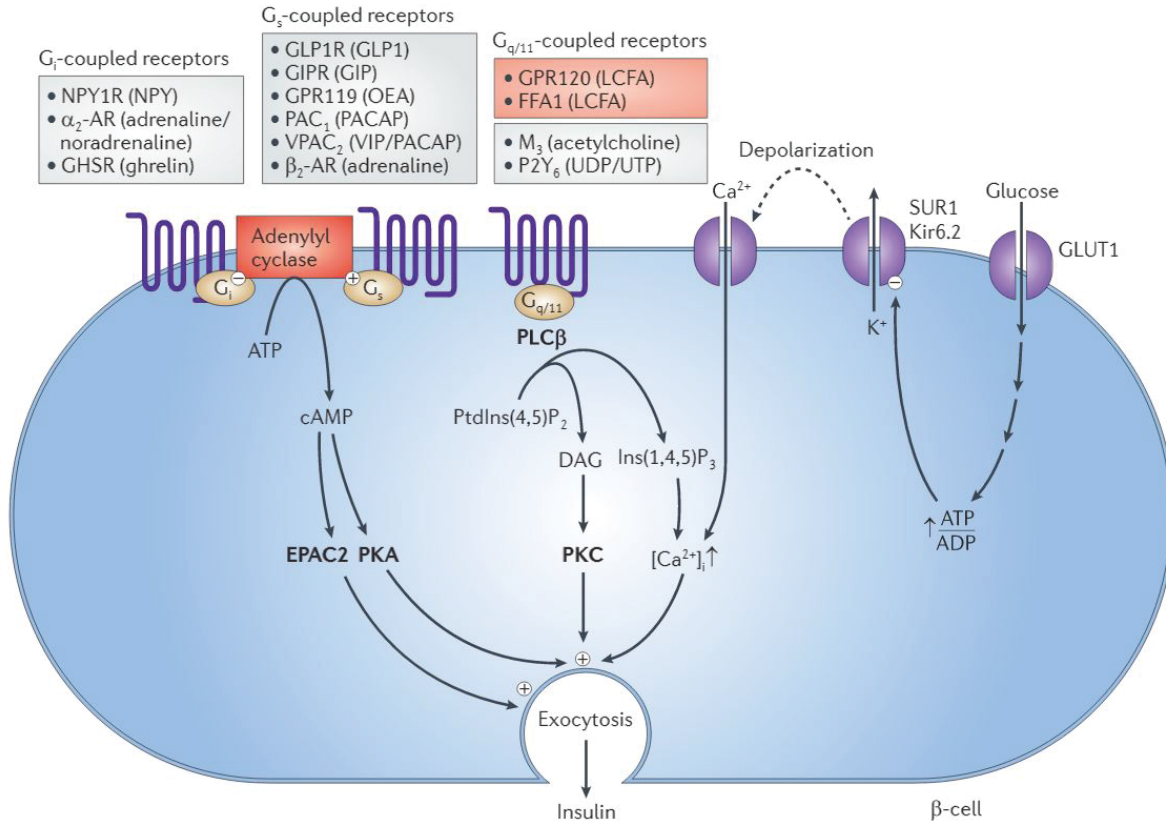


Figure 1.4: Simplified schematics of insulin secretion from  $\beta$  cell

This figure is reprinted with permission from ref [15] ©2012, Nature Publishing Group

ATP/ADP ratio inhibits the ATP-regulated potassium channel Kir6.2 and sulphonylurea receptor 1 (SUR1), which depolarizes the cell membrane, opens the voltage gated calcium channel, and increases the cytosolic calcium concentration. The influx of calcium triggers insulin release by exocytosis [15] (Figure 1.4).

Other than glucose, insulin secretion is also regulated by other factors through complex regulatory network (Figure 1.3). For example, glucagon-like peptide 1 (GLP-1), one of the most effective incretins produced by the gastrointestinal tract after a meal, increases insulin biosynthesis and enhances the  $\beta$  cells' glucose sensitivity [16].

## **Insulin and blood glucose regulation**

Upon nutrient uptake, insulin reduces the blood glucose mainly by increasing the glucose uptake into adipocytes and muscle cells through glucose transporter type 4 (GLUT4). GLUT4 is a high affinity glucose transporter mostly expressed in muscle cells and adipocytes. In the absence of insulin, only 5% of the GLUT4 is found on the cell surface. Insulin recruits GLUT4 to translocate to the plasma membrane from the specialized GLUT4 storage vesicles and thus increase the cell uptake [17]. Although the adipose tissue only accounts for 10% of the insulin-stimulated glucose uptake (the other 90% occurs in skeletal muscle), this process is important for energy homeostasis, as secreted adipokines from white adipose tissue (WAT) also regulate whole body metabolism (Table 1.2). Thus, understanding the dynamics of regulated glucose and other nutrients transportation in adipocytes can provide better opportunities for elucidating the physiology and pathophysiology mechanisms of energy homeostasis.

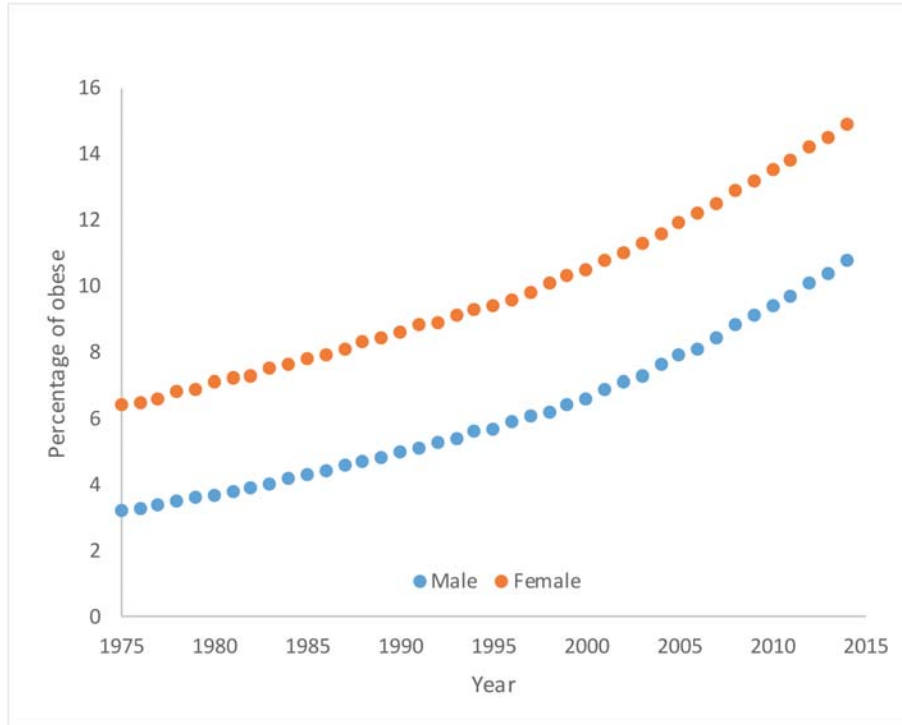


Figure 1.5: WHO Obesity Trends

Obesity (body mass index  $\geq 30$ ), age-standardized (%) Global estimates, data adopted from WHO report [25].

### 1.1.2 Obesity

The classifications of being overweight are defined by abnormal or excessive fat accumulation that may impair health. Adults with a body mass index (BMI) higher than 30 are considered as obese. During the past decades, the global incidence of obesity has increased drastically. According to the WHO, over 600 million people were clinically obese in 2014 [18]. Obesity is linked to multiple health problems, including type 2 diabetes [19, 20], fatty liver disease [21], Alzheimers disease [22], compromised immune function [23], aging [24], and many other diseases. Therefore, there is an urgent need for fundamental understanding of related physiology and pathophysiology to address obesity and its associated complications.

## **Adipose tissues**

The global epidemic of obesity has brought increasing attention to research for understanding the biology of adipocytes (fat cells). Adipose tissues or fat tissues, which account for 5% to 50% of human bodyweight, was traditionally thought to be a passive reservoir for long term energy storage, but now it is known to be a complex, essential, and highly active metabolic and endocrine organ playing profound roles in the integration of systemic metabolism [26]. There are mainly two types of adipose tissues in mammals: white adipose tissue (WAT) and brown adipose tissue (BAT) [27].

### **White adipose tissues and adipokines**

WAT is the main type of adipose tissue in the adult human and is mainly found in subcutaneous regions and visceral depots. WAT consist of adipocytes, (which are the main cellular component of WAT and crucial for both energy storage and endocrine activity), precursor cells, fibroblasts, vascular cells, macrophages, and immune cells. WAT is a critical regulator of system energy homeostasis and acts as both energy storage and an endocrine organ [28]. Extra energy obtained from food including glucose and fatty acids are absorbed by adipocytes and transformed into triacylglycerol during lipogenesis for long-term storage. Upon energy deficiency, triacylglycerol is hydrolyzed (lipolysis) and the non-esterified fatty acid (NEFA) and glycerol are released into circulation for delivery to other organs. Glucose and fatty acid uptake, lipogenesis and lipolysis process are precisely controlled by a complex regulatory network [29, 30].

WAT also secretes numerous hormones that regulate the metabolic functions of nearly all the organs [31]. Those hormones are referred to as adipokines. A detailed list of key adipokines and their sources and functions are summarized in Table 1.2. More importantly, under the obesity condition, WAT not only accumulates and expands throughout the body but also recruits the immune cells which infiltrate into adipose tissue and change the adipokine

secretion profile. This process is related to systemic inflammation and insulin resistance.

### **Brown adipose tissues and batokines**

BAT derives its brown color from the high number of mitochondria, and mainly participates in thermogenesis (heat production). BAT helps maintain normal body temperature in newborn infants and hibernating mammals. BAT regresses with age, but is still present in the normal adult human[7]. BAT is also known to have systemic effects by secreting regulatory molecules, which are called Batokines. The specific batokine profile is distinct from adipokines. The batokines and their functions are listed in Table 1.3 .

### **Obesity and insulin resistance**

Both obesity and type 2 diabetes are linked to insulin resistance [59]. Obese individuals have a increased risk of type 2 diabetes. Although many obese human do not progress to the diabetic state, it is generally accepted that obesity induces two critical features for type 2 diabetes pathogenesis [60].

First, in the obese state, adipose tissue is subject to oxidative stress, accumulation of macrophages, suppression of adiponectin secretion, and production of TNF- $\alpha$ , RBP4, lipocalin, and other proinflammatory cytokines. Chronic adipose tissue inflammation also impairs triglyceride (TG) deposition and increases lipolysis. The combined effects of increased proinflammatory factors, circulating TG and free fatty acid, and reduced adiponectin lead to insulin resistance in adipose tissue, liver, and muscle (Figure 1.6) [60, 24].

Second, obese individuals with insulin resistance, but not diabetes, have compensatory increased insulin secretion from islets in order to maintain normal blood glucose level, which over time causes  $\beta$  cells failure and mediates the progression to diabetes [61].

<b>Adipokines</b>	<b>Primary</b>	<b>Binding partner</b>	<b>Function</b>
Leptin [32]	Adipocytes	Leptin receptor	Appetite control through the central nervous system
Resistin [33]	Peripheral blood mononuclear cells (human), adipocytes (rodent)	unknown	Promotes insulin resistance and inflammation through IL-6 and TNF secretion from macrophages
RBP4 [34]	Liver, adipocytes, macrophages	Retinol (vitaminA), transthyretin	Implicated in systemic insulin resistance
Lipocalin 2 [35]	Adipocytes, macrophages	unknown	Promotes insulin resistance and inflammation through TNF secretion from adipocytes
ANGPTL2 [36]	Adipocytes, other cells	unknown	Local and vascular inflammation
TNF- $\alpha$ [37]	Stromal vascular fraction cells, adipocytes	TNF receptor	Inflammation, antagonism of insulin signalling
IL-6 [38]	Adipocytes, stromal vascular fraction cells, liver, muscle	IL-6 receptor	Changes with source and target tissue
IL-18 [39]	Stromal vascular fraction cells	IL-18 receptor, IL-18 binding protein	Broad-spectrum inflammation
CCL2 [40]	Adipocytes, stromal vascular fraction cells	CCR2	Monocyte recruitment
CXCL5 [41]	Stromal vascular fraction cells (macrophages)	CXCR2	Antagonism of insulin signalling through the JAKSTAT pathway
NAMPT [42]	Adipocytes, macrophages, other cells	unknown	Monocyte chemotactic activity
Adiponectin [43]	Adipocytes	Adiponectin receptors 1 and 2, T-cadherin, calreticulinCD91	Insulin sensitizer, anti-inflammatory
SFRP5 [44]	Adipocytes	WNT5a	Suppression of pro-inflammatory WNT signalling
Asprosin [45]	Adipocytes	unknown	induces hepatic glucose production

Table 1.2: Adipokines

The list was adopted from reference[31] with modification. RBP: Retinol binding protein; ANGPTL2: angiopoietin-like protein 2; TNF: tumour necrosis factor; IL: interleukin; CCL: chemokine (C-C motif) ligand; CCR: chemokine (C-C motif) receptor; CXCL: chemokine (C-X-C motif) ligand; CXCR: chemokine (C-X-C motif) receptor; JAK: Janus kinase; STAT: signal transducer and activator of transcription; NAMPT: nicotinamide phosphoribosyltransferase; SFRP5: secreted frizzled-related protein 5.

Batokines	Effects
BMP8b [46]	Enhance thermogenic activity through sympathetic nervous system and autocrine effects, increase sympathetic activation of BAT
Endothelin-1 [47]	Enhance thermogenic activity
IL-6 [48]	Enhance thermogenic activity, Improve insulin sensitivity
LPGDS [49]	Enhance thermogenic activity
sLR11 [50]	Inhibit thermogenic activity
NGF [51]	Promote sympathetic innervation
Metrn1 [52]	Increase in IL-4 expression and activate macrophages
VEGFA [53]	Promote vascularization of BAT
IGFBP2 [54]	Promote bone formation
FGF21 [55, 56]	Enhance thermogenic activity, Induce WAT browning, Improve insulin sensitivity, Increase cardiac substrate oxidation and protect heart from hypertrophy and oxidative stress
NRG4 [57]	Attenuate hepatic lipogenic signaling
IGF1 [58]	Induce insulin-like effect and regulate cell growth and development.

Table 1.3: Batokines

BMP8b: Bone morphogenetic protein 8b ; FGF21: fibroblast growth factor 21 ; LPGDS: lipocalin D synthase; sLR11: soluble LDL receptor 11; NGF: nerve growth fibre ; VEGFA: vascular endothelial growth factor A; Metrn1: Meteorin-like protein; IGFBP2: insulin-like growth factor binding protein 2; Slit2-C: Slit extracellular protein 2 c fragment; NRG4: neuregulin 4; IGF1: insulin-like growth factor 1.

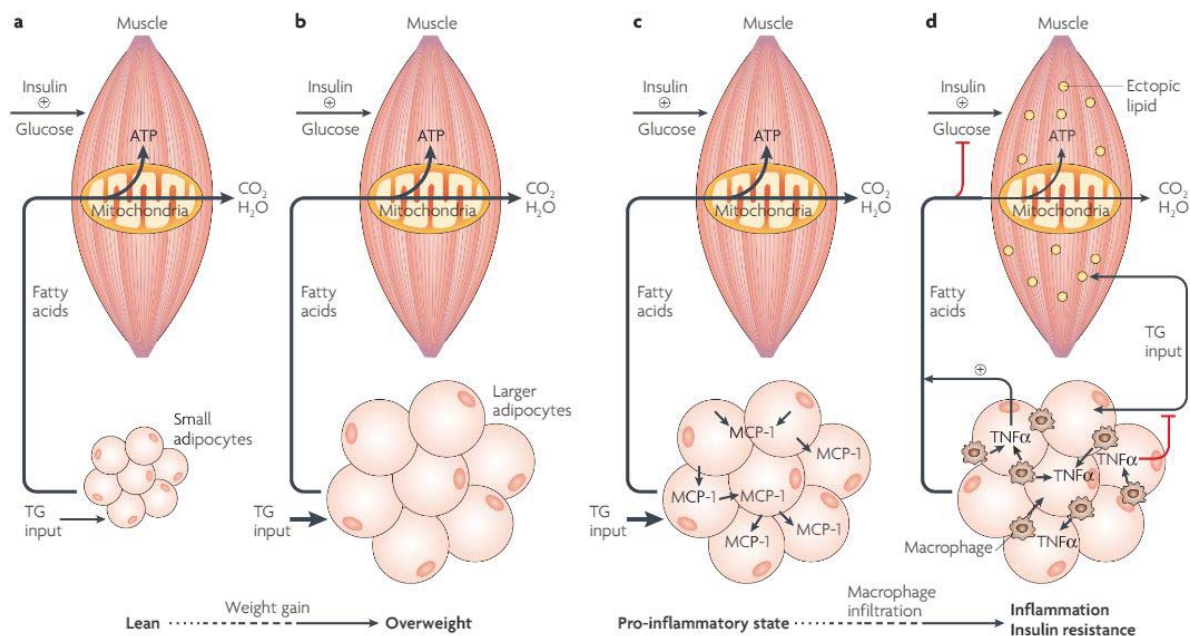


Figure 1.6: Chronic inflammation in adipose tissue triggers insulin resistance in skeletal muscle

This figure is reprinted with permission from ref [60] ©2010, Nature Publishing Group.

### 1.1.3 New methodology for endocrine tissues study?

With increasing knowledge about adipose tissue biology and its central roles in energy homeostasis, further studies are urgently needed to elucidate the functions and mechanisms of adipokines to better understand the pathogenesis of obesity related disorders and for development of therapeutic strategies. Especially important is an improved understanding of the dynamics of the hormone regulatory network. However, common methodology for biological studies is inadequate for this purpose due to high cost, low efficiency, and labor intensive nature, etc. The increasingly maturing microfluidics or organ-on-a-chip technologies provide possible solutions to overcome those bottle necks, as well as offer unique features to conduct studies not possible with macroscale tools. Examples of the benefits of microsystems include decreases in experiment cost and reagent volume, increased temporal and spatial resolution, and *in vivo* vasculature mimic with microfluidic channels. In the next section, microfluidic systems and their applications for improving the understanding of adipose tissue and islets will be introduced.

## 1.2 Introduction to Microfluidics

### 1.2.1 Microfluidics

Microfluidic devices handle and manipulate fluids within micrometer scale channels, with typical internal volumes of  $10^{-5}$  to  $10^{-12}$  litres. Such extremely small fluid volume handling allows integration of one or several lab functions on a single device. Thus, the microfluidic systems are also referred to as “Lab-on-a-chip” (LOC) or “micro total analysis systems” ( $\mu$ TAS). A typical microfluidic device consists of a series of general components: a method to introduce reagents and samples, methods for moving those solutions around on the chip and/or for mixing them, and other devices (such as detectors and purification components) [62]. Depending on the function, manufacturing materials, and detecting system, the design of the devices can be very different. A few examples are listed in Figure 1.7. Regardless their differences, microfluidic devices are designed based on the same basic concept: scaling down fluidic processes to the microscale.

### Precise fluid control at the microscale

At the micrometer scale, the relative gravity effect is greatly reduced compared to the macroscale. Thus, pressure driven flow inside microfluidic channels is typically laminar, in which the fluid in the middle of the channel is at the highest velocity and the fluid next to the surface is at the slowest [69] (Figure 1.8). This feature enables precise control over microenvironments in several ways, for example, permitting chemical gradients, predictable molecular transportation and diffusion, and different surface patterns within microchannels [70].

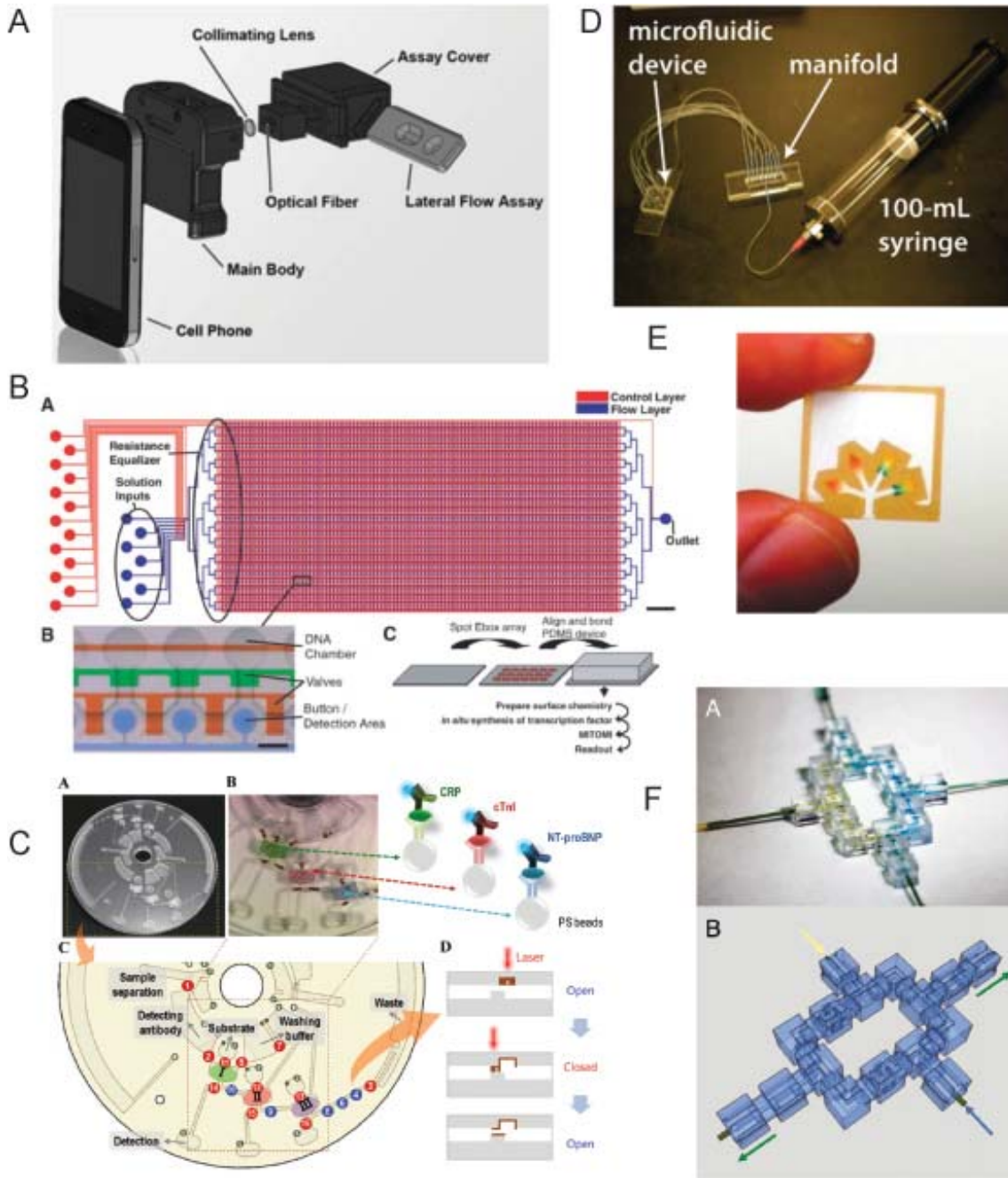


Figure 1.7: Example of microfluidic devices.

A. Cell-phone-based measurement of thyroid stimulating hormone using Mie scatter optimized lateral flow assays. B. Multilayer microfluidics plumbing networks. C. Lab-on-a-Disc for Fully Integrated Multiplex Immunoassays. D. Passively Operated Microfluidic Device. E. Microfluidic paper-based analytical devices ( $\mu$ PADs). F. 3D printed microfluidics. Figure A, B, C, D, E, and F are reprinted with permission from ref [63] ©2012 Elsevier B.V., ref [64] ©2007 The American Association for the Advancement of Science, ref [65] copy right ©2012 American Chemical Society, ref [66] ©2011 American Chemical Society, ref [67] ©2010 American Chemical Society, and ref [68] ©2014 National Academy of Sciences, respectively.

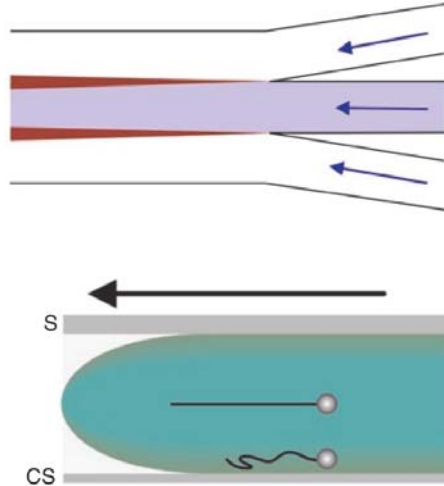


Figure 1.8: Laminar flow

This figure is reprinted with permission from ref [69] ©2008, Nature Publishing Group.

### Impact of microfluidics on biology research

As numerous researches have pointed out [71, 72, 73, 74, 75, 76, 77, 78, 79, 80, 81, 82, 83, 84, 85, 86, 87, 88, 89, 90, 91, 92, 62, 93, 94, 95, 96, 97, 98, 99, 100, 101] microfluidic systems offer many advantages. It would be difficult to exaggerate the revolutionary influences that microfluidic systems bring to areas including chemistry, biology, pharmacology and medicine. In this section, a few examples of successful applications of microfluidics in diagnostics and biology research will be discussed.

**Low cost diagnostics** The inability to diagnose numerous diseases in a timely manner is a significant cause of the disparity of death in the developing countries in comparison to the western countries [102]. Unlike in western countries, most patients in developing countries are treated at health facilities that do not have access to laboratory tests [102]. Alternative ways for low cost, but quick and accurate, diagnostics are urgently needed. Ideally, those methods need to follow the ASSURED criteria [103], which is short for, Affordable, Sensitive, Specific, User-friendly, Robust and rapid, Equipment-free or minimal equipment that can be solar-powered, and Deliverable to those who need them. Several features of microfluidic

devices suggest that they would be ideal for diagnostics in low-resource settings. These include their ability to reduce the consumption and cost of sample and reagents, to integrate multiple steps of liquid handling and detection, to adopt cheap materials (like paper, wax, and cloth. Figure 1.7 E), and to interface with ubiquitous equipment (such as a mobile phone camera. Figure 1.7 A).

As shown in Figure 1.7 E,  $\mu$ PADs (Microfluidic paper-based analytical devices) are a new class of point-of-care diagnostic devices that are inexpensive, easy to use, and designed specifically for use in developing countries. They have been successfully used in the detection of glucose, cholesterol, alkaline phosphatase, and other proteins [67].

**Single cells analysis** Understanding how individual cells process information and respond to perturbation is a central challenge of biology [104]. Much of current knowledge is based on population averaged assays, which refers to experimental measurements derived from assays that pool analytes from a large number of cells or to mathematical averages taken over distributions of single cell measurements. However, cell heterogeneity is now known to be a potential barrier to effective therapeutic intervention [105, 106]. In order to analyze individual cells, three different types of microfluidic structures are often used, namely, valve deflection formed cell isolation chambers, cell encapsulation in surfactant stabilized aqueous droplets in inert carrier oil, or nanowell arrays. Each of these can be used to set boundaries between single cells, capture their specific products, retain their components upon lysis, or perform manipulations [80]. Because of the development of the less expensive and more accessible next-generation DNA sequencing methods (NGS), researchers are able to sequence the transcriptome (mRNA) and whole genome at single cell levels (reviewed in ref [101]). Unlike nucleic acids, proteins lack an amplification mechanism like PCR. However, compared with traditional cell culture chambers, the small and confined microfluidic volumes enhance the immunoassay sensitivity and reaction speeds due to higher relative concentration and minimal diffusive loss [100]. A recently reported microfluidic device with nanowell array for

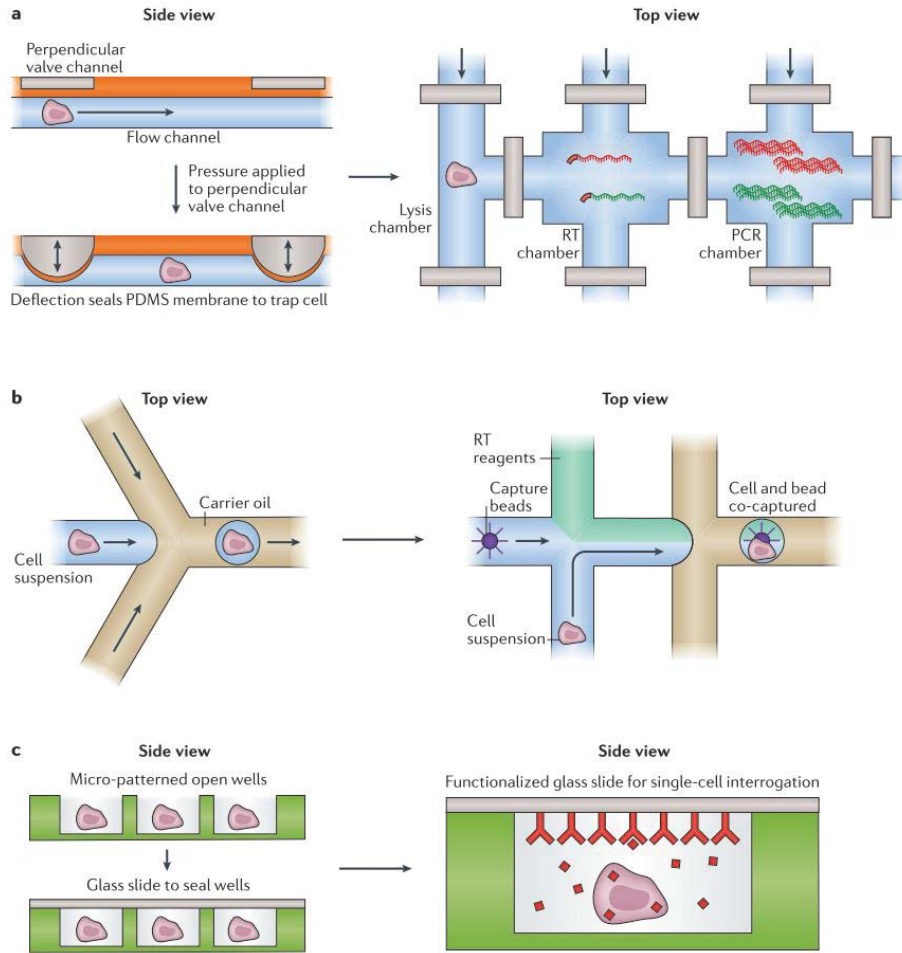


Figure 1.9: Microfluidic cell trapping.

a. Valve-based microfluidics. b. Droplet-based microfluidics c. Nanowells array for confining cells. Figure reprinted with permission from ref [80] ©2017, Nature Publishing Group.

single cell isolation and antibody barcode array for protein detection even achieved codetection of 42 different immune effector proteins from single cells [107].

**Dynamic process analysis** The laminar flows within microfluidic channel are predictable and straightforward to describe mathematically[108]. Pulsing of well controlled flows with cell treatment factors can dynamically and precisely perturb molecular pathways. As shown in Figure 1.10, the cell signaling processes occurs across varying timescales. The timescale of active microfluidic functions ranges from submilliseconds to seconds, which matches with

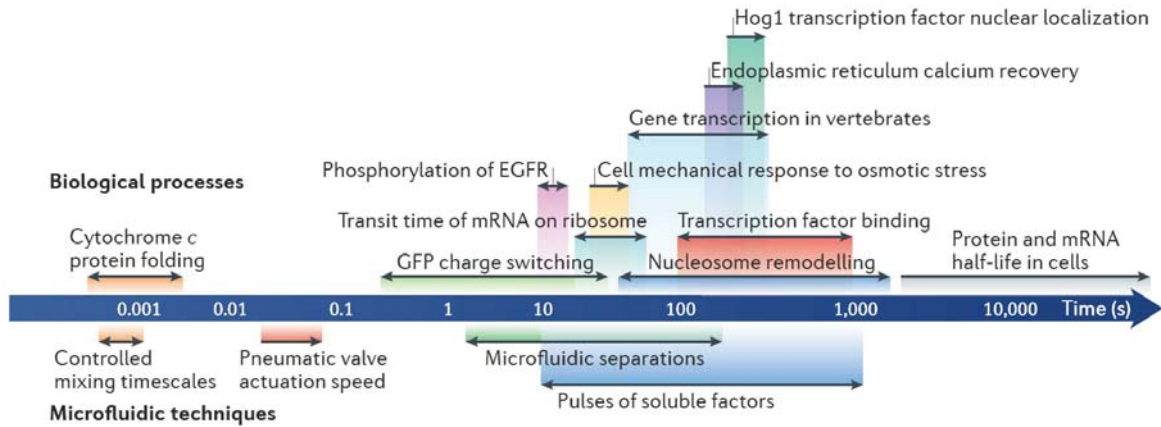


Figure 1.10: Biological dynamic processes time scale.

The logarithmic ruler shows the timescales of dynamic biological processes and the time resolutions of the corresponding microfluidic techniques that can be used to study them (as indicated by corresponding colours). EGFR, epidermal growth factor receptor. Figure reprinted with permission from ref [100] ©2017, Nature Publishing Group.

the transient molecular phenomena that are either not observable or not quantifiable with traditional approaches.

The molecular interactions play key roles in many cell signaling processes. For example, transcription factor-DNA binding partners have dissociation rate at  $0.1 \text{ s}^{-1}$  or slower. To catch the fast dissociation, Quake group developed a pneumatically actuated valves based microfluidic device which utilize the mechanically induced trapping of molecular interactions (MITOMI) (Figure 1.7 B) to rapidly squeeze the solvent out of the binding region by pressing a surface onto a spot of immobilized reagent [64]. In this way, the binding partners were physically trapped together, and the rapid dissociation interaction evaluation was achieved.

**More physiologically relevant *in vitro* model** A very large portion of biology research relies on *in vitro* cell models. The commonly used cell culturing techniques in petri dishes or multiwell plates lack the ability to realistically mimic *in vitro* environments. Microfluidic is well suited to replace the traditional way of cell study due to the capability of accurately

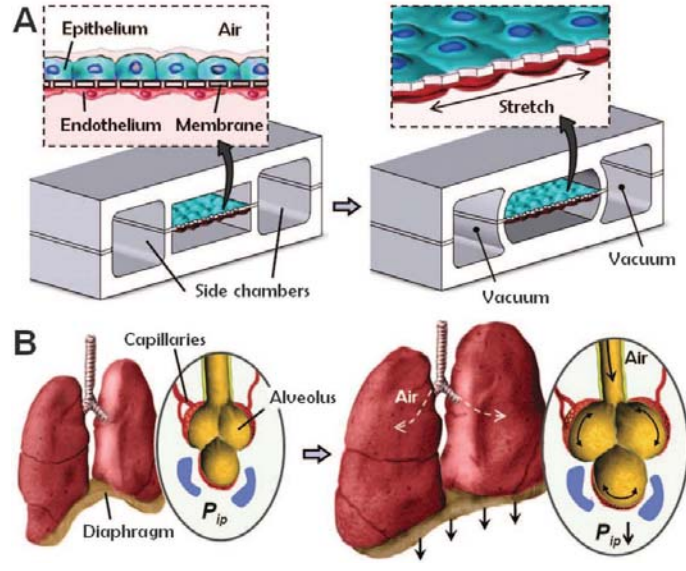


Figure 1.11: Biologically inspired design of a human breathing lung-on-a-chip microdevice. Figure reprinted with permission from ref [110] ©2010, American Association for the Advancement of Science.

flow controlling and forming gradients of stimuli. In addition, a new class of microfluidics, so called “organ-on-a-chip” technologies mimicking an entire organ, is an active area of research. Examples of organ-on-a-chip include gut-on-a-chip [109], lung-on-a-chip [110] (Figure 1.11), blood vessel-on-a-chip [111], cancer-on-a-chip [112], blood-brain barrier-on-a-chip [113], muscle-on-a-chip [114] and kidney-on-a-chip [115]. Of course, those systems are still in their infancy stage, and much more work is still required before the organ-on-a-chip models can be widely used in mainstream biomedical research. Theoretically, those organ-on-a-chip modules could be combined into a complete body-on-a-chip mode that mimics *in vitro* functions, and even eventually replace animal models.

### 1.2.2 Polydimethylsiloxane (PDMS) based microfluidics

The concept of microfluidics was first introduced when the ink-jet technology was developed in the early 1950s [116], and the first microfluidic chip was fabricated in 1979 when gas chromatograph (GC) was miniaturized onto a silicon wafer [117]. With great motivation from the need of analytical methods for molecular biology, such as high-throughput DNA sequencing, researchers started using the well developed semiconductor technologies to create glass or silicon based microfluidic devices in the early 1990s [118]. The earliest silicon and glass microfluidic systems were made with technologies directly adopted from semiconductor industry like wet etching, photolithography, and glass bonding. Those methods suffer from disadvantages including harsh chemicals, long fabrication time, expensive cost, and requirement of a clean room. Those microfluidics systems applications were also limited by material choice. For example, silicon is not transparent to visible and ultraviolet light, thus could not be used with optical detection methods. Both glass and silicon are not gas permeable, which limited their use for live cell culture.

Later, the usage of polymers and plastics for microfluidic device fabrication markedly reduced the cost and complexity of fabrication [62]. Especially after polydimethylsiloxane (PDMS) was firstly used as the material for microfluidics by Biebuyck and et. al. in 1997 [119], microfluidics has seen rapid development (Figure 1.12).

#### PDMS devices fabrication

PDMS is a soft elastomer with unique properties like optical transparency, gas permeability, and deformability. It is commercially available as a kit of two liquid reagents, a “base” and a “curing agent”. The structures and reaction leads to a cross-linked polymer is shown in Figure 1.13 [120]. The siloxane oligomers (Figure 1.13-1) or the “base” react with the crosslinker (Figure 1.13-2) or the “curing agent” via platinum catalyzed hydrosilation reaction. The multiple reaction sites on the “curing agent” molecules allow for three

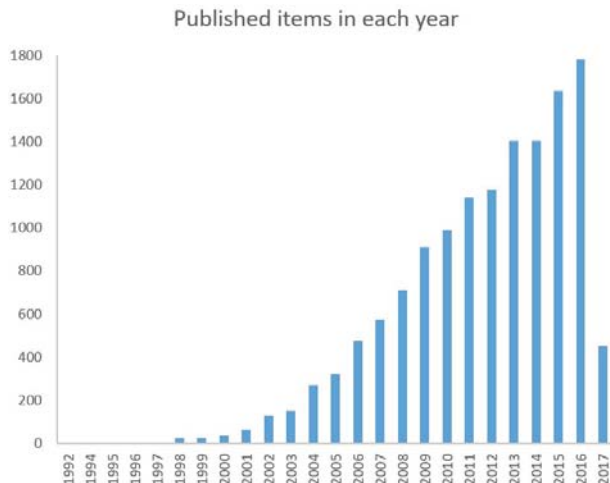


Figure 1.12: Growth of publications related to microfluidics.

Search result from ISI web of science with “microfluidics” as the key word (April, 18, 2017).

dimensional cross-linking to form a soft solid. It is worth mentioning that no waste is generated because the reaction type is an addition reaction. By changing the ratio of the two reactants, the properties of the resulting cured elastomer can be altered. Multiple layers of PDMS made from various curing ratios will continue to react on the contacting interface to form a single piece of PDMS, which is a great advantage for multilayer PDMS fabrication. If the PDMS is not fully cured, the uncrosslinked oligomers can leach into solutions and result in contamination or toxicity to the biology samples or cells. So, PDMS based microfluidics devices are normally thermally aged before use.

PDMS based microfluidic devices are fabricated using soft lithography technology (Figure 1.14) [94]. A silicon wafer with raised channel templates is first created by photolithography as a master mold. Channels are designed using computer-aided design tools and then printed as high resolution photomasks. Depending on the photoresists used, the photomasks are printed either mostly opaque except the channels, or only the channel designs are opaque. For negative photoresist, only the UV-exposed regions polymerize and stay on the wafer. In comparison, positive photoresist becomes soluble in developer after UV exposure and unexposed portions remain insoluble and stay on the wafer. Most of the devices shown in this dissertation were fabricated with combinations of negative photoresist (SU-8) and positive

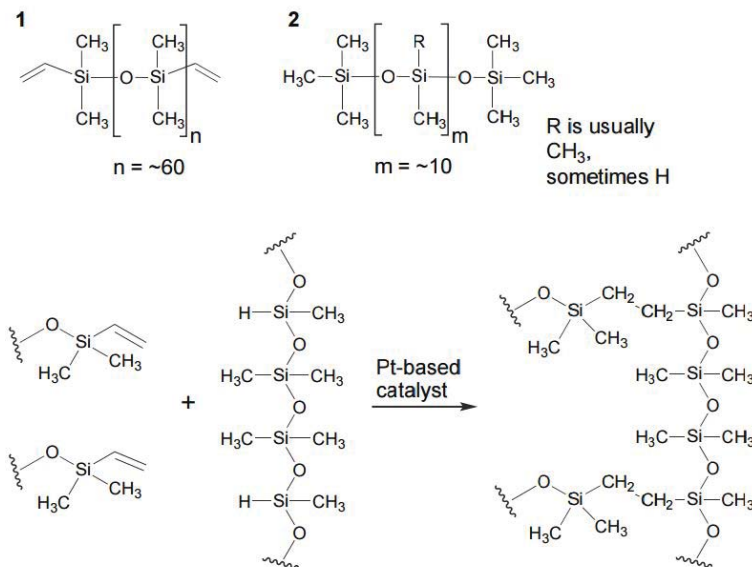


Figure 1.13: PDMS.

The structure of PDMS "base" (1) and "curing agent" (2), and the cross-linking reaction to form PDMS. The Pt-based catalyst is contained in the base liquid. This figure is reprinted with permission from ref [120] ©1999, American Chemical Society.

photoresist (AZ 40XT).

Once the photoresist structure is patterned on the wafer surface, the mixed and degassed liquid prepolymer of PDMS is poured onto the surface of the master wafer. After thermally curing, the layer of PDMS, which contains the inverse of the original pattern embossed on the surface of master wafer, is carefully peeled from the wafer and is then ready to use. One advantage of softlithography is that the template master can be used repeatedly to make hundreds of replicas, which largely reduces the fabrication time and cost. It also eliminates the need for clean room equipment and dangerous chemicals.

The patterned PDMS is cut into individual devices, and holes are punched for sample inlets and outlets. Each replica of PDMS is then bonded to a glass substrate or another layer of PDMS to form microchannels. The most commonly used bonding method is plasma oxidation. A plasma cleaner generates oxygen radicals to attack the  $\text{Si-CH}_3$  bonds and convert them to  $\text{Si-OH}$  groups. When two plasma oxidized surfaces come into contact, the condensation reaction between silanol groups creates an irreversible, strong bond capable

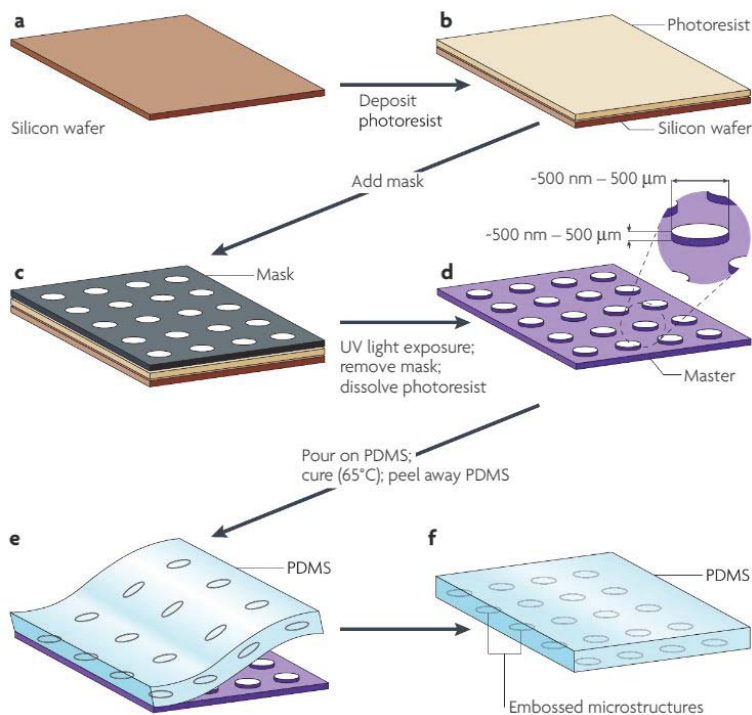


Figure 1.14: Soft lithography for micropatterned PDMS.

This figure is reprinted with permission from ref [94] ©2017, Nature Publishing Group.

of withstanding high pressure. Although the PDMS surface is inherently hydrophobic, the plasma oxidation induces silanol groups, which allows further surface treatments to change the surface property to meet the need for different applications including electrophoresis, cell attachment, immunoassay, biomolecule attachment, droplet generation, and others. The commonly used surface treatment includes plasma oxidization, layer-by-layer deposition, sol-gel coating, silanization, and dynamic surface modification. Because the migration of uncrosslinked PDMS oligomers can revert the surface back to its original state [121], the surface treatment should be done immediately after plasma oxidization.

### Properties of PDMS

Obliviously, PDMS is not the only material used to fabricate microfluidics devices. As shown in Figure 1.7, it is possible to make microfluidic devices with various materials, including glass, silicon, polymers other than PDMS, plastics, paper, cloth, and many other

materials. Compared with those materials, PDMS has its own limitations. For example, PDMS has been shown to leach uncrosslinked oligomer into the solution [122] and to absorb small molecules [123]. Additionally, high-throughput methods such as injection molding cannot be used with PDMS, thus it is not easy to scale up for manufacturing. Among many microfluidic supplier companies [75], very few of them (such as Fluidigm and SynVivo) provide PDMS based microfluidic systems.

In academic settings however, there are several key features of PDMS which made it the most popular in microfluidics. First, the relatively cheap and easy set-up for fabrication. Second, the ability to tune the surface property to fit for many different requirements is an advantage. Third, the ability to bond reversibly and irreversibly to glass, plastic, PDMS itself, and many other materials is important. Forth and perhaps most important, the elasticity of PDMS allows fabrications of multilayer microfluidics with integrated microvalves (discussed in detail in Section 1.2.3).

### **Other materials for multilayer microfluidics**

It is certainly feasible that other materials could be used for multilayer microfluidics with valves. In 2004, in collaboration with the DeSimone group, the Quake group introduced a photocurable perfluoropolyether (PFPE) material for microfluidic device fabrication to overcome the drawback of PDMS swelling in most organic solvents [124]. Compared to PDMS, this PFPE elastomer has low surface energy, low modulus, high gas permeability, low toxicity, and is extremely chemically resistance. More importantly, actuation of valves with pressurized air was accomplished with this material. However, although they mentioned "Current efforts to use a PFPE-based device in a novel approach to DNA synthesis are underway" towards the end of the paper [124], their later (2010) report of microfluidic oligonucleotide synthesizer [125] was made of PDMS! Instead of changing from PDMS to PFPE devices, the solvent used in deprotection step of the standard solid phase oligonucleotide synthesis procedure was changed from dichloromethane to acetonitrile to ensure solvent compatibility

with PDMS. While efforts were undoubtedly made to switch materials, PFPE elastomer was not mentioned in this work [125]. This partially supports the irreplaceable status of PDMS in the microfluidics field to-date, especially for the active microfluidic systems using pneumatic valving.

### 1.2.3 Active microfluidic systems using pneumatic valving

In 2000, Stephen Quake's group introduced revolutionary multilayer PDMS based microfluidic devices with integrated elastomer microvalves [99]. Since then, there has been remarkable progress in this field, and the complexity and capabilities of PDMS devices have improved exponentially [126] (Figure 1.15).

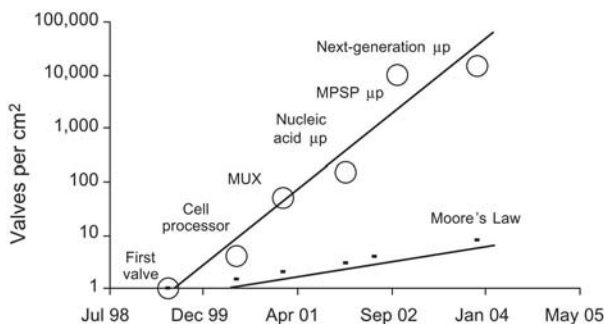


Figure 1.15: The analog of Moore's Law for nanofluidic systems.

The current growth rate of Valve densities in fluidic chips is four times faster than the rate of growth of transistor densities in the semiconductor industry. MPSP, massively partitioning sniper processor;  $\mu$ p, microprocessor; MUX, multiplexer. This figure is reprinted with permission from ref [126] ©2003, Nature Publishing Group.

### Elastomeric microvalves

One simple analogy of the operational mechanism of the PDMS microvalve is stepping on a soft garden hose. The hose is squeezed and shut by the pressure from the foot, and water stops flowing. PDMS microvalves contain a thin membrane that can be deflected by an external pressure and can block flow in the microchannel below or above the membrane. When pressure is relieved, the elasticity of the PDMS causes the membrane to return to the original position and open the channel. As shown in Figure 1.16, PDMS microvalves typically have 3 fundamental arrangements (push-down valve, push-up valve, or both push-up and push-down valves). Those structures are produced by molding from two or three master wafers and sealing the layers together [99].

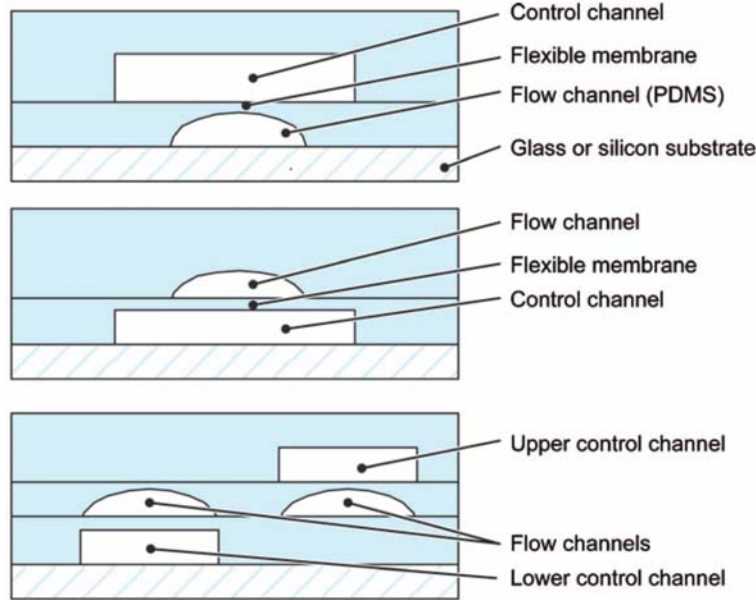


Figure 1.16: PDMS based elastomeric microvalves.

This figure is reprinted with permission from ref [127] ©2007, Annual Reviews.

The top layer is cast thicker for mechanical stability, where the other layers are spin coated onto wafers as thin membranes. Each layer is partially cured separately. The thick layer is then sealed onto the next thin layer. The bonded layers can then be sealed to another thin layer to form multilayer devices. The flowing fluidic channel must have a rounded cross-section to ensure complete closing (normally made from a wafer patterned with re-flowed photoresist such as AZ). If the control layer is bonded on top of the flow channel, push-down valves are formed. The push-up valves are made by bonding the thick, upper flow layer to the thin control layer.

The push-up valve arrangement requires smaller pressures to operate due to the membrane shape, thus it is more suitable for taller flow channels. However, the push-down valve allows the combination of liquid control with functionalized surfaces (such as DNA arrays). By combining both push-up and push-down valves in a single device, a higher density of valves and increased capabilities can be achieved [127, 97].

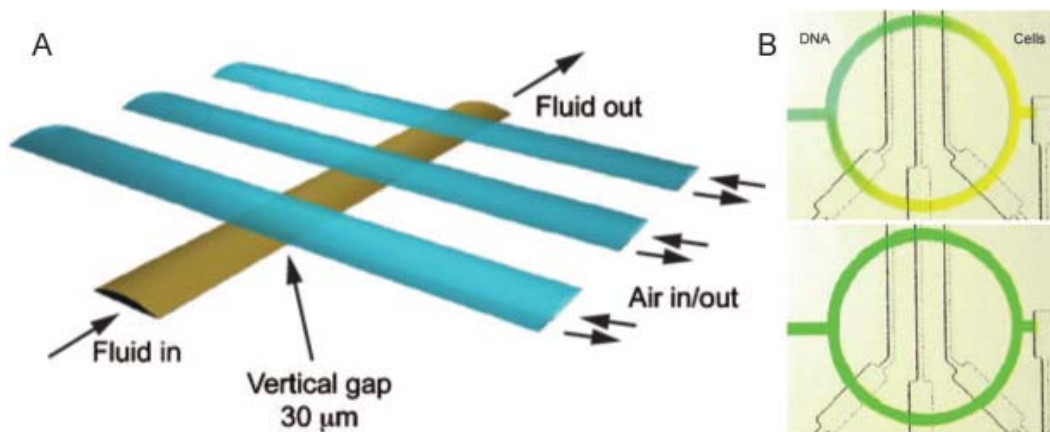


Figure 1.17: Peristaltic pumping and rotary mixer.

A. Schematic of a linear peristaltic pump using three membrane valves in a series. B. Rotary micromixer, where two colored liquids (aqua,DNA; yellow, cells) are loaded into the mixing loop and completely mixed after actuating the peristaltic pump. This figure is reprinted with permission from ref [127] ©2007, Annual Reviews.

## Pumping and mixing

Let's continue to use the water in hose analogy. Just as water within a flexible tube can be pumped in a peristaltic way, fluid can also be pumped by sequentially actuating a linear array of valves (Figure 1.17 A). Peristaltic pumping occurs when at least three valves are actuated in a 6 step pattern (101, 100, 110, 010, 100, 001), or a 5 step pattern (100, 110, 111, 001, 101), where 0 and 1 represent open and closed valves, respectively. In each pumping cycle, the maximum net volume dispensed down stream equals the volume displaced by the center valve membrane upon closing. Various flow rates can be achieved by changing the pumping frequency. The flow rate increases linearly with the pumping frequency, until the pumping frequency passes a certain threshold, where the membrane suffers from incomplete closing and opening [99].

Due to the laminar nature of flow in microfluidics, when two fluid streams come together in a microchannel, they flow side by side, and the only mixing is the result of diffusion of molecules across the interface between the fluids. Although some methods to speed up microfluidic mixing have been developed, such as introducing chaotic advection effects by increasing the contact area and/or contact time between mixing species, those passive mixing

mechanisms do not meet the requirement of many dynamic studies.

By simply combining a rotary geometry with a peristaltic pump, a more powerful mixer is achieved (Figure 1.17 B). After confining the reagents in the rotary channel, the valves pump the fluid circularly. As the center part of liquid travels faster than the liquid close to the channel walls, the rapid stretching and folding result in an increased interface between the two reagents, and a shorter diffusion distance is needed for mixing. Mixing times can be reduced to seconds compared to several hours for passive diffusion. As a versatile component, rotary mixer can be integrated with other components for a wide variety of biological and chemical assays.

### **Precise volume metering**

Precise metering of small volumes of liquid can be achieved in several ways. Firstly, as mentioned earlier, the peristaltic pump dispenses a predictable volume with each cycle, thus the sample volume can be controlled by pumping a controlled number of cycles. Secondly, two valves on the channel can be used like an injection loop to define the volume. Thirdly, since PDMS is gas permeable, an empty dead-ended chamber can be filled by pressurizing the solution. Upon filling, the valve at the interface is closed to confine the exact volume within the chamber.

### **Multiplexers**

Pneumatic microvalve-based microfluidic multiplexers were introduced soon after the invention of PDMS valving [97]. As in analogous electronic components, the microfluidic multiplexer can address large numbers ( $N$ ) of fluid channels with a smaller number ( $2\log_2 N$ ) of pneumatic controls and is normally used as one utility component of larger, integrated microfluidic frameworks. In the first design (Figure 1.18 A), cross-contamination between flow channels can occur because of the dead volume at the outlet. A later design based on a binary tree largely reduced this cross-contamination (Figure 1.18 B). A combinatorial

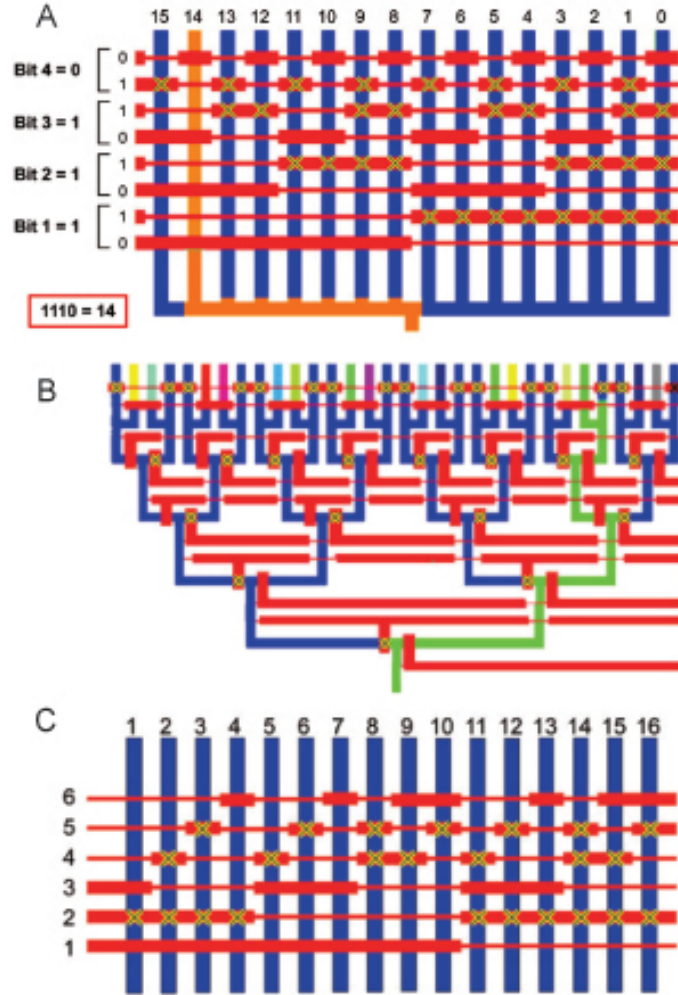


Figure 1.18: Microfluidic multiplexer.

This figure is reprinted with permission from ref [127] ©2007, Annual Reviews.

multiplexer has even higher efficiency (Figure 1.18 C) [128]. This device uses all the possible combinations of addressing valves, which is able to address  $N!/(N/2)!^2$  flow channels with only  $N$  control channels (for 16 control lines, 12870 lines can be addressed, compared with 256 addressable lines with binary method).

### Sieve valves

The sieve valves is another type of valve whose flow channel has a rectangular profile instead of a rounded profile. When the valve is closed, the edges of the valves are not sealed which allows liquid pass through (Figure 1.19 A) [129]. It is intentionally created for trapping

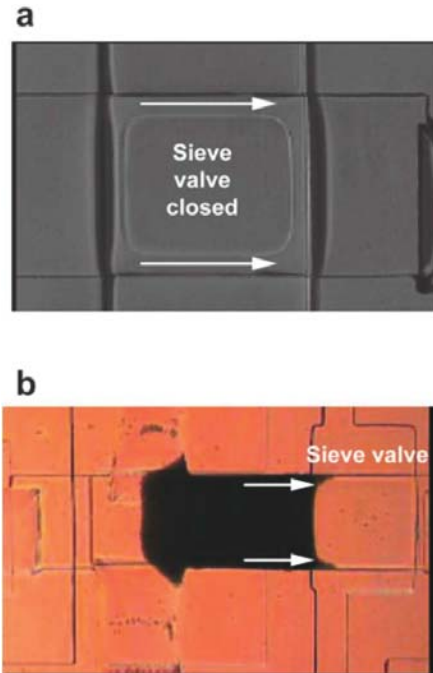


Figure 1.19: Sieve valve.

a. Leakage occurs along the edges of a rectangular profiled flow channel when the valve is actuated. b. A birds-eye view of a stacked affinity column of microspheres upstream of a sieve valve. This figure is reprinted with permission from ref [127] ©2007, Annual Reviews.

affinity columns of bead by blocking the movement of beads, but allowing reagents to flow through (Figure 1.19 B).

### Valve control system: solenoid switches and programming languages

Automated microfluidic chip control through on-chip valving requires hardware to deliver pressure to specified valves and software to implement different sequences of valve switching. Normally, an air pressure source is connected to solenoid arrays that directly pressurize specified valves on the chip. The solenoids are controlled with a computer through the DAQ (data acquisition) system. An application written in MATLAB, Python, LabVIEW or other computer programming languages enables the automation of chip function (see one example of detailed protocol in ref [130]).

## Microfluidic Large-Scale Integration

Just as complex electrical circuits consist of basic electronics including resistors, capacitors, transistors, and op-amps, sophisticated microfluidic based biology assays can be achieved by integration of multiple basic microfluidic modules such as valves, pumps, mixers, and multiplexers. Those integrations, often referred to as microfluidic large-scale integrations, have already been used in many areas of biology and chemistry, such as single cell transcriptome analysis [131], human antibody repertoire analysis [132], single-cell RNA-Seq [133, 134], tumor mutation detection [135], circulating cell-free DNA detection [136], gene expression and genome mutation correlation study [137], protein interaction measurements [138], transcription-factor binding site characterization [139], single-cell NF-kappaB signaling dynamics [140], on-chip oligonucleotide synthesis [125], noninvasive shotgun sequencing DNA from maternal blood [141], rational screens for protein crystallization [142], automated quick synthesis of short lifetime radioactive imaging probe [143], and other applications. Given the fact of its successful application in all of those areas and that one of the top microfluidics companies, Fluidigm [75], continues to grow, microfluidic large-scale integration is a revolutionary technology which will remarkably change the way of biology researches is conducted. This dissertation work provides another example of how this methods can provide novel insight into endocrine tissue dynamics, as discussed in the chapters to follow.

#### 1.2.4 Droplet based microfluidic systems

Droplet microfluidics is a sub-field of microfluidics that focus on making tiny water-in-oil droplets containing  $pLs$  to  $nLs$  solution at high frequency (up to several  $KHz$ ). Each of those droplets behaves as an individual nano-reactor. Consider the standard multi-well plate assays need at minimum  $1 \mu L$  volume, this "small" volume is big enough for making thousands to millions of microfluidic droplets. Obviously, the droplets increase throughput by reducing reaction volume and increasing the rate of assay performing. More importantly, the droplet systems have other unique advantages (such as single molecule confinement, single cell manipulation, high temporal resolution and et. al.), which will be discussed in details in the following sections.

#### Droplet generation

In 2001, the Quake group described the first discovery of monodisperse droplet formation in a T-junction microfluidic channel [144]. Since then, several different ways of droplet formation were reported. A few of them are summarized in Figure 1.20.

**T-junction generators** (Figure 1.20 A) with two perpendicular channels bring the two phase together, where the front of the dispersed fluid intrudes into the continuous phase and form droplet when the shearing force overcomes the interfacial tension.

**Flow focusing** (Figure 1.20 B) is another option for generating droplets. The dispersed phase is introduced in the center channel while the continuous phase enters from two side channels. The continuous phase squeezes the dispersed phase into droplets when they pass through the small orifice. Droplets formed in this way are normally more uniform in size

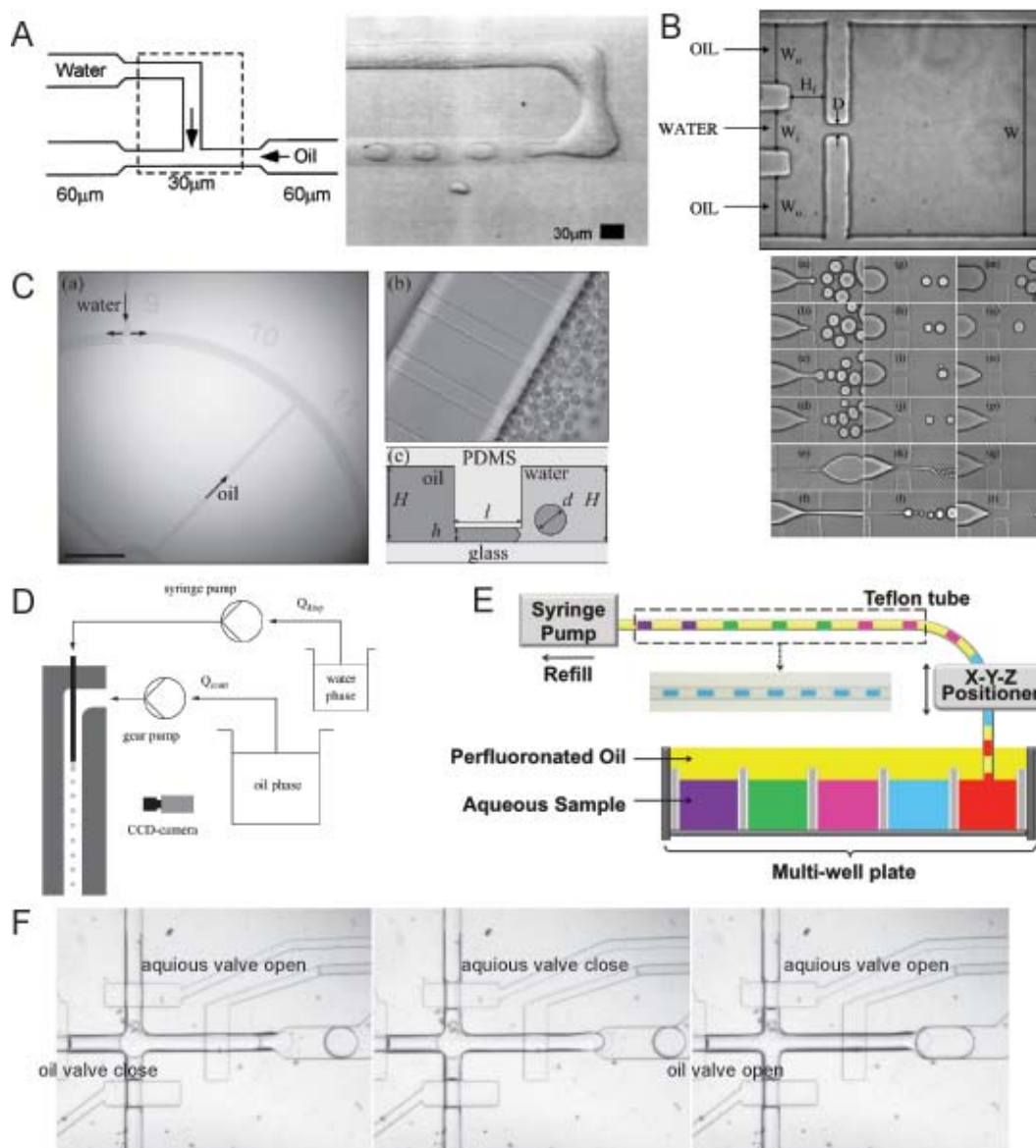


Figure 1.20: Droplet formation.

A. T-junction channel. B. Flow focusing. C. Step emulsification. D. Co-flow. E. oil-segmented droplet formation from multiwell plates. F. Valve segmentation based droplet formation. The figures A, B, C, D, E is reprinted with permission from ref [144] ©2001, American Physical Society, ref [145] ©2003, AIP Publishing LLC., ref [146] ©2014 AIP Publishing LLC., ref [147] ©2004 Elsevier Ltd, and ref [148] ©2012 American Chemical Society, respectively. Figure F is unpublished data, details shown in Chapter 4.

than the ones formed in T-junctions. By changing the flow rates, various sized droplet can be generated at various frequencies (up to several  $kHz$ ).

**Step emulsification** (Figure 1.20 C) is based on the fact that when a liquid is forced into strong curvature, the large pressure drop across the interface breaks the liquid into small droplets. Since the droplet size is mainly depending on the geometry and less influenced by the pressure difference between the two phases, it is often used in parallel to create a large number of uniform droplets.

**Co-flow** (Figure 1.20 D) is very similar to flow focusing, where droplets are also generated by a co-flowing geometry. This system is normally made by inserting a thin capillary into another channel. One advantage of this system is that higher order emulsions can be generated (such as water-in-oil-in-water droplets [149]).

**Oil-segmented droplets from multiwell plates** (Figure 1.20 E) is a new way to generate droplets from multiple samples within a multiwell plate. A robot arm positions a Teflon capillary to dwell in sample or oil for a predetermined time and then moves to another well. The syringe pump operates in refill mode at a constant flow rate. The size of the droplets and space in between are controllable. This technique allows interfacing the traditionally used multiwell plate based assays to droplet based assays.

**Mechanical segmentation** (Figure 1.20 F) induced droplet formation is based on valve actuation. The valves controlling the aqueous channel and the oil channel are alternatively opened and closed to permit oil and aqueous flow to generate droplets. More details of this mechanism will be discussed in Chapter 4.

## Oils and surfactants

Fluorocarbon oil is normally used as the continuous phase in biological applications because of the following reasons. Those oils are both hydrophobic and lipophobic, hence they have low solubility for biological reagent and eliminate molecular diffusion between droplets. Additionally, unlike other oils such as mineral oil, the fluorocarbon oils do not swell the PDMS. Finally, the gas permeability of fluorocarbon oil made cell culturing in droplets possible.

Surfactants need to be added to the oil to stabilize the droplets, or they coalesce. Short chain fluorotelomers have been used but do not provide sufficient droplet stability. Earlier, the only commercially available perfluorinated surfactant offering long term stabilization was an ionic surfactant such as "Krytox" by DuPont. However, their charged headgroup interacts with biomolecules within droplets.

Several non-ionic and biocompatible surfactants were synthesized based on Krytox [150, 151] (Figure 1.21) to overcome the non-biocompatible issues but retain the stability. The most famous one, PFPE-PEG-PFPE or "Kry-Jeffa" (Figure 1.21 A) synthesized by Weitz and et. al. in 2008 [150], which is widely used in single-cell-in-droplet study and digital PCR (will be discussed in details in next subsection), has now become commercially available from several sources, such as RainDance Technologies, RAN Biotechnologies, and Dolomite.

Other ways to introduce biocompatibility without synthesis are also achieved by additives such as our group's Jeffamine ED-90 (polyetherdiamine) [152], or bovine serum albumin (BSA) [153] to shield the droplet surface and to eliminate the ionic surfactant-biomolecule interaction. A protein-surfactant interaction study will be discussed in Chapter 5.

## Droplet manipulation

Many technologies have been developed to manipulate droplets for various purposes, such as droplet formation, droplet reinjection, pico-injection, droplet merging, droplet sorting, and other modules.

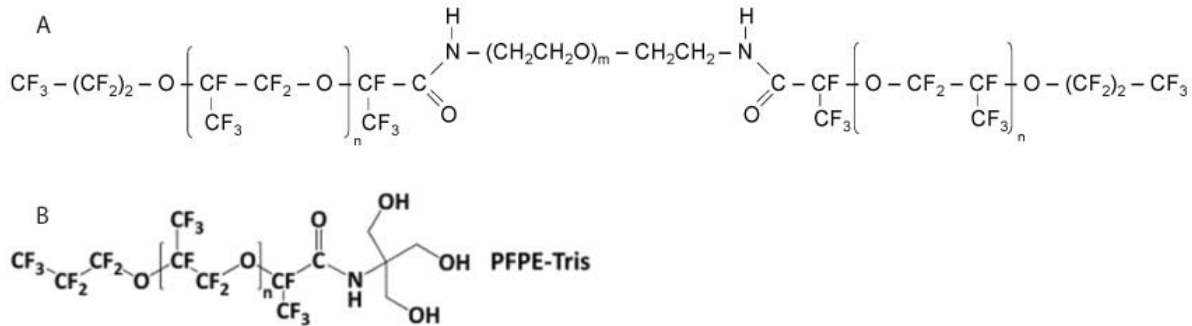


Figure 1.21: Biocompatible surfactants.

A. Synthesized surfactant PFPE-PEG-PFPE triblock copolymers. B. Synthesized surfactant PFPE-Tris. Tris: tris(hydroxymethyl)aminomethane, PFPE: perfluoropolyether. The figures A is reprinted with permission from ref [150] with permission, ©2008, Royal Society of Chemistry. The figures B is reprinted from ref [151] with permission granted from ACS AuthorChoice.

**Droplet sorting** is perhaps the most important application in droplet microfluidics. Fluorescence is the most common readout to determine whether a droplet should be sorted or not. The fluorescence generated from the in-droplet reaction or introduced by fluorescently labeled cell in droplet triggers various mechanisms to guide the droplet into a non-default channel. For example, in Figure 1.22 A, by using the pneumatic valve to squeeze the default channel (upper, with lower hydrodynamic resistance), droplets can be sorted to the lower channel at 250 Hz [154]. Another sorting mechanism is based on the electric field [155]; with an AC field applied in-plan the electrodes, droplets were deflected into the upper channel. In the absence of a field, the droplets flowed into the lower channel due to the lower hydraulic resistance (Figure 1.22 B). This electric field based system allows high speed sorting up to 2000  $Hz$ .

**Droplet merging** As most biological assays require sequential addition of reagents, for droplet microfluidics systems to be more useful, it is essential to develop a robust procedure for adding reagents into droplets. It sounds straightforward to merge two or more droplets with different contents in order to start or stop a reaction or to dilute a sample. However, because surfactant is added to the oil to stabilize the droplets, to separate droplet, and

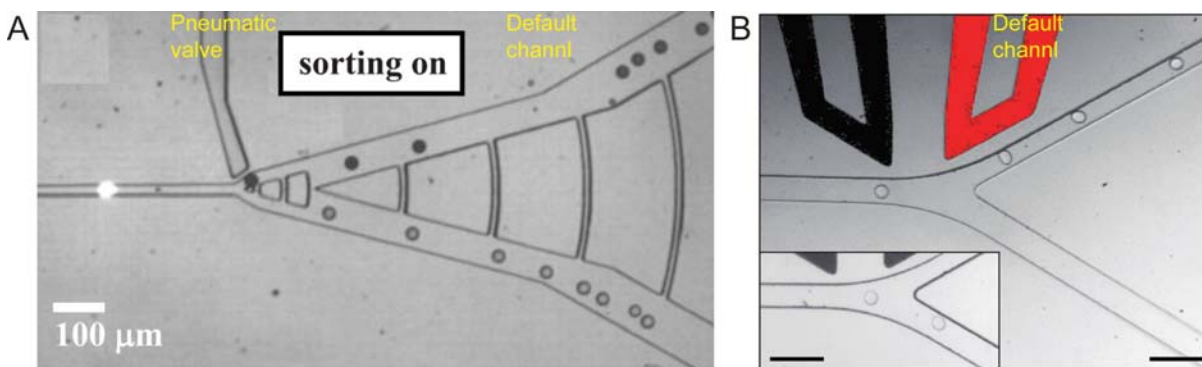


Figure 1.22: Droplet sorting.

A. Applying a pressure to the pneumatic valve changes the path of least resistance from the upper to the lower channel. B. By activating the electrode (red) an electric field gradient is created forcing water droplets to the upper channel. Figure A and B are reprinted with permission from ref [154] with permission, ©2010, AIP Publishing LLC, and ref [155], ©2009, Royal Society of Chemistry, respectively.

to ensure no crosstalk between droplets, droplets do not coalesce without external force. In fact, droplets made with certain fluorinated surfactants remain stable for years [156]. Electrocoalescence is the most adopted way to merge droplets. Two or more droplets in an electric field will be polarized as charges accumulate at the surface. If the interfaces between droplets are charged oppositely, the result is droplet coalescence [157] (Figure 1.23 A).

**Picoinjection** is another way for reagent addition into droplets. When an electric field applied, as the droplets pass through a pressurized channel, reagents are directly injected into the droplet [158] (Figure 1.23 B). Compared with the droplet merging technology, pico-injection does not require synchronization of two streams of droplets. In the original design of picoinjector, the electrodes were fabricated with low-temperature metal solder, which was the most complex step for the device fabrication. The Abate group simplified the fabrication of the picoinjector by using salt water electrodes [160] or applying the voltage through the injection fluid itself [161]. Moreover, during the picoinjection process, the droplets temporally merge with the injection fluid, which allows potential material transfer between droplet and reagent fluid or between droplets. To address the problem, the Bailey group [159] introduced

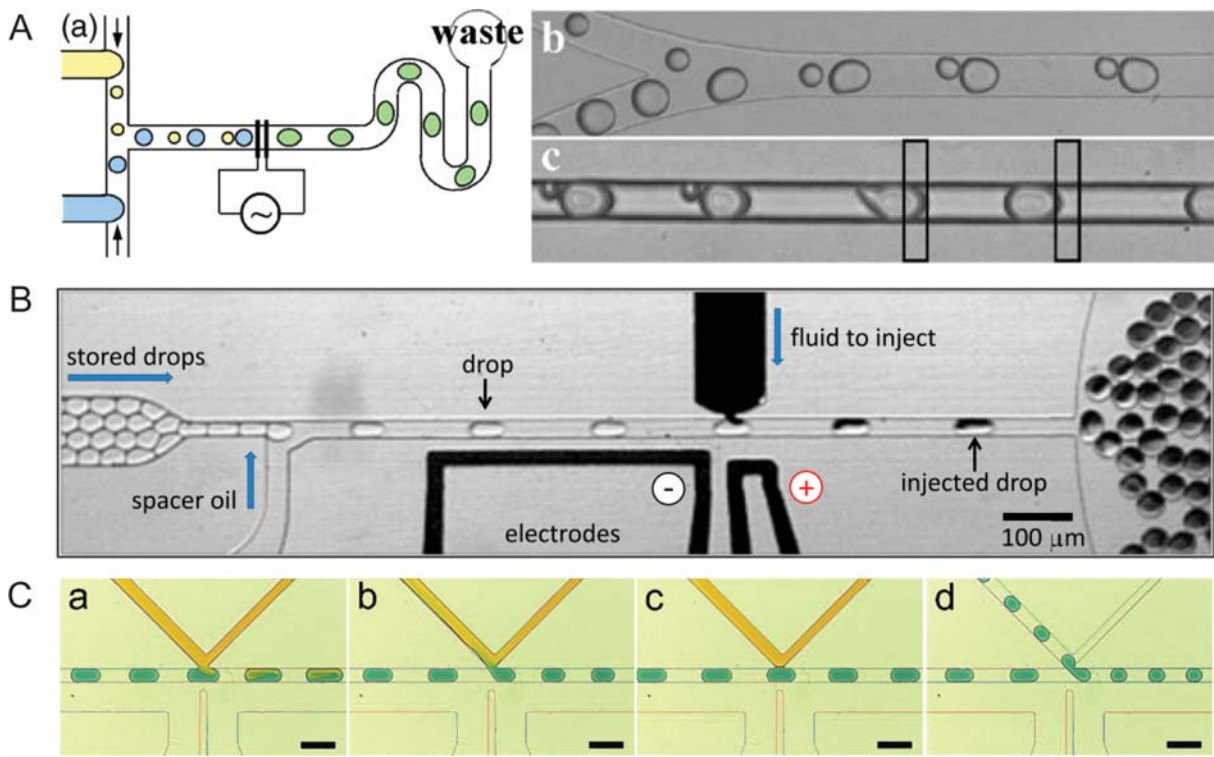


Figure 1.23: Picoinjection and droplet merger.

A. Droplet merger. B. Picoinjector. C. K channel droplet operations. Figure A, B, C are reprinted with permission from ref [157], ©2006, AIP Publishing LLC, ref [158], ©2010, National Academy of Sciences, and ref [159], ©2017, American Chemical Society, respectively.

a cross-channel flow, the "K-channel", to the segmented droplet flow to enable several operations on passing droplets. Different operation modes allow K-channels to achieve reagent injection, fluid extraction, and droplet splitting (Figure 1.23 C).

**Other droplet manipulation technologies** including splitting, trapping, reinjection, and incubation (reviewed in ref [162, 163, 164]), together with sorting, merging, and picoinjection, are important droplet manipulation modules that can be integrated in one device to meet the requirement of various complexed biology assays, such as single-cell-in-a-drop (Figure 1.9 B).

### Digital molecule detection

One important concept introduced by droplet base microfluidics detections is "digital" measurement. If the sample is sufficiently diluted, it is possible that only one or zero target molecules is compartmented within one of the  $pLs$  to  $nLs$  volume droplets. After a certain amplification mechanism such as PCR (polymerase chain reaction) amplification for nucleic acids [165, 166], an absolute number of the target molecules can be determined by counting the numbers of "positive" (in which target molecules are present) droplets versus "negative" (in which target molecules are not present) droplets. It is inevitable that two or more molecules are confined within one droplet because of the Poisson distribution of the molecule partitioning ( $P(n) = \frac{c^n e^{-c}}{n!}$ , where  $P(n)$  is the probability of a droplet containing  $n$  copies of target molecules,  $c$  is the averaged number of target molecule per droplet, and  $e$  is Euler's number, 2.71828...). The exact concentration of the target molecule is calculated with the following equations.

The probability that a empty droplet is:  $P(0) = e^{-c} = \frac{N_{neg}}{N_{total}}$ , where  $N_{neg}$  and  $N_{total}$  are the number of negative droplets and total number of droplets, respectively.

The average number of target molecule in each droplet is:  $c = -\ln(\frac{N_{neg}}{N_{total}}) = -\ln(P(0))$ .

Then, the concentration of sample is:  $C_{target} = \frac{c}{V_{droplet}}$ , where  $V_{droplet}$  is the volume of a single

droplet.

The 95% confident bounds (cb) of the average number of molecules ( $c$ ) can be calculated as:

$$c_{cb} = c \pm 1.96 \cdot \sqrt{\frac{N_{total} - N_{neg}}{N_{total} \cdot N_{neg}}}.$$

It is obvious from these expressions that increasing the total droplet number ( $N_{total}$ ) and keeping the proportion of negative droplets high ( $N_{neg}$ ) by dilution makes the digital measurement more accurate. Compared with other ways of sample compartment methods, such as valve based compartments and nanowell arrays (Figure 1.9 a and c), droplet systems allow several orders of magnitude higher numbers of individual partitions [167]. For example, the commercially available droplet based RainDance digital PCR allows up to 80,000,000 droplets to be formed per sample with only \$30 cost. Valve based digital PCR from Fluidigm (EP1) only allows 36,960 partitions per chip, and nanowell array based system from Life Technologies (OpenArray RealTime PCR) allows only 3,072 partitions per plate.

Digital PCR has been successfully used to significantly improve rare gene mutation detection, mRNA detection, virus and other low-level pathogens diagnostics [168]. Other examples of digital molecule detections include digital detection of proteins by incorporating proximate ligation assay (PLA) into droplets[169], and digital detection of enzymes with fluorogenic substrate in droplets [170].

It is imaginable that detecting up to millions of droplets can be time consuming, especially with single point detectors by which droplets are passing (as the one used for droplet sorting in Figure 1.22 A). Imaging in-parallel or 2-dimensional droplet measurement is still not sufficient given the large number of droplets. In 2014, the Zhao group [171] developed an integrated comprehensive droplet digital detection (IC3D) technology for high-throughput droplet detection in a 3-dimensional way. The IC3D droplet detection system consists of a small microscope that has a horizontal geometry and a mechanical sleeve that holds a cylindrical cuvette of diameter 1 cm. Two motors provide rotational and vertical motion of the cuvette. The excitation light generated by lasers is focused at the volume of observation. As the motors rotating, the positive droplets pass through the detection region,

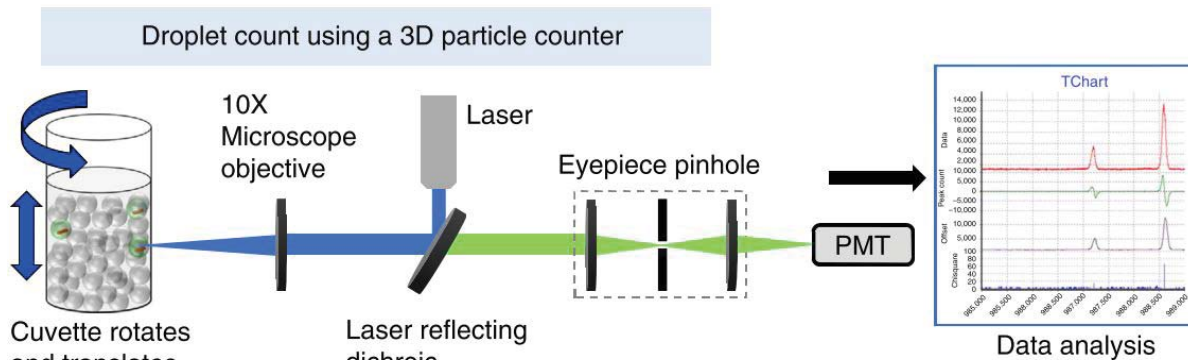


Figure 1.24: Droplet count using a 3D particle counter.

In the IC 3D, droplets are collected and analysed using a high-throughput 3D particle counter that permits accurate detection of single-fluorescent droplets in a several millilitre pool of non-fluorescent droplets within minutes. This figure is reprinted with permission from ref [171] with permission, ©Nature Publishing Group

the fluorescence emitted is collected by PMT detector. By fitting the data into a Gaussian distribution pattern recognition algorithm, positive droplets are detected. In this way, the time for measurement is largely reduced, as well as larger amount of sample ( $mLs$ ) can be analyzed.

### Analog measurements with high temporal resolution

Analog measurement is referred as a quantitative measurement of chemical concentration within single droplets. Compared with the recently well-adopted digital droplet detections, very few examples of direct concentration measurement were reported. The possible reasons are listed as follow.

Firstly, commonly used analytical methods for bulk solutions are not sensitive enough at such a small scale. Especially with absorption methods, large scale systems are not easily transferable to microfluidics systems due to the path length dependent of the Beer-Lambert law. As the light path is only at the micrometer scale, the absorption of the fluid is essentially indistinguishable from the blank solution even at high concentration. Secondly, fluorescence is very commonly used in microfluidics due to its high sensitivity and low background noise [172], but the requirement of specific labeling or fluorogenic reactions limit its application.

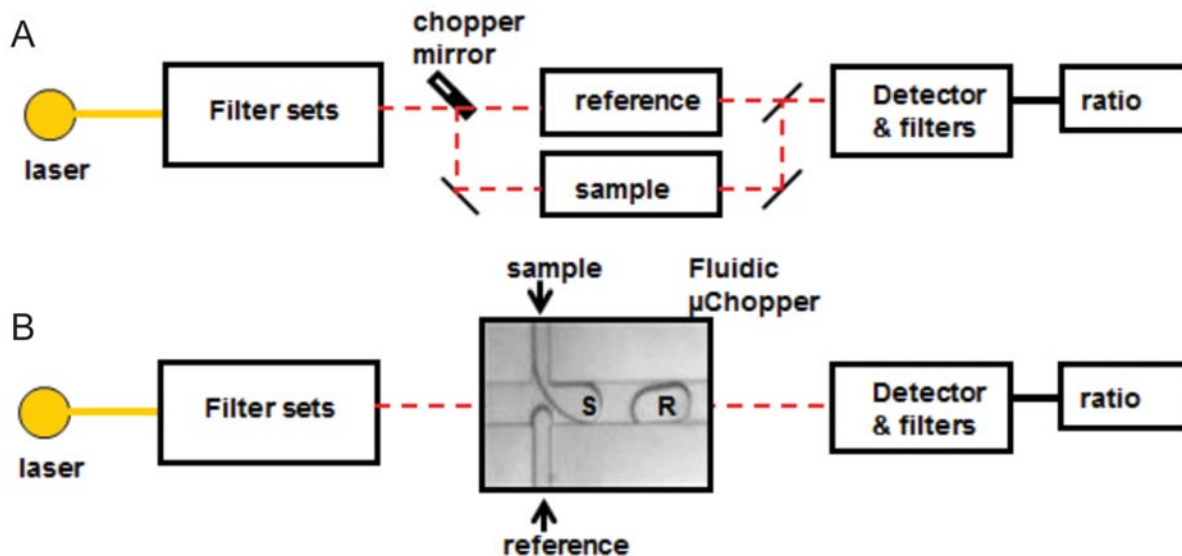


Figure 1.25: Block diagram of typical lock-in detection system and microfluidic  $\mu$ Chopper. A. Block diagram for a typical lock-in detection system using a chopper mirror to switch the investigation beam between sample and reference. B. Block diagram of Chopper set-up using alternating droplet design as a fluidic chopper instead of a chopper mirror. This figure is reprinted from ref [173], courtesy of Dr. Kennon Deal.

Moreover, fluorescence measurements suffers from signal drifting induced by temperature fluctuation, focus drift, or other factors, especially at low concentrations and over long periods of time used in many biological measurements. Thirdly, there are less driving forces for analytical chemists to develop sensitive quantitative chemical analysis methods in  $nL$  or  $pL$  volumes, as most of the biological assays can be done with only  $1 \mu L$  samples.

However, as mentioned in section 1.1.3, there is an urgent need for analytical tool development for accurate study of the dynamics of hormone regulatory networks. The droplet system provides great opportunities to achieve the highest temporal resolution in hormone secretion sampling. As already proved by the Ismagilov group [174] and the Piston group [175], real-time compartmentalization of secretions from endocrine cells or tissues into droplets effectively preserves the temporal chemical information. With a plug-based microfluidic device, or the “chemistrode”, Ismagilov et. al. were able to monitor the insulin secretion from a single islet of Langerhans at a resolution of 1.5 seconds using a competitive fluorescence immunoassay [174]. Dr. Easley (was a postdoctoral fellow at Piston group at that time) was

able to measure  $\text{Zn}^{2+}$  (cosecreted with insulin) from single islets at 1.09 second temporal resolution [175].

To overcome the micrometer light path limitation, a droplet lock-in detection approach was introduced in 2012 by our former group member, Dr. Deal. As shown in Figure 1.25, instead of using a chopper mirror to switch the investigation beam between sample and reference, a droplet generator alternatively making sample and reference droplets was used as a fluidic chopper to modulate the reference signal at the same frequency and phase. Since the reference is “locked-into” the sample, this method is capable of amplifying the signal of sample without amplifying the noise or background. With this  $\mu$ Chopper, sensitive absorbance detection in only a 27  $\mu\text{m}$  optical path length was achieved.

By combining multi-layer microfluidic technology, a newer version of  $\mu$ Chopper was recently developed for lock-in fluorescence droplet analysis [176]. With automated pneumatic valves, precision of droplet control in this  $\mu$ Chopper was improved, allowing strictly phase locked fluorescence measurement. A detection limit of 12 pM fluorescein, and direct measurement of single-cell fatty acid uptake rates quantification were achieved.

Additional, this idea is immediately transferable to other optical detection methods such as UV or IR absorption, and Raman scattering. Theoretically, it is also possible to apply this phase-locking technique to improve the sensitivity of any droplet-integrated detection by eliminating signal drift such as droplet-integrated mass spectrometry and electrochemical detection in droplets.

By integrating certain microfluidics modules mentioned in both section 1.2.3 and section 1.2.4, microfluidic devices are able to interrogate endocrine systems at a single cell or single tissue level. More details will be mentioned in the following sections and chapters.

### 1.2.5 Microfluidic methods for adipocyte study

#### *In-vitro* cell models and their integration onto microfluidic devices

Historically, most adipocyte-related studies, including adipocyte differentiation, lipogenesis, adipokine secretion and regulation, have been carried out with immortalized cell lines, such as mouse 3T3-L1 [177], 3t3-F442A [178] and human Simpson-Golabi-Behmel syndrome (SGBS) cells [179]. The differentiation of those cells into adipocytes can be achieved *in vitro* by treatment with adipogenic stimuli, including cAMP agonists, insulin, and glucocorticoids[180]. Those adipocyte cell lines share many similarity with primary adipocytes. For example, they exhibit fat storage in lipid droplets, insulin sensitivity, expression of adipocyte-specific genes, and adipokine secretion (such as leptin, adiponectin, and asprosin) [27]. However, there are some important differences. The primary white adipocyte from a host mammal contains a single large lipid droplet, but there are many smaller droplets in the cell lines. Also, the cell lines' adipokine secretion are not identical to that of primary adipocytes, for example, the leptin expression is at much lower levels in 3T3-L1 and 3T3-F442A cells [181].

Recently, the development of tissue engineering technology allows assembly of functional tissues with multiple cells and 3D extracellular matrix materials to capture many of the key features of both normal and pathological human organs *in vitro*. Researchers have successfully constructed those organ-on-a-chip models for the study of liver, kidney, intestine, lung, heart, smooth and striated muscle, fat, bone, marrow, cornea, skin, blood vessels, nerve, and blood-brain barrier over the past decades [93]. Various types of engineered adipose tissue were fabricated by incorporation of adipose cell lines into extracellular matrix materials including collagen [182, 183], silk fibroin [184], sponge-like porous polyurethane [185], decellularized extracellular matrices [186], or hyaluronic acid-based hydrogels [187]. Those novel *in vitro* models showed better simulation of functions of *in vivo* adipose tissue than cell lines cultured with traditional methods. Engineered adipose tissues were also used as a simplified

model to address several challenges in organ-on-a-chip engineering. For example, the right size of the tissue for maintaining in vivo basal metabolic rates were studied by measurement of insulin-induced glucose uptake by collagen confined adipose spheroids with various sizes [183]. The transport processes by diffusion through porous membrane within multilayer microfluidic devices, which provide shear stress protection to cells or tissues cultured on chip, were also visualized by fluorescently labeled fatty acid analog uptake by on-chip differentiated 3T3-L1 adipocytes [188]. Since this thesis is focusing on the dynamic of adipocytes metabolism, hormone secretion and other functions with microfluidics circulation mimicking, the bottom-up adipocyte-on-chip engineering, which has been reviewed elsewhere[54], is only covered wherever appropriate.

While the cell lines and engineered adipose tissue remain to be valuable in vitro models, much of the adipocyte can only be evaluated in primary cultures. The primary adipose tissues can be isolated from lab animals and cultured according to well established protocols [189]. The adipose tissue pad can be directly integrated onto microfluidic devices. Or, because of the complex composition of adipose tissues, in certain cases, it is beneficial to digest the fat tissue explant and only use the adipocytes to avoid the interference from other cell components.

Due to the inherent positive buoyancy of the lipid droplet, the adipocyte cells or tissue explant must be properly trapped or anchored in the microfluidic devices or they float in aqueous media and clog the microfluidic channels. This issue was addressed in several ways by our research group including, trapping with metal mash [190] or 3d-printed accessory [191], or collage matrix casting [192], and it was also addressed by others using a culture chamber with micropost array [193] or other methods (Table 1.4).

Cell type	Trapping mechanism	Assay target	Aetection methods	temp. Resl.	Chip design	Note
1 3T3-L1	Cover slip with 3T3-L1 in cell chamber	NEFA secretion	On chip Amplex red assay	83 s	Reversibly sealed 3-layer etched glass wafers	First example of temporally-resolved microfluidic NEFA sampling of 3T3-L1 adipocytes [194]
2 3T3-L1 spheroids	Collagen	Glucose uptake	Ample red assay	25 min*	PDMS chip	First study of the size effect of organ on chip design [183]
3 3T3-L1	Cover slip with 3T3-L1 in cell chamber	NEFA and glycerol secretion	On chip Amplex red assay	**	Reversibly sealed 3-layer etched glass wafers	First example of temporally-resolved microfluidic glycerol sampling of 3T3-L1 adipocytes [195]
4 3T3-L1	Cover slip with 3T3-L1 in cell chamber	NEFA and glycerol secretion	On chip Amplex red assay	**	Reversibly sealed 3-layer etched glass wafers	Same time glycerol and NEFA monitoring on chip [196]
5 Murine adipocytes	Collagen	Adiponectin secretion	ELISA	1 hour	PDMS chip with custom microfluidic interface	First example of microfluidic adipokine secretion sampling of primary adipocyte [192]
6 Human adipose explant	Cell chamber with micropost array	Glucose uptake	Glucose meter	high ***	PDMS chips with valves control	First comparsent of adipose glucose uptake by diabetic and nondiabetic human adipose tissue [193]
7 Murine adipose explant	3d printed accessory	Glycerol secretion	Amplex red assay	10 min	PDMS chip cured with 3D accessory	First example of temporally-resolved microfluidic sampling of murine WAT explants [191]
8 Brown adipocyte	Single cells trapped in micro channel	Heat generation	Silica resonator	real-time	Etched glass with silica resonate thermal sensor	First measurement of thermoal generation from single brown adipocyte cells [197]
9 3T3-L1	Squared lower cell chamber	NEFA and glycerol secretion	SPE-MS	30 min	PDMS chips with valves control	First integration of microfluidic and Mass spectral detection of NEFA from 3T3-L1 adipocyte [198]
10 Murine adipose explant	Platinum mesh	fatty acid uptake	On chip fluorescece imaging	real-time	PDMS chips with valves control	First observation of real-time free fatty acid exchange as a function of dynamic glucose and insulin inputs [190]

Table 1.4: Adipocytes and adipose tissues studies on microfluidic systems

\* sampled every 25 min; \*\* better than entry one (83 s); \*\*\* The paper did not state the exact temporal resolution. Based on the experiment description, the temporal resolution was calculated to be no less than 1.6 min (sample volume = 1  $\mu$ L and flow rate  $\leq$  0.6  $\mu$ L/min)

## Insulin induced glucose uptake

Blood glucose levels are strongly regulated by the hormones insulin and glucagon within a narrow normal range. At the feeding stage, insulin increases the glucose uptake into adipocytes and muscle cells through glucose transporter type 4 (GLUT4) [199]. GLUT4 is a high affinity glucose transporter mostly expressed in muscle cells and adipocytes. In the absence of insulin, only 5% of the GLUT4 is found on the cell surface. Insulin recruits GLUT4 to translocate to the plasma membrane from the specialized GLUT4 storage vesicles and thus increase the cell uptake [17]. Although adipose tissue only accounts for 10% of the insulin-stimulated glucose uptake (the other 90% occurs in skeletal muscle) [200], this process is important for energy homeostasis, as the secreted adipokines from WAT also regulate whole body metabolism as stated earlier. Thus understanding the dynamics of regulated glucose transportation in adipocytes using microfluidic methods provide better opportunities for elucidating the physiological and pathophysiological mechanisms of energy homeostasis. The Elvassore group reported the first microfluidic human adipose tissue glucose uptake study [193]. Adipose tissue were trapped on an automated microfluidic injection system which allows time resolved insulin stimulation. By comparing the tissues from Type 2 diabetes and non-diabetes patients, insulin-resistance effects were observed when the patient adipose biopsy was treated with an insulin and glucose step mimicking the postprandial phase. The healthy tissue showed a significant increase of glucose uptake upon insulin stimulation, while the diabetic tissue had no evidence of difference in glucose uptake rate. However, the authors applied only one treatment to each of the precious tissue samples even though the device was said to allow 1 week on-chip tissue culturing and the glucose concentration in the outflow was only measured every tens of minutes even though their system should allow high temporal interrogation of the adipose tissues (less than 2 min as reported). As a valuable in vitro model for metabolic study, 3T3-L1 adipocyte spheroids were used by the Takayama group to study the scaling effects in human-on-a-chip system designing [183]. Allometry, which describes the relationship between body size and shape including anatomy

and physiology, is a significant factor in organ-on-chip system design to estimate the right size of the chip organism for maintaining similar basal metabolism rate (BMR) as in vivo. The insulin-induced glucose uptake by intact 3T3-L1 spheroids or mechanically dispersed spheroids within collagen were compared. The significant glucose uptake difference between intact and mechanical dispersed spheroids demonstrates that tissue architecture can significantly affect scaling relationships in microfabricated devices.

### **Fatty acid uptake**

The energy reserves in the adipose tissues are stored as triacylglycerol (TAG) molecules, which are mainly obtained from two routes: de novo lipogenesis from non-lipid precursors such as glucose, or uptake of free fatty acid and TAG from plasma. As the solubility of free fatty acid and TAG in aqueous solution is extremely low [202], the fatty acid or TAG in plasma are carried by lipoproteins including chylomicron (CM), very low-density lipoprotein (VLDL), and by serum albumin. Lipoprotein lipase (LPL), which is a glycoprotein secreted by adipocytes and translocated to the lumen of endothelial cells, digest TAG in lipoproteins which releases free fatty acid for uptake by adipocytes [203]. The transport of FFA across the cell membrane are promoted by CD36/SR-B2, which is currently known as the predominant membrane protein facilitating fatty acid transport in adipocytes, enterocytes, cardiac myocytes, and skeletal myocytes [29]. The insulin-induced CD36/SR-B2 translocation from endosomal compartments to the cell membrane upregulates fatty acid uptake [29], which is a mechanism very similar to GLUT4 regulation. In one of our studies reported herein (see Chapter 2), fatty acid uptake and release was monitored by fluorescent imaging of adipocyte tissue explant confined within our novel 16 channel microfluidic multiplexer ( $\mu$ MUX) [190]. Adipose tissue explants were exposed to temporal mimics of post-prandial insulin and glucose levels, while simultaneous switching between fluorescently labeled and unlabeled free fatty acid permitted fluorescent imaging of fatty acid uptake dynamics in real

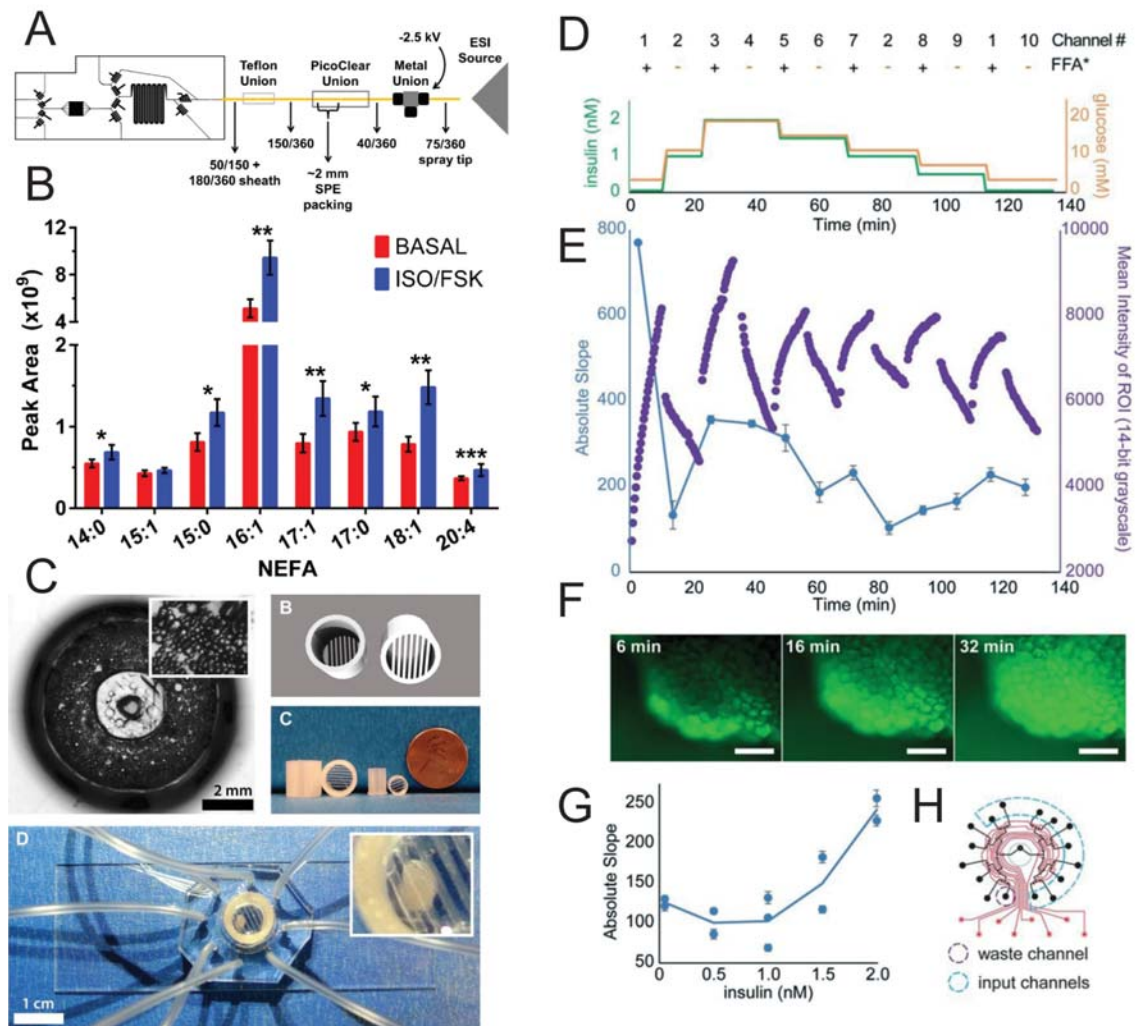


Figure 1.26: Examples of adipose studies on microfluidic devices.

A. Schematic of Microfluidic and mass spectrometry connection for the adipose NEFA secretion profile study. B. Averaged peak area of various NEFAs detected by MS from on-chip adipocyte secretion under basal and isoproterenol/forskolin stimulation. C. Adipocytes cultured on 8-channel microfluidic sampling devices. Topleft, Top-down view image of digested and reconstituted adipose tissue cultured on a microdevice made with a 3D printed interface; topleft, 3D renderings and example prints of adipose tissue explant traps; bottom, a trapped adipose tissue explant cultured on a microdevice and held in place with an explant trap. D-H. Fatty acid uptake assay on  $\mu$ MUX. D. Stimulation of adipose tissue explants with a mimic of post-prandial insulin and glucose at 5 different magnitudes was accomplished while sequentially pulsing labelled (FFA\*) and unlabeled free fatty acids. E. Adipose tissue responded with insulin-dependent FFA exchange rates that closely followed the input pattern. F. Representative fluorescent images of the tissue during FFA\* uptake. G. Insulin dependence plot using compiled data. H. Assignment map showing the required 10 timed input channels and 1 waste channel. Figures A and B are reprinted with permission from ref [198] with permission, ©2017, Springer. Figures C is reprinted with permission from ref [201] ©2017, Springer. Figures D-H are reprinted with permission granted from ref [190] ©2017, Royal Society of Chemistry.

time (Figure 1.26 D-H). Surprisingly, both the fatty acid uptake and release were observed to follow the pattern of glucose and insulin. Moreover, CD36/SR-B2 inhibitor [204] treatment suppressed both the fatty acid uptake and release [205]. Those results suggest the current understanding of fatty acid uptake and regulation is incomplete. Probably, the CD36/SR-B2 is not only involved in fatty acid uptake, but also plays key role in fatty acid release. This fatty acid exchange equilibrium between uptake and release is likely regulated by insulin induced CD36/SR-B2 translocation as well as the extracellular fatty acid concentration. This hypothesis agrees with our observations of fatty acid transportation between adipocytes. Adipocytes along the edges of the explants uptake fatty acid more rapidly than inner cells. Over time, fatty acid can be seen permeating central adipocytes [205]. Further experiments to test this hypothesis will be discussed in Chapter 3.

### **Non-esterified fatty acid and glycerol secretion**

In the starving state, TAG is hydrolyzed into non-esterified fatty acids (NEFAs) and glycerol by the lipase process, and the products are secreted into blood circulation by adipose tissues as an energy source for other tissues. The hydrolysis of stored TAG involves several lipases, including hormone-sensitive lipase (HSL), monoacylglycerol lipase (MGL), and adipose triglyceride lipase (ATGL) [206]. TAG is hydrolyzed by ATGL to diacylglycerol (DAG) and one molecule of fatty acid. HSL then converts DAG to a second fatty acid and monoacylglycerol (MAG). In the last step, MGL hydrolyze MAG to glycerol and the third fatty acid. The NEFAs and glycerol are not only used as nutrients for the rest of the body, but they also have important effects on energy homeostasis. For example, circulating NEFAs reduce glucose uptake by adipocytes and muscle and increase hepatic gluconeogenesis [207], and chronic exposure to elevated level of NEFAs decrease beta cell insulin secretion [208]. The Kennedy group reported several microfluidic studies of NEFAs and glycerol secretion

from 3T3-L1 adipocytes. The 3T3-L1 adipocytes were trapped in a reversibly sealed multilayer microfluidics system. The constant flow containing the secretomes were mixed with NEFA or Glycerol Amplex Ultra Red enzyme probe, and the concentration of NEFAs and/or glycerol were detected by fluorescence on-chip [196, 195, 194]. Upon treatment with a beta-adrenergic agonist, up to 6-fold sustained increase in NEFA and glycerol secretion were observed. The latest version of their microfluidic chip combined solid phase extraction and mass spectrometry and allowed them to identify the NEFA profiles from adipocytes [198] (Figure 1.26 A, B).

Our group has also studied the glycerol secretion from primary adipose tissue explants [191]. In order to counteract the adipose pad buoyancy, we used a custom 3D-printed accessory to trap adipose tissues on chip (Figure 1.26 C). After 30 min of high-insulin-high-glucose treatment, the explants were switched to low-glucose-low-insulin solution, and increased glycerol secretion rates were observed.

### **Adipokine secretion**

As stated earlier, adipose tissue plays significant endocrinological roles in maintaining whole body energy homeostasis. Despite its importance, however, to the best of our knowledge, to-date there is only one adipokine secretion study using microfluidics, which was from our group [192]. In our microfluidic design, adipocytes from dispersed primary mouse adipose tissue were cultured in collagen within a customized culture reservoir with a raised island interfacing to the microchannel. Adiponectin secreted from adipocytes, which is a large multimeric protein hormone with the main understood function of improving insulin sensitivity (Table 1.2), was quantified. Insulin and niacin treatments induced increased adiponectin secretion by 2.6 fold and 4.4 fold, respectively.

## Thermogenesis on a chip

Heat generation is one of the essential necessities for endotherms to maintain normal body temperature and routine metabolism. BAT is known as the main site of non-shivering thermogenesis which enables animals to adapt to a cold environment. Uncoupling protein 1 (UCP1) is a transmembrane protein only expressed in brown adipocytes. It located on the inner membrane of mitochondria, where it increases the inner membrane proton permeability, decreases the proton gradient generated in oxidative phosphorylation, uncouples the respiratory chain, and yields a higher oxidation rate for heat generation [209]. The UCP1 mediated proton leakage is regulated by the sympathetic nervous system via  $\beta$ -adrenergic receptors. Binding of catecholamines such as norepinephrine to  $\beta$ -adrenergic receptors in BAT trigger the thermogenesis. UCP1 is also activated by fatty acids and inhibited by purine nucleotide di- and triphosphates such as ATP, ADP, GTP, and GDP.

To investigate the heat generation property of BAT, the Inomata group [197] fabricated a microfluidic system with silicon resonator based thermal sensors for the thermal detection of single cells. Single brown adipose cells were captured at the Si sample stage, which was connected to the Si resonator as a heat guide. The heat generated from the cells was measured by the resonant frequency changes of the resonators. With their devices, two types of heat emissions from single brown fat cells were detected: continuous heat generation in the presence of stimulation by norepinephrine, and pulsed heat generation without any stimulation. Cells treated with sodium azide, a respiratory inhibitor, did not show any thermal response.

### 1.3 Concluding Remarks

In this chapter, three topics were covered. Firstly, we note that the global epidemic of obesity, diabetes, and related diseases is urgently calling for the development of new methodologies for endocrine tissue studies (especially adipose tissues). Secondly, we describe how microfluidics including pneumatic valve and droplet-based microfluidics are increasing in maturity and have been successfully used in many areas of biology research. Thirdly, the recent microfluidics applications to adipocytes are discussed.

As summarized in Table 1.4, the studies include adipocyte nutrient uptake, fatty acid and glycerol secretion, hormone secretion, and thermogenesis. Microfluidics provides more precise analysis tools for better understanding of the adipocyte biology. The new findings-especially the time resolved NEFAs secretion profile, adiponectin secretion, and first real time observation of the insulin regulated fatty acid uptake and release-have provided new opportunities to improve the understanding of the pathology of obesity, diabetes, and metabolism disorders. Compared to relatively effective application of microfluidics to other tissue or cells in recent years, especially islet of Langerhans [210, 211], fewer studies of adipose tissue were done on microfluidics. The possible reasons including the following. Firstly, the importance of adipocytes in energy homeostasis, and particularly the endocrine functions of adipose tissue, is still less exposed to the microfluidic community. Secondly, buoyancy of adipocytes introduces difficulties to incorporate those cells onto microfluidic chips. To prevent cell loss and channel clogging, device engineers must use creative ways to trap or anchor the cells on chip, such as the 3D-printing technology used by our group, allows simple and effective macro-to-micro interfacing to incorporate adipocytes on chip. Thirdly, the fundamental understanding of adipocytes is still relatively underdeveloped. For example, several new hormones were identified last year (2016) [212], namely a new adipokine (asprosin) and two new batokines (PM20D1, and SLT2). Those latest findings reflect difficulties but great opportunities for bioengineers to make contributions in the adipose biology field.

Further innovation in microfluidics would provide a unique toolbox that allows life scientists

to advance their research in a way that was never possible. Conversely, bioengineers are also seeking the right problems in medicine and biology to validate and improve their microfluidic technologies. As stated in this introduction, the relatively understudied adipose tissue could be an important target tissue for the microfluidics community. The improved adaptation of microfluidics into adipose tissue biology would provide great potential to lead to better preventions and treatments and meet urgent needs in the global epidemics of obesity, diabetes, and metabolism disorders.

## Chapter 2

### Development of automated microfluidic systems for endocrine tissue analyses

#### 2.1 Introduction

The increasingly prevalent, debilitating conditions of diabetes, obesity, and metabolic syndrome are fundamentally linked to endocrine tissues such as the liver, pancreatic islets, and the various adipose subclasses. In particular, adipose tissue (fat) is now understood to be a complex, multicellular endocrine organ that has profound systemic effects, altering the function of nearly all other organ systems [28]. A multitude of chronic factors result in adipose tissue expansion, which is linked to diabetes [19, 20], Alzheimers disease [22], compromised immune function[23] , and many other diseases. Despite its importance, however, there is a lack of information on the dynamic nature of adipokine secretion and nutrient uptake in adipose tissue, highlighting several unmet needs in methodology. Specifically, few techniques exist to interrogate small amounts of adipose tissue, and there is a shortage of methods to explore dynamic function of the organ. There has also been renewed interest in the dominant role of the pancreatic hormone, insulin, especially in the context of hyperglycemia and hyperinsulinemia induced by diets high in sucrose or refined carbohydrates[213, 214]. Unfortunately, we have a limited view of the dynamic relationship between glucose, insulin, and adipose function.

Microfluidic tools offer attractive features that could help fill this knowledge gap. This potential is exemplified by the recent outpouring of organs-on-chips that nicely simulate physiology at the tissue level or even the organ level; such devices recapitulate biological functions in a manner unmatched by standard culture methods [93]. Our group [175, 66, 191] and others [215, 216, 217, 218, 219, 220, 221, 222, 223, 224] have shown the utility of microsystems

to study biological function of pancreatic islets, and we have begun applying these systems to studying primary adipose tissue function [191, 192]. Although some studies have leveraged microfluidics to assay secretion from adipocyte cell lines[195, 196, 183], less has been accomplished toward studying dynamics of intact, primary adipose tissue on-chip [193]. In terms of fluid handling, although passively controlled microdevices provide simplicity of use[66, 191, 192, 225], the precision in fluidic control provided by actively valved devices is virtually unmatched in gleaning complex functions from biological systems[99, 226, 227, 228]. As such, a precisely valved, customized microdevice should be a fitting analytical solution to help decipher endocrine tissue dynamics.

Herein, a customized microfluidic input/output multiplexer ( $\mu$ MUX) using active microvalves is presented for generalizable dynamic control over hormones and nutrients to/from endocrine tissues. This system essentially serves as a mimic of the circulatory system and of upstream endocrine signals. The device is automated through feedback sensing of solution levels, and 3D-printed templates [191] are used to interface both islets and adipose tissue. High device flexibility is shown by varying from multiple fluidic outputs to primarily inputs, by operation in sampling and imaging modes, and by studying multiple murine tissues. This 3D-templated  $\mu$ MUX device should be applicable to a variety of tissue types, and it could feasibly serve as a single module in devices with further integrated functionality such as on-chip biosensing.

## 2.2 Experimental Methods

### 2.2.1 General materials

All buffers were prepared with deionized, ultrafiltered water (BDH1168-5G, VWR, Radnor, PA). The following reagents were used as received: Polydimethylsiloxane (PDMS) precursors (Sylgard 184, Dow Corning, Midland, MD); SU-8 2015 photoresist (Microchem, Newton, MA); AZ-40-XT photoresist (MicroChem, Westborough, MA); insulin, D-glucose, 4-hydroxyethyl-1-piperazineethanesulfonic acid (HEPES), (3-Aminopropyl)trimethoxysilane,

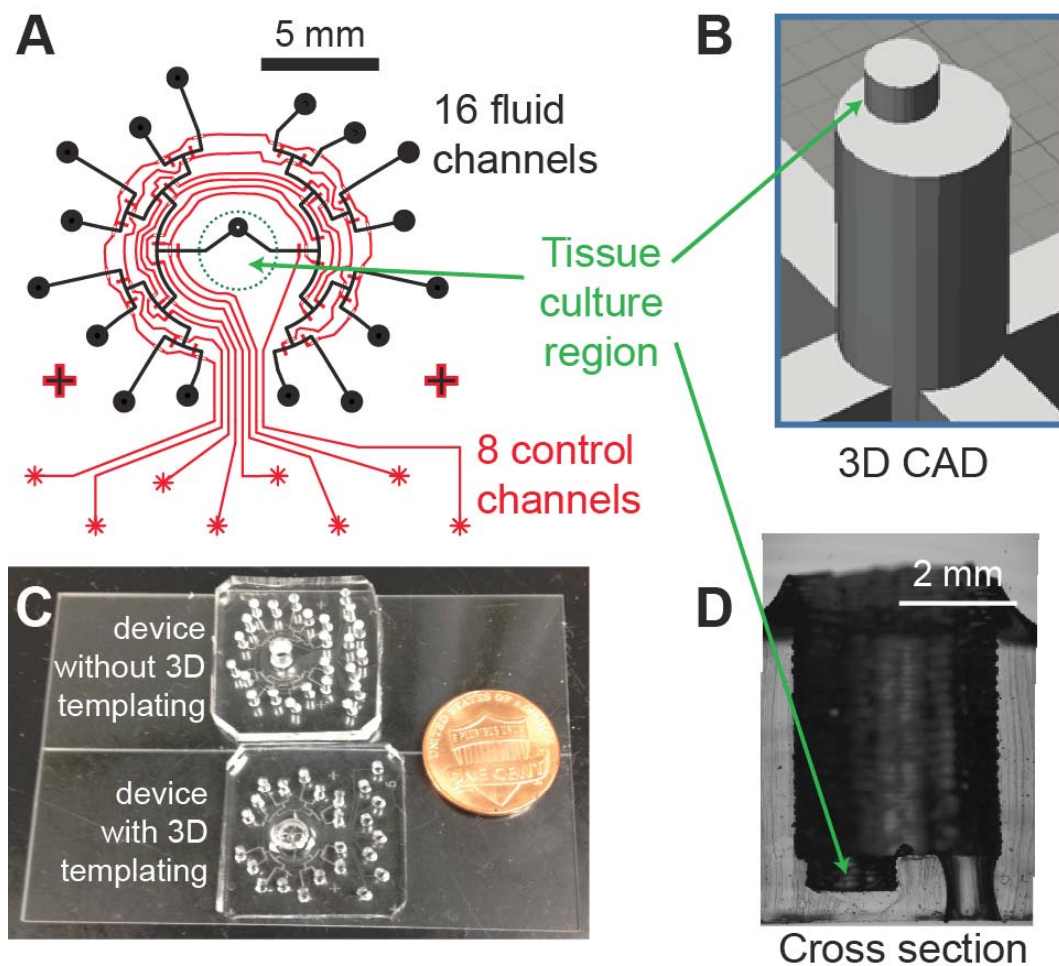


Figure 2.1:  $\mu$ MUX device design

(A) Schematic of the  $\mu$ MUX channel layouts, with fluidic channels shown in black and pneumatic control channels in red. (B) Photo of assembled devices with and without 3D-templated interfaces. (C) CAD rendering of the 3D-printed template and (D) example device cross-section with customized, 3D-templated tissue culture reservoir and channel interface. Figure reprinted from ref [190] with permission, ©2017 Royal Society of Chemistry .

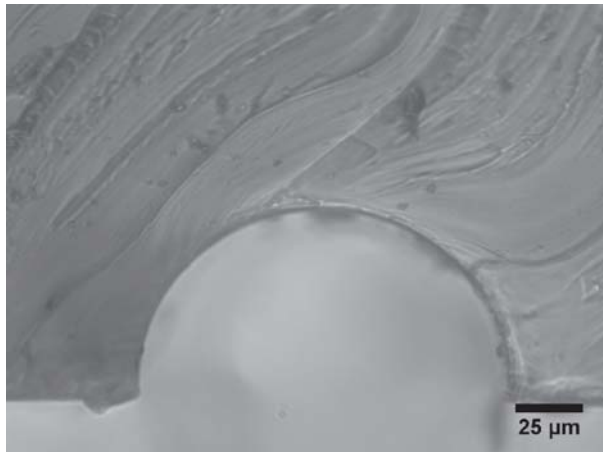


Figure 2.2: Cross-section of a  $\mu$ MUX fluidic channel

Using ImageJ software, the cross-sectional area of the channel was measured as  $7580 \pm 150 \mu\text{m}^2$  Figure reprinted from ref [190] with permission, ©2017 Royal Society of Chemistry .

trimethylsilyl chloride ( $\text{Me}_3\text{SiCl}$ ), sodium dodecanoate, fluorescein isothiocyanate (FITC),  $\text{KH}_2\text{PO}_4$ ,  $\text{NaH}_2\text{PO}_4$ , and  $\text{NaOH}$  were all obtained from Sigma-Aldrich (St. Louis, Missouri); Bovine serum albumin (BSA), fetal bovine serum (FBS),  $\text{NaCl}$ ,  $\text{CaCl}_2 \cdot 2\text{H}_2\text{O}$ ,  $\text{EtOH}$ ,  $\text{MeOH}$ , and  $\text{DMF}$  were purchased from VWR (West Chester, PA). 4,4-difluoro-5,7-dimethyl-4-bora-3a,4a-diaza-s-indacene-3-dodecanoic acid (BODIPY FL  $\text{C}_{12}$ , FFA\*; 'bodipy-laurate'), minimal Essential Media (MEM) non-essential amino acids solution 100x, collagenase P, collagenase type I, Dulbeccos Modified Eagle Medium (DMEM), and  $\text{MgSO}_4 \cdot 7\text{H}_2\text{O}$  were purchased from ThermoFisher Scientific (Grand Island, New York).

### 2.2.2 Microfluidic device master wafer fabrication

Two layer microfluidic devices were fabricated using standard multilayer soft lithography methods[143, 98] with 3D-printed templating[192, 191] of the tissue culture interfaces. Two different master wafers for fluidic channel and pneumatic/control channels were first fabricated by photolithography.

The channel layout was designed in Adobe Illustrator and printed at 50800 *dpi* resolution by Fineline Imaging (Colorado Spring, CO) to serve as the photolithographic mask. For the control channel (thin lower layer), 30- $\mu\text{m}$  thick negative photoresist (SU-8 2015) was spin

coated onto a silicon wafer (Silicon Inc., Boise, ID, USA). The wafers were then baked at 105 °C for 5 *min* on a hotplate. UV exposure through the mask was done at 330  $mJ/cm^2$  on an in-house built UV LED exposure unit [229]. The wafer was hard baked for 5 *min* at 105 °C then developed for 5 *min* in the SU-8 developer solution. For the fluidic channel layer, 50-m thick positive photoresist (AZ 40 XT) was spun onto the silicon wafer. The wafers were then baked at 105 °C for 5 *min* followed by UV exposure at 330  $mJ/cm^2$ . After hard baking at 105 °C for 5 *min* and wafer development in AZ developer for about 5 *min*, the master wafer was baked at 115 °C for 6 *min* to anneal the AZ photoresist and round out the cross-section of the fluidic channel template (see Figure 2.2). The silicon wafers were exposed to trimethylsilyl chloride vapor for 30 *min* before use to enhance PDMS removal. Channels were later characterized by slicing an assembled PDMS device and imaging the channel cross section (Figure 2.2).

### 2.2.3 3D-printed interface templates for tissue culture regions

All 3D-printed templates and devices were designed in SketchUp 3D modeling software, error checked in NetFab, and printed on a MakerBot Replicator 2 (100  $\mu m$  layer resolution in the  $z$ -direction) with polylactic acid filament (PLA, 1.75  $mM$  diameter). Six 3D-printed templates with varying tissue culture region heights (0.47, 0.48, 0.57, 0.72, 0.82, 1.24  $mM$ ) were design and printed for PDMS templating. In order to measure the height of the cell culturing regions, PDMS was cured with the 3D-template and a cross-section of the PDMS reservoir region was sliced with a razor blade and mounted onto a glass microscope slide. Images were captured on a Nikon *Ti-E* inverted uorescence microscope at 2X magnication, operating in wide-eld transmittance mode. The heights were measured with ImageJ software.

### 2.2.4 Microdevice fabrication

The  $\mu$ MUX devices were fabricated as described in Figure 2.3. 36 *g* of PDMS polymer mixture (5:1 ratio, monomer:curing agent) were mixed and degassed under vacuum and then

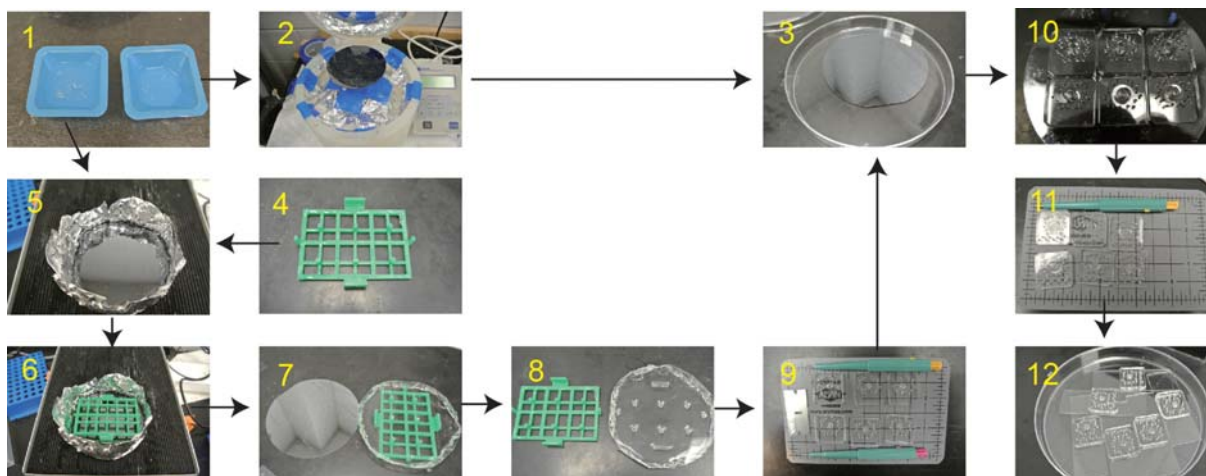


Figure 2.3: Fabrication procedure of  $\mu$ MUX devices including 3D-templated reservoir molding.

(1) 36 g of PDMS in 5:1 ratio (left) and 10.5 g of PDMS in a 20:1 ratio (right) were mixed and degassed under vacuum. (2) PDMS (20:1) was spin-coated over the control wafer. (3) The thin layer of PDMS on the control wafer was partially cured at 65 °C for 40 min, and fluidic channel layers (from step 9) were aligned for bonding. (4) 3D-printed template for sculpting tissue culture reservoirs. (5) PDMS (5:1) was poured onto the fluidic channel master in an aluminum foil boat. (6) 3D-printed insert was carefully aligned around the channel and set directly onto the wafer into the layer of uncured PDMS. The entire assembly was baked in the oven at 50 °C undisturbed for 4 h. (7) The cured PDMS with template was peeled from the wafer. (8) The 3D-printed template was removed. (9) Devices were diced, and holes were punched to prepare for bonding with the control channel PDMS layer. (10) After careful alignment (in step 3), the fluidic layer PDMS and partially cured control layer were permanently bonded together by placing in the oven at 65 °C for at least 4 hours. (11) Completed PDMS devices were diced, peeled from the wafer, and holes were punched for control channel pressure lines. (12) PDMS devices were finally plasma oxidized and bonded onto glass substrate, and these MUX chips were ready to use. Figure reprinted from ref [190] with permission, ©2017 Royal Society of Chemistry .

poured onto the fluidic master wafer (AZ) wrapped within aluminum foil. The 3D-printed template was carefully aligned around the channel and set directly onto the wafer and into the layer of uncured PDMS. The entire assembly was baked in the oven at  $50\text{ }^{\circ}\text{C}$  undisturbed for  $4\text{ h}$ . Following curing, the template was removed carefully, and the PDMS was peeled from the master, after which it was diced, access holes and vias were punched ( $1.5\text{ mM}$  inner diameter for interfacing with tubing,  $1.0\text{ mM}$  for the via connection between the reservoir and channels), and each device was cleaned with methanol and dried with  $\text{N}_2$  gas. Next,  $5\text{ g}$  of degassed PDMS polymer mixture (20:1 ratio, monomer:curing agent) was spin coated onto the pneumatic control channel master wafer (SU-8) at  $2300\text{ rpm}$  for  $60\text{ s}$  and baked at  $65\text{ }^{\circ}\text{C}$  for  $40\text{ min}$  to facilitate partial curing of the polymer. The freshly made fluidic layer PDMS, with access holes punched, was carefully aligned onto the partially cured control channel PDMS layer, and the two layers were permanently bonded by placing in the oven at  $65\text{ }^{\circ}\text{C}$  for at least 4 hours. The PDMS devices were then peeled from the wafer and diced, then access holes were punched where necessary. Finally, the assembled PDMS devices were plasma oxidized and bonded to a glass substrate. The  $\mu\text{MUX}$  devices were stored at room temperature. Immediately before use with islets or adipose explants, the devices were cleaned with an air plasma for  $45\text{ s}$  then treated with PBS buffer with 1% BSA to generate a hydrophilic, biocompatible surface.

### 2.2.5 Control interface

Pneumatic valves were actuated with solenoid switches (LHDA0533115H, The Lee Co., Westbrook, CT) controlled by a multifunction data acquisition system (USB-6002, National Instruments) and using a house nitrogen source adjusted to  $20\text{ psi}$  with a pressure regulator. The 16 fluidic channels were addressed by 8 pneumatic control channels connected to the corresponding solenoid switches with Tygon tubing ( $0.02\text{ inch}$  ID,  $0.06\text{ inch}$  OD, Cole-Parmer, Vernon Hills, IL). Dead-end control channels were filled with water to prevent air leakage through PDMS membranes. As a solenoid switch was activated, nitrogen gas pressurized a

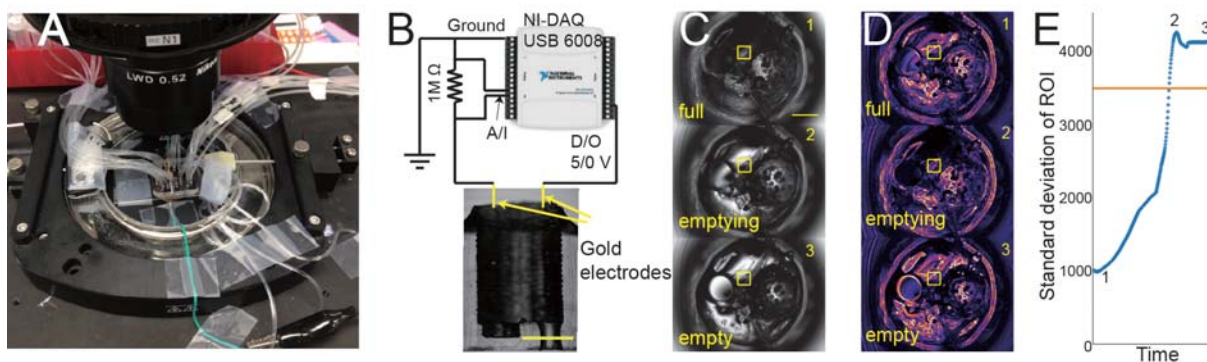


Figure 2.4: Automated solution level sensing.

(A) Photo of working device in the microscope stagetop incubator. Tubing was connected to both control channels and valved uidic channels. Two gold wires were positioned near the top of the 3D-templated reservoir to serve as the full sensor. (B) Circuit diagram of voltage divider for conductivity sensing as the full signal trigger. The source wire was connected to a digital output line of the NI-DAQ for voltage supply, and the sensing wire was connected to a 1  $M\Omega$  resistor across the differential analog input for voltage readout. (C) Microscope (bottom view) images of the  $\mu$ MUX tissue culture reservoir. Two possible ROIs (red and yellow regions) were analysed in real time for the empty signal (see Video S-2). (D) Corresponding edge detection images used for ROI analysis. (E) Representative data shows the standard deviation of pixel intensities within the example ROIs (red and yellow), and the empty trigger cutoff value (gray dotted line) is shown for the ROI with the most obvious change (red). Figure reprinted from ref [190] with permission, ©2017 Royal Society of Chemistry .

lower layer control channel and closed the fluidic channel in the upper layer (push-up valves). Valve actuation timing was regulated through an in-house written LabVIEW application on a PC.

### 2.2.6 Solution level sensing

Serving as the full sensor, two gold electrodes were placed over the reservoir and connected in a voltage divider configuration to sense solution conductivity (Figure 2.4 A-B), using the 5 V digital output line as a source. To protect cells and minimize electrochemical gas generation, the voltage was set to off (0 V) immediately after the full state was reached. The empty sensor utilized a cooled CCD (Coolsnap HQ2; Photometrics) and an inverted microscope (Nikon *Ti-E*) in differential interference contrast (DIC) mode. The CCD readout was interfaced with a LabVIEW application using the Scientific Instrument ToolKit for

real-time image analysis (R Cubed Software; Lawrenceville, New Jersey). As the reservoir was emptied, the image (focused on the reservoir bottom) was transformed to a 2D array, and a standard deviation of the region of interest ( $\sigma$ ROI) subarray was analysed as the signal for the empty trigger. As the reservoir emptied, roughness emerged in its features due to refractive index differences, and ROI abruptly increased. Example sensor traces are shown in Figure 2.5 B and Figure 2.2 7.

### 2.2.7 Time and channel programs

User-defined time and channel programs were preloaded into the LabVIEW application. Full and empty sensor readouts were used to automate the device according to the preloaded program (Figure 2.5 A).

### 2.2.8 $\mu$ MUX device characterization

Reproducibility in sampling volume was analysed by measuring the distance travelled by the leading meniscus of the sampled solution in the output tubing after each step. Measurements were repeated in triplicate (Figure 2.7 B).

Carry-over volumes were measured by connecting two input fluidic channels to two syringes filled with either buffer (phosphate buffered saline, PBS) or 100 *nm* fluorescein in PBS. Connections were made through Tygon tubing. The  $\mu$ MUX time program was designed as two cycles of five buffer rinses after a single input of fluorescein solution. Each input was incubated for 10 *s*, and the solution in the reservoir was collected and saved in one of the output channels (one solution per channel). Solutions in output channels were collected, and fluorescence intensities were measured using a small-volume spectrofluorometer (Nanodrop 3000) (Figure 2.7 A).

Solution exchange times were analysed by measuring the fluorescence output from pH-responsive glass beads ( 100-200  $\mu m$ ) in the tissue culture reservoir as solutions of varying

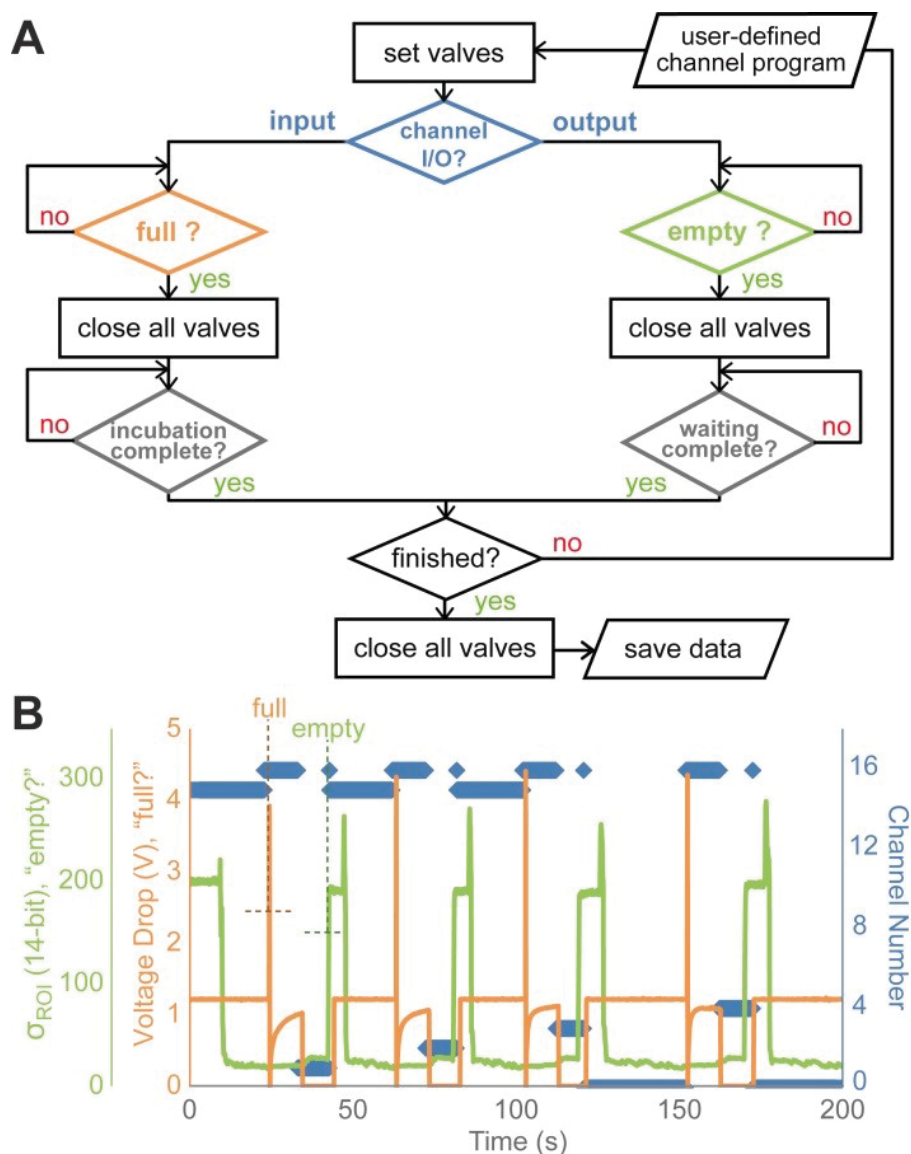


Figure 2.5:  $\mu$ MUX system automation.

(A) Programmatic flow chart LabVIEW application used for automation. Each of the 16 channels was assigned as input or output by a user-defined program. Depending on the input assignments and incubation/wait times, the controller followed the depicted logic flow until completion of a run. (B) Automation data from a test run of the  $\mu$ MUX. The imaging-based empty sensor (green) and the conductivity-based full sensor (orange) readouts were used to trigger sequential steps in the programming. With channels 0 and 15 as inputs, channels 1 to 4 outputs, and channel 16 as a close-all-valves code, this test run automatically switched channels (blue diamonds) in the following order: 15, 1, 15, 2, 15, 3, 0, 4, 0. Figure reprinted from ref [190] with permission, ©2017 Royal Society of Chemistry

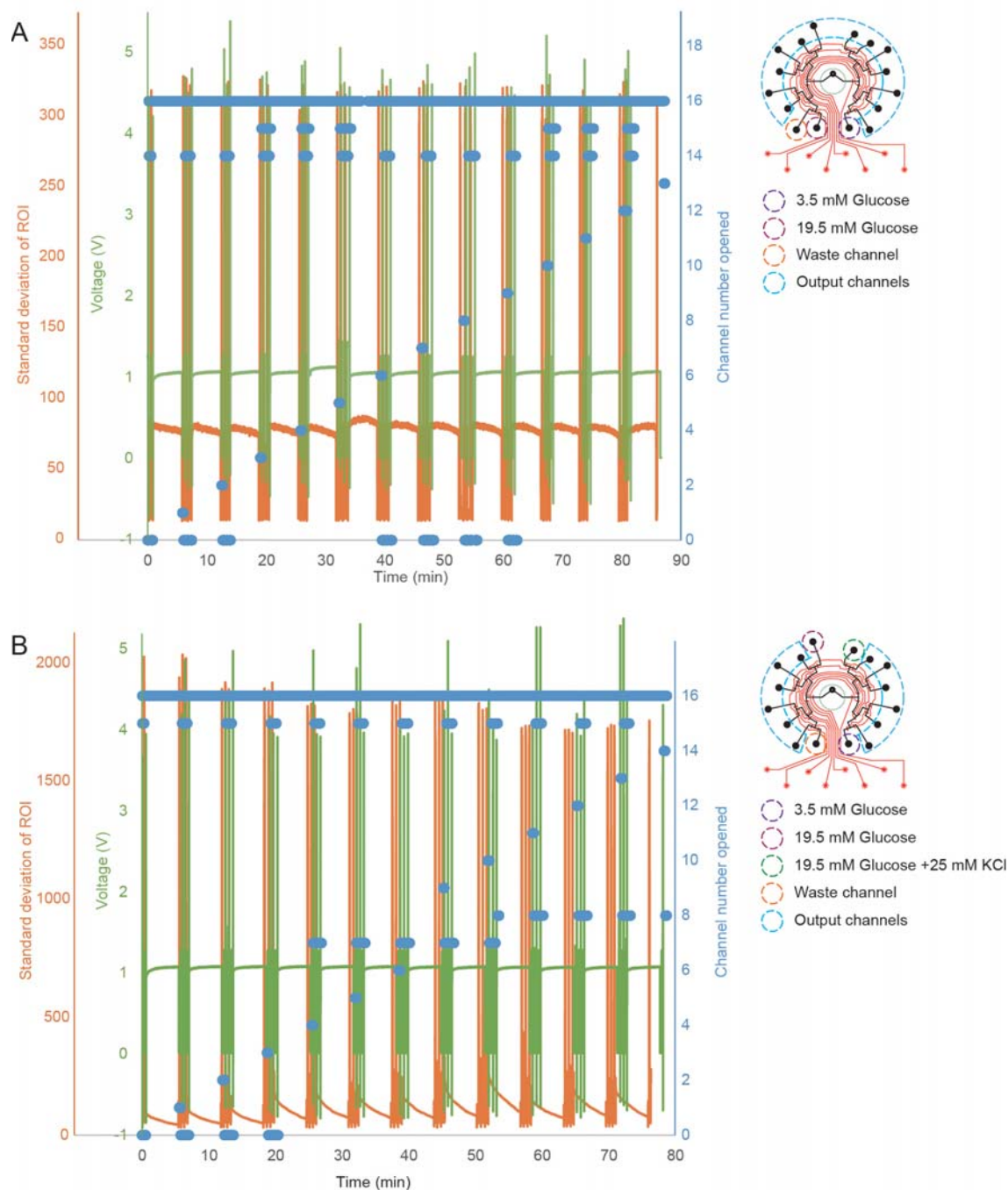


Figure 2.6: Full sets of automation data during time programs for dynamic insulin secretion sampling from pancreatic islets.

(A) Automation data from high-low glucose square wave treatment and (B) from high-low glucose square wave with KCl treatment. Channel assignment map is shown in the rightmost images. Reservoirs were rinsed 3 times between treatments, as indicated by the multiple triggers in the full (green and empty (orange) sensor traces. Further details of operation are included in the manuscript text. Figure reprinted from ref [190] with permission, ©2017 Royal Society of Chemistry .

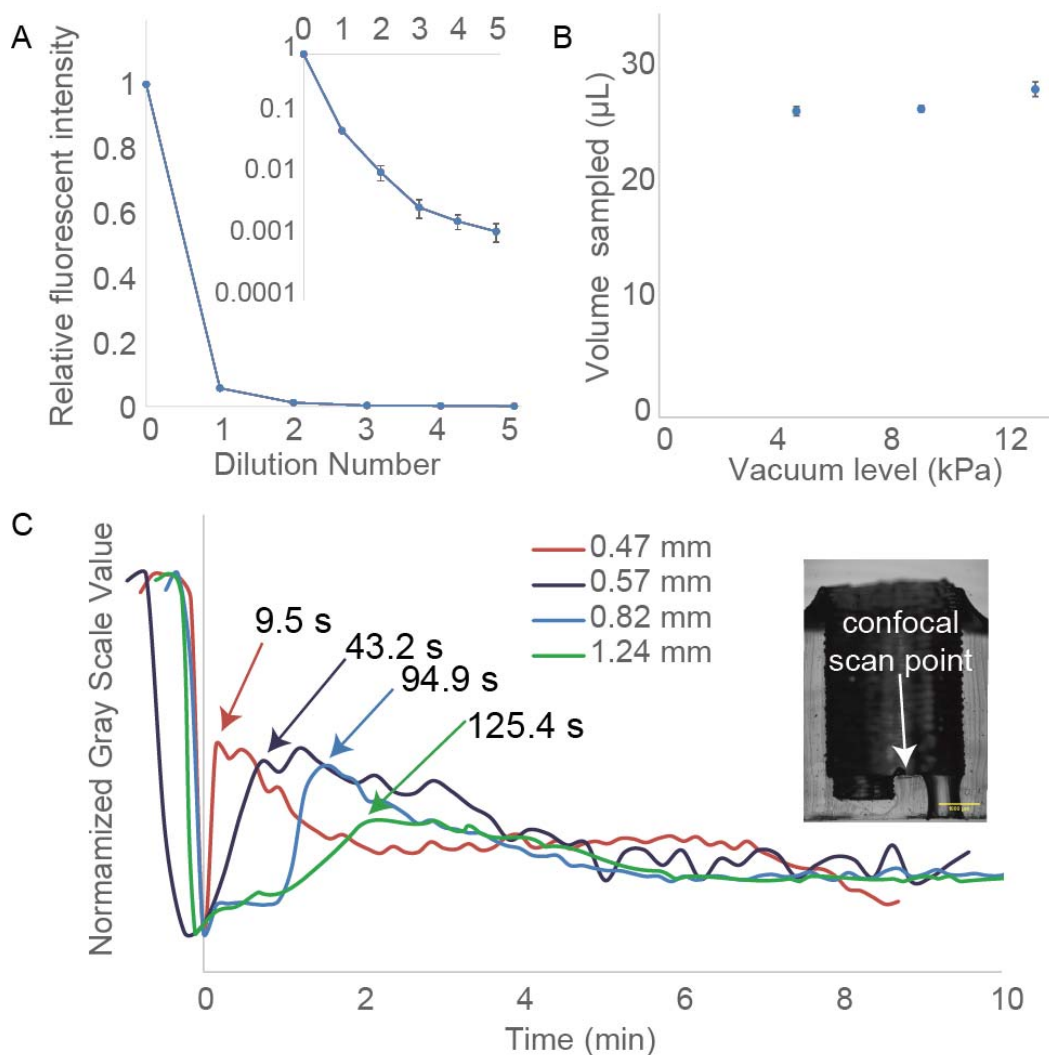


Figure 2.7:  $\mu$ MUX device characterization and optimization.

(A) Carry-over volume measurement by rinsing fluorescein with sequential buffer rinses. The fluorescence intensity of the rinsed buffer decreased to less than 1% after 2 rinse steps. (B) Sampling volume consistency study by measuring sample volume at different vacuum levels. Error bars show the standard deviations of 5 samplings. (C) Fluorescein diffusion studies via microscopy. The white rectangle in the inset image at the right shows the region of confocal scanning. Upon quickly switching the solution from 200  $nM$  fluorescein to 20  $nM$  fluorescein (from  $\mu$ MUX channels below), the leftover higher concentration fluorescein in the islet culturing was released by diffusion. As tissue culture region depths were increased, the time for the fluorescein diffusion to equilibrate increased. For the chosen optimum depth (0.57  $mm$ ), fluorescein required 40 s to diffuse from the culturing region, an acceptable result for secretion sampling at 5-minute temporal resolution. Figure reprinted from ref [190] with permission, ©2017 Royal Society of Chemistry .

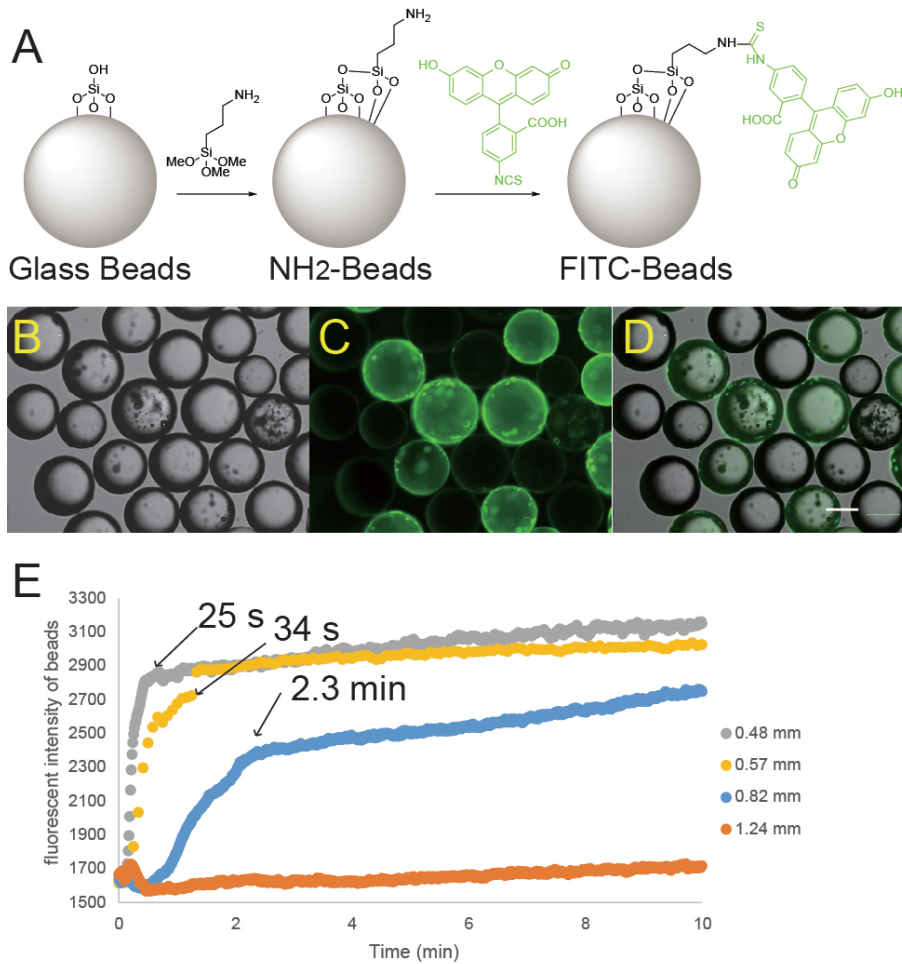


Figure 2.8: Islet mimics for solution exchange experiments.

(A) Scheme of pH-responsive bead synthesis. (B) A DIC image, (C) fluorescent image, and (D) combined image of modified beads mixed with untreated beads. (Scale bar is 100  $\mu\text{m}$ ). (E) Representative fluorescence intensities from pH-responsive beads placed in the tissue culture region of the  $\mu\text{MUX}$  device during automated operation. Solution exchange times were optimal (30 s) for devices with culture region depths of 0.48 mm and 0.57 mm. Deeper culture regions resulted in unacceptably long exchange times. Figure reprinted from ref [190] with permission, ©2017 Royal Society of Chemistry .

pH were applied (Figure 2.8). The pH-responsive beads were synthesized in the following manner: 100 mg glass beads ( $\sim 100\text{-}200\ \mu\text{m}$ , G1145-10G, Sigma-Aldrich) were placed in a centrifuge tube, washed with 1 M NaOH (1 mL, 3x), deionized H<sub>2</sub>O (1 mL, 3x), and MeOH (1 mL, 3x), then dried at 65 °C. 5.0% (3-Aminopropyl)trimethoxysilane (281778, Sigma-Aldrich) in EtOH was added to the beads, and the tube was agitated on a rocker at room temperature overnight to introduce the amine function group on the glass surface by silanization. The beads were washed with EtOH 3x to remove the unreacted silane. After again drying at 65 °C, the amine-glass beads were treated with FITC in DMF solution (0.1%, 1 mL) at room temperature and incubated for 2 h. The beads were then washed with DMF and EtOH, then stored in EtOH at 4 °C until use. Fluorescence images of beads during automated pH switching were measured (Nikon Ti-E), and images were analysed using ImageJ and Microsoft Excel.

The diffusion of hormones from the tissue culture region into bulk solution in the reservoir was simulated by scanning the fluorescent intensity through the depth of the tissue culture region with a confocal microscope. For devices with varying depths of the 3D-templated tissue culture region, two  $\mu\text{MUX}$  input channels were filled with 100 nm or 10 nm fluorescein in PBS, and 1 waste output channel was connected to a vacuum applied syringe. The reservoir and tissue culture region were prefilled with 100 nm fluorescein. As the reservoirs emptied, the device was programmed to fill with 10 nm fluorescein and incubate. Confocal Z-scanning was initiated from the bottom to the top of the tissue culture region (Nikon A1 Multiphoton Confocal Laser Scanning Microscope; 488.0 nm laser excitation, 525/50 nm emission filter). The images were analysed using ImageJ and Microsoft Excel (Figure 2.7 C).

### 2.2.9 Extraction of primary islets and adipose explants

Pancreatic islets [230, 231] and epididymal fat pads [192, 191, 232, 233] were isolated from C57BL/6J male mice (Jackson Laboratories) as described previously. Following isolation, islets were placed in RPMI media (10% FBS, 11 mM glucose) at 37 °C and 5% CO<sub>2</sub> to

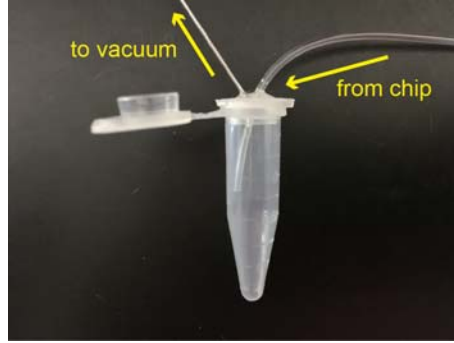


Figure 2.9: Buffer bottle for collecting islet secretion samples.

Caps of 1.7 *mL* microcentrifuge tubes were drilled with two holes. Tygon tubing (0.01 *inch* ID) and hollow steel tubing taken from 22 *gauge* blunt syringe needles were feed into the two holes and sealed with epoxy glue (Gorilla Glue Co., Cincinnati, OH). The Tygon tubing was deeper than the steel tubing. When used for secretion sampling, the other end of the Tygon tubing was inserted into the corresponding output channel interface on the  $\mu$ MUX device, and the steel tubing was connected to vacuum applied by a syringe through Tygon tubing (0.01 *inch* ID). Figure reprinted from ref [190] with permission, ©2017 Royal Society of Chemistry .

incubate overnight. Fat pads were transferred to a 60 *mM* petri dish containing a few *mL* of fresh phosphate-HEPES buffer. Excess vasculature and other non-adipose tissue was excised using micro surgical scissors. 2- and 3-*mm* sterile biopsy punches were used to form aliquots of the fat tissue. As explants were punched, they were transferred with surgical tweezers into a glass tube with 3-4 *mL* of phosphate-HEPES buffer. Explants were centrifuged at 1000 rpm for 3 *min*. Infranatant was removed with an 18-*gauge*, 1.5-*inch* needle. 3-4 *mL* of phosphate-HEPES buffer was added back to the tube. Cells were centrifuged and washed in this fashion one additional time with phosphate-HEPES buffer and 2 additional times with fat serum media. After the final rinse, explants were transferred to individual wells on a sterile 96-well plate containing 200  $\mu$ *L* of serum media in each well. The 96-well plate was incubated for 30 minutes at 5.0% CO<sub>2</sub> and 37 °C. 3D-printed explant traps were placed into each well and the plate was returned to the incubator. Prior to use in microfluidic stimulation experiments, explants were maintained for up to 7 days in the incubator with serum media replacement twice a day.

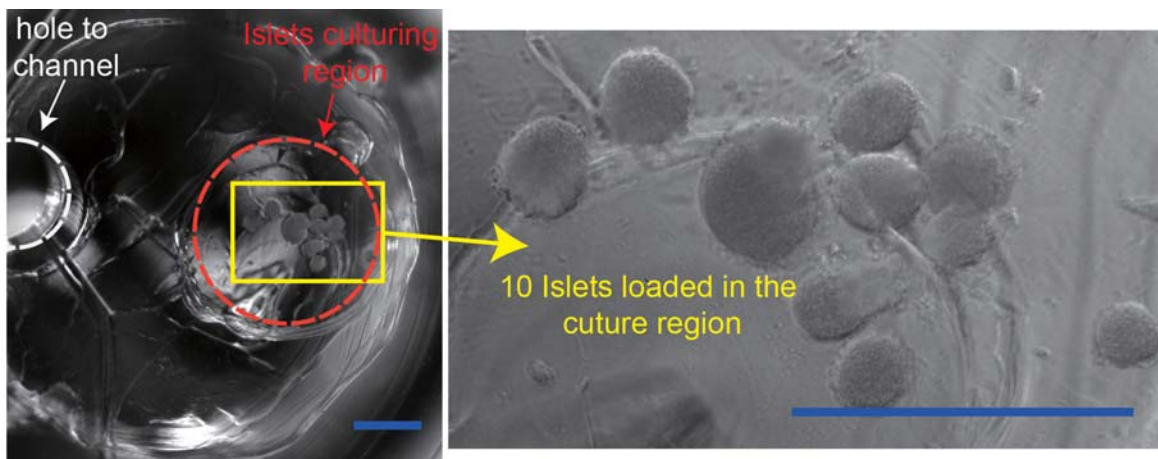


Figure 2.10: Images of pancreatic islets on a  $\mu$ MUX device. 10 islets were loaded into the tissue culture region. Scale bar = 500  $\mu$ m. Figure reprinted from ref [190] with permission, ©2017 Royal Society of Chemistry .

### 2.2.10 Islet secretion sampling and insulin quantification

The  $\mu$ MUX device was mounted within a microscope stage-top incubator (Tokai Hit, Japan) held at 37 °C. Input channels were connected to 5 mL syringes half-filled with treatment buffers through Tygon tubing. The waste channel was attached to vacuum via a syringe. Other channels were connected to buffer tubes with vacuum applied by syringes for sample output collection (Figure 2.9). The time and channel program was designed so that islets were incubated with one of the input solutions for 5 *min*, followed by sampling the buffer into one of the output channels with 2 rinses in between treatments.  $\sim$ 10 islets were loaded into the tissue culturing region on the  $\mu$ MUX device (Figure 2.10). After the islets were starved on-chip in BMHH buffer (3 *mM* glucose, 0.1% BSA) for 30 *min* to 1 *h*, the device was then set for fully automated operation by the user-defined program. Solutions in output tubing were then collected into the buffer tubes (Figure 2.9). The insulin levels were measured using a homogeneous fluorescence assay (Human Insulin FRET-PINCER Assay Kit; Mediomics, St. Louis, MO) analysed with minimized background interference using our recently developed thermofluorimetric analysis protocols [234, 235].

### 2.2.11 Fatty acid uptake analysis

Real time fatty acid uptake by adipose tissue explants was measured either with a kit (QBT Fatty Acid Uptake Assay Kit, Molecular Devices) or with a custom fluorescence quenching assay [191]. Each method used bodipy-labelled laurate (cell permeable fatty acid analogue, FFA\*) and a cell-impermeable fluorescent quencher. The  $\mu$ MUX device was mounted within a microscope stage-top incubator (Tokai Hit, Japan) held at  $37\text{ }^{\circ}\text{C}$ , and input channels were connected as before. The treatment buffer consisted of serum free DMEM, either 2 M of FFA\* or unlabelled free fatty acid (FFA), 1 M quencher, and five different levels of glucose and insulin (3 *mM* and 50 *pM*, 7 *mM* and 0.5 *nM*, 11 *mM* and 1.0 *nM*, 15 *mM* and 1.5 *nM*, and 19 *mM* and 2 *nM*). The waste channel was attached to vacuum via a syringe. 3-*mm* diameter adipose tissue explants were removed from storage serum media, washed 3x with fresh serum free media, and pre-treated in serum free DMEM buffer with 3 *mM* glucose, 0.5 *nM* insulin and 2.0  $\mu$ M FFA for 30 *min*. Each explant was then washed with serum free media and placed on a  $\mu$ MUX device fabricated without 3D printed templating, where a platinum mesh was used to hold the explant in place. In this instance, the  $\mu$ MUX device was semi-automatically controlled using the electrode wires for full sensing. During emptying, tubing connected to the waste channel was monitored by eye, since fluorescence imaging precluded the use of real-time DIC imaging of the reservoir bottom. All solutions with FFA\* or FFA were held at  $37\text{ }^{\circ}\text{C}$  and alternatively pulsed onto adipose explants as fluorescent images were captured using a 10X objective and FITC filter set every 20 second. Images were analysed using ImageJ and Microsoft Excel.

## 2.3 Result and Discussion

### 2.3.1 $\mu$ MUX device design

Pneumatic microvalve-based microfluidic multiplexers were introduced soon after the invention of PDMS valving [97]. As in analogous electronic components, the microfluidic

multiplexer can address large numbers ( $n$ ) of fluid channels with a smaller number ( $2\log_2 n$ ) of pneumatic controls and is normally used as one utility component of larger, integrated microfluidic frameworks [236]. More recently, others have demonstrated that the microfluidic multiplexer is valuable as a stand-alone component for automated handling of fluids and cell culture substrates [237, 238, 239]. Based on this concept, we designed our microfluidic multiplexer ( $\mu$ MUX) chip for delivering treatments and sampling secretions from tissues, serving as a kind of mimic of the circulation in the endocrine system.

The 16 fluidic channels, which were addressed by 8 pneumatic control channels ( $2\log_2 16 = 8$ ), served as either inputs or outputs for automated perfusion and sampling of endocrine tissue. For more economical space management, the standard multiplexer design was modified into a radially symmetric design surrounding a centralized tissue culture region (Figure 2.1 A). This approach reduced the channel footprint and minimized channel lengths, thus minimizing dead volume between stimulants or samplings. Since the fluidic channel cross-section was measured to be  $7580 \pm 150 \mu m^2$  (Figure 2.2), channel volumes could be accurately calculated. Switching between two different inputs (see Video S-3) for varying stimulation to cells, the carry-over volume from the first stimulant to the next would range from 31 to 68  $nL$  (Figure 2.11). Even without wash steps included, this dead volume represented a negligible fraction, merely 0.15% to 0.34%, of the typically transferred reservoir volume of 20  $\mu L$ . Note that reservoir carry-over was addressed later by including wash steps (ESI and Figure 2.7 A). The design also allowed higher density arrangement of fluidic reservoirs and/or tubing interfaces (filled black circles in Figure 2.1 A; smaller ports in Figure 2.1 B).

### 2.3.2 System Automation

The  $\mu$ MUX was operated through discrete sampling defined by drainage and replacement of the reservoirs solution every few minutes, as noted above. The tissue of interest was bathed in one solution introduced from a  $\mu$ MUX input channel, and following the designated

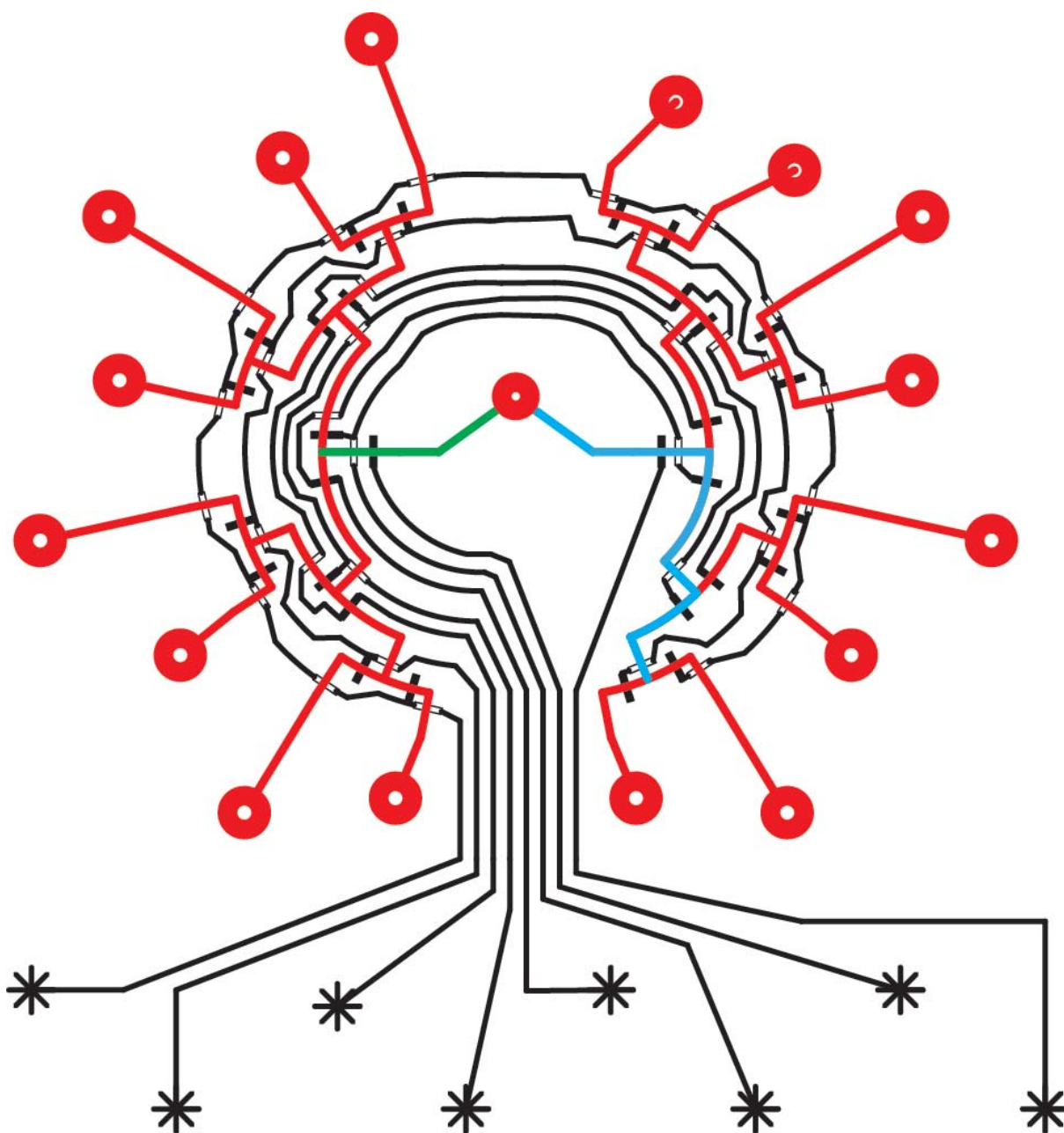


Figure 2.11: Schematic of the  $\mu$ MUX channel design at higher resolution. Control channels are shown in black and fluidic channels in red. Also highlighted here are the channel lengths representing the shortest (green, 4.08 *mm*) and longest (blue, 8.96 *mm*) possible plug lengths of dead volume when switching between input/output channels. As discussed in the text, these dead volumes represent a negligible amount ( $< 0.4\%$ ) of solution compared to the tissue culture volume, even without washing steps included. Note that this dead volume analysis assumes that  $> 9$  channels are used. Figure reprinted from ref [190] with permission, ©2017 Royal Society of Chemistry .

time, all solution in the reservoir was removed and collected in tubing for downstream assays using one of the  $\mu$ MUX channels as an output. With pneumatic micro-valving operated by computer controlled solenoids, cell media could be digitally controlled with minimal dead volume in a highly flexible manner. However, to fully automate this system, it was necessary to include real-time sensing of the solution level in the central reservoir. Peristaltic pumping with valves (3-valve pump) was not suitable to meet the flow rate requirement ( $20 \mu L$  in  $<10 s$ ), and our discrete sampling method is less compatible with constant-flow syringe pumps. By clearly defining starting and ending reservoir volumes (i.e. empty or full), the  $\mu$ MUX could be fully automated using the same software that was used for valve control.

As shown in Figure 2.4, a customized full sensor was fabricated based on solution conductivity [240]. Two gold electrodes were positioned onto the PDMS substrate and into the central device reservoir. A 5 V digital output (DO) line from a USB DAQ device (USB-6008, National Instruments) was applied to one electrode, and the other electrode was attached to a 1 M resistor. Upon filling of the reservoir to the point of contact with both electrodes, the circuit (Figure 2.4 B) was completed, placing the buffer solution in series with a 1 M resistor in a voltage divider configuration. By measuring the voltage drop across the fixed resistor using an analog input (AI) line, a simple thresholding algorithm could be used to electrically detect the full state of the reservoir in a straightforward and robust manner. In initial testing, an empty sensor was validated with aqueous buffer using the same voltage divider concept, but with an electrode at the bottom of the reservoir (Figure 2.12). Unfortunately, the BSA-containing cell media exhibited surfactant effects that resulted in irreproducible wetting of the electrode surface, making consistent empty sensing less desirable with this approach.

The final empty sensor design employed optical imaging, taking advantage of the patterned reservoir bottom, which was moulded with a 3D-printed template. Details in the surface pattern of the reservoir bottom were nearly invisible when solution was present, due

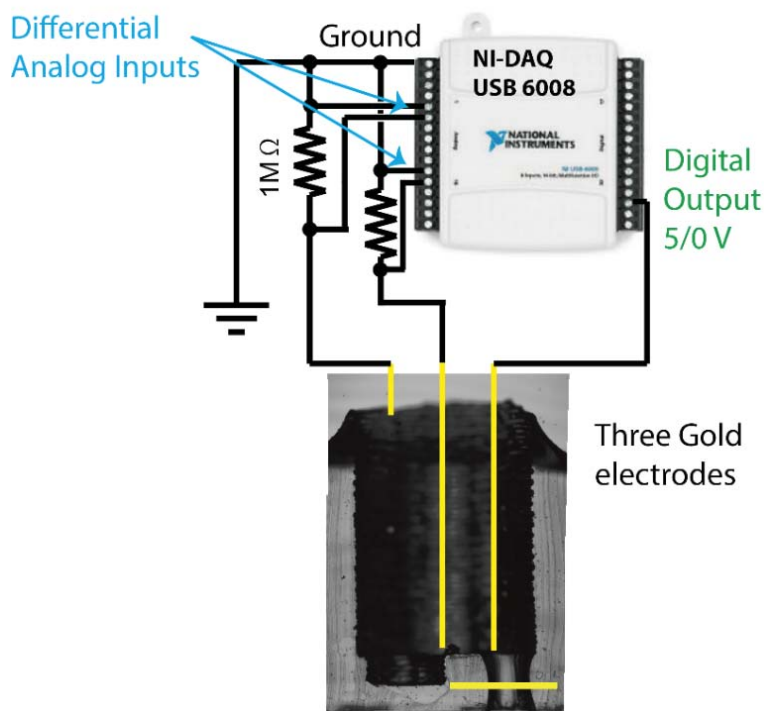


Figure 2.12: Circuitry of the initial three-electrode system for conductivity sensing of both the full and empty states.

The source electrode was wired to a 5-V digital output of the NI-DAQ. The full sensing electrode was placed at the opening of the reservoir, and the empty sensing electrode was placed just above the bottom of the reservoir. Both of the sensing electrodes were connected to 1  $M\Omega$  resistors across differential analog inputs for voltage readouts. The empty signal from this tri-electrode sensor was not reproducible in cell culture media (with BSA) due to inconsistent electrode wetting problems. Scale bar = 2  $mm$ . A video of the MUX device operation with these sensors is shown in Video S-1. Figure reprinted from ref [190] with permission, ©2017 Royal Society of Chemistry .

to the similarities in refractive index ( $\eta$ ) between PDMS ( $\eta_{\text{PDMS}} = 1.4$ ) and water ( $\eta_{\text{water}} = 1.33$ ). Upon emptying the reservoir, however, PDMS-to-air interfaces were easily detected by imaging in differential interference contrast (DIC) mode ( $\eta_{\text{air}} = 1.00$ ). One of various feature edges could be imaged, and the standard deviation of the region of interest (ROI) was used as a robust, real-time indicator of the empty state of the reservoir, as shown by the images and data in Figure 2.4 C-E.

The in-house written control program (LabVIEW) and hardware consisted of six main sections: (1) A software front panel with parameter inputs for assigning each microchannel as a fluidic input or output, setting the cut-off values for voltage or ROI standard deviation, and selecting the ROI for image analysis; (2) a time and channel program input array for stepwise chip operation; (3) valve control hardware for operating the fluidic channels through the DAQ system; (4) the conductivity sensor for the full signal voltage readout; (5) a camera interface for real-time image grabbing as the empty sensor; and (6) a software logic loop (flowchart in Figure 2.5A) to interpret the various inputs and sensors for automation of the  $\mu\text{MUX}$  system. As shown by representative automation data in Figure 2.5B, real-time measurements from the full sensor (voltage drop; orange trace) and the empty sensor (ROI; green trace) were the primary drivers of system automation according to the programmed logic in Figure 2.5A. Data from 3 *min* of an automated test run in temporal sampling mode are shown in Figure 2.5B. Channel numbers are represented as blue diamonds; channels 0 and 15 were set as input fluidic lines, channels 1 through 4 were set as output fluidic sampling lines, and channel 16 was used as a code for closing all valves. This test run automatically switched channels in the following channel order: 15, 1, 15, 2, 15, 3, 0, 4, 0. Complete data sets from this control system collected during endocrine tissue sampling or imaging are collected (Figure 2.2).

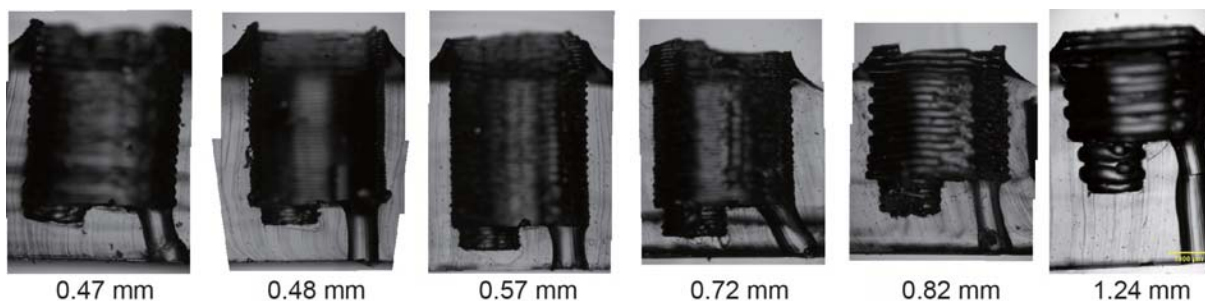


Figure 2.13: Cross-sections of multiple devices with varying depths of tissue culture regions. Tissue culture region depths are included below each image. Scale bar = 1.0 *mm*. Figure reprinted from ref [190] with permission, ©2017 Royal Society of Chemistry .

### 2.3.3 $\mu$ MUX device optimization

Continuous flow microsystems<sup>10-13, 15-18, 20</sup> for sampling endocrine cells require a relatively slow flow rate to protect cells from shear force induced damage. By contrast, in this  $\mu$ MUX design (Figure 2.1D), cells resting at the bottom of the culture/trapping region were shielded from shear stress, even at much higher flow rates. However, the design imposed an upper limit on the depth of the culture/trapping region. In order for stimulants to reach the cells quickly and for secreted hormones to be sampled with adequate temporal resolution, this region should be as shallow as possible, yet without washing away the cells or creating shear stress problems.

To optimize the depth of the cell culture/trapping region, devices with depths between 0.47 to 1.24 *mM* were fabricated using 3D-printed templates (Figures 2.13 and 2.14) and tested by operation with trapped murine islets. Devices with the most shallow trapping regions ( $< 500 \mu m$ ) were non-functional due to intermittent loss of islets during flow, but regions at or above a depth of 0.57 *mM* showed consistent retention of the cells. Next, to ensure acceptable temporal resolution during sampling, a novel method to mimic islets was devised. pH-responsive beads with a diameter distribution very similar to islets (100-200  $\mu m$ ) were synthesized by reacting glass beads with (3-Aminopropyl)triethoxysilane to introduce amine groups, followed by a reaction with FITC to create a thiourea linkage to a

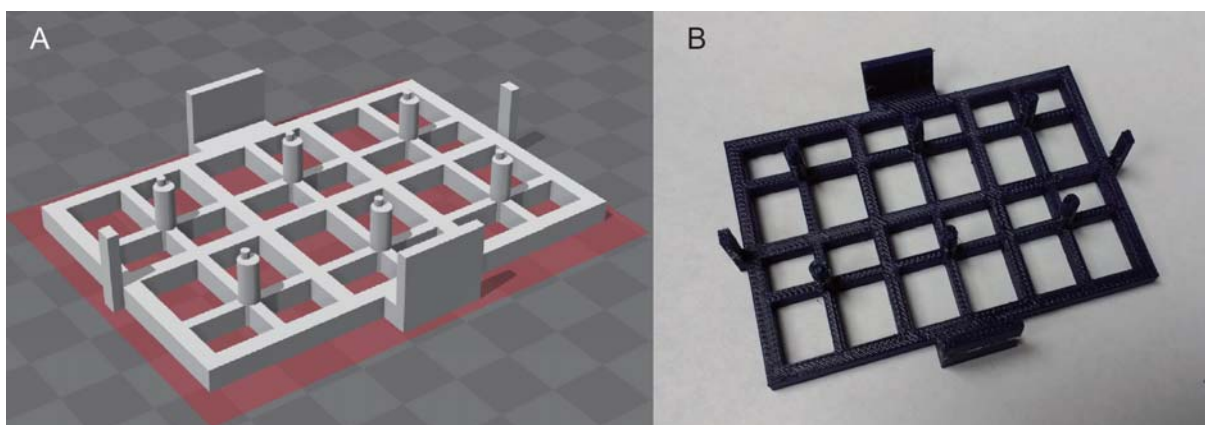


Figure 2.14: 3D-printed templates were used to fabricate customized tissue culture interfaces on the  $\mu$ MUX devices.

(A) 3D CAD rendering of a 6-device template and (B) an image of a printed template. By simply changing the design of the 3D CAD file, different templates could be created to give  $\mu$ MUX devices with varying tissue culture region depths (Figure 2.13). Figure reprinted from ref [190] with permission, ©2017 Royal Society of Chemistry .

fluorescein moiety (Figure 2.8 A-D). Since the phenolic pKa of fluorescein exhibits acid-base equilibrium, its fluorescence intensity is dramatically reduced at acidic pH [241]. By programming the  $\mu$ MUX device to switch between buffers of pH 5 and 9, this pH dependence was exploited to mimic the timing of islet stimulation (see Video S-4). At various culture/trapping region depths, the bead fluorescence intensities were increased to a maximum value following introduction of pH 9 buffer, indicating complete solution exchange (Figure 2.8 E). Relatively rapid exchange (30 s) was observed with depths of 0.48 and 0.57 mM, while deeper reservoirs caused proportionally longer solution exchange times. As the 0.57 mM depth was shown to alleviate islet loss during flow and to allow 30 s solution exchange, this depth was chosen for all experiments to follow.

Sampling volume consistency and solution carry-over were also optimized. The sampling volume was defined largely by the difference in solution levels marked by triggering of the empty and full sensors, but there was some dependence on the pressures and vacuum applied to input and output channels, respectively. As long as vacuum and pressure levels were relatively unchanged during the experiment, however, the variance in sampled volume was

$< 1\%$  on a given  $\mu$ MUX device (Figure 2.7 B). To avoid carry-over of treatments and samplings, particularly within the culture/trapping region, reservoirs were quickly emptied and refilled three times with the next treatment solution during  $\mu$ MUX operation, i.e. two rinsing steps and an incubation step. This approach was confirmed to decrease carry-over to  $< 1\%$  between treatments after the second rinse step (Figure 2.7 A).

#### 2.3.4 Temporal Sampling Mode: Dynamic Islet Function

The islets of Langerhans are composed of five different endocrine cells ( $\alpha$ ,  $\beta$ ,  $\delta$ , PP, and  $\epsilon$  cells), each of which secret characteristic hormones in response to metabolic changes, as well as other cells including vascular cells, resident immune cells, neurons, and glial cells [242].  $\beta$  cells secrete one of the more dominant endocrine hormones, insulin; defects in either secretory mechanisms or peripheral tissue responses to insulin are primary causes and/or symptoms of diabetes. With renewed interest in the blood glucose abnormalities induced by diets high in sucrose or refined carbohydrates [213, 214] there is a need for robust, programmable tools to study dynamic islet function. The input/output  $\mu$ MUX device presented herein was specifically tailored as a tool capable of not only introducing customized temporal patterns to the cells but also temporally sampling cellular secretions. The high flexibility and programmability of this digitally-operated device is a key advantage compared to other microdevices previously used to study islets [175, 66, 191, 215, 216, 218, 219, 220, 221, 223]. The 16 fluidic channels could be assigned as either inputs for treatments or outputs for sampling, allowing for example accurate mimics of postprandial blood glucose and gut hormone (incretin) levels.

To demonstrate the temporal sampling mode of the  $\mu$ MUX device, dynamic insulin secretion was first measured during treatment of islets with square waveforms of glucose at physiologically relevant concentrations (Figure 2.15 A). In this instance, the system was programmed with 2 input channels (3.5  $mM$  and 19.5  $mM$  glucose), 13 timed outputs for

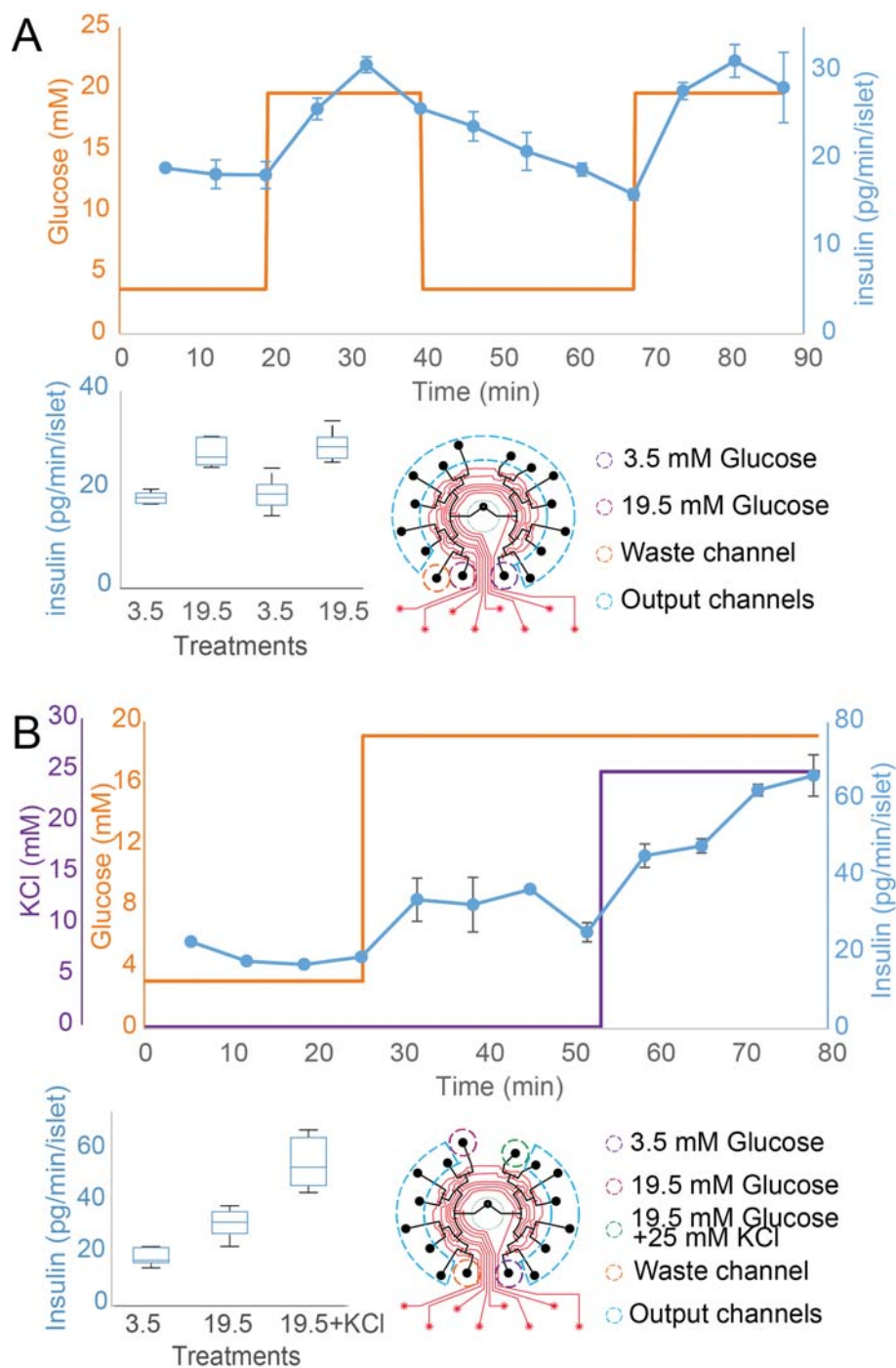


Figure 2.15: Temporal sampling mode of the  $\mu$ MUX.

(A) Dynamic insulin secretion sampling with 13 timed output channels was accomplished with a programmed glucose square wave treatment from 2 input channels. (B) Dynamic insulin secretion sampling with 12 timed output channels using programmed glucose and KCl treatments from 3 input channels. In both (A) and (B), upper right images show the channel assignments, while lower right box plots show aggregate cellular responses. Figure reprinted from ref [190] with permission, ©2017 Royal Society of Chemistry .

temporal secretion sampling, and 1 waste channel. The  $\mu$ MUX was operated under a square wave glucose program in automated fashion to collect 90 minutes insulin secretion profiles from groups of 10 islets. Islets responded with glucose-stimulated insulin secretion profiles that mirrored the input glucose waveforms, increasing to approximately  $30 \text{ pg} \cdot \text{islet}^{-1} \cdot \text{min}^{-1}$  then decreasing again within a few minutes of the glucose changes (Figure 2.15 A). To confirm the devices flexibility in temporal sampling mode, the program was then modified to 3 input channels (3.5 mM glucose, 19.5 mM glucose, and 19.5 mM glucose with 25 mM KCl), 12 timed outputs, and 1 waste channel. In this way, glucose concentration could be increased and held at the high level while adding KCl (Figure 2.15 B). Again, for all groups of islets, the increased glucose levels resulted in similar levels of secreted insulin (17 to 32  $\text{pg} \cdot \text{islet}^{-1} \cdot \text{min}^{-1}$ ). When 25 mM KCl was added, insulin secretion was increased even further to as high as  $65 \pm 5 \text{ pg} \cdot \text{islet}^{-1} \cdot \text{min}^{-1}$  due to exaggerated depolarization of the cell membranes, which enhances insulin vesicle recruitment. These results confirmed the  $\mu$ MUX device to be suitable for automated, microfluidic studies of insulin secretion dynamics.

### 2.3.5 Temporal Stimulation Mode: Dynamic Adipose Tissue Function

Although the principle function of white adipose tissue was traditionally assigned to energy storage, it is now understood that the tissue is a complex, multicellular endocrine organ with hormonal effects that modify the function of nearly all other organ systems [28]. In comparison to the case of pancreatic islets, however, there have been relatively few studies focused on the dynamic function of white adipose tissue. We have recently shown that the microfluidic platform is well suited for interrogating this tissue [191, 192], yet limited dynamic information was collected due to device limitations. Insulin is a dominant endocrine hormone, and its secretion by pancreatic islets is dynamically modified based on nutrient levels in the bloodstream, as evidenced from data shown in Figure 2.15. To improve our understanding of the dynamic response of adipose tissue to this hormone, the  $\mu$ MUX device

was programmed to mimic postprandial glucose and insulin levels and to apply these solutions to small samples (3-*mm* biopsies) of adipose tissue explants extracted from mice. At the same time, the system was programmed to facilitate functional imaging of the explants.

Recent work has shown that fatty acid uptake can be visualized with fluorescence imaging by using bodipy-modified free fatty acids (FFA) [243]. Exploiting the inherent flexibility of the  $\mu$ MUX device, an improved version of FFA uptake analysis was developed which permits real-time measurement of uptake rates. By alternatively pulsing labelled and unlabelled free fatty acids, uptake and release rates could be directly imaged as a function of treatments. An additional benefit of the  $\mu$ MUX system was revealed here, i.e. that the tissue is only *minimally* disturbed during automated operation, allowing high resolution fluorescence imaging in real time.

As such, the  $\mu$ MUX was operated in temporal stimulation and imaging mode to mimic postprandial glucose and insulin levels during real-time FFA uptake imaging (Video S-5). This mode required at least 10 of the channels to serve as inputs comprised of five different concentrations of insulin (0.05 – 2.0 *nM*) and glucose (3.0 – 19.0 *mM*), each with either labelled (FFA\*; bodipy-laurate) or unlabelled (sodium laurate) free fatty acids. The sequence of programmed treatments and input channel numbers during explant imaging is shown in Figure 2.16A. In other words, the 16-channel  $\mu$ MUX permitted a well-resolved, dynamic input program to be applied to cells with up to 4-bit resolution during real-time imaging. This program was designed to closely mimic the timing and magnitudes of serum glucose and insulin levels following a meal. As shown in Figure 2.16 B, the adipose explant began with an initial rapid uptake of available FFA followed by insulin-dependent exchange rates throughout the treatment program. The fluorescence intensity data (purple) was processed by measuring the initial uptake or release rate as a linear slope over a five-minute window, and the absolute values of these slopes were plotted over time (blue). Example explant images are shown in Figure 2.16 C, and an insulin dependence plot is shown in Figure 2.16 D.

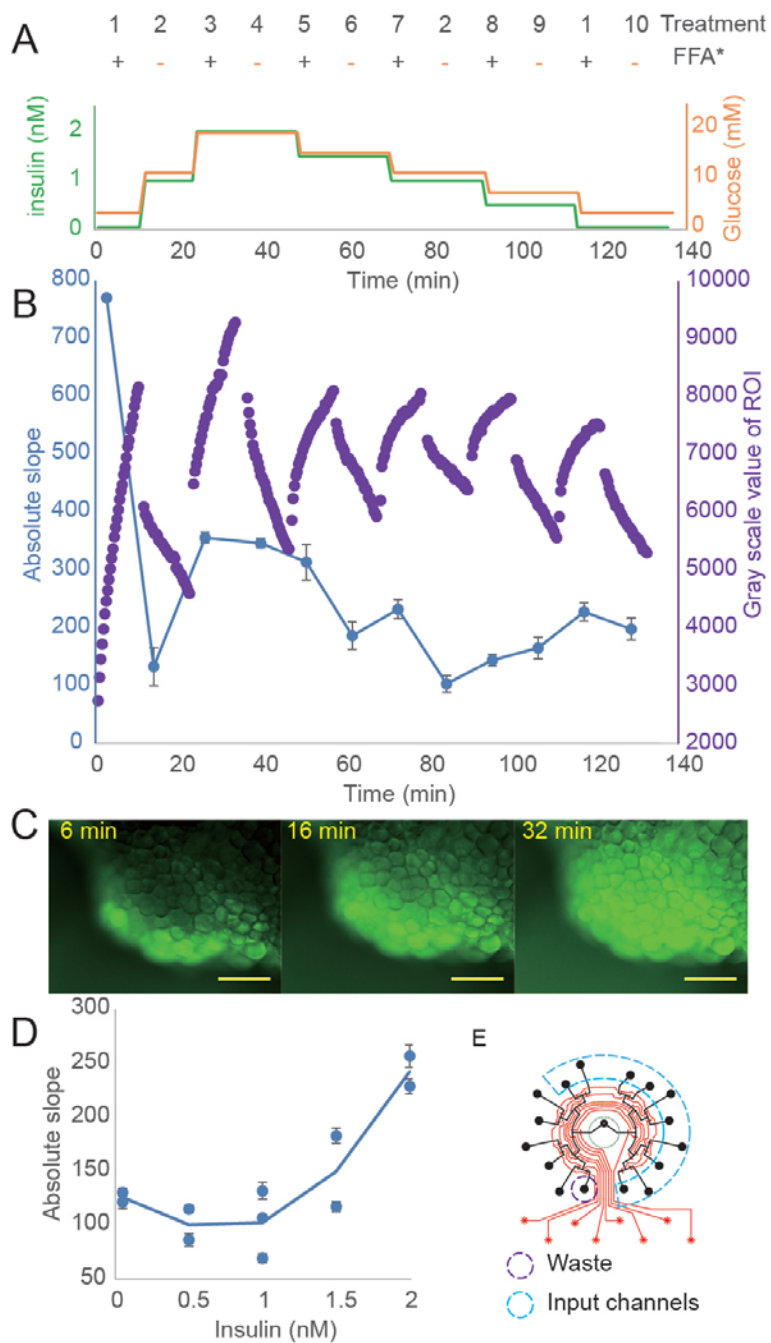


Figure 2.16: Temporal stimulation and imaging mode of the  $\mu$ MUX (A) Stimulation of adipose tissue explants with a mimic of post-prandial insulin and glucose at 5 different magnitudes was accomplished while sequentially pulsing labelled (FFA\*) and unlabeled free fatty acids (10 timed input channels). (B) Adipose tissue responded with insulin-dependent FFA exchange rates that closely followed the input pattern, with dynamic fluctuations even at the 10-min time scale. (C) Representative fluorescent images of the tissue during FFA\* uptake. (D) Insulin dependence plot using compiled data. (E) Assignment map showing the required 10 timed input channels and 1 waste channel. Figure reprinted from ref [190] with permission, ©2017 Royal Society of Chemistry .

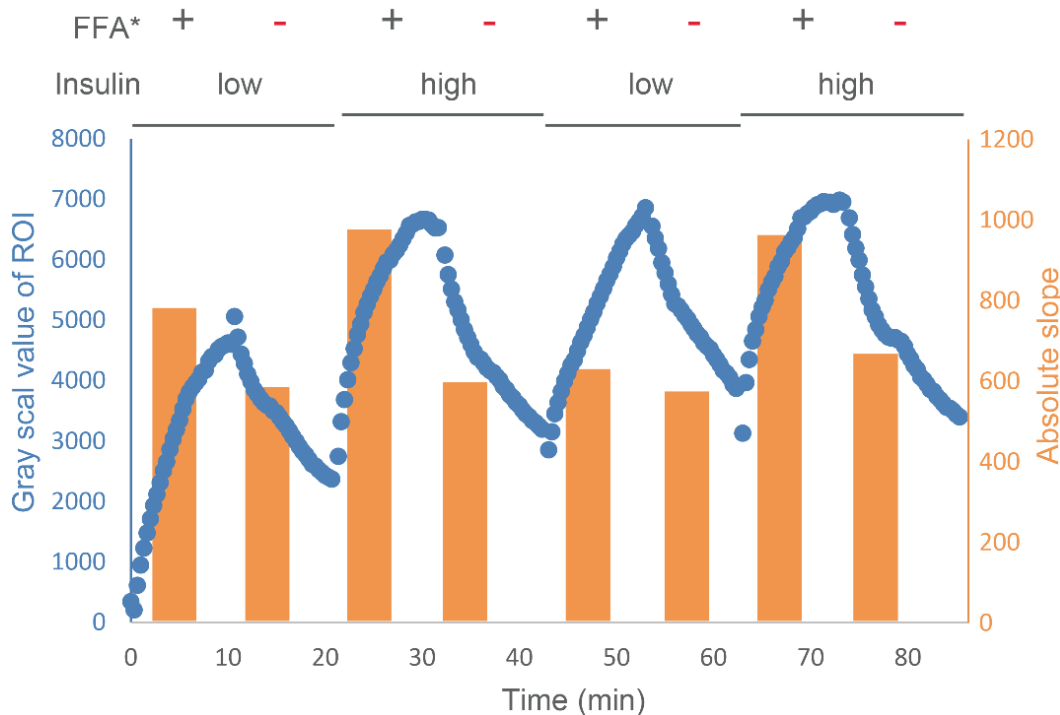


Figure 2.17: Dynamic fatty acid uptake with 2 treatments (4-input channels from  $\mu$ MUX). The adipose tissue explant was treated with a square wave of low and high insulin/glucose buffer while alternating bodipy-laurate (FFA\*) or unlabeled laurate. The explant was exposed to each solution for 10 *min* before switching to the next solution. The fluorescent microscopic images were taken in real time, and the background corrected gray scale value of the image is shown as blue dots. The initial rate of the fatty acid uptake is proportional to the absolute slope of gray scale value of ROI at the beginning of each treatment, which is shown in orange. Figure reprinted from ref [190] with permission, ©2017 Royal Society of Chemistry .

Interestingly, both uptake and release rates were observed to follow the pattern of glucose and insulin, in agreement with initial tests of the methodology (Figure S-10). These results suggest that FFA exchange machinery, e.g. FFA transport protein function, is temporally dependent upon insulin and glucose magnitudes with dynamic fluctuations even at the 10-min time scale. Enabled by the microfluidic platform, these measurements represent the first observation of real-time FFA exchange as a function of programmable, dynamic glucose and insulin inputs.

## 2.4 Conclusions

A microfluidic multiplexer device ( $\mu$ MUX) with a customized, 3D-templated tissue culture interface was developed and proven feasible for dynamic and quantitative measurements of both hormone secretion and nutrient sensing/uptake from two types of primary murine tissues. The device not only permitted confirmation of the dynamic function of pancreatic islets, but it also allowed new information to be gathered on temporally-resolved free fatty acid exchange in adipose tissue. These results reinforce the generalizability of the  $\mu$ MUX device, which should be translatable to other tissues such as liver, heart, skeletal muscle, etc. The device could also be envisioned as a single module in future integrated devices with, for example, on-chip bio-sensing or in-line separations. From an analytical standpoint, modest increases in the number of pneumatic valves should dramatically improve  $\mu$ MUX resolution in the future. 32 fluidic channels could be controlled by 10 pneumatic channels ( $2\log_2 32 = 10$ ), 64 controlled with 12 valves ( $2\log_2 64 = 12$ ), and so on. This would allow even finer stimulant gradients (e.g. post-prandial insulin/glucose) to be introduced to cells and would also promote increased temporal resolution on cell secretion sampling, all while maintaining the precision and flexibility of a digitally-controlled device. A reduction in tissue culture reservoir volume would also help improve input/output resolution. Nonetheless, as presented herein, the 16-channel  $\mu$ MUX is well-poised for a variety of novel dynamic studies on endocrine tissues.

## Chapter 3

### Analysis of dynamic nutrient exchange in murine adipose tissue with $\mu$ MUX

#### 3.1 Introduction

The global epidemic of obesity has brought increasing attention to research for understanding the biology of adipose tissues (fat tissues). Adipose tissues, which account for 5% to 50% of human bodyweight, was traditionally thought to be a passive reservoir for long term energy storage, but now is understood to be a complex, essential, and highly active metabolic and endocrine organ playing profound roles in systemic metabolism[26]. Despite its important, the dynamic nature of adipokine secretion, nutrient uptake and metabolism is still less studied, especially the study of mechanism and regulation of fatty acid uptake process of adipose tissue is urgently needed.

The triacylglycerol (TAG) stored within adipose tissues for energy reserves is mainly from two routes: *de novo* lipogenesis from glucose and other non-lipid precursors, or uptake of plasma fatty acid and TAG. Serum free fatty acids are generated from TAG carrier, plasma lipoprotein particles such as chylomicron (CM) and very low-density lipoprotein (VLDL) by the action of endothelial lipoprotein lipase (LpL), which is a glycoprotein enzyme secreted by adipocytes and translocated to the lumen of endothelial cells within the adipose tissue [244]. Because of their low solubility in aqueous solution [202], the majority free fatty acids are bound to albumin before being absorbed by cells[245]. The transport of FFA across the cell membrane is promoted by membrane proteins such as CD36/SR-B2, which is currently known as the predominant membrane protein facilitating fatty acid transport in adipocytes, enterocytes, cardiac myocytes, and skeletal myocytes [29]. Long-term fatty acid uptake regulation occurs by changes in the gene expression of CD36/SR-B2 in adipocytes via

fatty acid-induced PPAR $\gamma$  (peroxisome proliferator-activated receptor  $\gamma$ ) activation pathway. In the short-term, cellular fatty acid uptake is regulated by insulin-induced CD36/SR-B2 translocation from endosomal storage compartments to cell membranes and by intracellular recycling [29].

Direct observations of fatty acid uptake by adipocytes have been achieved by using radioactive labeled fatty acids [246] or fluorophore labeled fatty acid analogues [247]. Instead of using endpoint measurement, Liao et. al. [248] reported a real-time fluorescent fatty acid uptake assay by masking background fluorescence with a cell impermeable fluorescence quencher[249]. The fatty acid uptake rates of 3T3-L1 adipocytes under varying media insulin concentrations were monitored by this assay. Later, this assay was commercialized as QBT fatty acid uptake assay kit (Molecular Devices, Sunnyvale, CA). However, the product lifetime is limited to 5 days after rehydration of the lyophilized reagents. To overcome this limitation, we synthesized a BSA-BHQ (bovine serum albumin-Black hole quencher) conjugate to serve as the cell impermeable quencher based on a similar principle [205]. As a naturally occurring carrier protein for molecules of low water solubility, serum albumin is the most abundant plasma protein, and BSA is used in many biochemical applications such as a nutrient in cell culture, stabilizer for other proteins, and blocker in immunoassay. The combination of BSA-BHQ with fluorescence fatty acid conjugates (Bodipy-FL-C<sub>12</sub>, Bodipy-558/568-C<sub>12</sub>) allows us to monitor fatty acid uptake of adipose explants in real time with multiplexed color at lower cost[205, 190], and the reagents are much more stable than the QBT assay reagents.

Currently, few techniques and methods allow interrogation of small amounts of adipose tissue to explore the dynamic function of the organ. Microfluidic tools offer attractive features that could help fill this knowledge gap. Recent breakthroughs in cellular co-culture and organs-on-chips platforms have revealed that microfluidic analysis systems nicely simulate physiology at the single cell level and the tissue level, or even the organ level. These systems recapitulate biological functions in ways not possible with standard techniques[93].

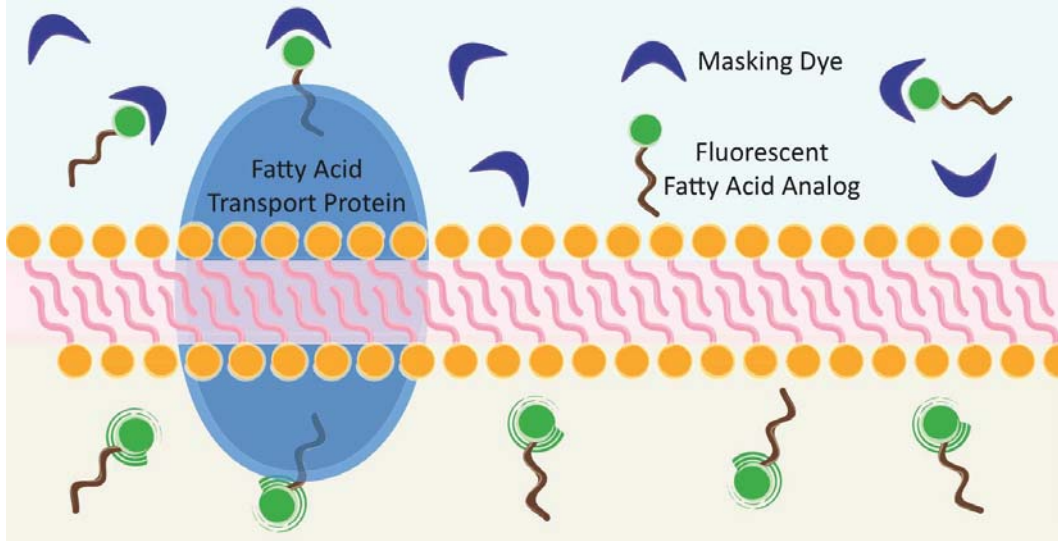


Figure 3.1: Cartoon Representation of BSA-Q Assay Mechanism

Excess masking dye (BSA-Q, purple) quenches fluorescent output from Bodipy-C<sub>12</sub> (green) when outside the cell. Bodipy-C<sub>12</sub> can be transported into cells through transport proteins (CD36, blue), but the masking dye cannot permeate the cell. Once inside, fluorescence from Bodipy-C<sub>12</sub> is no longer quenched and intensities within the cells begin to rise. This figure is reprinted from ref [205], courtesy of Dr. Jessica Brooks.

As previously discussed in Chapter 2, we designed a fully automated, 16-channel microfluidic input/output multiplexer ( $\mu$ MUX) for endocrine tissue culture and secretion sampling[190] (Figure 2.1). As in analogous electronic components, the pneumatic microvalve based microfluidic multiplexer can address large numbers ( $n$ ) of fluid channels with a smaller number ( $2\log_2 n$ ) of pneumatic controls. The 16 fluidic channels, which were addressed by 8 pneumatic control channels ( $2\log_2 16 = 8$ ), essentially serve as a mimic of the circulatory system and of upstream endocrine signals. Along with pancreatic islet analysis, fatty acid uptake and release was also monitored by fluorescent imaging of adipose tissue explants confined within the  $\mu$ MUX. Adipose tissue explants were exposed to a temporal mimic of postprandial insulin and glucose levels, while simultaneous switching between fluorescently labeled and unlabeled free fatty acid permitted fluorescent imaging of fatty acid uptake dynamics in real time. Surprisingly, both of the fatty acid uptake and release initial rate were observed to follow the pattern of glucose and insulin. It is likely that, CD36/SR-B2 or other fatty acid transport proteins are not only involved in fatty acid uptake, but also in fatty acid release,

with regulation by insulin. Here, we have expanded upon the work shown in Chapter 2 by focusing on insulin-dependent fatty acid uptake using the  $\mu$ MUX device along our custom fatty acid uptake imaging assay.

## 3.2 Experimental

### 3.2.1 General materials and reagents

All buffers were prepared with deionized, ultrafiltered water (BDH1168-5G, VWR, Radnor, PA). fatty acid free bovine serum albumin (FAF-BSA) was obtained from Akron Biotech (Boca Raton, FL), sodium dodecanoate was obtained from Spectrum Chemical (New Brunswick, NJ), Insulin, D-glucose, 4-2-hydroxyethyl-1-piperazineethanesulfonicacid, Dimethylformamide (DMF), dicyclohexylcarbodiimide (DCC), N-Hydroxysulfosuccinimide sodium salt (NHS-SO<sub>3</sub>Na), Diethylether (Et<sub>2</sub>O), KH<sub>2</sub>PO<sub>4</sub>, and NaH<sub>2</sub>PO<sub>4</sub> were purchased from Sigma-Aldrich (St. Louis, MO). Bovine serum albumin (BSA), fetal bovine serum (FBS), NaCl, CaCl<sub>2</sub> · 2H<sub>2</sub>O, EtOH, and MeOH were purchased from VWR (West Chester, PA). Penicillin-streptomycin, Minimal Essential Media (MEM), non-essential amino acids solution 100X, sodium pyruvate, L-glutamine, collagenase P, collagenase type I, Dulbecco's phosphate-buffered saline (DPBS), and Dulbeccos Modified Eagle Medium (DMEM), MgSO<sub>4</sub> · 7H<sub>2</sub>O, 10K molecular weight cut-off Slide-A-Lyzer MINI dialysis devices, 4,4-Difluoro-5,7-Dimethyl-4-Bora-3a,4a-Diaza-s-Indacene-3-Dodecanoic Acid (BODIPY FL C<sub>12</sub>, 505/512 nm), and 4,4-Difluoro-5-(2-Thienyl)-4-Bora-3a,4,a-Diaza-s-Indacene-3-Dodecanoic Acid (BODIPY 558/586 C<sub>12</sub>, 558/586 nm) were purchased from ThermoFisher Scientific (Grand Island, New York). Black hole quenchers (BHQ)-10 Succinimidyl Ester (BHQ-10-OSU, 516 nm max absorption) and BHQ-3 Succinimidyl Ester (BHQ-3-OSU, 612 nm max absorption) were purchased from Biosearch Technologies (Petaluma, CA).

### 3.2.2 Synthesis of BSA-Quencher

Fatty acid free BSA (FAF-BSA) was first dissolved in sterile DPBS (1%). BHQ-3-OSU and BHQ-10-OSU were dissolved in DMSO (0.33  $mg/mL$ ) immediately before use. FAF-BSA (1%), BHQ-3-OSU (0.33  $mg/mL$ ), and BHQ-10-OSU (0.33  $mg/mL$ ) were mixed with a ratio of 1:5:5 (1:0:10 for BSA-Q3, 1:10:0 for BSA-Q10) in a 50  $mL$  centrifuge tube, and allowed to shake on a rocker protected from light for 2  $h$  at room temperature then overnight at 4  $^{\circ}C$ . Unreacted BHQ-3 or BHQ-10 were then removed by dialysis (10K Slide-A-Lyzer) using DPBS. Purified product (BSA-Q) was aliquoted and stored at -80  $^{\circ}C$  until use. UV-VIS absorption was used for concentration and label ratio measurement. The labeling ratio was calculated based on the absorption spectrum with the following parameters:  $\varepsilon_{BSA}^{280} = 42824 M^{-1}cm^{-1}$ ,  $\varepsilon_{BHQ-3}^{616} = 40700 M^{-1}cm^{-1}$ ,  $\varepsilon_{BHQ-3}^{517} = 2207 M^{-1}cm^{-1}$ ,  $\varepsilon_{BHQ-3}^{280} = 22296 M^{-1}cm^{-1}$ ,  $\varepsilon_{BHQ-10}^{517} = 28700 M^{-1}cm^{-1}$ ,  $\varepsilon_{BHQ-10}^{280} = 8200 M^{-1}cm^{-1}$ ,  $\varepsilon_{BHQ-10}^{616} = 5975 M^{-1}cm^{-1}$ .

### 3.2.3 CD-36 inhibitor synthesis

Sulfo-N-Succinimidyl palmitate was synthesized as a CD36 inhibitor according to the previously reported procedure with modification [250, 204]. Palmitic acid (150.0  $mg$ , 0.5849  $mmol$ ), NHS-SO<sub>3</sub>Na (139.9  $mg$ , 0.6434  $mmol$ ), and DCC (241.4  $mg$ , 1.170  $mmol$ ) were mixed in 5  $mL$  of DMF, then stirred at room temperature overnight under N<sub>2</sub>. The precipitated dicyclohexylurea was removed by filtration (Whatman filter paper, 1005-055, GE healthcare, Buckinghamshire, UK). 40  $mL$  Et<sub>2</sub>O was added into the filtrate, and the solution was cooled to 4  $^{\circ}C$  to allow products to form colloids. Then, the colloid was collected by filtering with a 25  $\mu m$  syringe filter. The product was dried under vacuum to afford white solid (50.2  $mg$ , 18.8%) and saved at -20  $^{\circ}C$  until use. <sup>1</sup>H and <sup>13</sup>C nuclear magnetic resonance (NMR) spectra were recorded at 600  $MHz$ , calibrated using residual undeuterated solvent as an internal reference (DMSO-*d*<sub>6</sub>,  $\delta$  2.50  $ppm$ ). High-resolution mass spectrometric (HRMS) data were obtained using a quadrupole time-of-flight (Q-TOF) spectrometer and electrospray ionization

(ESI).  $^1\text{H}$  NMR (600  $\text{MHz}$ ,  $\text{DMSO-}d_6$ )  $\delta$  3.99 (bs, 1H), 2.92 (m, 2H), 2.77 (s, 1H), 2.68 (bs, 2H), 1.66-1.22 (m, 2H), 1.41-1.36 (m, 2H), 1.36-1.22 (m, 22H), 0.89(t, 3H);  $^{13}\text{C}$  NMR (151  $\text{MHz}$ ,  $\text{DMSO-}d_6$ )  $\delta$  168.85, 165.41, 162.35, 56.29, 31.33, 30.92, 30.79, 30.19, 29.08, 29.06, 29.05, 28.99, 28.89, 28.74, 28.57, 28.04, 24.32, 22.13, 14.00; HRMS (ESI) calculated for  $\text{C}_{20}\text{H}_{34}\text{O}_7\text{NS}$  ( $[\text{M-Na}]^-$ )  $m/z=432.2056$ , found 432.2007.

### 3.2.4 Adipocyte explant extraction and culture

All experiments involving animals (mice, C57BL/6J) were performed in compliance with relevant laws and institutional guidelines and were approved under protocol number 2014-2096 and 2017-3101 by the institutional animal care and use committee (IACUC) of Auburn University. Epididymal adipose tissue pads were extracted as described previously [251, 252, 201] from 18-20 week old male C57BL/6J mice (Jackson Laboratories), and transferred to 4 mL of prewarmed phosphate-HEPES buffer. Fat pads were transferred to a 60  $\text{mm}$  Petri dish containing a few milliliters of fresh phosphate-HEPES buffer. Excess vasculature and other non-adipose tissue was removed via micro surgical scissors. 3  $\text{mm}$  sterile biopsy punches were used to remove aliquots of the fat tissue. As explants were punched, they were transferred with surgical tweezers into a glass tube with 3-4 mL of phosphate-HEPES buffer. Explants were centrifuged at 1000  $\text{rpm}$  for 3  $\text{min}$ . Infranatant was removed with an 18G 1.5  $\text{inch}$  needle. 3-4  $\text{mL}$  of phosphate-HEPES buffer was added back to the tube. Cells were centrifuged and washed in this fashion one additional time with phosphate-HEPES buffer and 2 additional times with fat serum media. After the final rinse, explants were transferred to individual wells on a sterile 96-well plate containing 200  $\mu\text{L}$  of serum media in each well. The 96-well plate was incubated for 30 minutes at 5.0%  $\text{CO}_2$  and 37°C. 3D printed explant traps [252] were placed into each well, and the plate was returned to the incubator. Explants were maintained for up to 7 days in the incubator with serum media replacement conducted twice a day. Explants were starved in serum free DMEM containing 3.5  $\text{mM}$  Glucose and 50  $\text{pM}$  insulin for 30  $\text{min}$  before each treatment.

### 3.2.5 Microfluidic device fabrication and operation

The microfluidic devices ( $\mu$ MUX) were fabricated as described in section 2.2.2. 36 g of PDMS polymer mixture (5:1 ratio, monomer:curing agent) were mixed and degassed under vacuum, poured onto the fluidic master wafer (AZ) wrapped within aluminum foil, and then baked in the oven at 60 °C for 40 min. Following curing, the PDMS was peeled from the master, after which it was diced, access holes and vias were punched (1.5 mm inner diameter for interfacing with tubing, 1.0 mm for the via connection between the reservoir and channels, and 2.5 mm for explants trapping), and each device was cleaned with methanol and dried with N<sub>2</sub> gas. Next, 5 g of degassed PDMS polymer mixture (20:1 ratio, monomer:curing agent) was spin coated onto the pneumatic control channel master wafer (SU-8) at 2300 rpm for 60 s and baked at 65 °C for 40 min to facilitate partial curing of the polymer. The freshly made fluidic layer PDMS, with access holes punched, was carefully aligned onto the partially cured control channel PDMS layer, and the two layers were permanently bonded by placing in the oven at 65 °C for at least 4 hours. The PDMS devices were then peeled from the wafer and diced, then access holes were punched where necessary. Finally, the assembled PDMS devices were plasma oxidized and bonded to a glass substrate. The  $\mu$ MUX devices were stored at room temperature. Immediately before use with islets or adipose explants, the devices were cleaned with an air plasma for 45 s then treated with PBS buffer with 1% BSA to generate a hydrophilic, biocompatible surface.

Pneumatic valves were actuated with solenoid switches (LHDA0533115H, The Lee Co., Westbrook, CT) controlled by a multifunction data acquisition system (USB-6002, National Instruments) and using a house nitrogen source adjusted to 20 psi with a pressure regulator. The 16 fluidic channels were addressed by 8 pneumatic control channels connected to the corresponding solenoid switches with Tygon tubing (0.02 inch ID, 0.06 inch OD, Cole-Parmer, Vernon Hills, IL). Dead-end control channels were filled with water to prevent air leakage through PDMS membranes. As a solenoid switch was activated, nitrogen gas pressurized a lower layer control channel and closed the fluidic channel in the upper layer (push-up valves).

Valve actuation timing was manually controlled by the semi-automated mode of the in-house written LabVIEW application with electrodes for solution level sensing[190].

### 3.2.6 Fluorescent explant imaging

Real time fatty acid uptake by adipose tissue explants was measured with BODIPY FL C<sub>12</sub> and BODIPY 558/586 C<sub>12</sub> with the cell impermeable BSA-Q quencher. Serum free media used with the BSA-Q system was formulated to exclude glucose, phenol red, and BSA. Dilutions of glucose, insulin, free fatty acids (sodium dodecanoate), and BSA-Q were diluted in serum free media. Low glucose and insulin media (LGLI) consisted of serum free DMEM, 3.5 *mM* glucose, and 50 *pM* insulin; high glucose and insulin media (HGHI) consisted of serum free DMEM, 19.5 *mM* glucose, and 2 *nM* insulin.

BODIPY-FL-C<sub>12</sub>, BODIPY-558/586-C<sub>12</sub> and BSA-Q were diluted in LGLI and HGHI. 2.0  $\mu\text{M}$  fatty acid (unlabeled free fatty acid, BODIPY FL C<sub>12</sub>, or BODIPY 558/586 C<sub>12</sub>) and 1.0  $\mu\text{M}$  BSA-Q (which has 6 high affinity binding sites for FFA plus additional sites) were applied to cells for treatments and imaging for all samples unless specified otherwise. Each treatment solution was added to a syringe connected through Tygon tubing to the input channel of the  $\mu\text{MUX}$  chip mounted within a microscope stage-top incubator (Tokai Hit, Japan) held at 37 °C. The waste channel was attached to vacuum via another syringe. 2-*mm* diameter adipose tissue explants were removed from storage serum media, washed 3x with fresh serum free media, and pre-treated in serum free DMEM buffer with 3.5 *mM* glucose, 50 *pM* insulin, and 2.0  $\mu\text{M}$  FFA for 30 *min*. Each explant was then washed with serum free media and placed on a  $\mu\text{MUX}$  device, where a platinum mesh was used to hold the explant in place. In this instance, the  $\mu\text{MUX}$  device was semi-automatically controlled using the electrode wires for full sensing. During emptying, tubing connected to the waste channel was monitored by eye. All solutions with labeled fatty acid, unlabeled fatty acid or without fatty acid were protected from light and held at 37 °C and alternatively pulsed onto adipose explants as fluorescent images were captured using a 10X objective and FITC filter

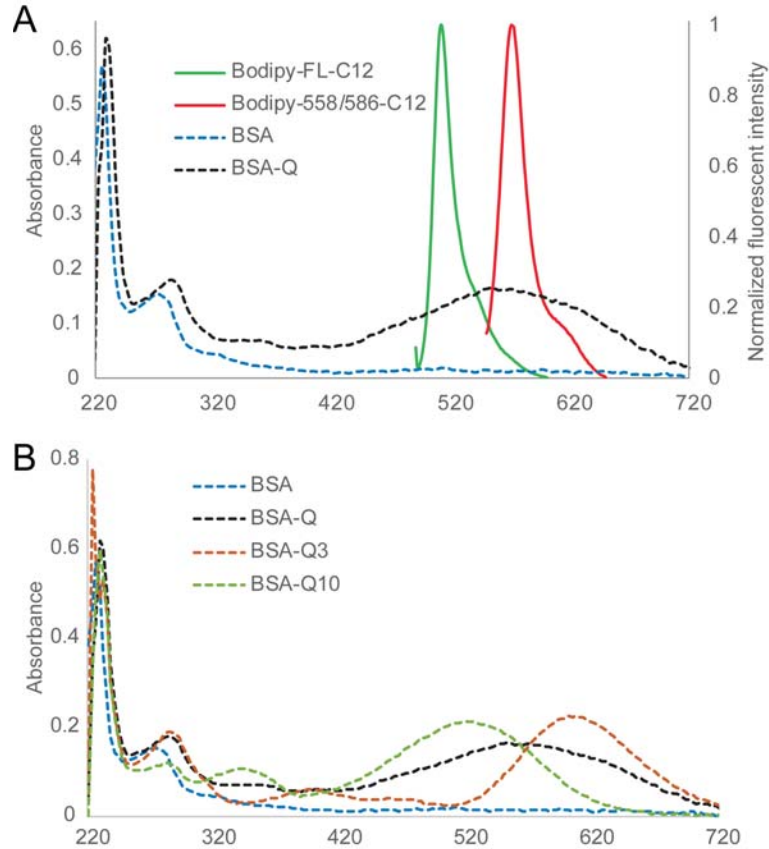


Figure 3.2: UV-Vis absorption (dashed curves) and fluorescent emission (solid curves) of BSA based quencher and Bodipy labeled fatty acid

(A) The spectrum overlap of the fluorescence emission of both Bodipy-FL-C<sub>12</sub> and Bodipy-558/586-C<sub>12</sub> with the absorption of BSA-Q indicate high efficiency fluorescent quenching. (B) The absorption spectrum of BSA, BSA-Q, BSA-Q3, and BSA-Q10.

set every 10 second. Images were analysed using ImageJ and Microsoft Excel.

For treatments with fatty acid uptake inhibitor (Sulfo-N-Succinimidyl Palmitate), an inhibitor solution (200 *mM*) in DMSO was freshly made and diluted to 200  $\mu$ M with HIHG (high insulin high glucose) or LILG (low insulin low glucose) DMEM buffer. The inhibitor solution was directly loaded into the cell reservoir with the adipose explant by pipette. Every 10 *min*, the reservoir was emptied via the waste channel and a new inhibitor was loaded. After 30 *min* inhibitor treatment, the explants were alternatively treated with labeled fatty acid, unlabeled fatty acid, or without fatty acid while imaging. 1000-fold diluted DMSO was used as a control.

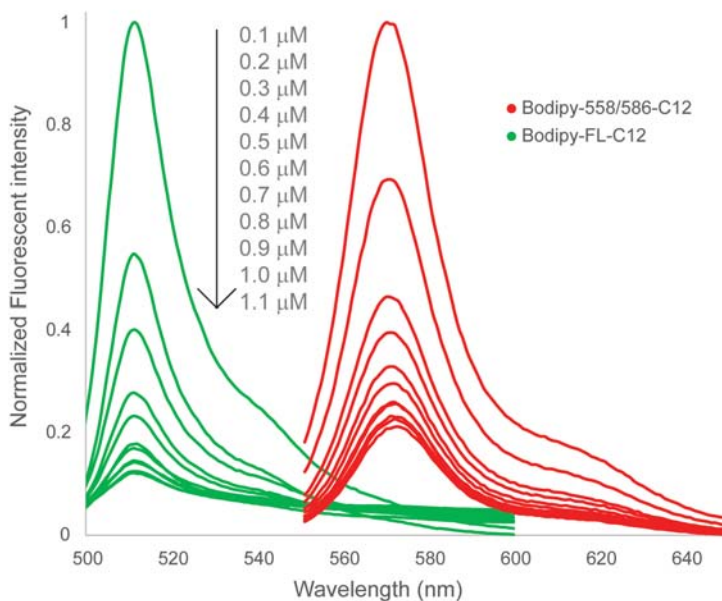


Figure 3.3: Bodipy fatty acid titration with BSA-Q  
 Fluorescent emission spectrum of  $2 \mu\text{M}$  Bodipy-FL- $\text{C}_{12}$  (green) and  $2 \mu\text{M}$  Bodipy-558/586- $\text{C}_{12}$ (red) with various concentration of BSA-Q ( $0.1$  to  $1.1 \mu\text{M}$  ).

### 3.3 Result and Discussion

#### 3.3.1 BSA-Quencher design and synthesis

One important function of serum albumin, such as BSA, is to bind long-chain fatty acids and thereby increase their aqueous solubility. Almost all the free fatty acid in serum binds to albumin in physiological conditions. BSA molecules have 6 high affinity binding sites ( $K_a > 10^5 \text{ M}^{-1}$ ) and more than 60 weak binding sites ( $K_a \approx 10^3 \text{ M}^{-1}$ ) [253]. Based on the interaction of BSA and fatty acid, a homogeneous, real time fluorescent assay for fatty acid uptake has been developed. The assay mechanism is shown in Figure 3.1, Background fluorescent is masked by the cell impermeable BSA-Q. As the fluorescent fatty acid is taken up by the cell, the fluorescence is no longer quenched and the intensities are proportional to the concentration of Bodipy- $\text{C}_{12}$  within cells.

The BSA based quencher has several advantages over previously used cell impermeable fluorescence quenchers [248]. Firstly, the quenching efficiency or the Förster resonance energy

transfer efficiency between the fluorophore and the quencher depends on the distance of those two molecules ( $r$ ) with an inverse 6th-power law ( $E_T = R_0^6/[R_0^6 + r^6]$ , where  $E_T$  is the efficiency of quenching, and  $R_0$  is the Förster radius of the given fluorophore and quencher pair). As the Bodipy- $C_{12}$  binds directly to the BSA-Q molecules, higher efficiency of fluorescent masking can be achieved with even low concentration of quencher. Secondly, as a relative large (molecular weight of around 66  $kD$ ) and negatively charged protein, BSA has 49 Lysine residues [254], which allows multiple quencher molecules to be installed and further increases the quenching efficiency. Various types of quencher can also be attached to the same BSA molecule in order to achieve a wider quenching window. In our case, both BHQ-3 and BHQ-10 were labeled to BSA-Q to mask the fluorescence of both Bodipy-FL- $C_{12}$  and Bodipy- 558/586- $C_{12}$  (green and red emissions). For the synthesis of BSA-quencher, a stoichiometric ratio of 30 (BHQ to BSA) was used, and the labeling ratio was calculated to be 3.56 for BSA-Q, 3.25 for BSA-Q3, and 5.36 for BSA-Q10 (Figure 3.2B). The emission study of 2  $\mu M$  Bodipy-FL- $C_{12}$  and 2  $\mu M$  Bodipy- 558/586- $C_{12}$  titration with BSA-Q indicate a ratio of 1:2(BSA-Q to Bodipy fatty acid) is sufficient to quench most of the fluorescence (Figure 3.3). The same ratio was used for the cell studies. Thirdly, BSA is essential for nearly all the cell media anyway. By only replacing BSA with BSA-Q without additive of any extra chemicals that potentially causes toxicity to cells, the background fluorescent can be shielded. And fourthly, BSA-Q has lower cost, better stability, and longer shelf life compared to other commercial assay reagents. With all the advantages, the BSA-Q based assay was then applied to adipocyte explants for real time fatty acid uptake measurement.

### 3.3.2 Fluorescence imaging for real time fatty acid uptake measurement

Previously, we designed an actively valve controlled microfluidic input/output multiplexer,  $\mu MUX$ , to mimic the circulatory system for dynamic controlling hormones and nutrients to/from endocrine tissues [190]. The system was applied to adipose tissue explants fatty acid uptake with a mimic of postprandial insulin and glucose at 5 different magnitudes.

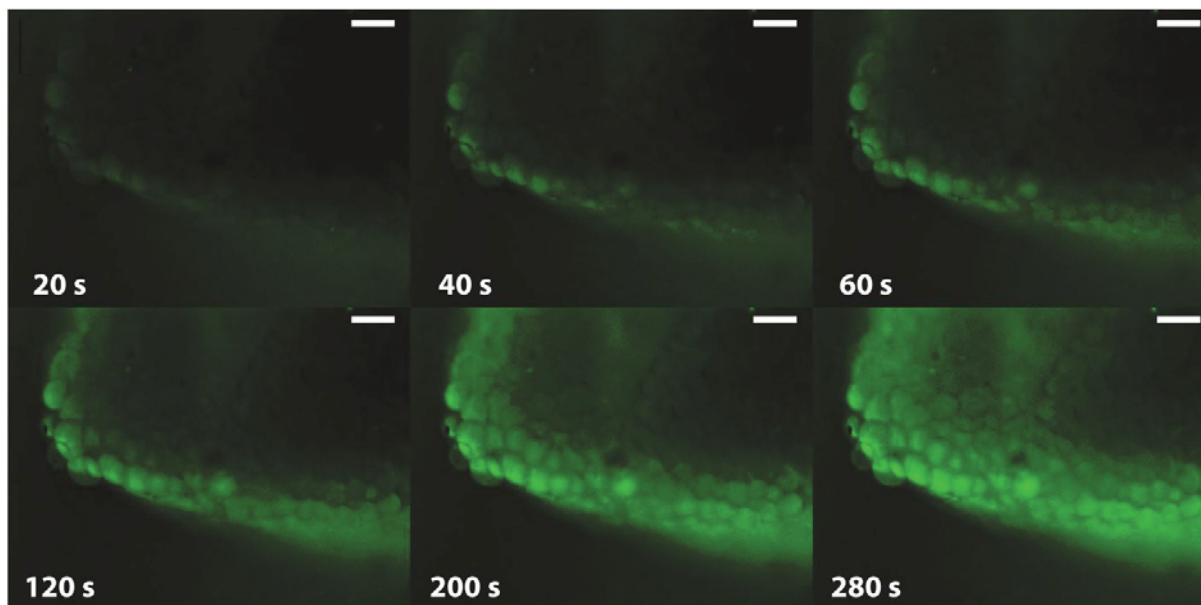


Figure 3.4: Example time lapse fluorescent imaging of adipose explants. Scale bar represent 100  $\mu m$ .

The adipose tissues was trapped within the center reservoir with a platinum mesh. The automated  $\mu$ MUX system allowed solution changes while the explants remain undisturbed for imaging. Here, we further employed the  $\mu$ MUX device for dynamic fatty acid uptake analysis in adipose tissues.

Adipose explants were imaged on the  $\mu$ MUX devices to monitor fatty acid uptake in various insulin and glucose conditions. Figure 3.4 portrays adipose explants stained with the BSA-Q assay. The solution containing BSA-Q and Bodipy-FL- $C_{12}$  did not show background fluorescence, while the cells became brighter as they absorbed Bodipy-FL- $C_{12}$ . The adipocytes on the edge of the explants were continuously exposed to fresh media and were observed to uptake fatty acid more rapidly, while the cells within the center of the explants were not directly exposed to the media. Initially, a fluorescent “ring” along the explant edge was observed. Over time, fatty acid permeated central cells, and fluorescence was observed in the bulk of explants. A higher fatty acid release rate was also observed in the edge of adipocytes while treated with unlabeled fatty acid or other colored fatty acid. As shown in Figure 3.5 B (bottom heat map), the fluorescence intensity in the center of the explants had a delayed

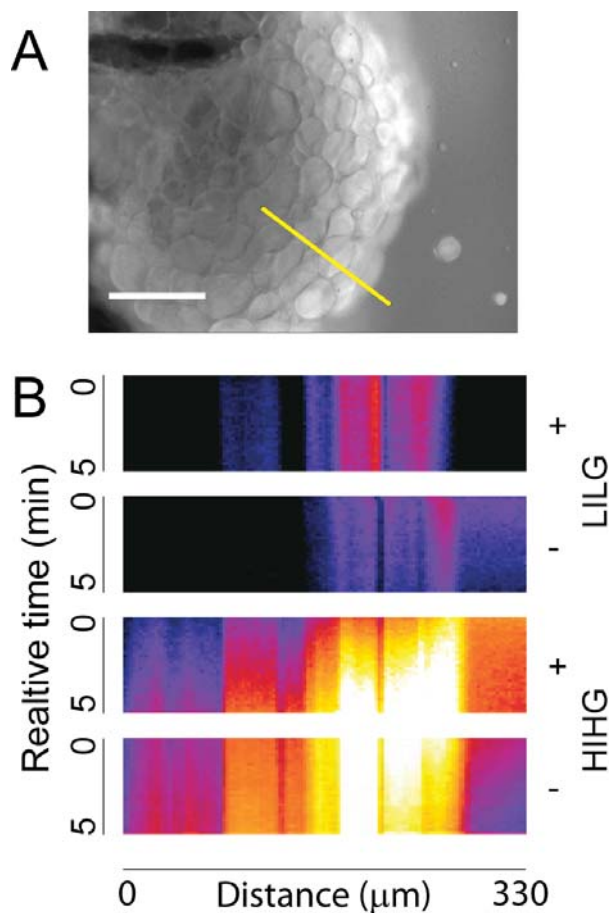


Figure 3.5: Fatty acid transport through cells

(A) Fluorescent image of adipose explant in BSA-Q assay. Scale bar (white) is  $200 \mu m$ .  
 (B) Heat map represents the time profile of yellow line in (A) as the explants were treated with LILG or HIHG (with + or without - Bodipy-FL- $C_{12}$ ) for 5 *min*.

increase compared to that on the edge when treating with HIHG+ treatment for 5 *min* (high insulin high glucose with Bodipy-FL- $C_{12}$ ), and the fluorescence intensity along the explant edge decreased while that of the center remain unchanged with 5 *min* HIHG- treatment (high insulin high glucose without Bodipy-FL- $C_{12}$ ). This wave effect is most likely due to fatty acid exchange between adipocytes.

To demonstrate the insulin and glucose induced effects on adipose fatty acid uptake, explants were treated with a step function of glucose and insulin at physiologically relevant concentrations, while alternating the fatty acid between Bodipy-FL- $C_{12}$  and Bodipy- 558/586- $C_{12}$  every 5 minutes (the treatment is show in Figure 3.6 Top). Fluorescent images were take

through both FITC and TRITC filter cubes, and three region of interest (ROI) from the edge to the center of explants were chosen to analyze. As shown in Figure 3.6, the left and right plots were from FITC and TRITC channel of the 3 corresponding ROI. With alternating Bodipy-FL-C<sub>12</sub> and Bodipy-558/586-C<sub>12</sub> treatments, fluorescent intensities from FITC and TRITC channels alternately rose. The elevated insulin and glucose boosted fatty acid uptake. The Savitzky-Golay 1st derivative of the fluorescent intensity, which represents the intensity change rate, and the linear fit slopes of the first 10 data points of each treatments, which is proportional to the initial fatty acid uptake rate, clearly showed an increase after introduction of HIHG. Compared to Bodipy-FL-C<sub>12</sub>, insulin-induced Bodipy-558/586-C<sub>12</sub> uptake increase had a delayed effects, which is likely due to the structural differences of the fatty acid analogues.

### 3.3.3 CD36 Inhibitor and its effect on fatty acid uptake

Fatty acid transport across the cell membrane is promoted by CD36/SR-B2 and other membrane proteins. To study the effect of CD36/SR-B2 on fatty acid uptake, Sulfo-N-succinimidyl (Sulfo-NHS) palmitate was synthesized as a CD36/SR-B2 inhibitor. Sulfo-NHS ester of long chain fatty acid was widely used as CD36/SR-B2 inhibitor[255, 256, 257, 258], which reacts with the lysine-164 residue of CD36/SR-B2 [204] and irreversibly blocks the fatty acid binding site of CD36/SR-B2. Since CD36/SR-B2 is regulated by insulin-induced translocation in the short term, and by fatty acid induced PPAR $\gamma$  pathway in long term, the exposure of adipose tissue to the inhibitor within buffer containing various concentrations of insulin would have different effects.

In the inhibitor effect study, the explants were first treated with freshly dissolved inhibitor in HIHG or LILG DMEM buffer for 30 *min*, then imaged on the  $\mu$ MUX devices to monitor Bodipy labeled fatty acid uptake under various insulin and glucose conditions. The adipose

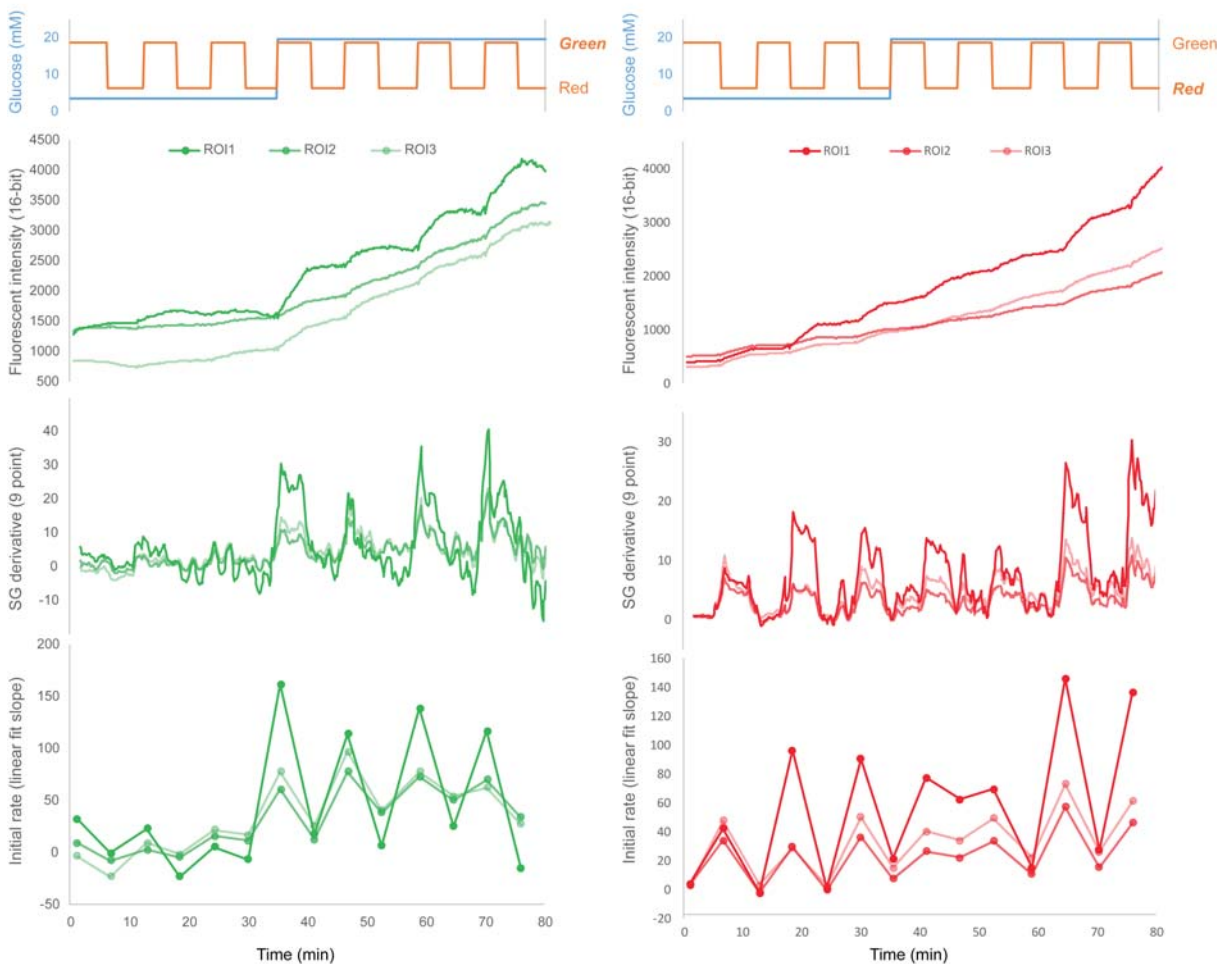


Figure 3.6: Dynamic fatty acid uptake by adipose tissue

From top to bottom: The treatments of the adipose explants while imaging; The fluorescent intensity traces of 3 representative region of interest or ROI (From ROI1 to ROI3, the region is further away from the edge of the explants.); Savitzky-Golay 1st derivative of the fluorescent intensity traces of 3 ROIs; and linear fit slopes of the first 10 data points of each treatments. (left is FITC channel, and right is TRITC channel)

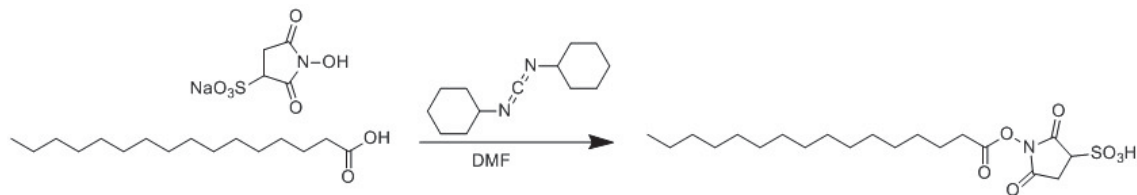


Figure 3.7: CD36 inhibitor synthesis

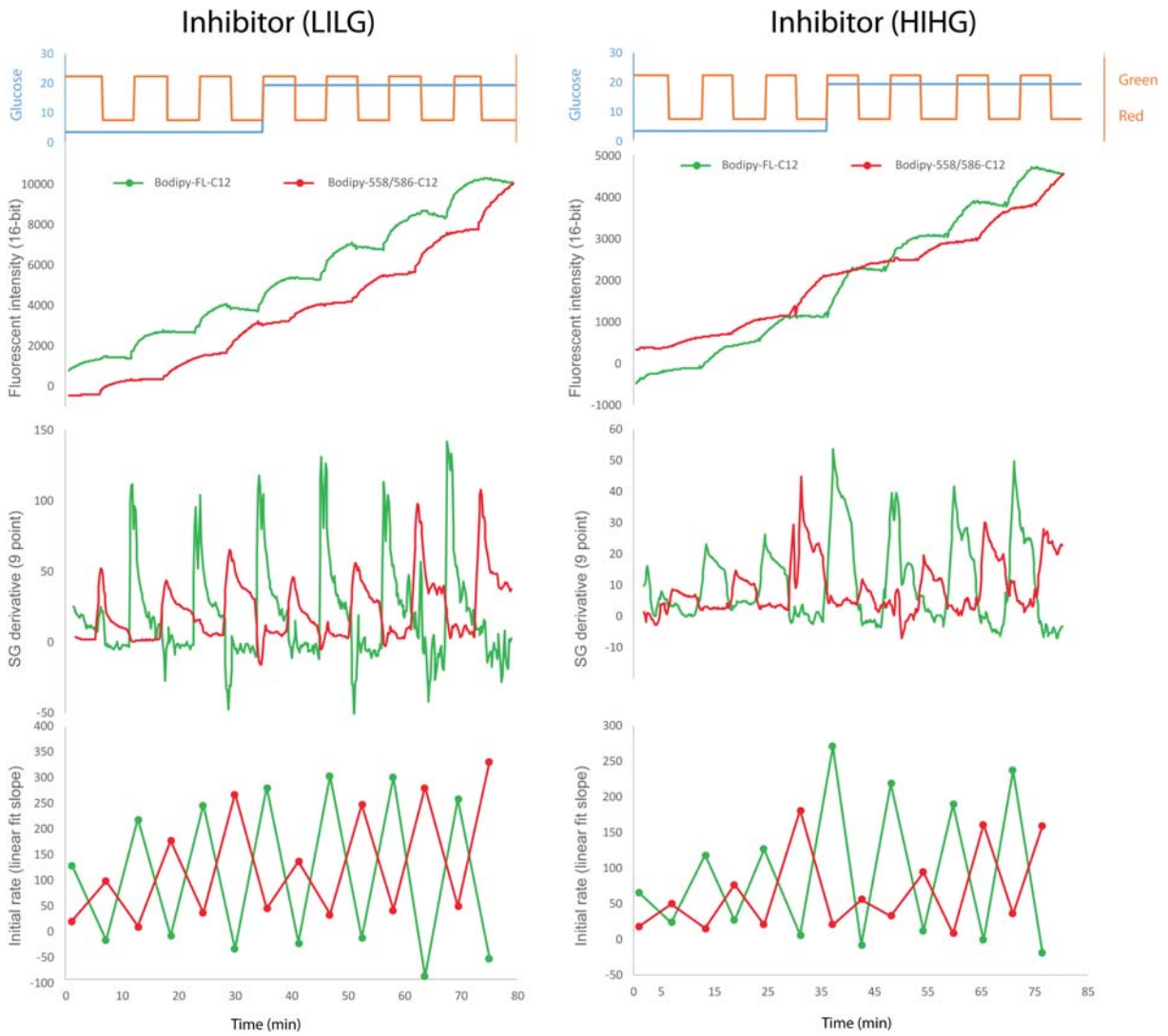


Figure 3.8: Dynamic fatty acid uptake by adipose tissue after inhibitor treatments

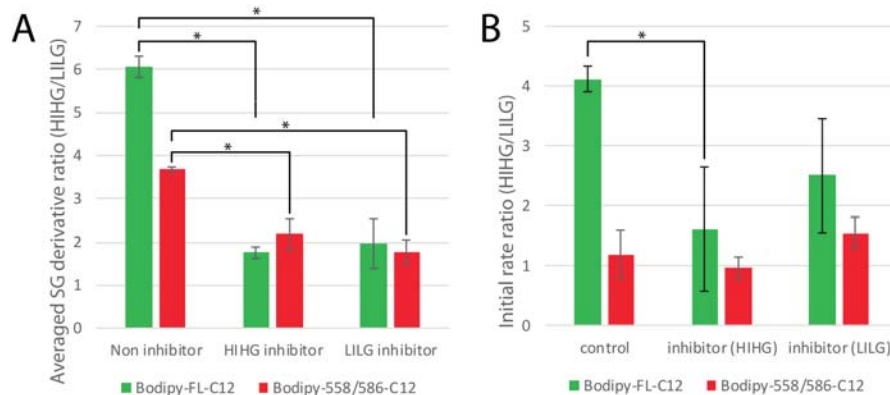


Figure 3.9: Inhibitor effects on fatty acid uptake, \* represents  $p < 0.05$  (t-Test: two sample assuming unequal variances)

treated inhibitor within both LILG and HIHG buffers did not show significant insulin promotion effect on fatty acid uptake (Figure 3.8).

The Savitzky-Golay 1st derivative or the linear fit slope of the fluorescent intensity trace were not directly comparable for quantitative analysis between individual explants. Ratio-metric methods were used to study the inhibitor effects. As shown in Figure 3.9, the insulin induced fatty acid uptake rate changes of adipose explants treated with inhibitor and the control group were compared. The ratios of averaged Savitzky-Golay 1st derivative [259, 260] of the fluorescent intensity traces with HIHG to that with LILG showed a significant different between the control group and the inhibitor groups.

### 3.4 Conclusions

A real time, two-color fluorescence assay for *in vitro* monitoring of fatty acid uptake by cells or tissues has been developed based on the interaction between a fluorescence quencher linked serum albumin (BSA-Q) and free fatty acid within aqueous solution. Compared to the other commercially available assay (QBT), our BSA-Q assay has the advantages of higher quenching efficiency, multicolor quenching, low toxicity, low cost, and better stability. The BSA-Q assay was applied to primary murine adipose tissues on our previously developed automated controlled microfluidic multiplexer ( $\mu$ MUX). An average 4-fold increase of fatty

acid uptake initial rates was observed after treatment with 2 *nM* insulin. An irreversible CD36/SR-B2 inhibitor, Sulfo-NHS palmitate, was synthesized and applied to adipose tissue within buffer containing high or low concentrations of insulin. The results clearly showed a significant inhibition on insulin-promoted fatty acid uptake.

To better illustrate the fatty acid uptake dynamics, more research should be conducted. First, immuno staining, western blot, or other techniques can be used to quantify the protein involved in fatty acid uptake. Secondly, fluorescently labeled CD36/SR-B2 inhibitor such as Sulfo-NHS-Bodipy-C12 can be synthesized for visualization of the inhibition of CD36/SR-B2. Third, *in vivo* most of the fatty acid exist as triglyceride in serum. In our BSA-Q assay, Bodipy labeled fatty acid was used, and the effect of lipoprotein lipase on fatty acid uptake regulation is ignored, which is known to be the rate limiting step of fatty acid uptake[261]. Instead of using fluorescently labeled fatty acids, fluorogenic triglyceride analog (such as STA-610 from Cell BioLabs Inc, San Diego, CA) could be used for better mimicking the *in vivo* conditions, and include the lipoprotein lipase in our assay.

Interestingly, fatty acid transport between adipocytes was observed as a wave from the edge to the center of adipose explants. Due to the nature of wide field microscope imaging, the out-of-focus light was also included in our images. Confocal laser scanning microscopy can eliminate out-of-focus light by using a pinhole at the confocal plane of the lens. It can also be used to construct a 3-dimensional structure. The fatty acid uptake studies with confocal microscope is underway, and the expected results would allow us to generate a 3D mathematical model of the fatty acid transport among cells within each adipose explant.

The BSA-Q is also applicable to any *in vitro* cell models or tissue models such as hepatocytes, myocytes, neurons, stem cells, and many other cell lines. Combined with protein quantification technologies such as immuno staining or Western blot, the BSA-Q assay would allow better understanding of the physiology and pathology related to fatty acid uptake and metabolism.

## Chapter 4

### Development of automated microfluidic droplet control system for high resolution sampling and optical analysis

#### 4.1 Introduction

Microfluidics has enabled many high-resolution temporal studies of dynamic cellular molecular events at the single cell or single tissue level [100], which often rely on fluorescent labeling and microscopic real-time imaging [262, 263, 140, 264, 64, 265, 139, 266, 267, 268, 269]. However, the dynamics of secreted proteins, including cytokines, coagulation factors, growth factors, hormones, enzymes, and other signaling molecules, that play crucial roles in many physiological and pathological processes, were less studied. The possible hurdles includes the following. Firstly, direct fluorescent labeling of a protein target using, for example, GFP (green fluorescent protein) fusion [270] or genetically encoded unnatural amino acids incorporation [271] requires sophisticated genetic modification. Secondly, commonly used heterogeneous immunoassays for protein quantification require multiple steps of fluid handling such as washing and separations, which are not easily transferable to microfluidic devices. Thirdly, off-chip measurement of collected microfluidic samples offers accurate quantification, however, this approach greatly sacrifices temporal resolution.

Because of its important role in the pathogenesis of type 1 and type 2 diabetes mellitus, obesity and metabolism syndrome, insulin from islet of Langerhans became one of the most studied secreted proteins on microfluidic systems [272]. Over the years, several groups developed microfluidic devices for islet secretion studies. These devices generally include several main components: a single or multiple islet trapping mechanism, a perfusion system for fresh nutrients and various treatments, and an analytical tool to monitor the hormone concentration secreted from the islets. Compared with commonly used off-chip immunoassays

for insulin quantification[66, 273, 274, 190, 222, 221], on-chip detection methods requires less volume of sample, thus allows higher spatial- and temporal-resolution and continuous monitoring. The Kennedy group introduced an on-chip capillary electrophoresis immunoassay for islet secretion sampling [220, 275, 218, 276, 277]. This approach ultimately allowed monitoring 15 islets in parallel at 10 s sampling rate [220].

A disadvantage is that this electrophoresis immunoassay requires complex setup including precise external pumps for fluid control, a high-voltage power supply, electrodes and surface chemistry for electro-osmotic fluid control. Nonetheless, both the Kennedy group [220, 275, 218, 276, 277] and Roper group [278, 223, 279] have succeeded in on-chip capillary electrophoresis immunoassay for islet secretion. Additionally, intermittent sampling nature of those systems may cause undersampling. Ultimately, the temporal resolution in this electrophoresis immunoassay is limited by longitudinal broadening that occurs as the sample flows and decreases the temporal resolution. Droplet based microfluidics provides an appealing way to preserve the temporal chemical information by digitizing the analog secretion signal. After measuring the analytes within droplets, the secretory time record can be reconstructed. Based on this concept, Professor Easley, during his postdoctoral work in the Piston group, was able to indirectly study insulin secretion dynamics by measuring  $\text{Zn}^{2+}$  (cosecreted with insulin) from single islets at 1.09 s temporal resolution [175]. Pushing such systems to their sampling limit should theoretically permit sub-second resolution.

Homogeneous immunoassays such as the molecular pincer assay [280] and proximity Förster resonance energy transfer (pFRET) assay [152] allow a simple mix-and-read procedure without the necessity of sample separation or washing, which is ideal for on-chip droplet protein measurement. Compared to heterogeneous assays like capillary electrophoresis immunoassay, the application of homogeneous assay within droplets would largely simplify the microfluidic chip design. To ensure accurate measurement, the sample/probe volume ratio, and the size of each droplet must remain consistent. Peristaltic pumping with pneumatic valves dispense

a predictable volume at each pumping cycle [99], thus ensuring an accurately volume metered in a digitally controllable way.

However, fluorescent based detection methods often suffer low frequency noise (1/f noise) introduced by optical system fluctuations or detector noise. Especially at low signal levels, the noise is often indistinguishable from signals. Previously, our group developed a lock-in droplet detection system [281], which modulated a reference signal at the same frequency as the sample by alternatively making sample and reference droplets. Highly sensitive absorbance [281] and fluorescence [176] detection were achieved with this lock-in droplet system, even at very short optical path lengths (tens of micrometers). However, for homogeneous fluorescence immunoassays to be quantified with this lock-in system, a limitation of our previous design is the detection was done immediately following droplet formation, which does not allow for the incubation requirement for the immunoassays. By adding a long channel for droplet storage in the new design reported herein, the information of the protein secretion dynamics can be digitally saved within droplets and measured after the proper incubation time.

In this work, we developed a microfluidic system (PumpDrop, Figure 4.1) integrating precise peristaltic pumping, a simple homogeneous immunoassay, sensitive lock-in droplet detection, and a long incubation channel for information storage. The device permits direct secretion sampling from single islets, mixing with assay probes, droplet formation, incubation, and detection with phase-locked referencing.

## 4.2 Materials and Methods

### Materials and Reagents

All buffers were prepared with deionized, ultrafiltered water (BDH1168-5G, VWR, Radnor, PA). The following reagents were used as received: Polydimethylsiloxane (PDMS) precursors, Sylgard 184 elastomer base and curing agent (Dow Corning, Midland, MD); SU-8

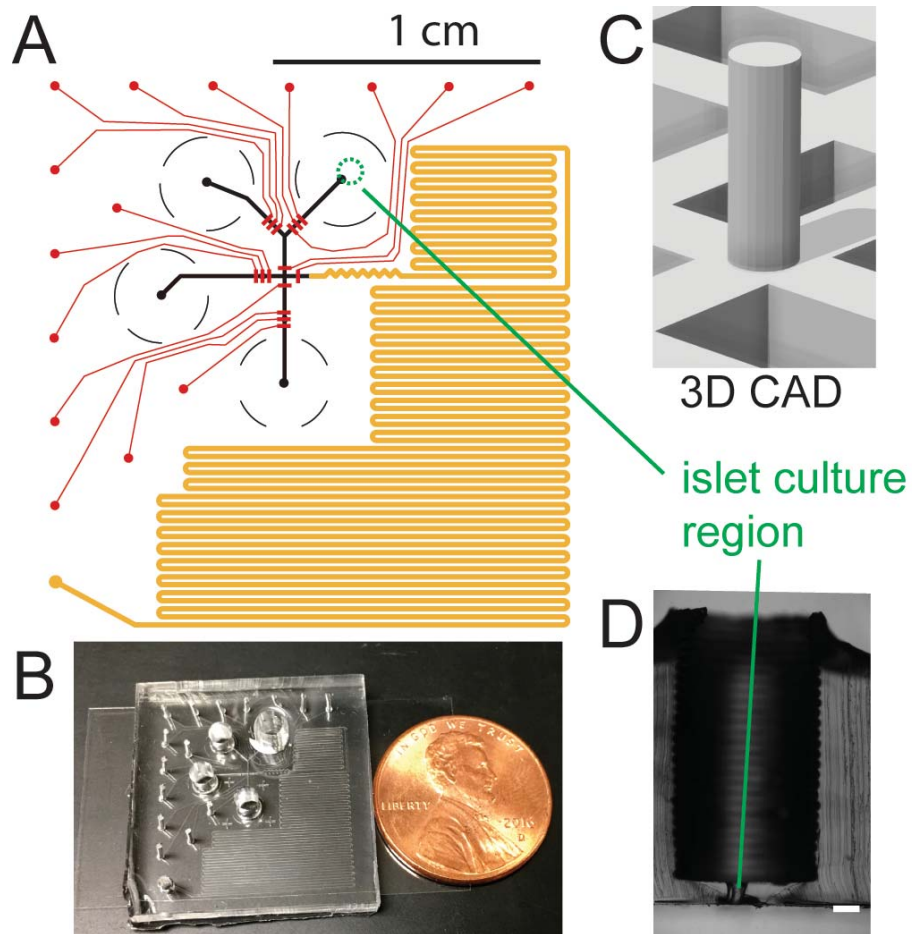


Figure 4.1: PumpDrop Chip Design

(A) Schematic of PumpDrop channel layouts, with rounded fluidic channels shown in black, rectangular fluidic channels in orange, and pneumatic control channels in red. (B) Photo of assembled device. (C) CAD rendering of the 3D-printed template and (D) example device cross-section with 3D-template islet culture reservoir.

2015 photoresist (Microchem, Newton, MA); AZ-40-XT photoresist (MicroChem, Westborough, MA); insulin, D-glucose, 4-(2-hydroxyethyl)-1-piperazineethanesulfonic acid (HEPES), (3-Aminopropyl)trimethoxysilane, trimethylsilyl chloride ( $\text{Me}_3\text{SiCl}$ ), fluorescein,  $\text{KH}_2\text{PO}_4$ ,  $\text{NaH}_2\text{PO}_4$ , and  $\text{NaOH}$  were all obtained from Sigma-Aldrich (St. Louis, Missouri); Bovine serum albumin (BSA), fetal bovine serum (FBS),  $\text{KCl}$ ,  $\text{NaCl}$ ,  $\text{MgCl}_2$ ,  $\text{CaCl}_2 \cdot 2\text{H}_2\text{O}$ ,  $\text{EtOH}$ ,  $\text{MeOH}$ , and  $\text{DMF}$  were purchased from VWR (West Chester, PA). Minimal Essential Media (MEM) non-essential amino acids solution 100x, collagenase P, collagenase type I, Dulbecco's Modified Eagle Medium (DMEM), and  $\text{MgSO}_4 \cdot 7\text{H}_2\text{O}$  were purchased from ThermoFisher Scientific (Grand Island, New York).

### Microfluidic Master Wafer Fabrication

Microfluidic devices were made by standard multilayer soft lithography methods [99, 97], with 3D-printed templating [190, 252, 251] of the tissue culture interfaces. Two master wafers for fluidic channel and pneumatic/control channels were first fabricated by photolithography. The channel layout was designed in Adobe Illustrator (San Jose, CA) and photolithographic masks were printed at 50,800 *dpi* resolution by Fineline Imaging (Colorado Spring, CO). For the pneumatic control channels (thin lower layer), 20- $\mu\text{m}$  thick negative photoresist (SU-8 2015) was spin-coated onto a  $\text{H}_2\text{SO}_4$  (1 *M*) and water washed silicon wafer (Polishing Corporation of America, Santa Clare, CA). The wafers were then baked at 105 °C for 5 *min*, and UV exposure through the mask was done at  $\sim 330 \text{ mJ/cm}^2$  on an in-house built UV LED exposure unit [229]. The wafer was hard baked for another 5 *min* at 105 °C then developed for 5 *min* in the SU-8 developer solution.

The fluidic channel layer wafers were made by two step photolithography. First, a 60- $\mu\text{m}$  thick microfluidic pattern was made on the silicon wafer by similar procedure for the control wafer with negative photoresist (SU-8 2050). 60- $\mu\text{m}$  thick SU-8 2050 photoresist was spin-coated on a silicon wafer ( $\text{H}_2\text{SO}_4$  and water washed), soft baked at 105 °C for 5 *min*, UV exposed through the mask at  $\sim 330 \text{ mJ/cm}^2$ , hard baked at 105 °C for 5 *min*, and developed

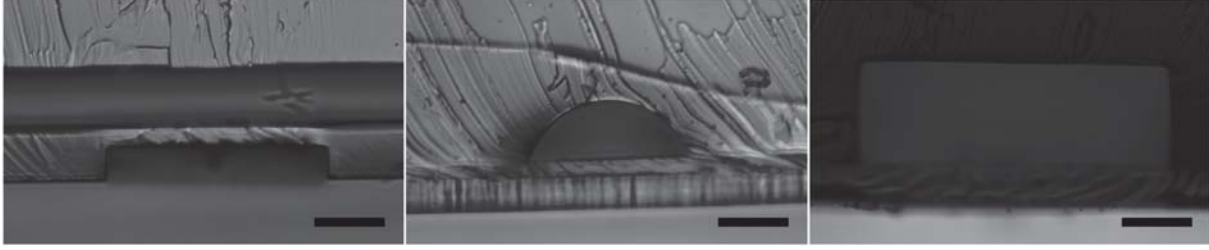


Figure 4.2: The cross section of microfluidic channels Control valve over flow channel (left), rounded flow channel (middle), and squared droplet storage channel (right). Scale bar =  $50 \mu\text{m}$

to form the SU-8 micro pattern. Second,  $40\text{-}\mu\text{m}$  thick positive photoresist (AZ 40 XT) was spun onto the silicon wafer along with the SU-8 pattern. The wafer was baking at  $105\text{ }^\circ\text{C}$  for  $7\text{ min}$ , and the photo mask was carefully aligned onto it under microscope (SE306R-PZ, AmScope). After UV exposure at  $\sim 330\text{ mJ}/\text{cm}^2$ , hard baked at  $105\text{ }^\circ\text{C}$  for  $5\text{ min}$ , and developed, the wafer was baked at  $115\text{ }^\circ\text{C}$  for  $6\text{ min}$  to anneal the AZ photoresist and round out the cross-section of the AZ fluidic channel template. The silicon wafers were exposed to trimethylsilyl chloride vapor for  $30\text{ min}$  before use to enhance PDMS removal. Channels were later characterized by slicing an assembled PDMS device and imaging the channel cross sections (Figure 4.2).

### Microfluidic Device Fabrication with 3D-printed Templating

All 3D-printed templates and devices were designed in SketchUp 3D modeling software, and printed on a MakerBot Replicator 2 ( $100\text{ }\mu\text{m}$  layer resolution in the  $z$ -direction) with polylactic acid filament (HatchBox PLA,  $1.75\text{ mm}$  diameter).  $36\text{ g}$  of PDMS precursor mixture (5:1 ratio, monomer:curing agent) were well mixed, degassed under vacuum, and poured onto the fluidic master wafer (AZ) wrapped within aluminum foil. The 3D-printed template was carefully aligned over the channel patterns and set directly onto the wafer and into the uncured PDMS.  $5\text{ g}$  of degassed PDMS polymer mixture (20:1 ratio, monomer:curing agent) was spin-coated onto the pneumatic control channel master wafer (SU-8) at  $2750\text{ rpm}$  for  $45\text{ s}$ . Both the assembly of fluid layer PDMS with 3D printed template and control layer

PDMS were partially cured at  $65\text{ }^{\circ}\text{C}$  for  $40\text{ min}$ . Following curing, the template was removed carefully, and the thick fluidic PDMS was peeled from the master, after which it was diced, and access holes and vias were punched.  $1.5\text{-mm}$  inner diameter (ID) punches was used for waste outlets, and  $2.5\text{ mm}$  ID punches were used for the solution reservoirs (Miltex biopsy punch 33-31A and 33-31B, Miltex, York, PA).  $0.5\text{-mm}$  ID punches were used for the islet trapping channel in between the 3D-templated reservoir and channels (EMS-Core Sampling Tool  $0.5\text{ mm}$ , 69039-05, Electron Microscopy Sciences, Hatfield, PA). Each PDMS replica was washed with methanol, dried with  $\text{N}_2$  gas, and cleaned with Scotch tape (3M, St. Paul, MN). The freshly made fluidic PDMS replicas, with access holes punched, were carefully aligned onto the partially cured control channel PDMS layer, and the two layers were permanently bonded by placing in the oven at  $65\text{ }^{\circ}\text{C}$  for at least 4 hours. The PDMS devices were then peeled from the wafer and diced, then holes for control lines connections were punched with a  $0.75\text{ mm}$  ID punch (69039-07, Electron Microscopy Sciences, Hatfield, PA). Finally, the assembled PDMS devices were plasma oxidized and bonded to a glass substrate. (see Figure 4.3) The microfluidic devices were thermally aged at  $65\text{ }^{\circ}\text{C}$  for 1 week before use to limit uncured PDMS monomer leakage.

### **Automated Flow Control Interface**

Pneumatic valves were actuated with solenoid switches (LHDA0533115H, The Lee Co., Westbrook, CT) controlled by a multifunction data acquisition system (PCI-6259, National Instruments) and using an in-house nitrogen source adjusted to  $30\text{ psi}$  with a pressure regulator. The 15 control channels were connected to the corresponding solenoid switches with hollow iron tubing from  $22\text{ gauge}$  blunt syringe needles (JG22-0.5HP-90, JensenGlobal, Santa Barbara, CA) through Tygon tubing ( $0.02\text{ inch}$  ID,  $0.06\text{ inch}$  OD, Cole-Parmer, Vernon Hills, IL). Dead-end control channels were filled with water to prevent air leakage through PDMS membranes. As a solenoid switch was activated, nitrogen gas pressurized a lower layer control channel and closed the fluidic channel in the upper layer (push-up valves). Valve actuation

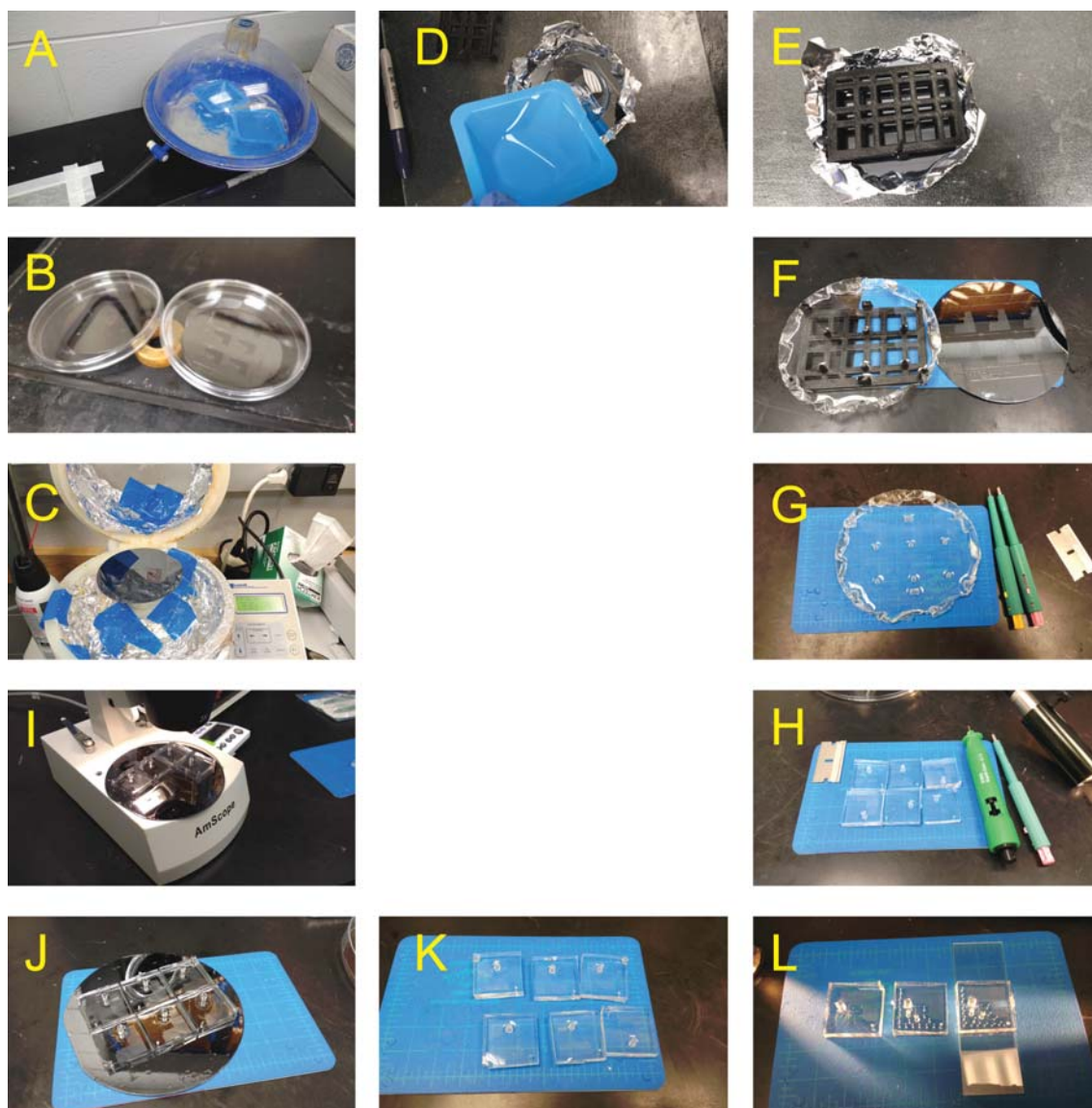


Figure 4.3: Fabrication procedure of PumpDrop devices

(A) 36 g of PDMS in 5:1 ratio and 10.5 g of PDMS in a 20:1 ratio were mixed and degassed under vacuum. (B) Both of the control wafer and fluidic wafer was treated with trimethylsilyl chloride vapor for 30 min. (C) PDMS (20:1) was spin-coated over the control wafer. (D) PDMS (5:1) was poured onto the fluidic channel master in an aluminum foil boat. (E) 3D-printed insert was carefully aligned around the channel and set directly onto the wafer into the layer of uncured PDMS. The entire assembly was baked in the oven at 60 °C undisturbed for 40 min. (F, G, H) The cured PDMS with template was peeled from the wafer, after the 3D-printed template was removed, Devices were diced, and holes were punched to prepare for bonding with the control channel PDMS layer. (I) After careful alignment (in step I) under microscope, the fluidic layer PDMS and partially cured control layer were permanently bonded together (J) by placing in the oven at 65 °C for at least 2 hours. (K) Completed PDMS devices were diced, peeled from the wafer, and holes were punched for control channel pressure lines. (L) PDMS devices were finally plasma oxidized and bonded onto glass substrate (left: before hole-punch, middle: after hole-punch, and right: fully assembled device).

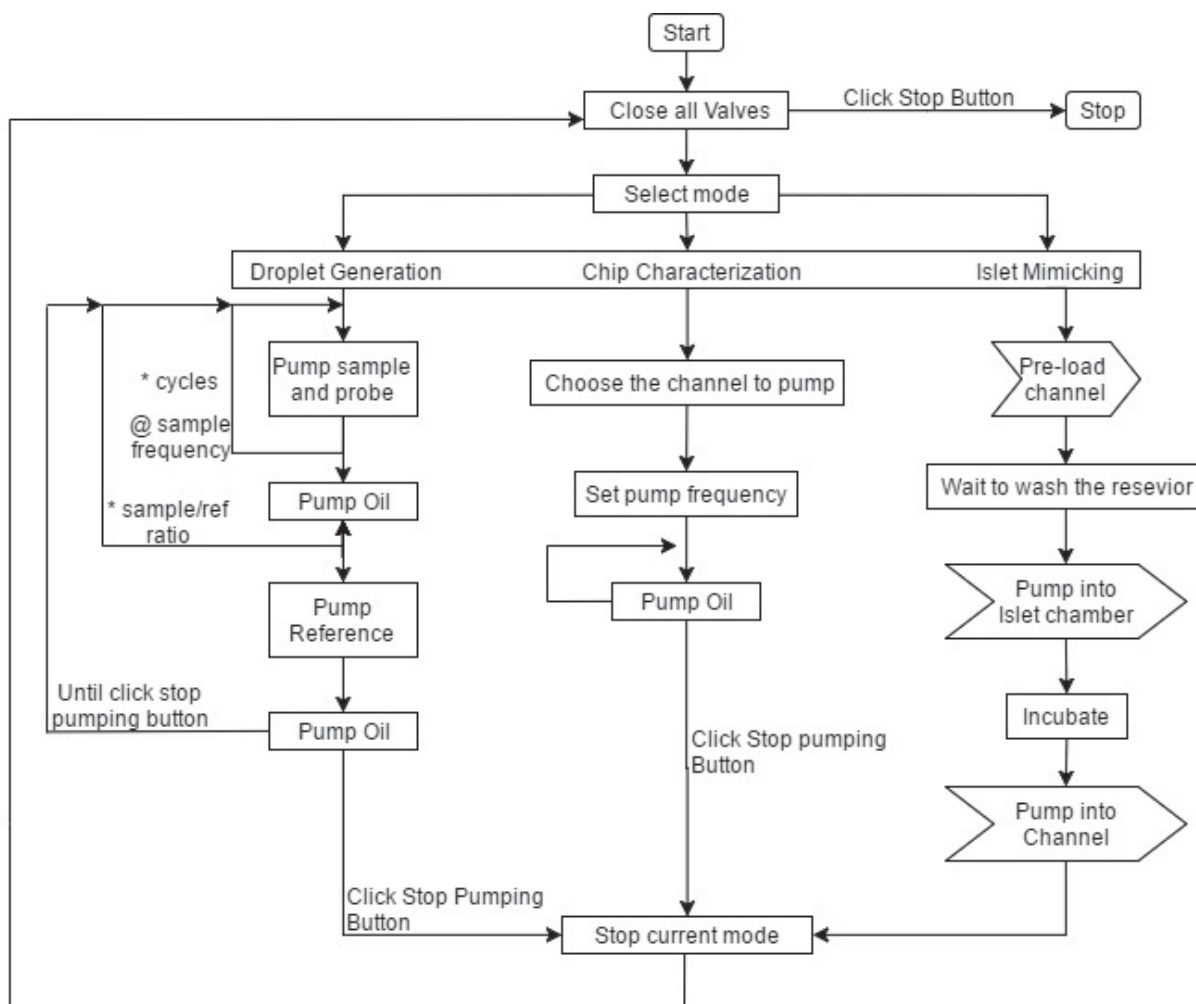


Figure 4.4: Programmatic flow chart of LabVIEW application for PumpDrop chip automation

timing was regulated through an in-house written LabVIEW application on a PC (program details see Figure 4.4).

### Chip Characterization

The sample and probe ratio within one droplet was initially analyzed by measuring the fluorescence intensity of the droplets made from fluorescein solution and buffer (Figure 4.12). The PumpDrop chip with all control lines connected was taped on the microscope stage. 100 *nM* fluorescein in PBS buffer (pH 7.4, 0.1% BSA) were loaded in both reference and probe reservoir, PBS buffer with 0.1% BSA was loaded in cell culturing reservoir, fluorocarbon oil

(Novec 7500, 3M, St. Paul, MN) with 1% surfactant (Pico-Surf 1, Dolomite, Royston, UK) was loaded in the oil reservoir. Vacuum was applied at the outlet using a syringe to remove air trapped in the microchannel. Valves were opened sequentially to let fluids from oil, cell culturing, probe, reference, and oil to flow through the channel. The vacuum syringe was detached and the end of Tygon tubing connecting to the outlet was placed in a waste bottle for fluid waste collection. Droplets were then formed by running the droplet-formation-mode of the LabVIEW application. The parameters for droplet formation were adjusted in the LabVIEW application front panel (for example, pumping frequency and cycles, sample/reference ratio, and etc.) to acquire droplets with consistent sizes, ratio, and space-in-between. Fluorescence images of droplets were measured (Nikon *Ti-E*), and images were analysed using ImageJ and Microsoft Excel.

The peristaltic pumping-induced chaotic mixing of sample and probe solutions was studied by fluorescence imaging of fluorescein solution during mixing with buffer within the microchannel. 100 *nM* fluorescein in PBS buffer (pH 7.4, 0.1% BSA) and PBS buffer with 0.1% BSA were loaded in probe reservoir and cell culturing reservoir, respectively. Air trapped in microchannel was removed by applying vacuum at the outlet and sequentially opening valves to let fluids from cell culturing, and probe reservoirs to flow through the channel. The LabVIEW application was set to chip characterization mode and fluids from each individual reservoirs were pumped to the droplet storage channel continuously. Fluorescent images were taken at various location of the channel (Nikon *Ti-E*). Images were analysed using ImageJ and Microsoft Excel.

The pumping flow rate and dispensing volume of each pumping cycle were analyzed by measuring the distance traveled by the leading meniscus of the fluid. A microfluidic device were specially made with 0.75*mm* ID reference reservoir (instead of 2.5 *mm*). A 50 *cm*-long, 100  $\mu$ *m*-ID, transparent capillary (1068162095, Molex, Lisle, IL) was connected to the reference reservoir via a tygon tubing (EW-06419-00, Cole-Parmer, Vernon Hills, IL). Red food coloring diluted with PBS buffer (pH 7.4, 0.1% BSA), were loaded into cell culturing reservoir

and probe reservoir, and fluorocarbon oil with 1% surfactant was loaded in the oil reservoir. Air trapped in the channel was removed by applying vacuum at the outlet and sequentially opening valves to let fluids from oil, cell culturing, and probe reservoirs to flow through the channel. The capillary was filled with about 1 *cm* of red buffer. The LabVIEW application was set to chip characterization mode and fluids from each individual reservoirs were continuously pumped at 2 *Hz* into the reference channel. The distances traveled by the leading meniscus of the fluid after about 5 *min* were measured with a ruler. The flow rates and the volumes per pump cycle of each fluid were then calculated with the equation  $r = \frac{\pi(\frac{d}{2})^2 L}{t}$  and  $r = \frac{\pi(\frac{d}{2})^2 L}{c}$ , where  $d$  is the ID of the capillary (100  $\mu m$ ),  $L$  is the distances traveled by the leading meniscus,  $t$  is the pumping time, and  $c$  is the cycle number of pumping.

To confirm that our device was capable of high temporal resolution sampling, insulin diffusion was mimicked by pulsing FITC-labeled insulin into the islet culturing chamber and measuring the recovery with fluorescence imaging. 100 *nM* FITC-insulin in PBS buffer (pH 7.4, 0.1% BSA) and PBS buffer with 0.1% BSA were loaded in probe reservoir and cell culturing reservoir, respectively. Air trapped in microchannel was removed by applying vacuum at the outlet and sequentially opening valves to let fluids from cell culturing, and probe reservoirs to flow through the channel. The LabVIEW application was set to islet mimicking mode and the FITC-insulin solution was pumped 20 cycles to fill the “right side” of the Y channel. Extra FITC-insulin in the islet chamber was washed with PBS buffer 3 times by pipetting. After pumping the FITC-insulin solution into the islet chamber for another cycle, and waited for 1 to 20 *s*, the solution was pumped from islet reservoir to the incubation channel while the fluorescence imaging was taken (see Figure 4.15). Images were analysed using ImageJ and Microsoft Excel.

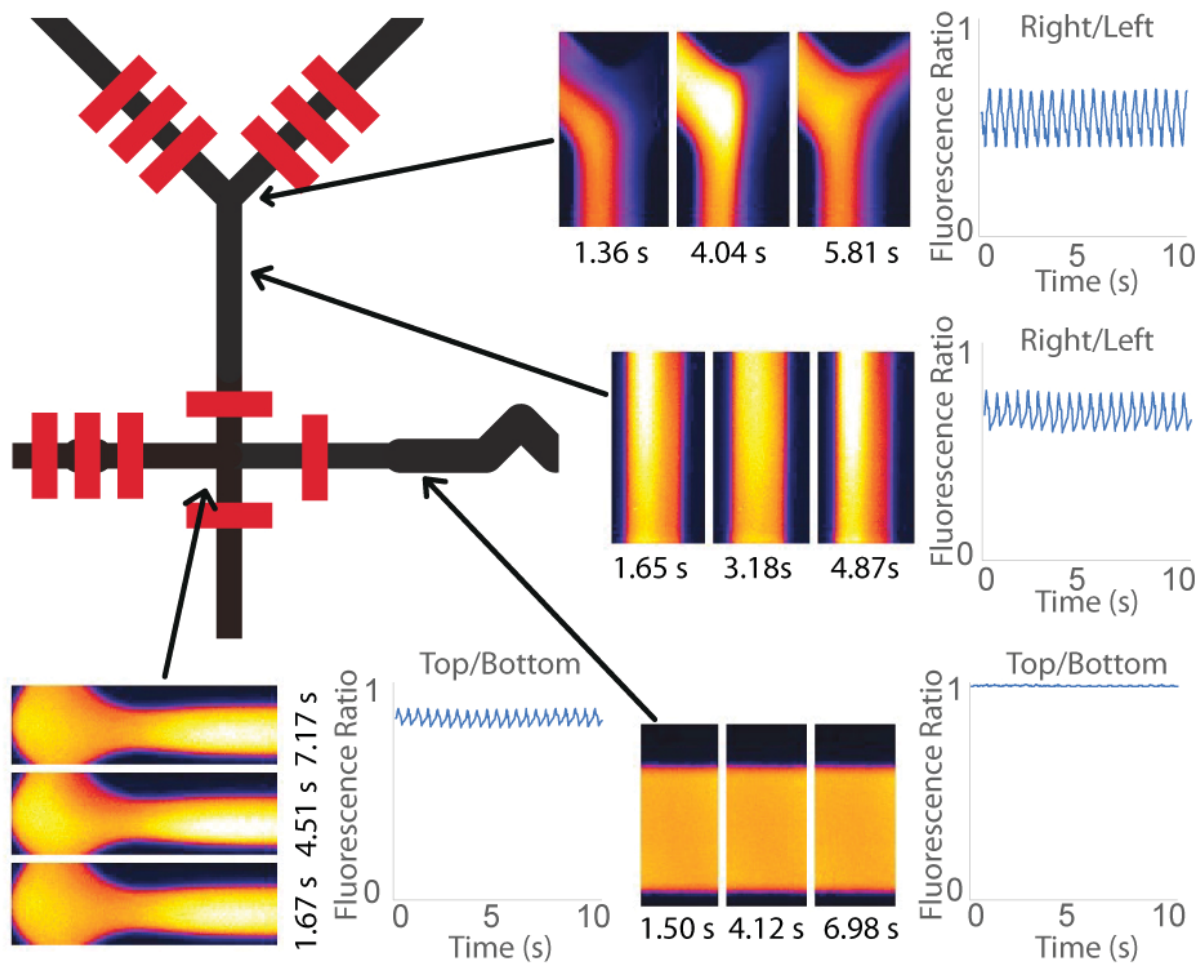


Figure 4.5: Peristaltic pumping induced chaotic mixing fluorescent imaging of fluorescein solution (left) mixed with buffer (right side). The fluorescent images indicate the relative concentration of fluorescent at various locations and times. The plots show the ratio of fluorescent intensity from right and left sides (or top and bottom sides) of the channel at the corresponding location.

## Extraction of Primary Islets

All experiments involving animals (mice, C57BL/6J) were performed in compliance with relevant laws and institutional guidelines and were approved under protocol numbers 2014-2096 or 2017-3101 by the institutional animal care and use committee (IACUC) of Auburn University. Pancreatic islets were extracted as described previously [230, 231] from 18-20 week old male C57BL/6J mice (Jackson Laboratories). Following isolation, islets were placed in RPMI media (10% FBS, 11 *mM* glucose) at 37 °C and 5% CO<sub>2</sub> to incubate overnight.

## Islet Secretion and Insulin Quantification

The insulin was quantified using a homogeneous fluorescence assay (Human Insulin FRET-PINCER Assay Kit; Mediomics, St. Louis, MO) within droplets. The PumpDrop chip was mounted within a microscope stagetop incubator (Tokai Hit, Japan) held at 37 °C. 50  $\mu L$  of pincer assay probes (Antibody A and B, 16-fold concentration of the kit suggested level) mixture was loaded in the probe reservoir, and of 50  $\mu L$  of probe mixture (8-fold concentration of the kit suggested level) was loaded into the reference reservoir to serve as the reference. 10  $\mu L$  of mineral oil was added on top of both of the probe and reference reservoir to prevent evaporation during the prolonged experiment at 37 °C.

BMHH buffer (3.5 *mM* glucose, 0.1% BSA) was added into the islet reservoir. After air removal and channel priming with oil, the islet (prestarved for 30 *min* in BMHH buffer with 3.5 *mM* glucose and 0.1% BSA) was carefully loaded into the islet chamber at the bottom of the reservoir with a 2  $\mu L$  pipette guided with the microscope. Next, sample droplets and reference droplets were alternatively formed with the droplet formation mode of the LabVIEW application. After 15 *min*, the buffer was changed to a high glucose buffer (19.5 *mM* glucose in BMHH with 0.1% BSA) by gentle pipetting to avoid disturbing the trapped islet. After another 20 *min*, the buffer was changed back to 3.5 *mM* glucose to treat the islet for another 10 *min*. The droplets were continuously formed as the buffer was changed. Once the glucose stimulation was completed, the incubator was switched off to cool the system back to room

temperature, and specially sequenced droplets were generated (for example 1 reference after 3 sample droplets) to serve as an addressing code for time stamping in subsequent analysis. The islets were removed, and various concentrations of insulin (0, 32, 64, 128, 256, 512, 902.5  $ng/mL$ ) were loaded to generate a standard curve. Droplets were allowed to generate for 10 *min* at each concentration before changing to next level of insulin. As the droplets formed, fluorescence imaging was performed (Nikon *Ti-E*, 40X objective lens through FITC filter cube) at the imaging region where all the formed droplets passed through sequentially. The stagetop incubator was turned to 37 °C, and the temperature was equilibrated. Then, the procedures were repeated to measure additional islets. One calibration curve was made after each islet sampling experiment. For all the experiments, sample droplets and reference droplets were intentionally controlled to be different sizes for easy identification during analysis. Images were analyzed with ImageJ and Excel for insulin quantification.

### 4.3 Results and Discussion

#### PumpDrop Chip Design

As shown in Figure 4.1A and Figure 4.6, the PumpDrop chip consisted of several components: (1) Y-shaped channel for reagent and sample mixing; (2) T-junction channel for droplet formation; (3) reference channel for reference droplet generation used for “lock-in” detection; (4) long incubation channel for droplet storage and imaging; (5) 3D-templated reservoir for single cell or single tissue culturing; and (6) control channels for fully automated chip operation (Figure 4.6 and 4.7-A).

One key feature of the PumpDrop device is that all the fluid is moved through channels by peristaltic pumps, which include three valves arranged on a single channel [99]. Peristaltic pumping occurs when actuated in the 6 step pattern (101, 100, 110, 010, 011, 001), or the 5 step pattern (100, 110, 011, 001, 101), where 0 and 1 represent open and closed valves, respectively. In each pumping cycle, the net volume dispensed down stream equals the volume occupied by the center valve membrane upon closing, thus the sample volume can be

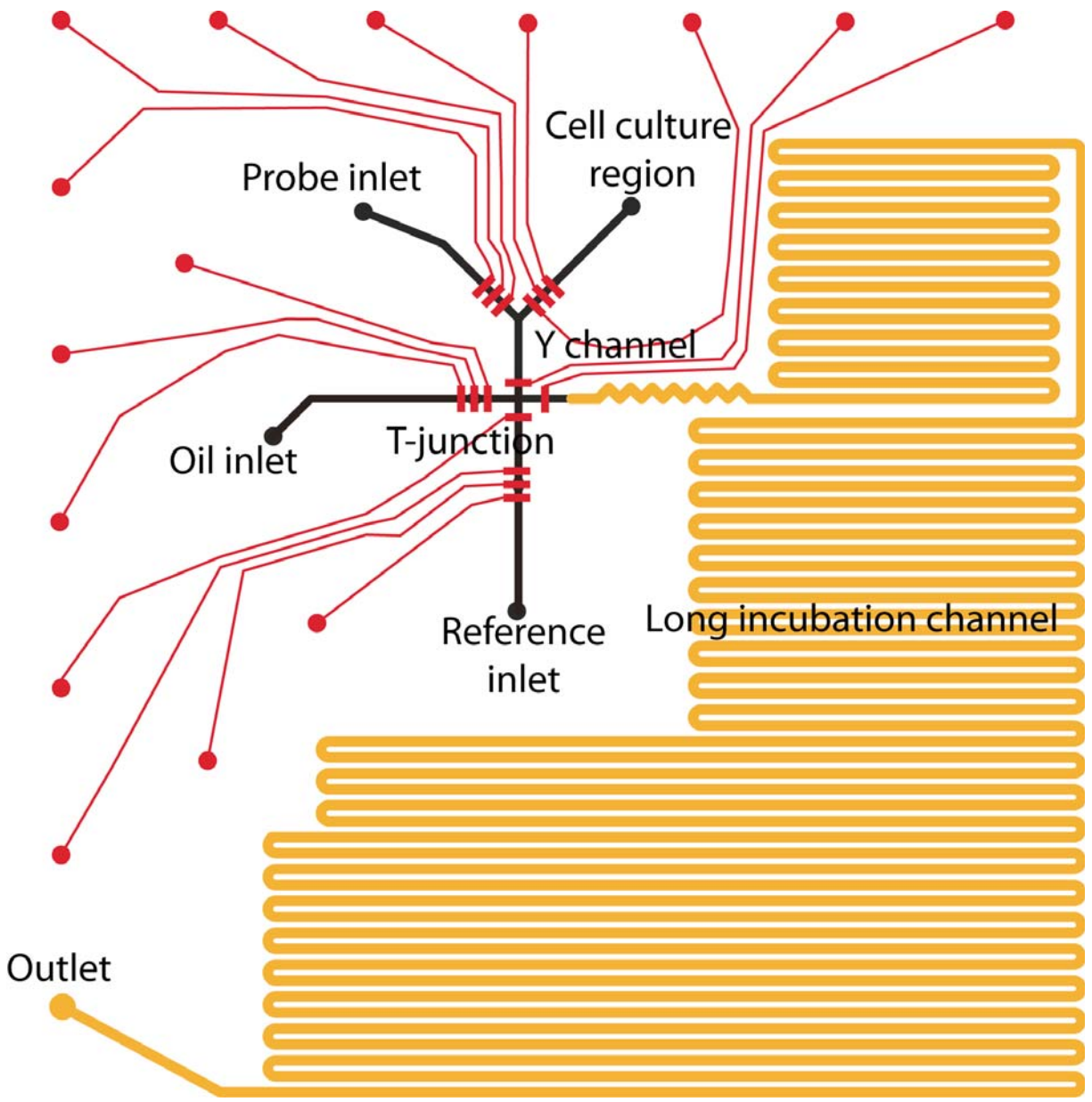


Figure 4.6: Enlarged PumpDrop channel layout with fluidic channel description

accurately controlled by pumping a specified number of cycles. To get a faster pumping rate, the 5 step pattern was used, and the center valves of the oil and reference pumps were enlarged. Compared to more passively controlled microfluidic systems - such as systems that are driven by syringe pump, pressure, or vacuum and that rely on laminar flow to control the ratio of mixed components and suffer from fluctuation over long periods of time - the peristaltic pumps provide much higher precision over the volume metered (Figure 4.7). The pulsed flow nature of pumping also facilitates mixing of the two components. As the two solutions reached the T-junction channel, they were already well mixed (Figure 4.5). The zig-zag channel at the beginning of incubation channel also helped mixing after droplets were formed, without compromising temporal resolution.

The long droplet incubation channel was patterned with SU-8 photoresist (shown in orange in Figure 4.1A) instead of AZ photoresist because of the following three reasons. First, unlike the rounded AZ patterned channel, the squared channel provided better fluorescence imaging quality. Second, the two step patterning allowed different depths for the droplet formation channel and droplet storage channel. Thus, deeper channels can hold more droplets and allowed more information buffering. Third, The squared profile helps maintain the spacing in between droplets (Figure 4.8). Within rounded channel (if patterned with AZ photoresist), as one droplet propagate through a squared channel, oil with low viscosity goes faster around it. As a result, the droplets packed tightly in the channel, which introduce difficulties in the data analysis (see section for data analysis) and even causes droplets merging.

To successfully generate droplets, the continuous phase (oil in our case) must effectively wet the channel surface. As a hydrophobic material, PDMS is ideal for water-in-oil droplet generation. Plasma oxidization treatment for bonding the PDMS to glass slides produces transient hydrophilic surfaces, but the surface slowly recovers to be hydrophobic because of the migration of the uncured polymers [282]. Thermal aging facilitates this process as well as cures most of the remaining polymers to prevent them leaching into cell culturing buffer. Our previous PumpDrop design (Figure 4.9) included a shorter connection between

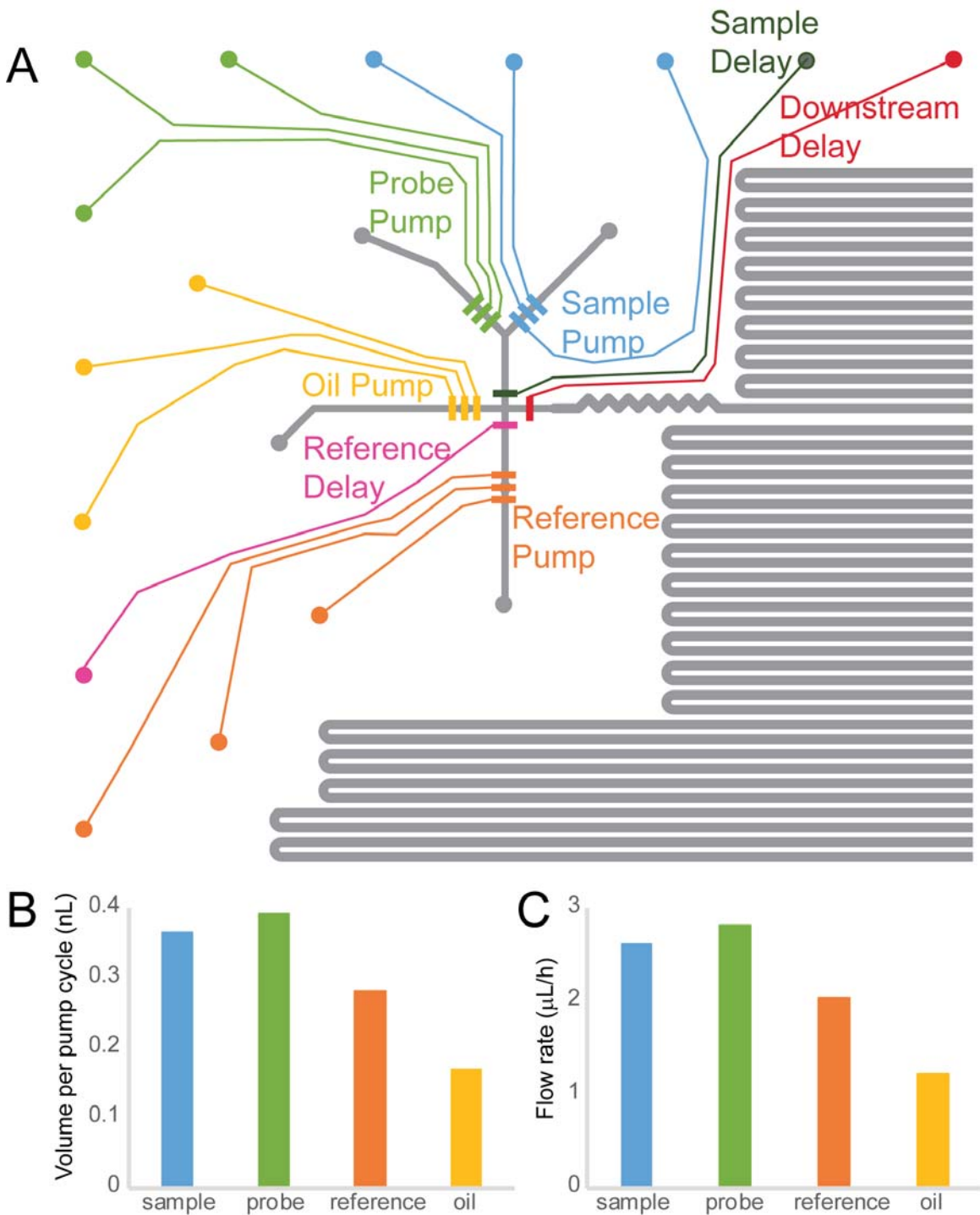


Figure 4.7: PumpDrop control channel description and pumping test (A) Enlarged PumpDrop channel layout with control channel description. (B) Measured dispensing volume per pump cycle at 2 Hz pumping frequency and 30 psi pressure. (C) Measured flow rate of each pump at 2 Hz pumping frequency and 30 psi pressure.



Figure 4.8: Droplets pack up within channels

Scale bar = 500  $\mu m$ .

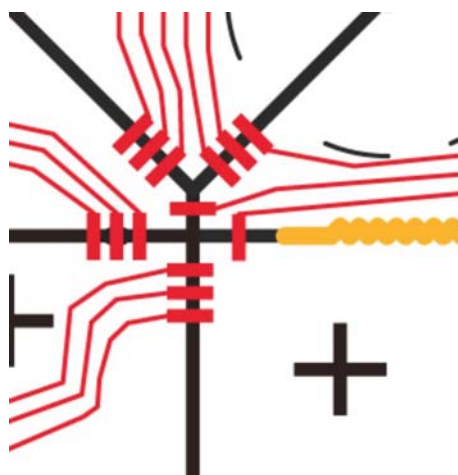


Figure 4.9: Previous version of PumpDrop Channel layout.

the Y-channel and T-junction and no delay valves. Attracted by the wettability of PDMS surface and partially due to the pulsing nature of pumped flow, the oil adhered to the channel surface and slowly migrated into the Y-channel. Consequently, unwanted smaller droplets formed. To avoid this, the Y-channel was moved further away (15  $mm$ ) from the T-junction and delay valves were also added (Figures 4.6 and 4.7).

### Automated droplet formation

The custom LabVIEW application was programmed to alternatively pump aqueous and oil to generate droplets (see Figure 4.4 and Figure 4.10). The LabVIEW application had controls over several parameters of droplets. The droplets, size was changeable by pumping

aqueous phase for more or less cycles, the spacing in between droplets was controlled by varying the pump cycles of the oil phase, and the sample and reference droplet ratio as well as the droplet generation frequency were also controllable by the pumping codes (Figure 4.11).

Since droplet formation was digitally controlled, and the droplets were sequentially sent into the storage channel, the incubation time of each droplet were individually addressable. Ideally, as droplets passed through the detection region, all the components inside each droplet had reacted for the same time period. Due to the smaller oil fluid resistance, the space in between droplets was observed to decrease as the droplets advanced downstream, particularly if the droplets were small. This issue was partially solved by using SU-8 patterned, rectangular channels. Another solution was alternatively making large and small droplets, which paired up during flow downstream (Figure 4.8) and allowed easier data analysis (details in next section). After making droplets for a long period of time, the oil and droplets accumulate in the waste outlet tubing and their gravity pulls up the opened valve membrane, which narrowed the channel and breaks the newly formed droplet into smaller ones. Thus the accumulated fluid needs to be frequently cleaned.

It is worth mentioning that the droplet formation mechanism is different from T-junction, co-flow, flow-focusing, or step emulsification. As the oil wets the hydrophobic PDMS surface, a small amount of oil was confined in between the membranes above the sample delay valve and reference valve. After pumping aqueous solution, the delay valve closes and creates a new oil-water interface formation. Compared with T-junction droplet formation mechanism, which suffers from droplet size variations caused by pressure and flow rate differences, our valve segmentation based droplet formation method allows accurate volume control of droplets.

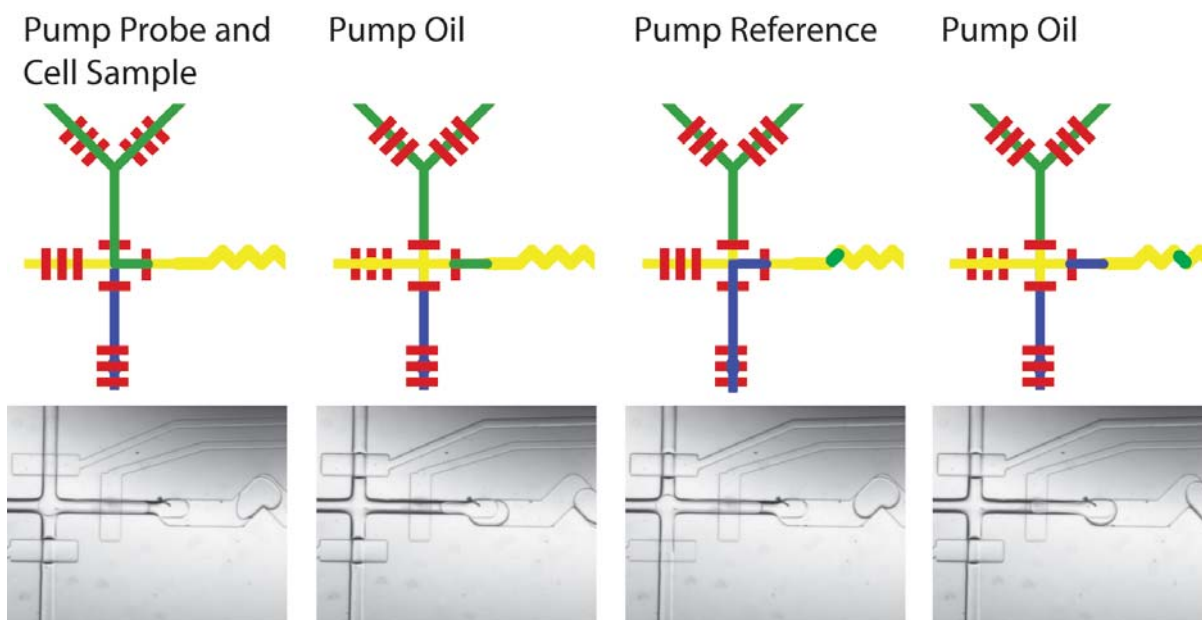


Figure 4.10: Droplet formation steps

Droplets were formed by alternatively pumping aqueous (probe/cell sample or reference) solution and oil into the droplet storage channel.

### Mixing Ratio Consistency

Consistent sample and probe mixing ratio within each droplet is crucial for droplet immunoassay accuracy. The mixing ratio was measured by fluorescence imaging of sample droplets made from fluorescein solution mixing with buffer and reference droplets made with undiluted fluorescein solution. As shown in Figure 4.12, the fluorescent intensity of mixed sample droplets was  $48.05 \pm 0.22\%$  of the reference droplets, which indicated the mixing ratio was 1 : 1.08. This mixing ratio was nearly 1 : 1 as designed, and the mixing precision was high at  $< 0.5\%$  relative standard deviation.

### Islet Trapping Region

The islet must be confined within a microfluidic channel or chamber that brings nutrients to and hormone from the tissue, or the hormones will diffuse into the bulk solution, and temporal dynamic information will be lost. Previously, we used a deep microchannel (156

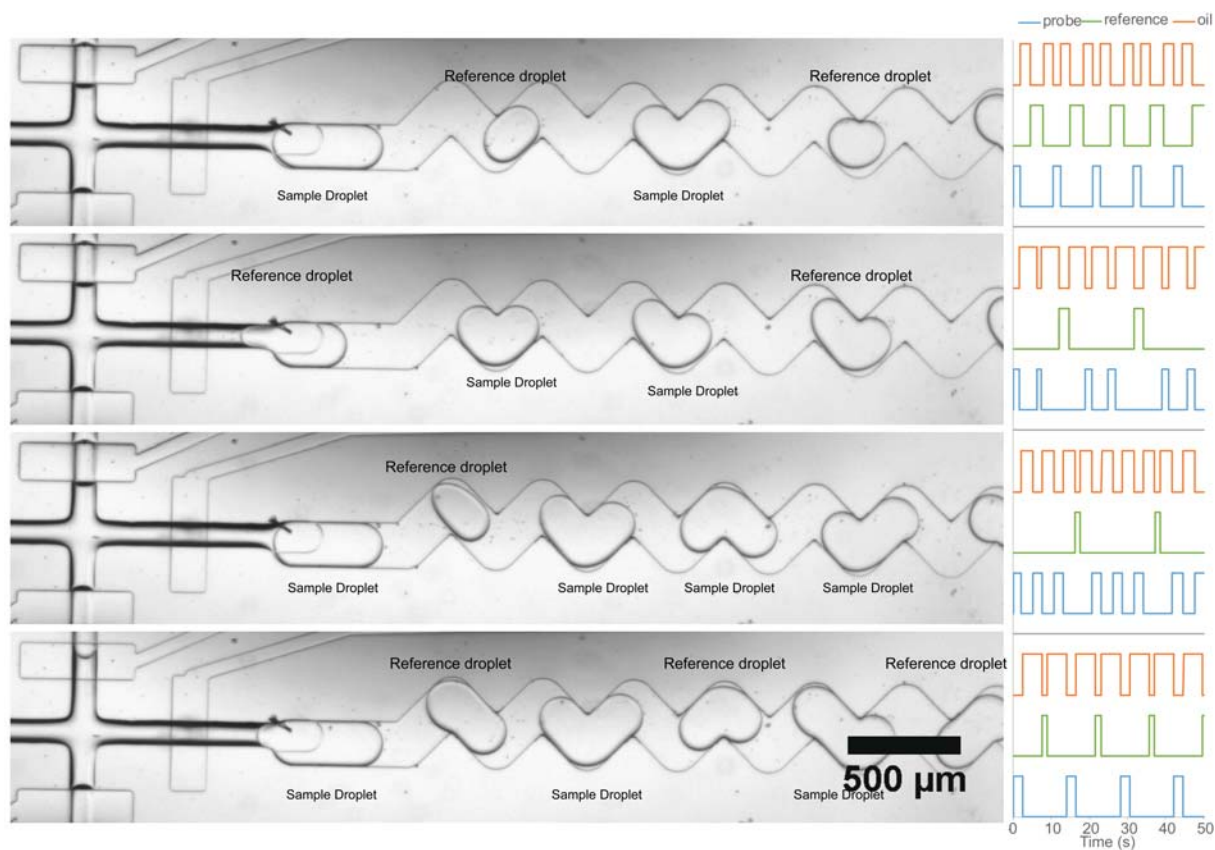


Figure 4.11: Droplet formation with various parameters

The left side shows the representative images of droplet formation with various pumping cycle, sample/reference ratio, and oil pumping cycle. The right side is the corresponding pumping codes. Up indicates pumping and down represents closing, and each pump cycle was 500 *ms*.

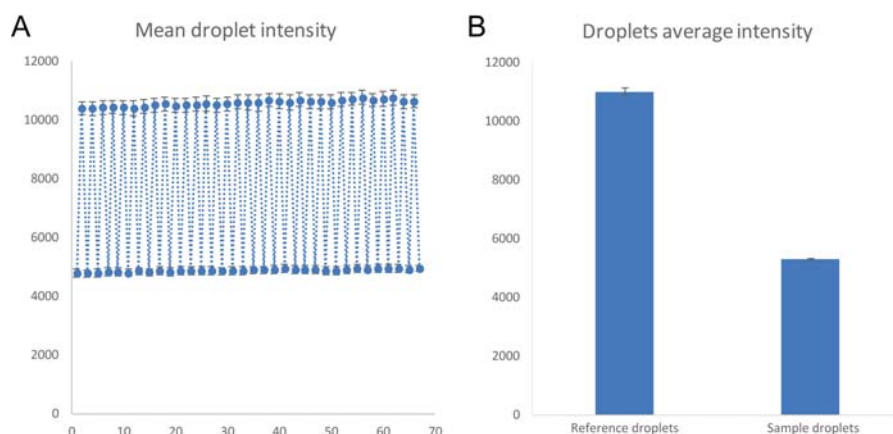


Figure 4.12: PumpDrop device characterization

(A) Fluorescent measurement of sample droplets made of fluorescein solution and buffer, and reference droplets of fluorescein solution. (B) Averaged fluorescent intensity from reference droplets and sample droplets.

$\mu\text{m}$  deep \* 600  $\mu\text{m}$  wide) for islet trapping [66]. The deep channel was patterned with SU-8 on the master wafer and interfaced with the solution reservoir via a 1.5 mm hole. Here, by simply making the interfacing hole with a 500  $\mu\text{m}$  punch, a vertical microfluidic channel for islet trapping was created. The islet chamber was punched into the wide area (300  $\mu\text{m}$  diameter) of the fluidic channel to prevent islet loss into the downstream channel (as shown in Figure 4.13). A typical islet chamber is 500  $\mu\text{m}$  in diameter and 500  $\mu\text{m}$  depth, and the total volume is about 100  $n\text{L}$ . As solution in the reservoir changed by pipette, the solution within the islet chamber was completely switched to the new solution within 1 to 3  $\text{min}$  (Figure 4.16). The islets were not disturbed if the solution was gently removed and added. while the islets can be removed by pipetting directly toward the cell trapping region in order to reuse the chip for another islet test.

### **Temporal Resolution Assessment by Mimicking Insulin Secretion**

Because the PumpDrop device operates by alternatively pumping aqueous solution and oil, the insulin secreted by an islet in the culture chamber was sampled into the droplets only when sample pumping is active. During the rest of the droplet formation cycle, the secreted insulin was freely diffusing into the islet trapping region and perhaps into the bulk reservoir. To evaluate the temporal resolution of our system, the diffusion of insulin was tested with Islet Mimicking mode of the LabVIEW application (Figure 4.4 and Figure 4.15). FITC-insulin (similar volume as a single islet) was pumped into the islet trapping region, left to diffuse for 1 to 30  $s$  and then sampled into the channel(Figure 4.15 A and B). Assume the islet is a sphere with 150  $\mu\text{m}$  diameter (a normal islet size is in between 100-200  $\mu\text{m}$  [66]), the volume of this islet is 1.7  $n\text{L}$ , which requires 5 cycle of pump (dispensing volume of each cycle is 0.365  $n\text{L}$ ). During the incubation time, the fluorescence intensity decrease follow a exponential decay with 10.5  $s$  half life. Upon sampling, the fluorescence intensity decrease at a faster rate (exponential decay with 1.38  $s$  half life). The time for sampling half

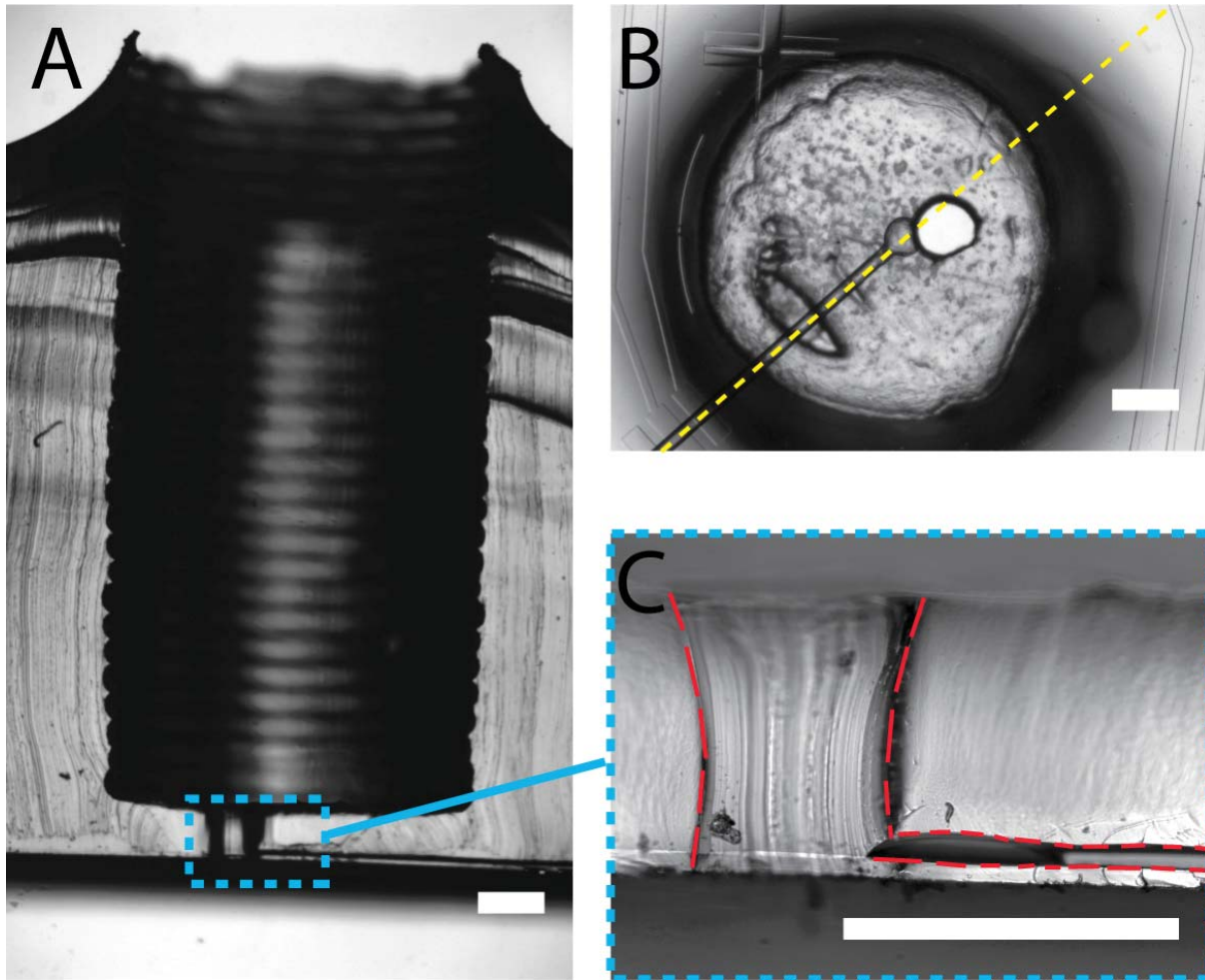


Figure 4.13: Cross-section of the islet trapping region  
(A) cross-section of the big reservoir and the cell culturing region. (B) bottom view of the reservoir with a line indicating the cutting line of the cross-section in (A and C). (C) the enlarged image of the islet trapping region with red dash line for the chamber and the microchannel. Scale bar = 500  $\mu m$ .

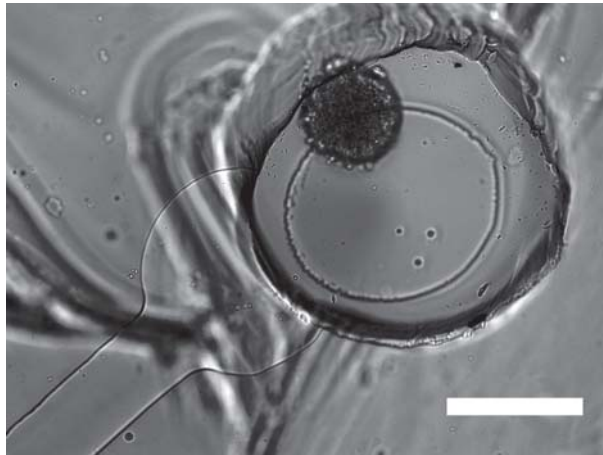


Figure 4.14: Example of bottom view of single islet in the trapping chamber  
Scale bar = 200  $\mu\text{m}$ .

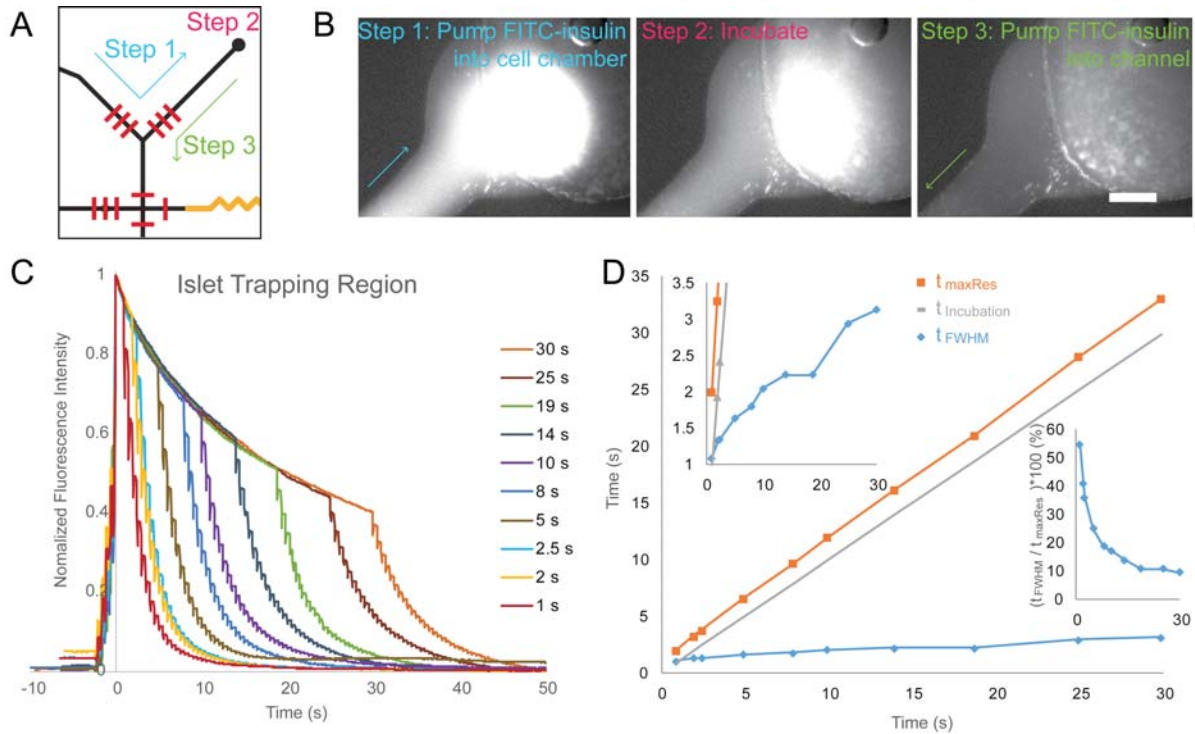


Figure 4.15: Insulin diffusion test

(A) Procedure of the islet mimicking, FITC-insulin was pumped into cell chamber, incubated, and pumped into the channel. (B) Example fluorescent images of each steps. (C) Normalized fluorescence in islet trapping region during the islet mimicking with various incubation time (1 to 30 s). (D) Measured time for fluorescence drop to half of the sampling start point. Top-left inset is zoomed-in plot highlighting the  $t_{FWHM}$  (time to reach Full width at half maximum). Bottom-right inset shows the percentage of the  $t_{FWHM}$  in  $t_{maxRes}$  (measured best temporal resolution).

of the solution into channel was plotted in Figure 4.15D. With increased incubation time, the contribution of free diffusion induced temporal resolution lost was decreased, which indicates that in our system, the temporal resolution is actually limited by the time for making droplets.

## Insulin Quantification within Droplets

Previously, we reported an automated microfluidic sample chopper ( $\mu$ Chopper) which was successfully used for insulin quantification within droplets by using a fluorescence quenching based homogeneous immunoassay[176]. This  $\mu$ Chopper was not able to mix the sample and immunoassay probes, nor accomplish on-chip incubation. Thus, all the samples were premixed and incubated before loading onto the  $\mu$ Chopper. However, an important feature of the  $\mu$ Chopper is the ability discriminate very small differences in optical signals (fluorescence, absorbance) even with high background or at very low concentrations due the drift correction and  $1/f$  noise reduction. This concept is used herein within the PumpDrop analysis channel.

Here, the PumpDrop allows continuous droplet formation with islet samples and assay probes with a consistent ratio. The droplets formed were also able to be stored within channels to meet the reaction time requirements (30 *min* at least in this case) for signal accumulation. Firstly, the assay performance was tested by manually changing the insulin solution (0, 32, 64, 128, 256, 502, and then 0 *nM*) within the reservoir, and diluted assay probe was used as a constant reference. As shown in Figure 4.16, the fluorescence intensity of sample droplets (blue trace) decreased as the insulin concentration increased, while that of reference droplets (orange trace) held within a narrow range albeit with some drift. The fluorescence quenching effect was proportional to insulin concentration (Figure 4.16 B and D) and signal drifts were corrected by lock-in analysis. The limit of detection (LOD) was calculated to be 77.7 *ng/mL* (or 13.4 *nM*), and the mass LOD was  $5.07 \times 10^{-17}$  *mol* (50.7

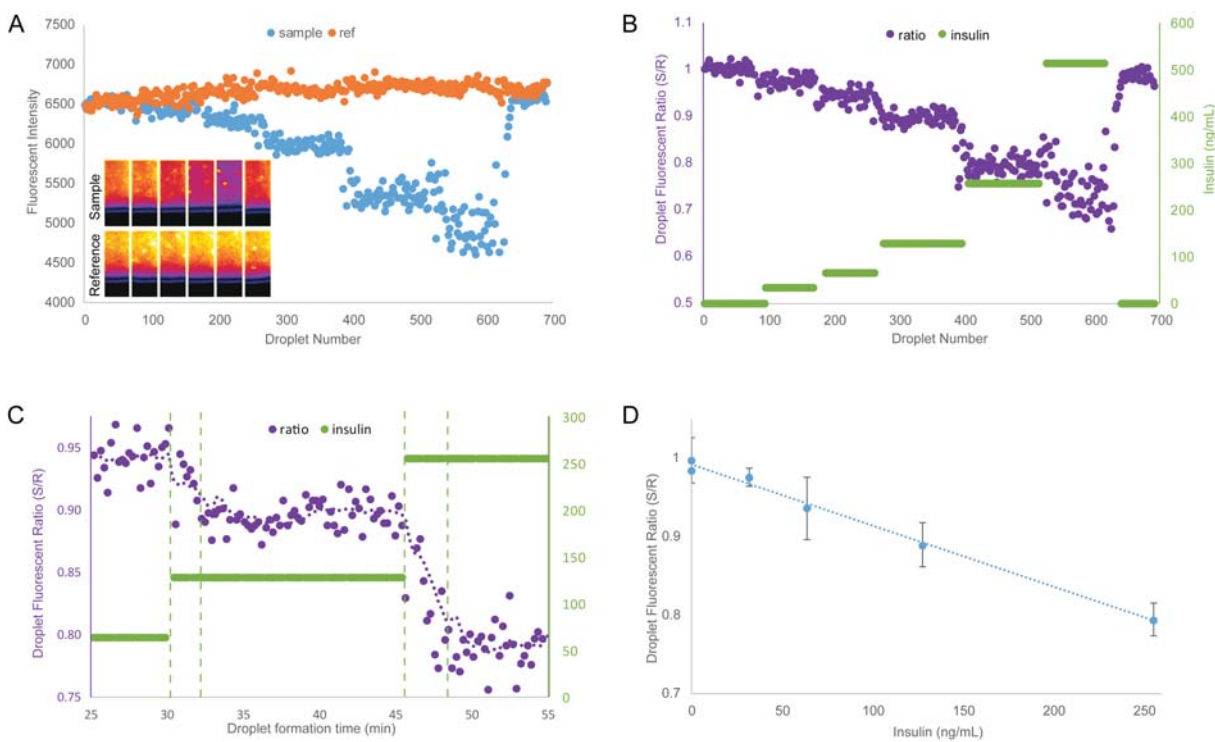


Figure 4.16: Insulin concentration measurement within droplets

(A) Averaged fluorescence intensity of individual sample droplets and references, with inset of examples fluorescent images of sample and reference droplets. (B) Fluorescence ratios of sample and neighboring reference droplets (Purple). The glucose concentration is shown in green. A zoomed-in plot (C) shows the ratio changing after changing insulin concentration. (D) Insulin standard curve, error bar indicate the standard deviations of 30 droplet pair ratios.

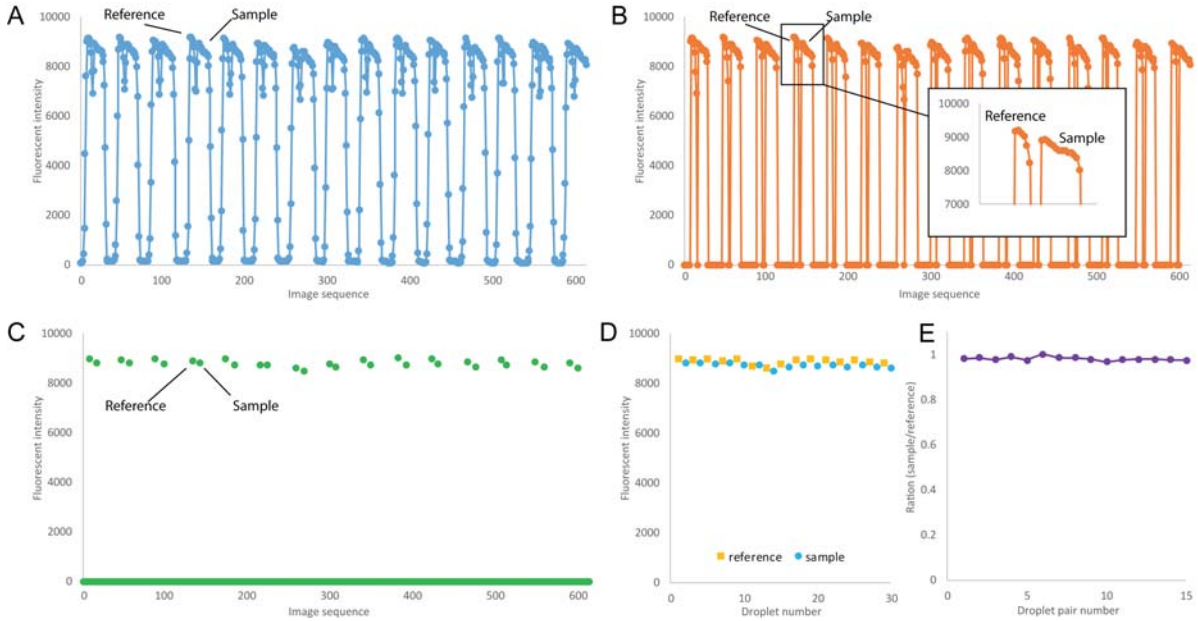


Figure 4.17: Example of droplet insulin assay data analysis

(A) The raw data was determined directly from the average intensity of fluorescence images by ImageJ. (B) A standard deviation filter and intensity filter were applied to select the data points of droplets (other data points were set to 0). (C) Mean intensity of each individual droplet. (D) Mean intensities of droplet was sorted into sample and reference. (E) Fluorescent ratio of sample droplets and corresponding reference droplet was calculated.

*amol*) with each pair of droplets. Upon solution changing, the fluorescence ratio between sample and reference quickly equilibrated within 3 min (Figure 4.16 C), which indicate the levels of glucose treatment for single islet sampling could be switched within 3 min. The stepwise data analysis procedure is shown in Figure 4.17.

## Single Islet Insulin Secretion Dynamics

In pancreatic islets, insulin secretion is synchronized with the elevation of cytosolic  $\text{Ca}^{2+}$  levels throughout the electrically coupled cell clusters at high glucose level. During the glucose induced insulin secretion process, the uptake of glucose into  $\beta$ -cells through glucose transporter GLUT2 increases the production of ATP via the glycolytic pathway and tricarboxylic acid (TCA) cycle. The increased ATP/ADP ratio closes the ATP-sensitive

$K^+$  channels, and the decreased  $K^+$  permeability leads to membrane depolarization. Consequently, the voltage-dependent  $Ca^{2+}$  channel opens,  $Ca^{2+}$  influx occurs, and the increased  $Ca^{2+}$  concentration triggers exocytosis machinery of insulin granules. It is known that insulin secretion is a pulsatile phenomenon with three types of oscillations: regular and slow (frequency of  $\sim 0.2 /min$ ), regular and rapid (frequency of 2-3  $/min$ ), or mixed, in which rapid oscillations are superimposed on slow ones[283].

The slow oscillations of insulin secretion were observed by many examples of direct insulin immunoassays[220]. However, the fast oscillations of insulin were only directly observed by proinsulin genetic GFP and mCherry fusions and total internal reflection fluorescence microscopy[284]. Other observations of the rapid oscillation rely on indirect measurement, such as fluorescence  $Ca^{2+}$  imaging[283, 285, 286, 287], electrophysiology analysis of membrane potential using patch clamp[288], and  $Zn^{2+}$  (corelease at 2:6 ratio with insulin) quantification[175].

To test if the PumpDrop device was capable of observing the rapid oscillation of insulin secretion, single islets' dynamic insulin secretion were measured during treatment with approximate square waveforms of physiologically relevant levels of glucose. Single islets were loaded into the trapping chamber (Figure 4.14), and droplets containing both the secretome and assay probes were continuously made at  $\sim 0.1 Hz$  and allowed to incubate and analyze in the incubation channel. With constantly referencing to the droplet made with diluted assay probe ( $\mu$ Chopper concept), the insulin secretions were quantified. The glucose induced insulin secretion from single islets was observed to be generally in line with the input glucose waveforms. As shown in Figure 4.18, the islets exposed to low level glucose (3.5  $mM$ ) exhibited insulin secretion oscillations with periods of 20-30  $s$  at low magnitude (0.7, 0.3, and 0.35  $pg/islet/min$  for Figure 4.18A, B, and C, respectively). Upon high glucose treatment (19.5  $mM$ ), the oscillation magnitude increased to more than double compared to that with low glucose treatment, and the oscillations with longer periods ( $\sim 1$  to 3  $min$ ) became dominant. These results confirmed the PumpDrop to be suitable for automated,

high-temporal resolution secretome dynamics studies, which should be suitable for a variety of cells or tissue types.

#### 4.4 Conclusions

A microfluidic droplet generator using on-chip peristaltic pumping for accurate fluid metering was developed and proven feasible for high temporal resolution insulin secretion dynamics analysis from single islets. These results suggest this PumpDrop device should be translatable to other proteins or small molecule secretion dynamic studies for other tissues or cells, especially for cytokines, coagulation factors, hormones, enzymes, growth factors, and other proteins playing crucial roles in many physiological and pathological processes. The device could also be integrated with other microfluidics modules, like controllable perfusion system for tissue and cell culturing[190, 217, 211, 289, 290, 291, 292], for automated stimulation.

Compared with other microfluidic droplet generators that allows  $kHz$  frequencies droplet formation[293], our device only forms droplet at a frequency up to  $1 Hz$  due to the slow pneumatic valve actuation and relative small dispensing volume per pumping cycle. To improve the sampling rate without sacrificing the sensitivity, sophisticated droplet manipulation technologies, such as droplet merging[294] or pico-injection [154], could be integrated into our device for introducing reagents into sample droplets. This would also help multi-step immunoassays or enzyme based assays to be transferred into the microfluidic droplet system in a more controllable manner. A microfluidic first-in-first-out droplet shift register [295] could also be useful to synchronize the detection of droplets, which would allow in line data collection within the LabVIEW application and largely simplify the data analysis.

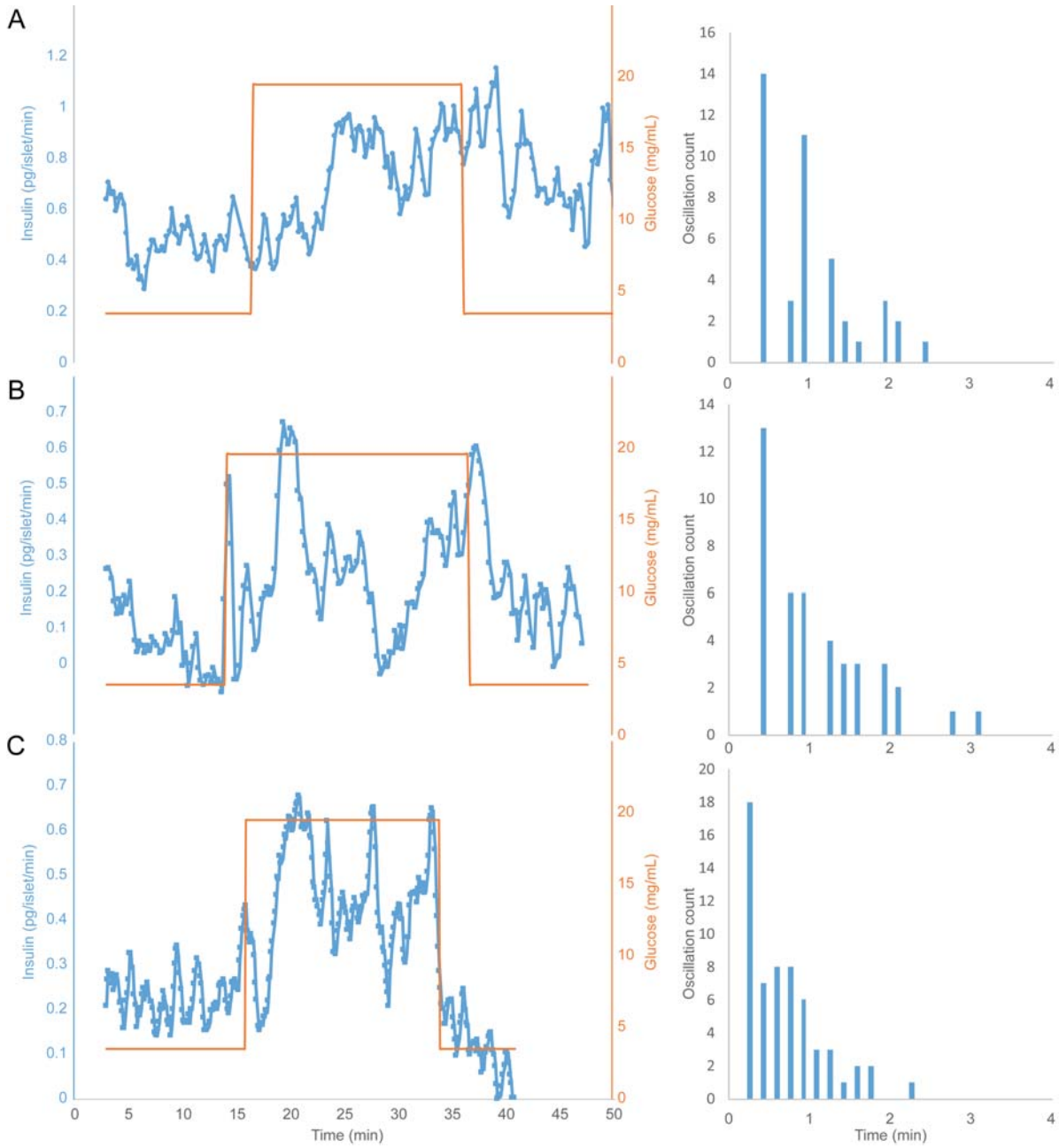


Figure 4.18: Insulin secretion from three different single islets  
 Insulin was shown in blue and glucose treatment was shown in orange.

## Chapter 5

### Controlled protein coatings at aqueous-in-oil droplet surfaces with biotinylated surfactants

#### 5.1 Introduction

As a sub-field of microfluidics, droplet microfluidics focuses on the production of water-in-oil droplets containing  $pLs$  to  $nLs$  solution at high frequency (up to several  $kHz$ ) in channels with tens of micrometers dimensions. Each of those droplets behave as individual nano-reactors for performing chemical, and biological reactions, and single cell studies [296]. The application of droplet microfluidics provides numerous advantages for biology and chemical assays, such as high throughput, high temporal resolution, and greatly reduced cost. For many of biological assays conducted within droplets, fluorocarbon oils [297] are used as the continuous phase for the following reasons. Those oils are both hydrophobic and lipophobic, hence they have low solubility for biological reagents of the aqueous phase and eliminate molecular diffusion between droplets. Additionally, unlike other oils such as mineral oil, the fluorocarbon oils does not swell the commonly used PDMS (Polydimethylsiloxane) for fabrication of microfluidic devices. Finally, the gas permeability of fluorocarbon oil makes cell culturing in droplets possible.

To prevent droplets from coalescing, surfactants are employed to stabilize them. Several non-ionic biocompatible perfluorocarbon-surfactants were developed such as Kry-Jeffa [150], and PFPE-tris [151] (Figure 1.21). Ionic surfactants such as Krytox also prevent the coalescence of droplets, but their charged head groups are incompatible with most biomolecules. Additives such as Jeffamine ED-90 (polyetherdiamine) [152] or bovine serum albumin (BSA) [153] interact with the ionic groups on the water-oil interface, thus were used to protect the biomolecules within droplets. A gold nanoparticles linked surfactant was also developed to

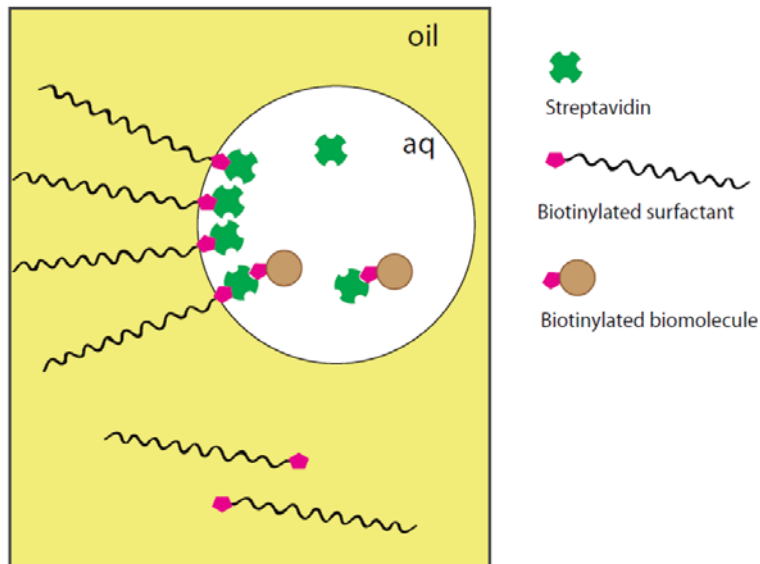


Figure 5.1: Schematics of biotin-STV interaction on the aqueous-oil interface of droplet anchor sulfur containing biomolecules like His<sub>6</sub> proteins to the droplet surface for creating a microenvironment for T-cells homing studies [298].

The interaction between streptavidin (STV) and biotin is one of the strongest non-covalent interactions known in nature[299, 300]. The STV-biotin complex is powerful biology tool and already has been widely used in isolation (affinity chromatography[301]), localization (affinity cytochemistry[302], cell cytometry[303], blotting technology[304]), and diagnostics (immunoassay[305], histopathology[306], and gene probes[307]). Here, we synthesized a biotinylated perfluorocarbon surfactant for droplet surface protein coating and for future droplet-based bioassays. The interactions between STV and biotin were monitored by confocal fluorescent microscope imaging.

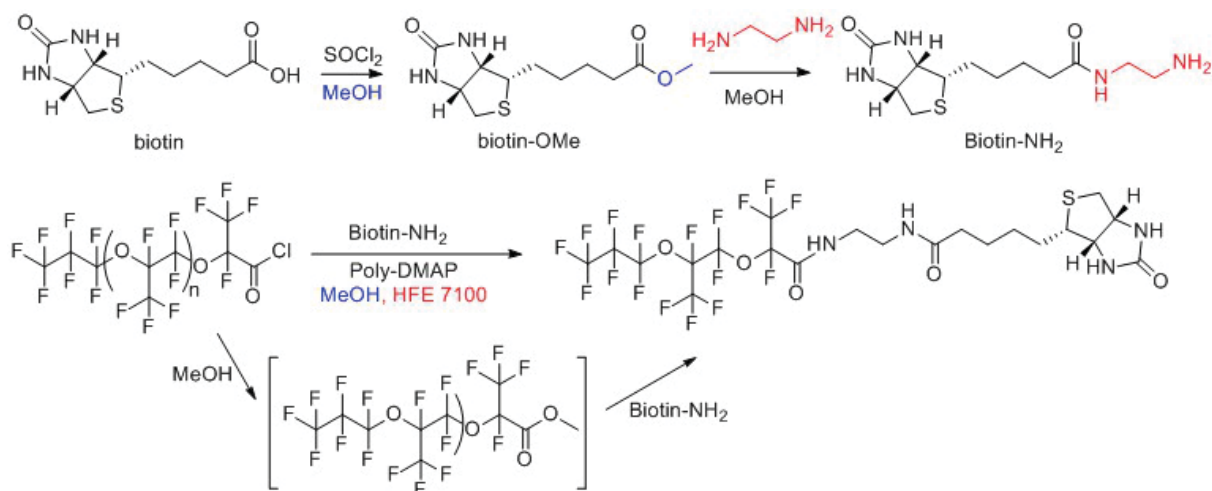


Figure 5.2: Schematics for Kry-Biotin synthesis

## 5.2 Experimental and methods

### 5.2.1 Materials

Krytox 157 FSH was obtained from DuPont (Wilmington, DE). Novec engineering fluid HFE-7500 and HFE-7100 were purchased from 3M (Maplewood, MN). D-Biotin, thionyl chloride ( $\text{SOCl}_2$ ), diethylaminemethanol, and polymer-bound 4-(Dimethylamino)pyridine (poly-DMAP) were obtained from Sigma-Aldrich (St. Louis, MO). Streptavidin-Alexa Fluor 488 conjugate was purchased from ThermoFisher Scientific (Grand Island, New York). Polydimethylsiloxane (PDMS) precursors, Sylgard 184 elastomer base and curing agent, were from Dow Corning (Midland, MD). Pico-Surf 1 surfactant 5% in HFE-7500 were obtained from Dolomite (Royston, UK).

### 5.2.2 Kry-Biotin surfactant synthesis

**Biotin-OMe**  $\text{SOCl}_2$  (0.30 mL, 4.0 mmol) was added drop-wise to a suspension of biotin (300 mg, 1.23 mmol) in MeOH (3 mL), and the solution was stirred 6 h at room temperature to give a clear solution. After evaporation of the solvent and excess  $\text{SOCl}_2$  under reduced pressure, biotin methyl ester (296 mg) was obtained in 93% yield as a white solid. ESI-MS ( $m/z$ ) 259.11 ( $[\text{M}+\text{H}]^+$ ).

**Biotin-NH<sub>2</sub>** Ethylene diamine (2.0 mL) was added to a solution of Biotin-OMe (250 mg, 0.97 mmol) in methanol (5.0 mL). After stirring at 60 °C for 48 h, excess ethylene diamine and methanol were removed under reduced pressure. Biotin 2'-Aminoethylamide was obtained as white solid (247 mg, 89%). ESI-MS (*m/z*) 287.10 ([M+H]<sup>+</sup>).

**Kry-Cl** SOCl<sub>2</sub> (0.5 mL, 6.897 mmol) were added to an HFE-7100 solution of Krytox (5 g, ~0.69 mmol) under N<sub>2</sub>. After this mixture was refluxed for 6 h at 60 °C, the excess SOCl<sub>2</sub>, hydrochloric acid, sulfur dioxide byproducts, and HFE-7100 were removed under reduced pressure. The resulting transparent viscous liquid was used directly in the next step.

**Kry-Biotin** HFE-7100 (50 mL) and THF (10 mL) were added to dissolve Kry-Cl obtained in last step, followed by the addition of Biotin-NH<sub>2</sub> (197 mg, 0.69 mmol) in methanol solution (5 mL). The mixture were refluxed overnight at 60 °C under N<sub>2</sub>. The removal of solvent under vacuum gave the transparent viscous liquid product. ESI-MS (*m/z*) 1429.12 ([M+H]<sup>+</sup>).

### 5.2.3 Microfluidic device fabrication and droplet formation

PDMS devices for droplet generation were fabricated with standard soft lithography. PDMS elastomer base and curing agent were mixed in a 10:1 ratio, poured over the master defined by photoresist (SU-8, Microchem) on a silicon wafer, and cured overnight at 65 °C. Patterned PDMS was removed from the silicon master, and holes were punched for channel access. The device was then cleaned with methanol, air dried with nitrogen spray, then bonded immediately to a glass slide after plasma oxidization (Harrick Plasma) treatment for 45 s. Microchannels were then treated with Aquapel (Pittsburgh Glass Works), rinsed with methanol, and placed in an oven at 65 °C overnight prior to use.

Kry-Biotin and Pico-Surf 1 surfactant were diluted to 1% (w/w) with HFE-7500, and respectively loaded into the two oil reservoirs. STV-AF488 in PBS buffer was loaded into the sample reservoir. Droplets were formed by applying vacuum using two handheld 25 mL

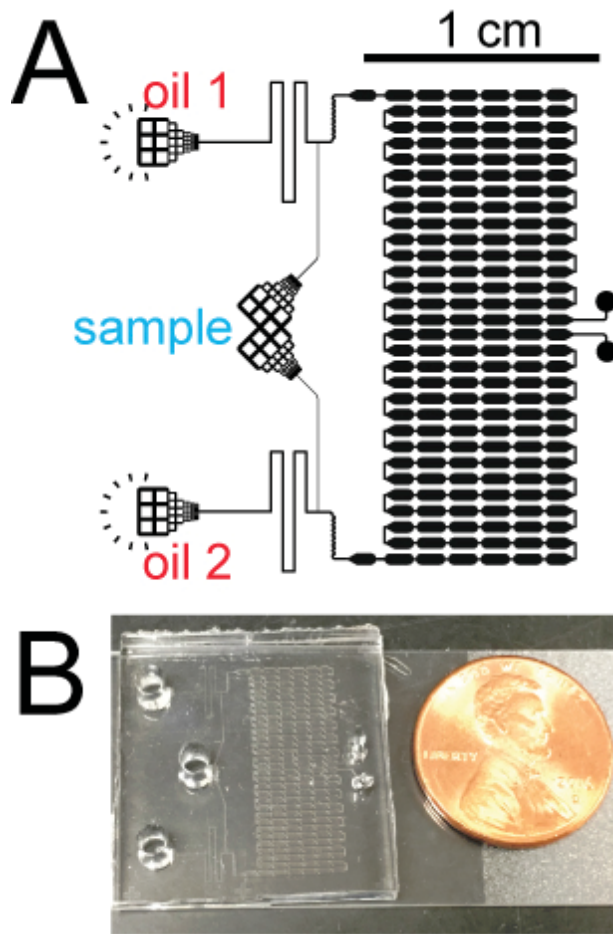


Figure 5.3: TwoOil chip design schematics and image

syringes connected to the two outlets via Tygon tubing. After the droplet fills up the droplet imaging chamber, the syringes were detached, and droplets were left to equilibrate for at least 1 *min*. The image of droplets were taken by confocal fluorescent microscope (Nikon-Ti) with 488 nm laser excitation, FITC filter set, and a minimum pinhole size (1.2 airy unites). The sample reservoir was then washed and the next concentration of STV-AF488 was loaded for droplet formation and imaging. The images were analyzed with ImageJ and Excel.

### 5.3 Result and Discussion

#### 5.3.1 Biotinylated surfactant synthesis

The synthesis of Kry-Biotin was achieved by covalently linking Krytox and biotin with an ethylene diamine linker (Figure 5.2). First, the ethylene diamine was reacted with Biotin-OMe to introduce the -NH<sub>2</sub> group. The Krytox was treated with thionyl chloride to form acyl chloride (Kry-Cl). Because the Kry-Cl is only soluble in perfluorocarbon based solvent, in which Biotin-NH<sub>2</sub> is insoluble, the reaction of Kry-Cl and Biotin-NH<sub>2</sub> was not successful with several mixed solvents such as THF and HFE-7100. A Biotin-NH<sub>2</sub> favorable solvent, such as MeOH, reacts with Krytox acyl chloride to form methyl ester, which was shown to further react with ammonia to yield amide [308]. So MeOH, THF, and HFE-7500 mixture was used to carry the Biotin-NH<sub>2</sub> and Kry-Cl reaction. The biotinylated surfactant, Kry-Biotin, was presumably formed via a methyl ester intermediate (Figure 5.2).

The formed viscous surfactant was directly used for droplet formation (Figure 5.4). In the reaction, excess Biotin-NH<sub>2</sub> was used to consume all the Kry-Cl or the intermediate Kry-OMe. Because of the insolubility of Biotin-NH<sub>2</sub> in droplet carrier oil, HFE-7500, the leftover Biotin-NH<sub>2</sub> was easlily removed by filtering. However, the Kry-Biotin was found not stable at 4 °C storage. As shown in Figure B.4 and B.5, nearly all Kry-Biotin degraded after one month. The trace amount of unreacted Krytox could possibly serve as a catalyst for the hydrolysis of Kry-Biotin. In order to achieve consistent results, the surfactant was freshly

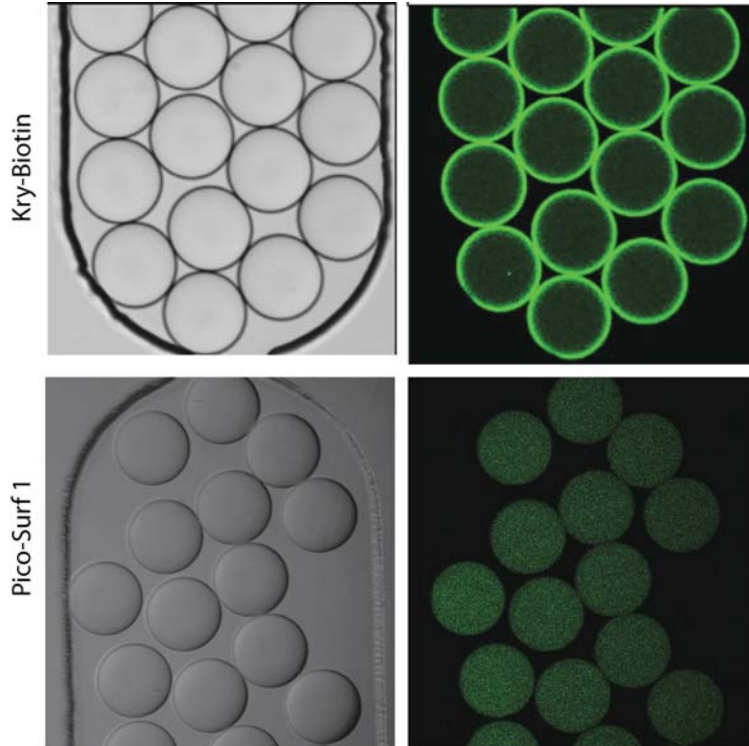


Figure 5.4: Images of droplets made with Kry-Biotin and PicoSurf 1 surfactant containing oils in the presence of fluorescently labeled streptavidin proteins (STV-AF488). The Kry-Biotin clearly recruited streptavidin proteins to the droplet surfaces. (Confocal transmission on left and fluorescence on right.)

prepared before each use.

### 5.3.2 Microfluidic device design and droplet formation

The microfluidic device design consisted of two parallel T-junction channels sharing a common aqueous input for droplet formation from two separate oil input channels (Figure 5.3). After droplet formation, the droplets move downstream into a “zigzag” mixing channel followed by an incubation portion of the chip. The droplets within the incubation portion are in close proximity with each other. No coalescence to the droplets made with Kry-Biotin was observed, which suggest the Kry-Biotin is able to lower the surface tension and stabilize the droplets similar to the pico-surf1. The confocal fluorescence images clearly (Figure 5.4)

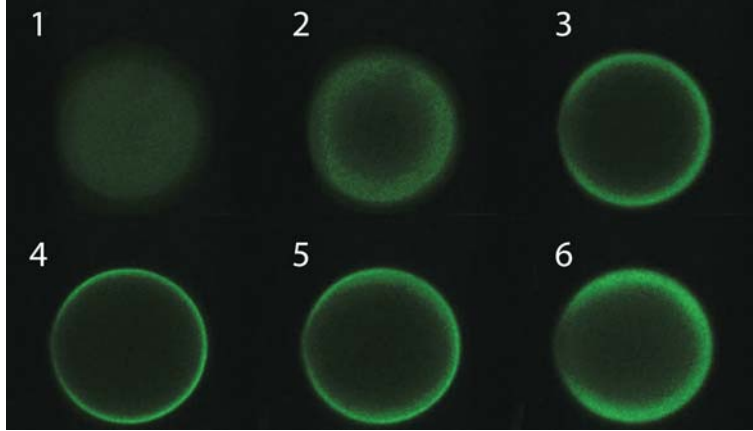


Figure 5.5: Confocal z-scanning fluorescent images a droplet stabilized by Kry-biotin, which is bound to STV-AF 488

show STV-AF 488 were bound to the droplet surface formed with Kry-Biotin, while STV-AF 488 evenly distributed within the droplets made with Pico-Surf 1. The z-stack scanning images shows more clearly the STV recruitment to the interface (Figure 5.5).

### 5.3.3 Surface interaction simulation

As shown in Figure 5.1, the water-soluble portion of the surfactant Kry-Biotin, the biotin residue, assembled at the oil-water interface of emulsion droplets, while the oil-soluble portion stays in the oil phase. STV molecules are absorbed to the oil-water interface by the strong affinity to biotin head groups of the surfactants. Although each STV molecule has 4 biotin binding sites, in this surface confined interaction, only one biotin could bind to STV molecule due to the steric hindrance effect. This absorption can be described by a single layer Langmuir absorption model.

The interaction between STV and biotin on the droplet surface ( $S$ ) is shown as the equilibrium equation.



Where  $S$  is surface biotin,  $A$  is streptavidin, and  $SA$  is the surface biotin-STV complex.

The surface coverage of the droplet interface is assumed to follow a single layer Langmuir absorption model, and the equilibrium constant of the reaction is calculated as:

$$K = \frac{\Gamma_{SA}}{\Gamma_S * [A]} \quad (5.2)$$

$\Gamma_{SA}$  is the amount of biotin-STV complex per area unit, or, the concentration of the biotin-STV complex on the surface.  $\Gamma_S$  is the concentration of the free effective biotin on the surface, and  $[A]$  is the free STV concentration within droplets. The STV-biotin association constant  $K$  is known to be  $\sim 10^{15} M^{-1}$  [299].

Let  $[A] = c$ , and  $\Gamma_{max} = \Gamma_{SA} + \Gamma_S$ , where  $\Gamma_{max}$  is described as:

$$\Gamma_{max} = \frac{\text{maximum amount of STV}}{\text{surface area}} = \frac{1}{A_{STV} * N_A} \quad (5.3)$$

$A_{STV}$ , the area that a single STV molecule occupies,  $N_A$ , Avogadro's constant.

The fraction of biotin-complex on the surface is

$$\frac{\Gamma_{SA}}{\Gamma_{max}} = \frac{\Gamma_{SA}}{\Gamma_{SA} + \frac{\Gamma_{SA}}{c * K}} = \frac{1}{1 + \frac{1}{c * K}} = \frac{cK}{1 + c * K} \quad (5.4)$$

The initial concentration of the STV is known as  $C^*$ . So,

$$C^*V = \Gamma_{SA} * A + c * V \quad (5.5)$$

$V$ , the volume of droplets ( $V = 4\pi r^3/3$ ),  $A$ , surface area of the droplets ( $A = 4\pi r^2$ ), where  $r$  is the radius of droplet.

The concentration of the free STV in the center of a droplet after STV binding to the surface is:

$$c = \frac{C^* * V - \Gamma_{SA} * A}{V} = C^* - \frac{\Gamma_{SA} * A}{V} = C^* - \frac{3}{r} * \Gamma_{SA} \quad (5.6)$$

If we bring the  $c$  value into equation 5.4,

$$\frac{\Gamma_{SA}}{\Gamma_{max}} = \frac{(C^* - \frac{3}{r} * \Gamma_{SA}) * K}{1 + (C^* - \frac{3}{r} * \Gamma_{SA}) * K} \quad (5.7)$$

Therefore,

$$\Gamma_{SA} + C^* * K * \Gamma_{SA} - \frac{3}{r} * K * \Gamma_{SA}^2 = \Gamma_{max} * K * C^* - \frac{3}{r} * K * \Gamma_{max} * \Gamma_{SA} \quad (5.8)$$

The two possible solutions to this equation are:

$$\Gamma_{SA} = \frac{(1 + C * K + \frac{3}{r} * K * \Gamma_{max}) \pm \sqrt{(1 + C * K + \frac{3}{r} * K * \Gamma_{max})^2 - 4 * \frac{3}{r} * \Gamma_{max} * K^2 * C^*}}{2 * \frac{3}{r} * K} \quad (5.9)$$

Since  $\lim_{x \rightarrow \infty} x = \Gamma_{max}$ , we can choose the following solution:

$$\Gamma_{SA} = \frac{(1 + C * K + \frac{3}{r} * K * \Gamma_{max}) - \sqrt{(1 + C * K + \frac{3}{r} * K * \Gamma_{max})^2 - 4 * \frac{3}{r} * \Gamma_{max} * K^2 * C^*}}{2 * \frac{3}{r} * K} \quad (5.10)$$

And because  $c = C^* - \frac{3}{r} * \Gamma_{SA}$ ,

$$c = -\frac{1}{2K} - \frac{3 * C^*}{2} - \frac{3 * \Gamma_{max}}{2 * r} + \sqrt{\left(\frac{1}{2K} + \frac{3 * C^*}{2} + \frac{3 * \Gamma_{max}}{2 * r}\right)^2 - \frac{3 * C^* * \Gamma_{max}}{r}} \quad (5.11)$$

The diameter of STV was previously observed to be 11 *nm* [309]. If we assume each STV molecule to occupy a square area on the droplet surface, then,  $\Gamma_{max} = 4\pi r^2 / [(11 \text{ nm})^2 * N_A]$ . The concentration of surface bound STV ( $\Gamma_{SA}$ ) and the free STV ( $c$ ) were thus only dependents of the droplets size ( $r$ ) and the initial concentration ( $C^*$ ). As shown in Figure 5.6, with increased initial STV concentration, the surface bound STV increased until it reached its saturation point, and the concentration of STV in solution linearly increased only after the surface saturated. The saturation points of the droplets surface is defined by the droplet size, as shown in the multiple simulated curves in Figure 5.6. This model system should

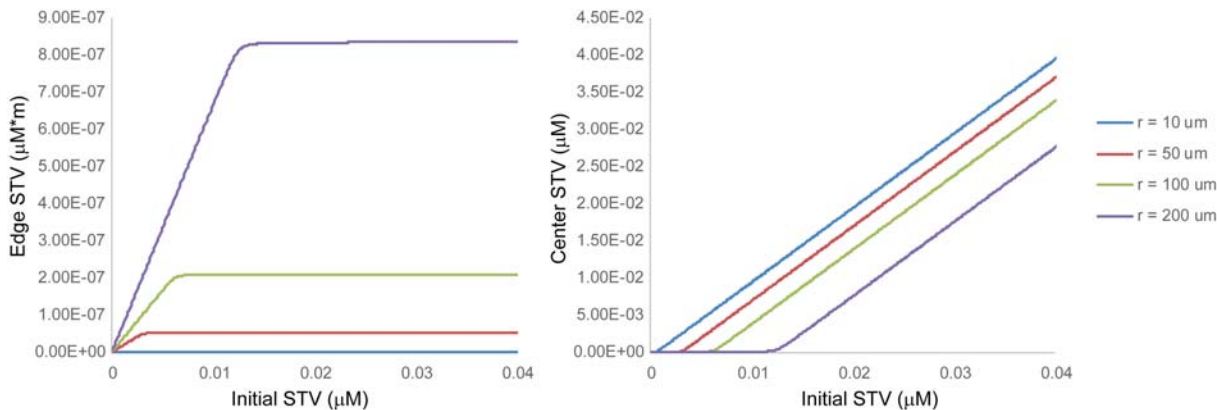


Figure 5.6: Streptavidin distribution within droplets simulation  
 The calculated streptavidin concentration on the surface (left) and in the solution (right) of droplets with radius of 10, 50, 100, and 200  $\mu\text{m}$ .

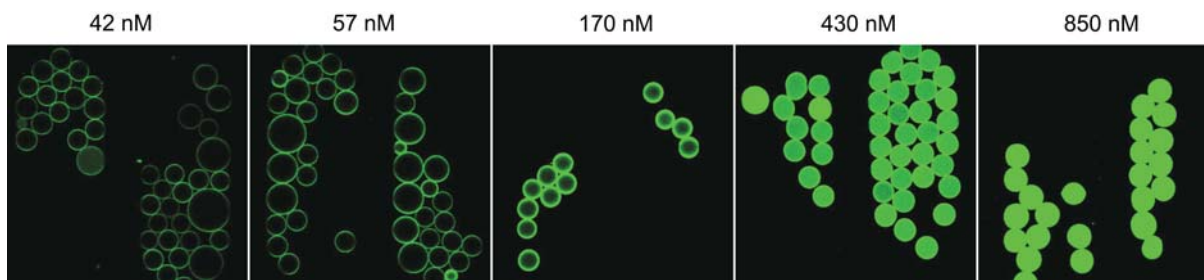


Figure 5.7: Fluorescent images of droplets with various concentration of STV-AF 488

prove useful in future droplet bioassay development exploiting Kry-Biotin.

### 5.3.4 Interfacial streptavidin/biotin interactions

Droplets containing various concentrations of STV-AF488 were imaged with a confocal microscope (Figure 5.7). The fluorescent intensity of the droplets' edges and the center were measured (Figure 5.8). As expected, the fluorescence intensity of the droplet edge increased first as STV-AF 488 concentration increased, while the intensity of the center increasing was lagged behind.

The deviation between the measured data and the simulation was induced by the imperfect scanning of confocal microscope. As shown in Figure 5.9, the fluorescence intensities are proportional to the total fluorophore molecules within the scan regions (shown in red).

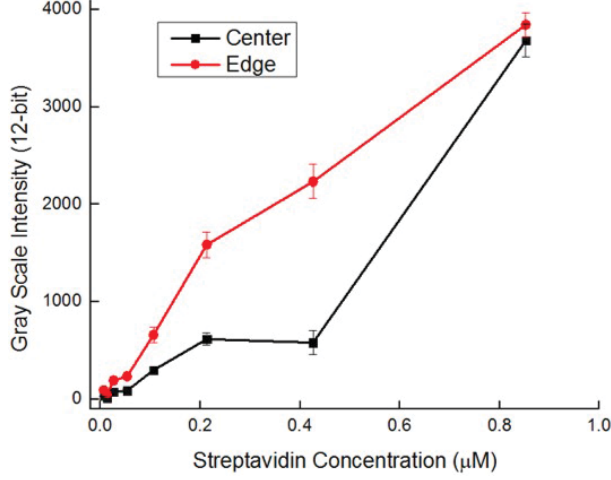


Figure 5.8: Fluorescent intensity of the droplet centers and edges

For the center, the fluorescence intensity can be simply represented by the following equation.

$$F_{center} \propto (h * p * c) \quad (5.12)$$

Where  $c$  is the concentration of the free STV in the center of a droplet after STV binding to the surface (Equation 5.11).

However, the fluorescence intensity on the edge is from both the molecules on the edge and that in the solution of the edge scan region.

$$F_{edge} \propto [\alpha * r * \Gamma_{SA} + (\frac{\alpha * r^2}{2} - \frac{h * \sqrt{r^2 - (\frac{d}{2})^2}}{2}) * c] \quad (5.13)$$

Where the angle of scanned sector of the edge,  $\alpha$  equals  $2 * \sin^{-1}(\frac{h}{2*r})$ , and the concentration of the biotin-STV complex on the surface of droplet,  $\Gamma_{SA}$ , is given in Equation 5.10. The contribution of the solution within the edge scan region  $((\frac{\alpha*r^2}{2} - \frac{h*\sqrt{r^2-(\frac{d}{2})^2}}{2}) * c)$  continuously increased even after the surface saturation point.

Moreover, the position of the z-plane that laser sliced the droplets was manually tuned for each image. This process would introduce a error to the edge intensity. As shown in Figure 5.53-5, the center intensities at different z-plane were similar, while the edge signal varied

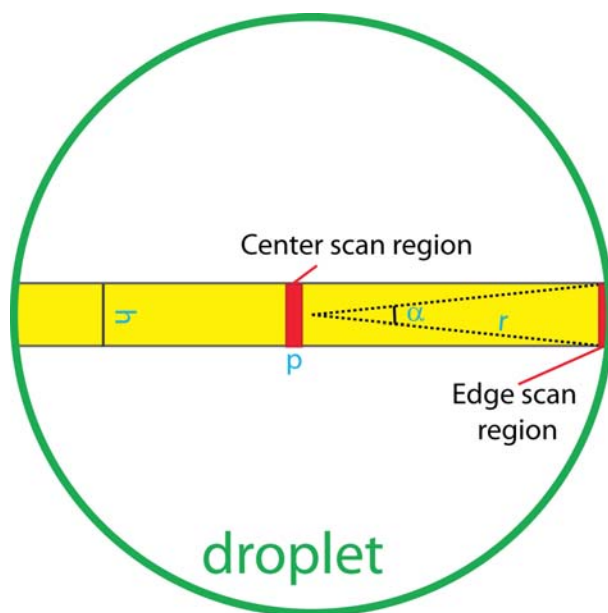


Figure 5.9: Simplified confocal microscope scanning model

The yellow region shows the scanned plate across the center of a droplet. The two red rectangular represent the scanned edge and center.  $h$ ,  $p$ ,  $r$ , and  $\alpha$  indicate the confocal z-scan thickness, pixel width, droplet radius, and the angle of scanned sector (z direction), respectively.

greatly. The different size of droplets also led to a scanning plane thorough droplets at various positions.

## 5.4 Conclusions

In summary, we designed a new biotinylated perfluorocarbon surfactant which was used for recruiting streptavidin proteins to the aqueous-oil interface. This proof-of-concept paves the way for development of interfacial binding based homogeneous bioassays.

The degradation of Kry-Biotin catalyzed by the leftover Krytox due to low yield reaction limited the shelf life of the Kry-Biotin and inconsistent experiment results. To overcome this hurdle, a simplified synthesis of perfluorocarbon labeled biotin could be achieved by a FluoroFlash tags technique (FLUOROUS Technologies, Ambridge, PA) often used in peptide, oligonucleotide, and carbohydrate synthesis[310]. Biotin-perfluorocarbon conjugate can be simply synthesized with commercially available perfluorocarbon reagents and purified by

fluorous solid phase extraction. Since the FluoroFlash tags are normally small molecules, to stabilize the droplet interface, Kry-Jeffa can be added for the purpose of the surfactant, while the FluoroFlash tagged biotin serves as the streptavidin recruiting reagents. Of course, recently commercialized biotin fluoro-surfactant such as FS-Biotin from RanBiotechnologies (Beverly, MA) can now also be used for this purpose.

According to our model, two factors, the radius and initial concentration of streptavidin, are the only adjustable factors controlling the distribution of streptavidin molecules (as show in equation 5.11 and 5.10). The error introduced by the inconsistent of droplet size due to T-junction droplet formation mechanism of the TwoOil devices can be minimized by adoption of flow-focusing or step emulsification mechanisms that allow more uniform droplet sizes.

In the droplet imaging process, to slice a thin layer of droplets, minimum pinhole size of the confocal microscope were used. Longer pixel dwell time were needed for to maintain the same sensitivity. Therefore, the motion of droplets while imaging would introduce errors. By confining droplets within trapping regions, more accurate images could be achieved.

## Chapter 6

### Conclusion and Future Directions

#### 6.1 Conclusions

This dissertation set out to develop automated microfluidic systems, along with compatible small volume biochemical assays, for studying the dynamics of metabolism, nutrient uptake, and hormone secretion in primary endocrine tissues. In this closing chapter, the major accomplishments and their impact are summarized, followed by a discussion of possible future experiments, that build upon the work.

##### 6.1.1 Automated microfluidic systems

Two automated microfluidic systems ( $\mu$ MUX [190] and PumpDrop) were developed to aid in the understanding of primary endocrine tissue dynamics. Both of the devices were fabricated with multilayer PDMS technology and were digitally controlled by in-house written LabVIEW applications. novel 3D-printed templates were designed to sculpt devices, creating millimeter scale reservoirs and confinement chambers to interface endocrine tissues to the channels. The 16 individually addressable channels of the  $\mu$ MUX device were used as either input or output channels for mimicking the circulation in the endocrine system. Dynamic insulin secretion profiles from islets and fatty acid uptake dynamics by adipose tissue were quantified in the  $\mu$ MUX device. The PumpDrop device integrated precise peristaltic pumping, a simple homogeneous assay, sensitive lock-in droplet detection, and a long incubation channel for information storage. This device was proven useful for high temporal resolution insulin secretion dynamics analysis from single islets. Both of these microfluidic systems should be transferable to the dynamic studies of other tissues or cells.

### 6.1.2 Bioassay development

A fluorescence assay for real-time monitoring of fatty acid uptake by cells or tissues was developed based on the interaction between fluorescent quencher labeled serum albumin (BSA-Q) and Bodipy labeled fatty acid analogues. The background fluorescence of the labeled fatty acid is quenched by BSA-Q in solution, and the fluorescent is restored when the molecules are taken up by cells. Compared to other similar assays, this BSA-Q assay has the advantages of higher quenching efficiency, multicolor quenching, non-toxic nature, low cost, and better stability. The fatty acid uptake of murine primary adipose tissues was monitored in real-time with the BSA-Q assay, and insulin induced promotion effects was observed. This assay should be applicable to any *in vitro* cell and tissue models for fatty acid uptake studies.

A protein recruiting surfactant was designed to study protein coating at aqueous-in-oil droplet interfaces. The biotin was covalently linked to a perfluorocarbon-surfactant. Upon droplet formation, the aqueous soluble biotin moieties, that assembled at the oil-water interface of emulsion droplets, was shown to recruit streptavidin molecules to the aqueous-oil interface. This proof-of-concept paves the way for the development of interface binding based homogeneous bioassays within droplets, which could further improve the discrimination between signal and background in immunoassays.

## 6.2 Future Directions

### 6.2.1 Automated endocrine tissue culture and on-chip detection system

The functions of the  $\mu$ MUX and PumpDrop devices are complementary. The  $\mu$ MUX device is designed as a mimic of the circulatory system for tissue or cell treatment and secretion sampling. The secretome quantification was done by off-chip assays (except imaging).

In contrast, the PumpDrop devices is able to quantify secreted protein on-chip, but different cell treatments were introduced by manual pipetting. The integration of both  $\mu$ MUX and PumpDrop modules onto a single device would allow us to interrogate endocrine tissues in a fully automated fashion with fine stimulant gradients and high temporal resolution on-chip biosensing. This type of integrated devices could help to significantly improve our understanding the dynamic actions of cells, tissues, and even the recently developed organ-on-a-chip platforms [93].

### 6.2.2 More sensitive droplet assays for dynamic tissue secretion study

The homogeneous immunoassay for insulin quantification on PumpDrop is a simple mix-and-read type of assay. However, this type of Förster resonance energy transfer readout lacks the ability of signal amplification. More sensitive homogeneous assay such as enzyme amplification based assay or AlphaLISA normally require mixing of two reagent with cell samples. The PumpDrop (Figure 4.1A) was designed with a Y-channel for mixing only one reagent (or premixed probes) with cell samples. Figure 6.1 depicts a potential design with tri-mixing channel for more flexible and sensitive assays. One direct application of this device could be the analysis of dynamic adipokine secretion (such as adiponectin and leptin) from adipocytes with AlphaLISA kits. Small molecules such as glycerol secreted from adipocytes could also be studied on this new device with enzyme based assays like glycerol fluorescence assay kits based on coupled enzyme cascades.

### 6.2.3 Improve the temporal resolution of droplet based analog assay

Compared with passively controlled droplet generators that allows up to  $kHz$  frequency droplet formation, PumpDrop only forms droplets at a frequency up to  $1 Hz$  because of the slow response of valve actuation. To improve the sampling rate and to achieve higher temporal resolution measurement, more sophisticated droplet manipulation (see Chapter 1

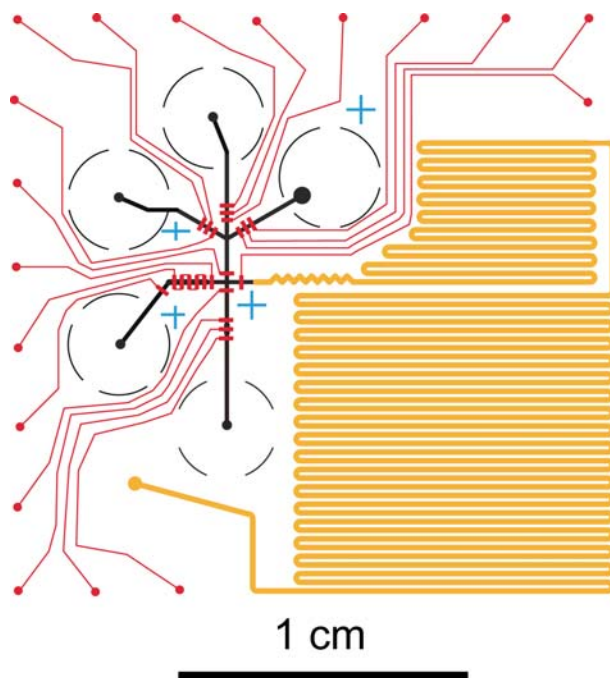


Figure 6.1: Microfluidic device design for more sensitive droplet assays

Section 1.2.4) such as droplet merging and pico-injection can be integrated to the PumpDrop device. This improvement would have the following advantages. Firstly, higher secretion sampling frequency can be achieved. Secondly, multiple reagents can be added into droplets stepwisely to meet various assay requirement. Of course, a challenge of implementing merging and pico-injection would be to ensure high precision in the reagent mixing process, as we demonstrated in Chapter 4.

#### 6.2.4 Better understanding of adipocytes fatty acid uptake

In serum, most of the fatty acid exists as triglycerides. The BSA-Q assays discribed in Chapter 3 was based on quencher labeled BSA and Bodipy-labeled free fatty acid, thus, we ignored the contribution of lipoprotein lipase on fatty acid uptake regulation. Instead of using fluorescently labeled fatty acids, fluorogenic triglyceride analog (such as STA-610 from Cell BioLabs Inc, San Diego, CA) could possibly be used for better mimicking the *in vivo* conditions.

### 6.2.5 Closing Remarks

*“He sendeth forth springs into the valleys;  
They run among the mountains;  
They give drink to every beast of the field;  
The wild asses quench their thirst.  
By them the birds of the heavens have their habitation;  
They sing among the branches.  
He watereth the mountains from his chambers;  
The earth is filled with the fruit of thy works.  
He causeth the grass to grow for the cattle,  
And herb for the service of man;  
That he may bring forth food out of the earth,  
And wine that maketh glad the heart of man,  
And oil to make his face to shine,  
And bread that strengtheneth mans heart.”*

*Psalm 104: 10–15*

Analytical chemistry provides tools and methods for determine the chemical composition of samples of matter, both qualitatively and quantitatively. It is of great value not only for fulfilling our curiosity to know this amazing world, but also for addressing major social issues, such as the increasing epidemics of obesity, diabetes and metabolic syndrome.

For the past few years, my work in Dr. Easleys laboratory focused on the development of miniaturized analytical instrumentation (automated microfluidic devices), and chemical assays for better understanding of dynamic of metabolism, nutrient uptake, and hormone secretion in primary endocrine tissues. A few small achievements towards the goal has been made:

1. Previously, we accomplished 5-min resolution measurement of insulin secretion from primary murine islets. The PumpDrop device accomplished 20-second resolution. Based on the

similar design concepts, future devices would improve the temporal resolution of secretion sampling measurements, and could be used for other single cells or tissues study.

2. Active controlled microfluidic devices with pneumatically actuated valves were first introduced to the Easley lab by this work. They are slowly replacing the previously used passively controlled devices. In the future, microfluidic devices with these active controls would improve fluidic manipulation and allow bioassays in a fully automated fashion.

3. The microfluidic study of real-time fatty acid uptake into adipose tissue was first achieved by using our custom made BSA-Q assay. The future applications of this assay would improve the modeling of the cell nutrient absorption.

4. This work also reported the first on-chip simulation of islets response to environment change, and insulin diffusion test. Without complexed computer simulation, the temporal resolutions of the microfluidic systems were directly measured by using pH-responsive fluorescent glass beads, and by fluorescent imaging of programmed fluid pumping of FITC-insulin solution.

Overall, these works represent a first step toward our laboratorys goal of developing integrated mouse-on-a-chip systems that can recapitulate dynamic endocrine function.

## Bibliography

- [1] Fact sheet. Diabetes, <http://www.who.int/mediacentre/factsheets/fs312/en/>, November 2016.
- [2] World Health Organization. Definition, diagnosis and classification of diabetes mellitus and its complications. Part 1: Diagnosis and classification of diabetes mellitus. Report Number: WHO/NMH/MND/13.2., 1999.
- [3] Geneva World Health Organization. Global report on diabetes. Technical report, 2016.
- [4] Anastasia Katsarou, Soffia Gudbjörnsdottir, Araz Rawshani, Dana Dabelea, Ezio Bonifacio, Barbara J Anderson, Laura M Jacobsen, Desmond A Schatz, and Åke Lernmark. Type 1 diabetes mellitus. Nat. Rev. Dis. Primers, 3:17016, mar 2017.
- [5] Charlotte Ridler. Diabetes: Islet transplantation for T1DM. Nat. Rev. Endocrinol., 12(7):373–373, may 2016.
- [6] Cristina Aguayo-Mazzucato and Susan Bonner-Weir. Stem cell therapy for type 1 diabetes mellitus. Nat. Rev. Endocrinol., 6(3):139–148, mar 2010.
- [7] Paolo Pozzilli, Ernesto Maddaloni, and Raffaella Buzzetti. Combination immunotherapies for type 1 diabetes mellitus. Nat. Rev. Endocrinol., 11(5):289–297, feb 2015.
- [8] Abdulfatai B. Olokoba, Olusegun A. Obateru, and Lateefat B. Olokoba. Type 2 diabetes mellitus: a review of current trends. Oman Med. J., 27(4):269–73, jul 2012.
- [9] Helena Edlund. Pancreatic organogenesis developmental mechanisms and implications for therapy. Nat. Rev. Genet., 3(7):524–532, jul 2002.
- [10] Kirk M Habegger, Kristy M Heppner, Nori Geary, Timothy J Bartness, Richard Dimarchi, and Matthias H Tschöp. The metabolic actions of glucagon revisited. Nat. Rev. Endocrinol., 6(12):689–697, 2010.
- [11] James R Sowers and Edward D Frohlich. Insulin and insulin resistance:. Med. Clin. North Am., 88(1):63–82, jan 2004.
- [12] Gisbert Weckbecker, Ian Lewis, Rainer Albert, Herbert A Schmid, Daniel Hoyer, and Christian Bruns. Opportunities in somatostatin research: biological, chemical and therapeutic aspects. Nat. Rev. Drug Discov., 2(12):999–1017, dec 2003.
- [13] J Lonovics, P Devitt, L C Watson, P L Rayford, and J C Thompson. Pancreatic polypeptide. A review. Arch. Surg., 116(10):1256–64, oct 1981.

- [14] Joseph P Tiano and Franck Mauvais-Jarvis. Importance of oestrogen receptors to preserve functional  $\beta$ -cell mass in diabetes. Nat. Rev. Endocrinol., 8(6):342–351, feb 2012.
- [15] Clara C Blad, Cong Tang, and Stefan Offermanns. G protein-coupled receptors for energy metabolites as new therapeutic targets. Nat. Rev. Drug Discov., 11(8):603–619, jul 2012.
- [16] George G. Holz IV, Willem M. Kiihtreiber, and Joel F. Habener. Pancreatic beta-cells are rendered glucose-competent by the insulinotropic hormone glucagon-like peptide-1(7-37). Nature, 361(6410):362–365, jan 1993.
- [17] Dara Leto and Alan R Saltiel. Regulation of glucose transport by insulin: traffic control of GLUT4. Nat. Rev. Mol. Cell Biol., 13(6):383–396, may 2012.
- [18] Fact sheet. Obesity and overweight, <http://www.who.int/mediacentre/factsheets/fs311/en/>, June 2016.
- [19] Steven E Kahn, Rebecca L Hull, and Kristina M Utzschneider. Mechanisms linking obesity to insulin resistance and type 2 diabetes. Nature, 444(7121):840–846, dec 2006.
- [20] S E Kahn, B Zinman, S M Haffner, M C O’Neill, B G Kravitz, D Yu, M I Freed, W H Herman, R R Holman, N P Jones, J M Lachin, and G C Viberti. Obesity is a major determinant of the association of c-reactive protein levels and the metabolic syndrome in type 2 diabetes. Diabetes, 55(8):2357–2364, 2006.
- [21] Kareem Hassan. Nonalcoholic fatty liver disease: A comprehensive review of a growing epidemic. World J. Gastroenterol., 20(34):12082, 2014.
- [22] T A Dar, I A Sheikh, S A Ganie, R Ali, L R Singh, S H Gan, M A Kamal, and M A Zargar. Molecular linkages between diabetes and Alzheimer’s disease: current scenario and future prospects. CNS Neurol. Disord. Drug Targets, 13(2):290–298, 2014.
- [23] R MacLaren, W Cui, and K Cianflone. Adipokines and the immune system: an adipocentric view. Adv Exp Med Biol, 632:1–21, 2008.
- [24] Rexford S Ahima. Connecting obesity, aging and diabetes. Nat. Med., 15(9):996–997, sep 2009.
- [25] Fact sheet. Obesity (body mass index  $\geq 30$ ), age-standardized (%) global estimates, <http://apps.who.int/gho/data/view.main.global2480a?lang=en>, January 2017.
- [26] Nicolas Musi and Rodolfo Guardado-Mendoza. Adipose Tissue as an Endocrine Organ. In Cellular Endocrinology in Health and Disease, volume 89, pages 229–237. Elsevier, 2014.
- [27] Ana G Cristancho and Mitchell A Lazar. Forming functional fat: a growing understanding of adipocyte differentiation. Nat. Rev. Mol. Cell Biol., 12(11):722–34, 2011.

- [28] Joseph M. Rutkowski, Jennifer H. Stern, and Philipp E. Scherer. The cell biology of fat expansion. *J. Cell Biol.*, 208(5):501–512, 2015.
- [29] Jan F.C. Glatz and Joost J.F.P. Luiken. From fat to FAT (CD36/SR-B2): Understanding the regulation of cellular fatty acid uptake. *Biochimie*, 136:21–26, 2017.
- [30] Yuguang Shi and Paul Burn. Lipid metabolic enzymes: emerging drug targets for the treatment of obesity. *Nat. Rev. Drug Discov.*, 3(8):695–710, aug 2004.
- [31] Noriyuki Ouchi, Jennifer L Parker, Jesse J Lugus, and Kenneth Walsh. Adipokines in inflammation and metabolic disease. *Nat. Rev. Immunol.*, 11(2):85–97, 2011.
- [32] Yiyang Zhang, Ricardo Proenca, Margherita Maffei, Marisa Barone, Lori Leopold, and Jeffrey M. Friedman. Positional cloning of the mouse obese gene and its human homologue. *Nature*, 372(6505):425–432, dec 1994.
- [33] C M Steppan, S T Bailey, S Bhat, E J Brown, R R Banerjee, C M Wright, H R Patel, R S Ahima, and M A Lazar. The hormone resistin links obesity to diabetes. *Nature*, 409(6818):307–312, 2001.
- [34] Loredana Quadro, William S. Blaner, Daniel J. Salchow, Silke Vogel, Roseann Piantedosi, Peter Gouras, Sarah Freeman, Maria P. Cosma, Vittorio Colantuoni, and Max E. Gottesman. Impaired retinal function and vitamin A availability in mice lacking retinol-binding protein. *EMBO Journal*, 18(17):4633–4644, 1999.
- [35] Q.-W. Yan, Qin Yang, Nimesh Mody, Timothy E Graham, Chung-hsin Hsu, Zhao Xu, Nicholas E Houstis, Barbara B Kahn, and Evan D Rosen. The Adipokine Lipocalin 2 Is Regulated by Obesity and Promotes Insulin Resistance. *Diabetes*, 56(10):2533–2540, oct 2007.
- [36] Mitsuhsa Tabata, Tsuyoshi Kadomatsu, Shigetomo Fukuhara, Keishi Miyata, Yasuhiro Ito, Motoyoshi Endo, Takashi Urano, Hui Juan Zhu, Hiroto Tsukano, Hirokazu Tazume, Koichi Kaikita, Kazuya Miyashita, Takao Iwawaki, Michio Shimabukuro, Kazuhiko Sakaguchi, Takaaki Ito, Naomi Nakagata, Tetsuya Yamada, Hideki Katagiri, Masato Kasuga, Yukio Ando, Hisao Ogawa, Naoki Mochizuki, Hiroshi Itoh, Toshio Suda, and Yuichi Oike. Angiopoietin-like Protein 2 Promotes Chronic Adipose Tissue Inflammation and Obesity-Related Systemic Insulin Resistance. *Cell Metab.*, 10(3):178–188, 2009.
- [37] G S Hotamisligil, N S Shargill, and B M Spiegelman. Adipose expression of tumor necrosis factor- $\alpha$ : direct role in obesity-linked insulin resistance. *Science*, 259(5091):87–91, jan 1993.
- [38] Susan K Fried, Dove A Bunkin, and Andrew S Greenberg. Omental and Subcutaneous Adipose Tissues of Obese Subjects Release Interleukin-6 : Depot Difference and Regulation by Glucocorticoid. 83(3):30–33, 2016.

- [39] I. Stuart Wood, Bohan Wang, John R. Jenkins, and Paul Trayhurn. The pro-inflammatory cytokine IL-18 is expressed in human adipose tissue and strongly up-regulated by TNF-alpha in human adipocytes. Biochem. Biophys. Res. Commun., 337(2):422–429, 2005.
- [40] Hajime Kanda, Sanshiro Tateya, Yoshikazu Tamori, Ko Kotani, Ken-ichi Hiasa, Riko Kitazawa, Sohei Kitazawa, Hitoshi Miyachi, Sakan Maeda, Kensuke Egashira, and Masato Kasuga. MCP-1 contributes to macrophage infiltration into adipose tissue, insulin resistance, and hepatic steatosis in obesity. J. Clin. Invest., 116(6):1494–1505, jun 2006.
- [41] Carine Chavey, Gwendal Lazennec, Sylviane Lagarrigue, Cyrielle Clapé, Irena Iankova, Jacques Teyssier, Jean Sébastien Annicotte, Julien Schmidt, Chikage Matak, Hiroyasu Yamamoto, Rosario Sanches, Anna Guma, Vladimir Stich, Michaela Vitkova, Bénédicte Jardin-Watelet, Eric Renard, Robert Strieter, Antoinette Tuthill, Gökhan S. Hotamisligil, Antonio Vidal-Puig, Antonio Zorzano, Dominique Langin, and Lluís Fajas. CXC Ligand 5 Is an Adipose-Tissue Derived Factor that Links Obesity to Insulin Resistance. Cell Metab., 9(4):339–349, 2009.
- [42] Javier R. Revollo, Antje Körner, Kathryn F. Mills, Akiko Satoh, Tao Wang, Antje Garten, Biplab Dasgupta, Yo Sasaki, Cynthia Wolberger, R. Reid Townsend, Jeffrey Milbrandt, Wieland Kiess, and Shin ichiro Imai. Nampt/PBEF/Visfatin Regulates Insulin Secretion in beta Cells as a Systemic NAD Biosynthetic Enzyme. Cell Metab., 6(5):363–375, 2007.
- [43] Philipp E Scherer, Suzanne Williams, Michael Fogliano, Giulia Baldini, and Harvey F Lodish. A Novel Serum Protein Similar to C1q, Produced Exclusively in Adipocytes. J. Biol. Chem., 270(45):26746–26749, nov 1995.
- [44] N. Ouchi, A. Higuchi, K. Ohashi, Y. Oshima, N. Gokce, R. Shibata, Y. Akasaki, A. Shimono, and K. Walsh. Sfrp5 Is an Anti-Inflammatory Adipokine That Modulates Metabolic Dysfunction in Obesity. Science, 329(5990):454–457, jul 2010.
- [45] Chase Romere, Clemens Duerschmid, Juan Bournat, Petra Constable, Mahim Jain, Fan Xia, Pradip K K. Saha, Maria Del Solar, Bokai Zhu, Brian York, Poonam Sarkar, David A A. Rendon, M. Waleed Waleed Gaber, Scott A A. LeMaire, Joseph S S. Coselli, Dianna M M. Milewicz, V. Reid Reid Sutton, Nancy F F. Butte, David D D. Moore, Atul R R. Chopra, Maria Del Solar, Bokai Zhu, Brian York, Poonam Sarkar, David A A. Rendon, M. Waleed Waleed Gaber, Scott A A. LeMaire, Joseph S S. Coselli, Dianna M M. Milewicz, V. Reid Reid Sutton, Nancy F F. Butte, David D D. Moore, and Atul R R. Chopra. Asprosin, a Fasting-Induced Glucogenic Protein Hormone. Cell, 165(3):566–579, 2016.
- [46] Andrew J. Whittle, Stefania Carobbio, Luís Martins, Marc Slawik, Elayne Hondares, María Jesús Vázquez, Donald Morgan, Robert I. Csikasz, Rosalía Gallego, Sergio Rodríguez-Cuenca, Martin Dale, Samuel Virtue, Francesc Villarroya, Barbara Cannon, Kamal Rahmouni, Miguel López, and Antonio Vidal-Puig. BMP8B increases

- brown adipose tissue thermogenesis through both central and peripheral actions. Cell, 149(4):871–885, 2012.
- [47] Katarina Klepac, Ana Kilić, Thorsten Gnad, Loren M Brown, Beate Herrmann, Andrea Wilderman, Aileen Balkow, Anja Glöde, Katharina Simon, Martin E Lidell, Matthias J Betz, Sven Enerbäck, Jürgen Wess, Marc Freichel, Matthias Blüher, Gabi König, Evi Kostenis, Paul A Insel, and Alexander Pfeifer. The Gq signalling pathway inhibits brown and beige adipose tissue. Nat. Commun., 7:10895, 2016.
- [48] Ffolliott M. Fisher, Sandra Kleiner, Nicholas Douris, Elliott C Fox, Rina J Mepani, Francisco Verdeguer, Jun Wu, Alexei Kharitonov, Jeffrey S Flier, Eleftheria Maratos-Flier, and Bruce M Spiegelman. FGF21 regulates PGC-1 $\alpha$  and browning of white adipose tissues in adaptive thermogenesis. Genes. Dev., 26(3):271–81, feb 2012.
- [49] Sam Virtue, Helena Feldmann, Mark Christian, Chong Yew Tan, Mojgan Masoodi, Martin Dale, Chris Lelliott, Keith Burling, Mark Campbell, Naomi Eguchi, Peter Voshol, Jaswinder K. Sethi, Malcolm Parker, Yoshihiro Urade, Julian L. Griffin, Barbara Cannon, and Antonio Vidal-Puig. A New Role for Lipocalin Prostaglandin D Synthase in the Regulation of Brown Adipose Tissue Substrate Utilization. Diabetes, 61(12):3139–3147, dec 2012.
- [50] Andrew J. Whittle, Meizi Jiang, Vivian Peirce, Joana Relat, Sam Virtue, Hiroyuki Ebinuma, Isamu Fukamachi, Takashi Yamaguchi, Mao Takahashi, Takeyoshi Murano, Ichiro Tatsuno, Masahiro Takeuchi, Chiaki Nakaseko, Wenlong Jin, Zhehu Jin, Mark Campbell, Wolfgang J. Schneider, Antonio Vidal-Puig, and Hideaki Bujo. Soluble LR11/SorLA represses thermogenesis in adipose tissue and correlates with BMI in humans. Nat. Commun., 6(May):8951, nov 2015.
- [51] Myriam Né Chad, Ethem Ruka, and Jean Thibault. Production of nerve growth factor by brown fat in culture: relation with the in vivo developmental stage of the tissue. Comp. Biochem. Phys. A, 107(2):381–388, feb 1994.
- [52] Rajesh R. Rao, Jonathan Z. Long, James P. White, Katrin J. Svensson, Jesse Lou, Isha Lokurkar, Mark P. Jedrychowski, Jorge L. Ruas, Christiane D. Wrann, James C. Lo, Donny M. Camera, Jenn Lachey, Steven Gygi, Jasbir Sehra, John A. Hawley, and Bruce M. Spiegelman. Meteorin-like Is a Hormone that Regulates Immune-Adipose Interactions to Increase Beige Fat Thermogenesis. Cell, 157(6):1279–1291, jun 2014.
- [53] Atsushi Asano, Kazuhiro Kimura, and Masayuki Saito. Cold-Induced mRNA Expression of Angiogenic Factors in Rat Brown Adipose Tissue. J. Vet. Med. Sci., 61(4):403–409, apr 1999.
- [54] Sima Rahman, Yalin Lu, Piotr J. Czernik, Clifford J. Rosen, Sven Enerback, and Beata Lecka-Czernik. Inducible brown adipose tissue, or beige fat, is anabolic for the skeleton. Endocrinology, 154(8):2687–2701, 2013.

- [55] Marta Giralt, Aleix Gavaldà-Navarro, and Francesc Villarroya. Fibroblast growth factor-21, energy balance and obesity. Mol. Cell. Endocrinol., 418:66–73, 2015.
- [56] David a Sarruf, Joshua P Thaler, Gregory J Morton, Jonathan German, Jonathan D Fischer, Kayoko Ogimoto, and Michael W Schwartz. Fibroblast Growth Factor 21 Action in the Brain Increases Energy Expenditure and Insulin Sensitivity in Obese Rats. Diabetes, 59(July):1817–1824, 2010.
- [57] Guo-Xiao Wang, Xu-Yun Zhao, Zhuo-Xian Meng, Matthias Kern, Arne Dietrich, Zhimin Chen, Zoharit Cozacov, Dequan Zhou, Adewole L Okunade, Xiong Su, Siming Li, Matthias Blüher, and Jiandie D Lin. The brown fat-enriched secreted factor Nrg4 preserves metabolic homeostasis through attenuation of hepatic lipogenesis. Nat. Med., 20(12):1436–1443, nov 2014.
- [58] Subhadra C. Gunawardana and David W. Piston. Reversal of type 1 diabetes in mice by brown adipose tissue transplant. Diabetes, 61(3):674–682, 2012.
- [59] Gerald M Reaven. Role of insulin resistance in human disease. Diabetes, 37(12):1595–1607, 1988.
- [60] Adilson Guilherme, Joseph V. Virbasius, Vishwajeet Puri, and Michael P. Czech. Adipocyte dysfunctions linking obesity to insulin resistance and type 2 diabetes. Nat. Rev. Mol. Cell Biol., 9(5):367–377, 2010.
- [61] Steven E. Kahn. The Importance of  $\beta$ -Cell Failure in the Development and Progression of Type 2 Diabetes. J. Clin. Endocrinol. Metab., 86(9):4047–4058, sep 2001.
- [62] George M Whitesides. The origins and the future of microfluidics. Nature, 442(7101):368–373, jul 2006.
- [63] David J. You, Tu San Park, and Jeong-Yeol Yoon. Cell-phone-based measurement of TSH using Mie scatter optimized lateral flow assays. Biosens. Bioelectron., 40(1):180–185, feb 2013.
- [64] Sebastian J. Maerkl and Stephen R. Quake. A systems approach to measuring the binding energy landscapes of transcription factors. Science, 315(5809):233–237, 2007.
- [65] Jiwoon Park, Vijaya Sunkara, Tae-Hyeong Kim, Hyundoo Hwang, and Yoon-Kyoung Cho. Lab-on-a-Disc for Fully Integrated Multiplex Immunoassays. Anal. Chem., 84(5):2133–2140, mar 2012.
- [66] Leah A Godwin, Meagan E Pilkerton, Kennon S Deal, Desiree Wanders, L Robert, Christopher J Easley, Robert L Judd, and Christopher J Easley. Passively operated microfluidic device for stimulation and secretion sampling of single pancreatic islets. Anal. Chem., 83(18):7166–7172, sep 2011.
- [67] Andres W. Martinez, Scott T. Phillips, George M. Whitesides, and Emanuel Carrilho. Diagnostics for the Developing World: Microfluidic Paper-Based Analytical Devices. Anal. Chem., 82(1):3–10, jan 2010.

- [68] Krisna C Bhargava, Bryant Thompson, and Noah Malmstadt. Discrete elements for 3D microfluidics. Proc. Natl. Acad. Sci. U S A, 111(42):15013–15018, oct 2014.
- [69] Laurence R Brewer and Piero R Bianco. Laminar flow cells for single-molecule studies of DNA-protein interactions. Nat. Methods, 5(6):517–525, jun 2008.
- [70] Kwangmin Son, Douglas R Brumley, and Roman Stocker. Live from under the lens: exploring microbial motility with dynamic imaging and microfluidics. Nat. Rev. Microbiol., 13(12):761–775, dec 2015.
- [71] Meera. Swami. Technology: Dropping in on single-cell epigenetic profiles. Nat. Rev. Genet., 16(12):684–685, 2015.
- [72] Felix J H Hol and Cees. Dekker. Zooming in to see the bigger picture: Microfluidic and nanofabrication tools to study bacteria. Science, 346(6208):1251821–1251821, oct 2014.
- [73] Robert C R Wootton and Andrew J. DeMello. Microfluidics: Analog-to-digital drug screening. Nature, 483(7387):43–44, feb 2012.
- [74] Monya. Baker. Clever PCR: more genotyping, smaller volumes. Nat. Methods, 7(5):351–356, may 2010.
- [75] Nathan. Blow. Microfluidics: the great divide. Nat. Methods, 6(9):683–686, sep 2009.
- [76] Peter K Sorger. Microfluidics closes in on point-of-care assays. Nat. Biotechnol., 26(12):1345–1346, 2008.
- [77] C Monat, P Domachuk, and B J Eggleton. Integrated optofluidics: A new river of light. Nat. Photon., 1(2):106–114, feb 2007.
- [78] David L Allara. A perspective on surfaces and interfaces. Nature, 437(7059):638–639, sep 2005.
- [79] Mathieu Joanicot. APPLIED PHYSICS: Droplet Control for Microfluidics. Science, 309(5736):887–888, aug 2005.
- [80] Sanjay M Prakadan, Alex K Shalek, and David A Weitz. Scaling by shrinking: empowering single-cell ‘omics’ with microfluidic devices. Nat. Rev. Genet., apr 2017.
- [81] Michael Davenport, Kathleen E Mach, Linda M Dairiki Shortliffe, Niaz Banaei, Tza-Huei Wang, and Joseph C Liao. New and developing diagnostic technologies for urinary tract infections. Nat. Rev. Urol., mar 2017.
- [82] R Zenobi. Single-Cell Metabolomics: Analytical and Biological Perspectives. Science, 342(6163):1243259–1243259, dec 2013.
- [83] Aimee K Wessel, Laura Hmelo, Matthew R Parsek, and Marvin Whiteley. Going local: technologies for exploring bacterial microenvironments. Nat. Rev. Microbiol., 11(5):337–348, apr 2013.

- [84] Xiao Xu and Stuart K Kim. The early bird catches the worm: new technologies for the *Caenorhabditis elegans* toolkit. Nat. Rev. Genet., 12(11):793–801, oct 2011.
- [85] David G Spiller, Christopher D Wood, David A Rand, and Michael R H White. Measurement of single-cell dynamics. Nature, 465(7299):736–745, jun 2010.
- [86] Paul Yager, Thayne Edwards, Elain Fu, Kristen Helton, Kjell Nelson, Milton R Tam, and Bernhard H Weigl. Microfluidic diagnostic technologies for global public health. Nature, 442(7101):412–418, jul 2006.
- [87] Andrew J. DeMello. Control and detection of chemical reactions in microfluidic systems. Nature, 442(7101):394–402, jul 2006.
- [88] Petra S Dittrich and Andreas. Manz. Lab-on-a-chip: microfluidics in drug discovery. Nat. Rev. Drug Discov., 5(3):210–218, 2006.
- [89] Javier Atencia and David J Beebe. Controlled microfluidic interfaces. Nature, 437(7059):648–655, sep 2005.
- [90] Pavel Neuzi, Stefan Giselbrecht, Kerstin Länge, Tony Jun Huang, and Andreas. Manz. Revisiting lab-on-a-chip technology for drug discovery. Nat. Rev. Drug Discov., 11(8):620–632, aug 2012.
- [91] Eric K Sackmann, Anna L Fulton, and David J Beebe. The present and future role of microfluidics in biomedical research. Nature, 507(7491):181–189, 2014.
- [92] Demetri Psaltis, Stephen R Quake, and Changhui Yang. Developing optofluidic technology through the fusion of microfluidics and optics. Nature, 442(7101):381–386, 2006.
- [93] Sangeeta N Bhatia and Donald E Ingber. Microfluidic organs-on-chips. Nat. Biotechnol., 32(8):760–72, aug 2014.
- [94] Douglas B. Weibel, Willow R. DiLuzio, and George M. Whitesides. Microfabrication meets microbiology. Nature Rev. Microbiol., 5(3):209–218, mar 2007.
- [95] Alex Groisman, Markus Enzelberger, and Stephen R Quake. Microfluidic memory and control devices. Science, 300(5621):955–958, 2003.
- [96] A D Stroock, S K W Dertinger, A Ajdari, I Mezic, H A Stone, and G M Whitesides. Chaotic mixer for microchannels. Science, 295(5555):647–651, 2002.
- [97] Todd Thorsen, Sebastian J Maerkl, and Stephen R Quake. Microfluidic Large-Scale Integration. Science, 298(5593):580, oct 2002.
- [98] S R Quake and A Scherer. From micro- to nanofabrication with soft materials. Science, 290(5496):1536–1540, 2000.

- [99] M. A. Unger, H P Chou, T Thorsen, A Scherer, and S R Quake. Monolithic Microfabricated Valves and Pumps by Multilayer Soft Lithography. Science, 288(5463):113–116, 2000.
- [100] Todd A Duncombe, Augusto M Tentori, and Amy E Herr. Microfluidics: reframing biological enquiry. Nat. Rev. Mol. Cell. Biol., 16(9):554–567, sep 2015.
- [101] Charles Gawad, Winston Koh, and Stephen R Quake. Single-cell genome sequencing: current state of the science. Nat. Rev. Genet., 17(3):175–188, 2016.
- [102] Vladimir Gubala, Leanne F. Harris, Antonio J. Ricco, Ming X. Tan, and David E. Williams. Point of Care Diagnostics: Status and Future. Anal. Chem., 84(2):487–515, jan 2012.
- [103] Hannah Kettler, Karen White, and Sarah Hawkes. Mapping the landscape of diagnostics for sexually transmitted infections: Key findings and recommendations. UNICEF/UNDP/World Bank/WHO, pages 1–44, 2004.
- [104] Steven J. Altschuler and Lani F. Wu. Cellular heterogeneity: do differences make a difference? Cell, 141(4):559–63, may 2010.
- [105] Karen E Gascoigne and Stephen S Taylor. Cancer Cells Display Profound Intra- and Interline Variation following Prolonged Exposure to Antimitotic Drugs. Cancer Cell, 14(2):111–122, aug 2008.
- [106] A. A. Cohen, N Geva-Zatorsky, E Eden, M Frenkel-Morgenstern, I Issaeva, A Sigal, R Milo, C Cohen-Saidon, Y Liron, Z Kam, L Cohen, T Danon, N Perzov, and U Alon. Dynamic Proteomics of Individual Cancer Cells in Response to a Drug. Science, 322(5907):1511–1516, dec 2008.
- [107] Yao Lu, Qiong Xue, Markus R. Eisele, Endah S. Sulistijo, Kara Brower, Lin Han, El-ad David Amir, Dana Pe’er, Kathryn Miller-Jensen, and Rong Fan. Highly multiplexed profiling of single-cell effector functions reveals deep functional heterogeneity in response to pathogenic ligands. Proc. Natl. Acad. Sci. U S A, 112(7):E607–E615, feb 2015.
- [108] Nancy Bannach. Characterizing the Flow and Choosing the Right Interface, <https://www.comsol.com/blogs/characterizing-flow-choosing-right-interface/>. 2014.
- [109] Hiroshi Kimura, Takatoki Yamamoto, Hitomi Sakai, Yasuyuki Sakai, and Teruo Fujii. An integrated microfluidic system for long-term perfusion culture and on-line monitoring of intestinal tissue models. Lab Chip, 8(5):741, 2008.
- [110] Dongeun Huh, Benjamin D Matthews, Akiko Mammoto, Martín Montoya-Zavala, Hong Yuan Hsin, and Donald E Ingber. Reconstituting Organ-Level Lung Functions on a Chip. Science, 328(5986):1662–1668, jun 2010.

- [111] Michelle Tsai, Ashley Kita, Joseph Leach, Ross Rounsevell, James N. Huang, Joel Moake, Russell E. Ware, Daniel A. Fletcher, and Wilbur A. Lam. In vitro modeling of the microvascular occlusion and thrombosis that occur in hematologic diseases using microfluidic technology. J. Clin. Invest., 122(1):408–418, jan 2012.
- [112] Colin L. Walsh, Brett M. Babin, Rachel W. Kasinskas, Jean A. Foster, Marissa J. McGarry, and Neil S. Forbes. A multipurpose microfluidic device designed to mimic microenvironment gradients and develop targeted cancer therapeutics. Lab Chip, 9(4):545–554, 2009.
- [113] Ross Booth and Hanseup Kim. Characterization of a microfluidic in vitro model of the blood-brain barrier ( $\mu$ BBB). Lab Chip, 12(10):1784, 2012.
- [114] Kerry Wilson, Mainak Das, Kathryn J. Wahl, Richard J. Colton, and James Hickman. Measurement of Contractile Stress Generated by Cultured Rat Muscle on Silicon Cantilevers for Toxin Detection and Muscle Performance Enhancement. PLoS One, 5(6):e11042, jun 2010.
- [115] Kyung-Jin Jang and Kahp-Yang Suh. A multi-layer microfluidic device for efficient culture and analysis of renal tubular cells. Lab Chip, 10(1):36–42, 2010.
- [116] Hue P Le. Progress and trends in ink-jet printing technology. J. Imaging Sci. Technol., 42(1):49–62, 1998.
- [117] S.C. Terry, J.H. Jerman, and J.B. Angell. A gas chromatographic air analyzer fabricated on a silicon wafer. IEEE Trans. Electron Dev., 26(12):1880–1886, dec 1979.
- [118] Andreas Manz, N Graber, and H.M. Widmer. Miniaturized total chemical analysis systems: A novel concept for chemical sensing. Sens. Actuators B Chem., 1(1-6):244–248, jan 1990.
- [119] E Delamarche, A Bernard, H Schmid, B Michel, and H Biebuyck. Patterned delivery of immunoglobulins to surfaces using microfluidic networks. Science, 276(5313):779–81, may 1997.
- [120] George C. Lisensky, Dean J. Campbell, Katie J. Beckman, Camilo E. Calderon, Patrick W. Doolan, Rebecca M. Ottosen, and Arthur B. Ellis. Replication and Compression of Surface Structures with Polydimethylsiloxane Elastomer. J. Chem. Educ., 76(4):537, 1999.
- [121] Jinwen Zhou, Amanda Vera Ellis, and Nicolas Hans Voelcker. Recent developments in PDMS surface modification for microfluidic devices. Electrophoresis, 31(1):2–16, jan 2010.
- [122] Keil J. Regehr, Maribella Domenech, Justin T. Koepsel, Kristopher C. Carver, Stephanie J. Ellison-Zelski, William L. Murphy, Linda A. Schuler, Elaine T. Alarid, and David J. Beebe. Biological implications of polydimethylsiloxane-based microfluidic cell culture. Lab Chip, 9(15):2132, 2009.

- [123] Michael W. Toepke and David J. Beebe. PDMS absorption of small molecules and consequences in microfluidic applications. Lab Chip, 6(12):1484, 2006.
- [124] Jason P. Rolland, Erik C Hagberg, Ginger M Denison, Kenneth R Carter, and Joseph M De Simone. High-resolution soft lithography: enabling materials for nanotechnologies. Angew. Chem. Int. Ed., 43(43):5796–9, nov 2004.
- [125] Cheng-Chung Lee, Thomas M Snyder, and Stephen R Quake. A microfluidic oligonucleotide synthesizer. Nucleic Acids Res., 38(8):2514–2521, may 2010.
- [126] J W Hong and S R Quake. Integrated nanoliter systems. Nat. Biotechnol., 21(10):1179–1183, 2003.
- [127] Jessica Melin and Stephen R. Quake. Microfluidic large-scale integration: The evolution of design rules for biological automation. In Annu. Rev. Biophys. Biomol. Struct., volume 36, pages 213–231. 2007.
- [128] Zhishan Hua, Yongmei Xia, Onnop Srivannavit, Jean-Marie Rouillard, Xiaochuan Zhou, Xiaolian Gao, and Erdogan Gulari. A versatile microreactor platform featuring a chemical-resistant microvalve array for addressable multiplex syntheses and assays. J. Micromech. Microeng., 16(8):1433–1443, aug 2006.
- [129] J W Hong, V Studer, G Hang, W F Anderson, and S R Quake. A nanoliter-scale nucleic acid processor with parallel architecture. Nat. Biotechnol., 22(4):435–439, 2004.
- [130] Ryan A Kellogg, Rafael Gómez-Sjöberg, Anne A Leyrat, and Sava Tay. High-throughput microfluidic single-cell analysis pipeline for studies of signaling dynamics. Nat. Protoc., 9(7):1713–1726, jun 2014.
- [131] Spyros Darmanis, Steven A Sloan, Ye Zhang, Martin Enge, Christine Caneda, Lawrence M Shuer, Melanie G Hayden Gephart, Ben A Barres, and Stephen R Quake. A survey of human brain transcriptome diversity at the single cell level. Proc. Natl. Acad. Sci. U S A, 112(23):7285–7290, 2015.
- [132] Charles F. A. de Bourcy, Cesar J. Lopez Angel, Christopher Vollmers, Cornelia L. Dekker, Mark M. Davis, and Stephen R. Quake. Phylogenetic analysis of the human antibody repertoire reveals quantitative signatures of immune senescence and aging. Proc. Natl. Acad. Sci. U S A, 114(5):1105–1110, jan 2017.
- [133] Ozgun Gokce, Geoffrey M. Stanley, Barbara Treutlein, Norma F. Neff, J. Gray Camp, Robert C. Malenka, Patrick E. Rothwell, Marc V. Fuccillo, Thomas C. Südhof, and Stephen R. Quake. Cellular Taxonomy of the Mouse Striatum as Revealed by Single-Cell RNA-Seq. Cell Rep., 16(4):1126–1137, jul 2016.
- [134] Barbara Treutlein, Qian Yi Lee, J. Gray Camp, Moritz Mall, Winston Koh, Seyed Ali Mohammad Shariati, Sopheak Sim, Norma F. Neff, Jan M. Skotheim, Marius Wernig, and Stephen R. Quake. Dissecting direct reprogramming from fibroblast to neuron using single-cell RNA-seq. Nature, 534(7607):391–395, jun 2016.

- [135] Wenying Pan, Wei Gu, Seema Nagpal, Melanie Hayden Gephart, and Stephen R Quake. Brain Tumor Mutations Detected in Cerebral Spinal Fluid. Clin. Chem., 61(3):514–522, 2015.
- [136] Iwijn De Vlaminck, Hannah A Valantine, Thomas M Snyder, Calvin Strehl, Garrett Cohen, Helen Luikart, Norma F Neff, Jennifer Okamoto, Daniel Bernstein, Dana Weisshaar, Stephen R Quake, and Kiran K Khush. Circulating Cell-Free DNA Enables Noninvasive Diagnosis of Heart Transplant Rejection. Sci. Transl. Med., 6(241), 2014.
- [137] Joshua A Weinstein, Xun Zeng, Yueh-Hsiu Chien, and Stephen R Quake. Correlation of Gene Expression and Genome Mutation in Single B-Cells. PLoS One, 8(6), 2013.
- [138] Matthias Meier, Rene V Sit, and Stephen R Quake. Proteome-wide protein interaction measurements of bacterial proteins of unknown function. Proc. Natl. Acad. Sci. U S A, 110(2):477–482, 2013.
- [139] Polly M Fordyce, Doron Gerber, Danh Tran, Jiashun Zheng, Hao Li, Joseph L DeRisi, and Stephen R Quake. De novo identification and biophysical characterization of transcription-factor binding sites with microfluidic affinity analysis. Nat. Biotechnol., 28(9):970–976, 2010.
- [140] Sava Tay, Jacob J Hughey, Timothy K Lee, Tomasz Lipniacki, Stephen R Quake, and Markus W Covert. Single-cell NF- $\kappa$ B dynamics reveal digital activation and analogue information processing. Nature, 466(7303):267–271, jul 2010.
- [141] H Christina Fan, Yair J Blumenfeld, Usha Chitkara, Louanne Hudgins, and Stephen R Quake. Noninvasive diagnosis of fetal aneuploidy by shotgun sequencing DNA from maternal blood. Proc. Natl. Acad. Sci. U S A, 105(42):16266–16271, 2008.
- [142] Megan J Anderson, Carl L Hansen, and Stephen R Quake. Phase knowledge enables rational screens for protein crystallization. Proc. Natl. Acad. Sci. U S A, 103(45):16746–16751, 2006.
- [143] C C Lee, G D Sui, A Elizarov, C Y J Shu, Y S Shin, A N Dooley, J Huang, A Daridon, P Wyatt, D Stout, H C Kolb, O N Witte, N Satyamurthy, J R Heath, M E Phelps, S R Quake, and H R Tseng. Multistep synthesis of a radiolabeled imaging probe using integrated microfluidics. Science, 310(5755):1793–1796, 2005.
- [144] Todd Thorsen, Richard W. Roberts, Frances H. Arnold, and Stephen R. Quake. Dynamic pattern formation in a vesicle-generating microfluidic device. Phys. Rev. Lett., 86(18):4163–4166, 2001.
- [145] Shelley L. Anna, Nathalie Bontoux, and Howard A. Stone. Formation of dispersions using flow focusing in microchannels. Appl. Phys. Lett., 82(3):364–366, jan 2003.
- [146] Nitesh Mittal, Céline Cohen, Jérôme Bibette, and Nicolas Bremond. Dynamics of step-emulsification: From a single to a collection of emulsion droplet generators. Phys. Fluids, 26(8):082109, aug 2014.

- [147] Carsten Cramer, Peter Fischer, and Erich J. Windhab. Drop formation in a co-flowing ambient fluid. Chem. Eng. Sci., 59(15):3045–3058, aug 2004.
- [148] Shuwen Sun, Thomas R. Slaney, and Robert T. Kennedy. Label Free Screening of Enzyme Inhibitors at Femtomole Scale Using Segmented Flow Electrospray Ionization Mass Spectrometry. Anal. Chem., 84(13):5794–5800, jul 2012.
- [149] a S Utada, L.-Y. Chu, A. Fernandez-Nieves, D R Link, C Holtze, and D a Weitz. Dripping, Jetting, Drops, and Wetting: The Magic of Microfluidics. MRS Bulletin, 32(09):702–708, sep 2007.
- [150] C Holtze, A C Rowat, J J Agresti, J B Hutchison, F E Angile, C H J Schmitz, S Koster, H Duan, K J Humphry, R A Scanga, J S Johnson, D Pisignano, D A Weitz, F E Angilè, C H J Schmitz, S Köster, H Duan, K J Humphry, R A Scanga, J S Johnson, D Pisignano, and D A Weitz. Biocompatible surfactants for water-in-fluorocarbon emulsions. Lab Chip, 8(10):1632–1639, 2008.
- [151] Ya-Ling Chiu, Hon Fai Chan, Kyle K L Phua, Ying Zhang, Sissel Juul, Birgitta R. Knudsen, Yi-Ping Ho, and Kam W. Leong. Synthesis of fluorosurfactants for emulsion-based biological applications. ACS nano, 8(4):3913–20, apr 2014.
- [152] Cheryl J. Dejournette, Joonyul Kim, Haley Medlen, Xiangpeng Li, Luke J. Vincent, and Christopher J. Easley. Creating biocompatible oil-water interfaces without synthesis: Direct interactions between primary amines and carboxylated perfluorocarbon surfactants. Anal. Chem., 85(21):10556–10564, 2013.
- [153] David J. Sukovich, Shea T. Lance, and Adam R. Abate. Sequence specific sorting of DNA molecules with FACS using 3dPCR. Sci. Rep., 7:39385, jan 2017.
- [154] Adam R. Abate, Jeremy J. Agresti, and David A. Weitz. Microfluidic sorting with high-speed single-layer membrane valves. Appl. Phys. Lett., 96(20):203509, may 2010.
- [155] Jean-Christophe Baret, Oliver J. Miller, Valerie Taly, Michaël Ryckelynck, Abdeslam El-Harrak, Lucas Frenz, Christian Rick, Michael L. Samuels, J. Brian Hutchison, Jeremy J. Agresti, Darren R. Link, David A. Weitz, and Andrew D. Griffiths. Fluorescence-activated droplet sorting (FADS): efficient microfluidic cell sorting based on enzymatic activity. Lab Chip, 9(13):1850, 2009.
- [156] R. Follana, D. Klein, M-P. Krafft, D. M. Long, CD. Long, Y. Ni, J. G. Riess, and A. Valla. Prolonged Shelf Stability and Biocompatibility of a Concentrated Injectable Fluorocarbon Emulsion. Biomater. Artif. Cells Immobilization Biotechnol., 20(2-4):1059–1061, jan 1992.
- [157] Keunho Ahn, Jeremy Agresti, Henry Chong, Manuel Marquez, and D. A. Weitz. Electrocoalescence of drops synchronized by size-dependent flow in microfluidic channels. Appl. Phys. Lett., 88(26):264105, jun 2006.

- [158] Adam R Abate, Tony Hung, Pascaline Mary, Jeremy J Agresti, and David a Weitz. High-throughput injection with microfluidics using picoinjectors. Proc. Natl. Acad. Sci. U S A, 107(45):19163–19166, nov 2010.
- [159] Steven R Doonan and Ryan C. Bailey. K-Channel: A Multifunctional Architecture for Dynamically Reconfigurable Sample Processing in Droplet Microfluidics. Anal. Chem., 89(7):4091–4099, apr 2017.
- [160] Adam Sciambi and Adam R Abate. Generating electric fields in PDMS microfluidic devices with salt water electrodes. Lab Chip, 14(15):2605, 2014.
- [161] Brian O’Donovan, Dennis J. Eastburn, and Adam R. Abate. Electrode-free picoinjection of microfluidic drops. Lab Chip, 12(20):4029, 2012.
- [162] Melinda G. Simon and Abraham P. Lee. Microfluidic Droplet Manipulations and Their Applications. In Microdroplet Technology, volume 7, pages 23–50. Springer New York, New York, NY, may 2012.
- [163] Hengdong Xi, Hao Zheng, Wei Guo, Alfonso M. Gañán-Calvo, Ye Ai, Chia-Wen Tsao, Jun Zhou, Weihua Li, Yanyi Huang, Nam-Trung Nguyen, and Say Hwa Tan. Active droplet sorting in microfluidics: a review. Lab Chip, 17(5):751–771, 2017.
- [164] Arjen Pit, Michèl Duits, and Frieder Mugele. Droplet Manipulations in Two Phase Flow Microfluidics. Micromachines, 6(12):1768–1793, nov 2015.
- [165] B Vogelstein and K W Kinzler. Digital PCR. Proc. Natl. Acad. Sci. U S A, 96(16):9236–9241, aug 1999.
- [166] Christopher M Hindson, John R Chevillet, Hilary A Briggs, Emily N Gallichotte, Ingrid K Ruf, Benjamin J Hindson, Robert L Vessella, and Muneesh Tewari. Absolute quantification by droplet digital PCR versus analog real-time PCR. Nat. Methods, 10(10):1003–1005, sep 2013.
- [167] Monya Baker. Digital PCR hits its stride. Nat. Methods, 9(6):541–544, 2012.
- [168] Alexander A. Morley. Digital PCR: A brief history. Biomolecular Detection and Quantification, 1(1):1–2, sep 2014.
- [169] Cem Albayrak, Christian A. Jordi, Christoph Zechner, Jing Lin, Colette A. Bichsel, Mustafa Khammash, and Sava Tay. Digital Quantification of Proteins and mRNA in Single Mammalian Cells. Mol. Cell, 61(6):914–924, mar 2016.
- [170] Zhichao Guan, Yuan Zou, Mingxia Zhang, Jiangquan Lv, Huali Shen, Pengyuan Yang, Huimin Zhang, Zhi Zhu, and Chaoyong James Yang. A highly parallel microfluidic droplet method enabling single-molecule counting for digital enzyme detection. Biomicrofluidics, 8(1):014110, jan 2014.

- [171] Dong-Ku Kang, M Monsur Ali, Kaixiang Zhang, Susan S Huang, Ellena Peterson, Michelle a Digman, Enrico Gratton, and Weian Zhao. Rapid detection of single bacteria in unprocessed blood using Integrated Comprehensive Droplet Digital Detection. Nat. Commun., 5:5427, nov 2014.
- [172] Mitchell E. Johnson and James P. Landers. Fundamentals and practice for ultrasensitive laser-induced fluorescence detection in microanalytical systems. Electrophoresis, 25(21-22):3513–3527, nov 2004.
- [173] Kennon S Deal. Lock-In Detection with Microfluidic Droplets for Quantitative Bioanalysis in Sub- Nanoliter Volumes. Phd thesis, Auburn University PhD Thesis, 2013.
- [174] Delai Chen, Wenbin Du, Y. Liu, Weishan Liu, Andrey Kuznetsov, Felipe E Mendez, Louis H Philipson, and Rustem F Ismagilov. The chemistode: A droplet-based microfluidic device for stimulation and recording with high temporal, spatial, and chemical resolution. Proc. Natl. Acad. Sci. U S A, 105(44):16843–16848, nov 2008.
- [175] Christopher J Easley, Jonathan V Rocheleau, W Steven Head, and David W Piston. Quantitative Measurement of Zinc Secretion from Pancreatic Islets with High Temporal Resolution Using Droplet-Based Microfluidics. Anal. Chem., 81(21):9086–9095, nov 2009.
- [176] Jean T. Negou, L. Adriana Avila, Xiangpeng Li, Tesfagebriel M. Hagos, and Christopher J. Easley. Automated Microfluidic Droplet-Based Sample Chopper for Detection of Small Fluorescence Differences Using Lock-In Analysis. Anal. Chem., page acs.analchem.7b00991, may 2017.
- [177] Howard Green and Olaniyi Kehinde. An established preadipose cell line and its differentiation in culture II. Factors affecting the adipose conversion. Cell, 5(1):19–27, 1975.
- [178] W Kuri-Harcuch and H Green. Adipose conversion of 3T3 cells depends on a serum factor. Proc. Natl. Acad. Sci. U S A, 75(12):6107–6109, dec 1978.
- [179] Pamela Fischer-Posovszky, Felicity S Newell, Martin Wabitsch, and Hans E Tornqvist. Human SGBS Cells-a Unique Tool for Studies of Human Fat Cell Biology. Obesity Facts, 1(4):184–189, 2008.
- [180] T H Chang and S E Polakis. Differentiation of 3T3-L1 fibroblasts to adipocytes. Effect of insulin and indomethacin on the levels of insulin receptors. J. Biol. Chem., 253(13):4693–6, jul 1978.
- [181] Susanne Mandrup, Thomas M Loftus, Ormond A MacDougald, Francis P Kuhajda, and M Daniel Lane. Obese gene expression at in vivo levels by fat pads derived from s.c. implanted 3T3-F442Apreadipocytes. Proc. Natl. Acad. Sci. U S A, 94(9):4300–4305, apr 1997.

- [182] Rui Yao, Yanan Du, Renji Zhang, Feng Lin, and Jie Luan. A biomimetic physiological model for human adipose tissue by adipocytes and endothelial cell cocultures with spatially controlled distribution. *Biomed. Mater.*, 8(4):045005, jun 2013.
- [183] Christopher Moraes, Joseph M Labuz, Brendan M Leung, Mayumi Inoue, Tae-Hwa Chun, and Shuichi Takayama. On being the right size: scaling effects in designing a human-on-a-chip. *Integr. Biol.*, 5(9):1149, 2013.
- [184] Joshua R. Mauney, Trang Nguyen, Kelly Gillen, Carl Kirker-Head, Jeffrey M. Gimble, and David L. Kaplan. Engineering adipose-like tissue in vitro and in vivo utilizing human bone marrow and adipose-derived mesenchymal stem cells with silk fibroin 3D scaffolds. *Biomaterials*, 28(35):5280–90, dec 2007.
- [185] Paul S. Wigganhauser, Daniel F. Müller, Ferry P W Melchels, José T. Egaña, Katharina Storck, Helena Mayer, Peter Leuthner, Daniel Skodacek, Ursula Hopfner, Hans G. Machens, Rainer Staudenmaier, and Jan T. Schantz. Engineering of vascularized adipose constructs. *Cell Tissue Res.*, 347(3):747–757, mar 2012.
- [186] Lina Wang, Joshua A. Johnson, Qixu Zhang, and Elisabeth K. Beahm. Combining decellularized human adipose tissue extracellular matrix and adipose-derived stem cells for adipose tissue engineering. *Acta Biomater.*, 9(11):8921–8931, nov 2013.
- [187] Kevin M. Tharp, Amit K. Jha, Judith Kraiczky, Alexandra Yesian, Grigory Karateev, Riccardo Sinisi, Elena A. Dubikovskaya, Kevin E. Healy, and Andreas Stahl. Matrix-Assisted Transplantation of Functional Beige Adipose Tissue. *Diabetes*, 64(11):3713–24, nov 2015.
- [188] Peter Loskill, Thiagarajan Sezhian, Kevin Tharp, Felipe T. Lee-Montiel, Shaheen Jeeawoody, Willie Mae Reese, Pete-James H Zushin, Andreas Stahl, and Kevin Healy. WAT-on-a-chip: A physiologically relevant microfluidic system incorporating white adipose tissue. *Lab Chip*, 2017.
- [189] Jun Wu. *Thermogenic Fat*, volume 1566 of *Methods in Molecular Biology*. Springer New York, New York, NY, 2017.
- [190] Xiangpeng Li, Jessica C Brooks, Juan Hu, Katarena I Ford, and Christopher J Easley. 3D-templated, fully automated microfluidic input/output multiplexer for endocrine tissue culture and secretion sampling. *Lab Chip*, 17(2):341–349, 2017.
- [191] Jessica C Brooks, Katarena I Ford, Dylan H Holder, Mark D Holtan, and Christopher J Easley. Macro-to-micro interfacing to microfluidic channels using 3D-printed templates: application to time-resolved secretion sampling of endocrine tissue. *Analyst*, 141(20):5714–5721, 2016.
- [192] Leah a. Godwin, Jessica C. Brooks, Lauren D. Hoepfner, Desiree Wanders, Robert L. Judd, and Christopher J. Easley. A microfluidic interface for the culture and sampling of adiponectin from primary adipocytes. *Analyst*, 140(4):1019–1025, 2015.

- [193] Alessandro Zambon, Alice Zoso, Onelia Gagliano, Enrico Magrofuoco, Gian Paolo Fadini, Angelo Avogaro, Mirto Foletto, Stephen Quake, and Nicola Elvassore. High Temporal Resolution Detection of Patient-Specific Glucose Uptake from Human ex Vivo Adipose Tissue On-Chip. Anal. Chem., 87(13):6535–6543, 2015.
- [194] Anna M. Clark, Kyle M. Sousa, Claire N. Chisolm, Ormond a. MacDougald, and Robert T. Kennedy. Reversibly sealed multilayer microfluidic device for integrated cell perfusion and on-line chemical analysis of cultured adipocyte secretions. Anal. Bioanal. Chem., 397(7):2939–2947, 2010.
- [195] Colleen E Dugan and Robert T Kennedy. Measurement of lipolysis products secreted by 3T3-L1 adipocytes using microfluidics. Methods Enzymol., 538(Methods of Adipose Tissue Biology, Part B):195–209, 2014.
- [196] Colleen E Dugan, William P Cawthorn, Ormond A MacDougald, and Robert T Kennedy. Multiplexed microfluidic enzyme assays for simultaneous detection of lipolysis products from adipocytes. Anal. Bioanal. Chem., 406(20):4851–4859, 2014.
- [197] Naoki Inomata, Masaya Toda, and Takahito. Ono. Highly sensitive thermometer using a vacuum-packed Si resonator in a microfluidic chip for the thermal measurement of single cells. Lab Chip, 16(18):3597–3603, 2016.
- [198] Colleen E Dugan, James P Grinias, Sebastian D Parlee, Mahmoud El-Azzouny, Charles R Evans, and Robert T Kennedy. Monitoring cell secretions on microfluidic chips using solid-phase extraction with mass spectrometry. Anal. Bioanal. Chem., 409(1):169–178, jan 2017.
- [199] Jan W. Slot. Immuno-localization of the insulin regulatable glucose transporter in brown adipose tissue of the rat. J. Cell Biol., 113(1):123–135, apr 1991.
- [200] E W Kraegen, D E James, a B Jenkins, and D J Chisholm. Dose-response curves for in vivo insulin sensitivity in individual tissues in rats. Am. J. Physiol., 248(3 Pt 1):E353–62, mar 1985.
- [201] Jessica C Brooks, Robert L Judd, and Christopher J Easley. Culture and Sampling of Primary Adipose Tissue in Practical Microfluidic Systems. In Methods Mol Biol, volume 1566, pages 185–201. 2017/03/01 edition, 2017.
- [202] H Vorum, R Brodersen, U Kragh-Hansen, and A O Pedersen. Solubility of long-chain fatty acids in phosphate buffer at pH 7.4. Biochim. Biophys. Acta, 1126(2):135–42, jun 1992.
- [203] M Lafontan. Advances in adipose tissue metabolism. Int. J. Obes., 32 Suppl 7:S39–51, 2008.
- [204] Ondrej Kuda, Terri A. Pietka, Zuzana Demianova, Eva Kudova, Josef Cvacka, Jan Kopecky, and Nada A. Abumrad. Sulfo-N-succinimidyl Oleate (SSO) Inhibits Fatty Acid Uptake and Signaling for Intracellular Calcium via Binding CD36 Lysine 164. J. Biol. Chem., 288(22):15547–15555, may 2013.

- [205] Jessica C Brooks. Microfluidic interfacing for primary endocrine tissue: developing bioanalytical methodologies and novel fabrication methods for cell culture and analysis. Phd thesis, Auburn University PhD Thesis, 2016.
- [206] Andressa Bolsoni-Lopes and Maria Isabel C Alonso-Vale. Lipolysis and lipases in white adipose tissue - An update. Arch. Endocrinol. Metab., 59(4):335–42, aug 2015.
- [207] Michael Roden, Thomas B Price, Gianluca Perseghin, Kitt Falk Petersen, Douglas L Rothman, Gary W Cline, and Gerald I Shulman. Mechanism of free fatty acid-induced insulin resistance in humans. J. Clin. Invest., 97(12):2859–65, jun 1996.
- [208] Roy Eldor and Itamar Raz. Lipotoxicity versus adipotoxicity The deleterious effects of adipose tissue on beta cells in the pathogenesis of type 2 diabetes. Diabetes Res. Clin. Pract., 74(2):S3–S8, nov 2006.
- [209] Francesc Villarroya, Ruben Cereijo, Joan Villarroya, and Marta Giralt. Brown adipose tissue as a secretory organ. Nat. Rev. Endocrinol., 13(1):26–35, jan 2017.
- [210] Yong Wang, Joe F Lo, Joshua E Mendoza-Elias, Adeola F Adewola, Tricia A Harvat, Katie P Kinzer, Dongyoung Lee, Meirigeng Qi, David T Eddington, and Jose Oberholzer. Application of microfluidic technology to pancreatic islet research: first decade of endeavor. Bioanalysis, 2(10):1729–1744, oct 2010.
- [211] Francisco Rafael Castiello, Khalil Leon Heileman, and Maryam Tabrizian. Microfluidic perfusion systems for secretion fingerprint analysis of pancreatic islets: applications, challenges and opportunities. Lab Chip, 16(3):409–431, jan 2016.
- [212] Shingo Kajimura. Adipose tissue in 2016: Advances in the understanding of adipose tissue biology. Nat. Rev. Endocrinol., 13(2):69–70, feb 2017.
- [213] Jean A Welsh and Solveig A Cunningham. The Role of Added Sugars in Pediatric Obesity. Pediatr. Clin. North Am., 58(6):1455–1466, dec 2011.
- [214] JiaWei Wang, Kelly Light, Mélanie Henderson, Jennifer O’Loughlin, Marie-Eve Mathieu, Gilles Paradis, and Katherine Gray-Donald. Consumption of Added Sugars from Liquid but Not Solid Sources Predicts Impaired Glucose Homeostasis and Insulin Resistance among Youth at Risk of Obesity. J Nutr, 2014.
- [215] Pamuditha N Silva, Brenda J Green, Svetlana M Altamentova, and Jonathan V Rocheleau. A microfluidic device designed to induce media flow throughout pancreatic islets while limiting shear-induced damage. Lab Chip, 13(22):4374–84, nov 2013.
- [216] Xue Wang, Lian Yi, Christelle Guillo, and Michael G Roper. Micellar electrokinetic chromatography method for measuring amino acid secretions from islets of Langerhans. Electrophoresis, 36(9-10):1172–1178, 2015.
- [217] Xinyu Zhang and Michael G Roper. Microfluidic Perfusion System for Automated Delivery of Temporal Gradients to Islets of Langerhans. Anal. Chem., 81(3):1162–1168, 2009.

- [218] Michael G Roper, Jonathan G Shackman, Gabriella M Dahlgren, and Robert T Kennedy. Microfluidic chip for continuous monitoring of hormone secretion from live cells using an electrophoresis-based immunoassay. Anal. Chem., 75(18):4711–4717, sep 2003.
- [219] Jonathan G Shackman, Kendra R Reid, Colleen E Dugan, and Robert T Kennedy. Dynamic monitoring of glucagon secretion from living cells on a microfluidic chip. Anal. Bioanal. Chem., 402(9):2797–2803, 2012.
- [220] John F Dishinger, Kendra R Reid, and Robert T Kennedy. Quantitative monitoring of insulin secretion from single islets of Langerhans in parallel on a microfluidic chip. Anal. Chem., 81(8):3119–3127, apr 2009.
- [221] Javeed Shaikh Mohammed, Yong Wang, Tricia A Harvat, Jose Oberholzer, and David T Eddington. Microfluidic device for multimodal characterization of pancreatic islets. Lab Chip, 9(1):97–106, jan 2009.
- [222] Adeola F Adewola, Dongyoung Lee, Tricia Harvat, Javeed Mohammed, David T Eddington, Jose Oberholzer, and Yong Wang. Biomed. Microdevices.
- [223] Lian Yi, Xue Wang, Raghuram Dhumpa, Adrian M Schrell, Nikita Mukhitov, and Michael G Roper. Integrated perfusion and separation systems for entrainment of insulin secretion from islets of Langerhans. Lab Chip, 15(3):823–32, feb 2015.
- [224] Jonathan V Rocheleau, Glenn M Walker, W Steven Head, Owen P McGuinness, and David W Piston. Microfluidic glucose stimulation reveals limited coordination of intracellular  $\text{Ca}^{2+}$  activity oscillations in pancreatic islets. Proc. Natl. Acad. Sci. U S A, 101(35):12899–12903, aug 2004.
- [225] Daniel C. Leslie, Christopher J. Easley, Erkin Seker, James M. Karlinsey, Marcel Utz, Matthew R. Begley, and James P. Landers. Frequency-specific flow control in microfluidic circuits with passive elastomeric features. Nat. Phys., 5(3):231–235, 2009.
- [226] Barbara Treutlein, Doug G Brownfield, Angela R Wu, Norma F Neff, Gary L Mantalas, F Hernan Espinoza, Tushar J Desai, Mark A Krasnow, and Stephen R Quake. Reconstructing lineage hierarchies of the distal lung epithelium using single-cell RNA-seq. Nature, 509(7500):371–+, 2014.
- [227] Elizabeth A Ottesen, Jong Wook Hong, Stephen R Quake, and Jared R Leadbetter. Microfluidic digital PCR enables multigene analysis of individual environmental bacteria. Science, 314(5804):1464–1467, 2006.
- [228] Kwanghun Chung, Matthew M Crane, and Hang Lu. Automated on-chip rapid microscopy, phenotyping and sorting of *C. elegans*. Nat. Methods, 5(7):637–643, 2008.
- [229] M Erickstad, E Gutierrez, and A Groisman. A low-cost low-maintenance ultraviolet lithography light source based on light-emitting diodes. Lab Chip, 15(1):57–61, 2015.

- [230] Y Stefan, P Meda, M Neufeld, and L Orci. Stimulation of insulin secretion reveals heterogeneity of pancreatic B cells in vivo. J. Clin. Invest., 80(1):175–183, 1987.
- [231] R C Karl, D W Scharp, W F Ballinger, and P E Lacy. Transplantation of insulin-secreting tissues. Gut, 18(12):1062–1072, 1977.
- [232] E P Plaisance, M Lukasova, S Offermanns, Y Zhang, G Cao, and R L Judd. Niacin stimulates adiponectin secretion through the GPR109A receptor. Am. J. Physiol. Endocrinol. Metab., 296(3):E549–58, 2009.
- [233] D Langin. Control of fatty acid and glycerol release in adipose tissue lipolysis. C R Biol, 329(8):595–598, 2006.
- [234] Joonyul Kim, Juan Hu, Andresa B. Bezerra, Mark D. Holtan, Jessica C. Brooks, and Christopher J. Easley. Protein Quantification Using Controlled DNA Melting Transitions in Bivalent Probe Assemblies. Anal. Chem., 87(19):9576–9579, 2015.
- [235] Juan Hu, Joonyul Kim, and Christopher J Easley. Quantifying aptamer-protein binding via thermofluorimetric analysis. Analytical Methods, 7(17):7358–7362, 2015.
- [236] N Ghorashian, S K Gokce, S X Guo, W N Everett, and A Ben-Yakar. An automated microfluidic multiplexer for fast delivery of *C. elegans* populations from multiwells. PLoS One, 8(9):e74480, 2013.
- [237] Gregory a Cooksey, Christopher G Sip, and Albert Folch. A multi-purpose microfluidic perfusion system with combinatorial choice of inputs, mixtures, gradient patterns, and flow rates. Lab Chip, 9(3):417–426, 2009.
- [238] D W Lee, I Doh, Y Kim, and Y H Cho. Advanced combinatorial microfluidic multiplexer using multiple levels of control pressures. Lab Chip, 13(18):3658–3662, 2013.
- [239] D W Lee and Y H Cho. High-radix microfluidic multiplexer with pressure valves of different thresholds. Lab Chip, 9(12):1681–1686, 2009.
- [240] Leah a. Godwin, Kennon S. Deal, Lauren D. Hoepfner, Louis a. Jackson, and Christopher J. Easley. Measurement of microchannel fluidic resistance with a standard voltage meter. Anal Chim Acta, 758:101–107, 2013.
- [241] I Johnson. The Molecular Probes Handbook: A Guide to Fluorescent Probes and Labeling Technologies, 11th Edition. Life Technologies Corporation, 2010.
- [242] Teresa L Mastracci and Lori Sussel. The endocrine pancreas: insights into development, differentiation, and diabetes. Wiley Interdisciplinary Reviews: Developmental Biology, 1(5):609–628, 2012.
- [243] Oleg Varlamov, Romel Somwar, Anda Cornea, Paul Kievit, Kevin L Grove, and Charles T Roberts. Single-cell analysis of insulin-regulated fatty acid uptake in adipocytes. Am. J. Physiol. Endocrinol. Metab., 299(3):E486, 2010.

- [244] J E Braun and D L Severson. Regulation of the synthesis, processing and translocation of lipoprotein lipase. Biochem. J., 287(Pt 2):337–347, 1992.
- [245] H. Doege. Protein-Mediated Fatty Acid Uptake: Novel Insights from In Vivo Models. Physiology, 21(4):259–268, 2006.
- [246] Paul D. Berk, S.-L. Zhou, C.-L. Kiang, Decherd Stump, Michael Bradbury, and Luis M. Isola. Uptake of Long Chain Free Fatty Acids Is Selectively Up-regulated in Adipocytes of Zucker Rats with Genetic Obesity and Non-insulin-dependent Diabetes Mellitus. J. Biol. Chem., 272(13):8830–8835, mar 1997.
- [247] Huan Huang. Liver Fatty Acid-binding Protein Targets Fatty Acids to the Nucleus. Real time confocal and multiphoton fluorescent imaging in living cells. J. Biol. Chem., 277(32):29139–29151, aug 2002.
- [248] Jinfang Liao, Richard Sportsman, Jeff Harris, and Andreas Stahl. Real-time quantification of fatty acid uptake using a novel fluorescence assay. J. Lipid Res., 46(3):597–602, 2005.
- [249] T Krahn, W Paffhausen, A Schade, M Bechem, and D Schmidt. Masking background fluorescence and luminescence in optical analysis of biomedical assays, US patent, US6420183, 2002.
- [250] Carroll M. Harmon, Paul Luce, Albert H. Beth, and Nada A. Abumrad. Labeling of adipocyte membranes by sulfo-N-succinimidyl derivatives of long-chain fatty acids: Inhibition of fatty acid transport. J. Membr. Biol., 121(3):261–268, may 1991.
- [251] Leah A Godwin, Jessica C Brooks, Lauren D Hoepfner, Desiree Wanders, Robert L Judd, and Christopher J Easley. A microfluidic interface for the culture and sampling of adiponectin from primary adipocytes. Analyst, 140(4):1019–1025, 2015.
- [252] J C Brooks, K I Ford, D H Holder, M D Holtan, and C J Easley. Macro-to-micro interfacing to microfluidic channels using 3D-printed templates: application to time-resolved secretion sampling of endocrine tissue. Analyst, 141(20):5714–5721, 2016.
- [253] A A Spector, K John, and J E Fletcher. Binding of long-chain fatty acids to bovine serum albumin. J. Lipid Res., 10(1):56–67, jan 1969.
- [254] Karolina A. Majorek, Przemyslaw J. Porebski, Arjun Dayal, Matthew D. Zimmerman, Kamila Jablonska, Alan J. Stewart, Maksymilian Chruszcz, and Wladek Minor. Structural and immunologic characterization of bovine, horse, and rabbit serum albumins. Mol. Immunol., 52(3-4):174–182, oct 2012.
- [255] S L M Coort, J Willems, W A Coumans, G J van der Vusse, A Bonen, J F C Glatz, and Jjfp Luiken. Sulfo-N-succinimidyl esters of long chain fatty acids specifically inhibit fatty acid translocase (FAT/CD36)-mediated cellular fatty acid uptake. Mol. Cell Biochem., 239(1-2):213–219, 2002.

- [256] Claus Kerkhoff, Clemens Sorg, Narendra N Tandon, and Wolfgang Nacken. Interaction of S100A8/S100A9 Arachidonic Acid Complexes with the Scavenger Receptor CD36 May Facilitate Fatty Acid Uptake by Endothelial Cells . Biochemistry, 40(1):241–248, jan 2001.
- [257] J Pohl. FAT/CD36-mediated Long-Chain Fatty Acid Uptake in Adipocytes Requires Plasma Membrane Rafts. Mol. Biol. Cell, 16(1):24–31, oct 2004.
- [258] Hayley T. Nicholls, Greg Kowalski, David J. Kennedy, Steve Risis, Lee A. Zaffino, Nadine Watson, Peter Kanellakis, Matthew J. Watt, Alex Bobik, Arend Bonen, M. Febbraio, Graeme I. Lancaster, and Mark A. Febbraio. Hematopoietic Cell-Restricted Deletion of CD36 Reduces High-Fat Diet-Induced Macrophage Infiltration and Improves Insulin Signaling in Adipose Tissue. Diabetes, 60(4):1100–1110, apr 2011.
- [259] Abraham. Savitzky Golay and M. J. E. Smoothing and Differentiation of Data by Simplified Least Squares Procedures. 36(8):1627–1639, 1964.
- [260] Jules. Deltour Jean. Steinier, Yves. Termonia. Comments on Smoothing and differentiation of data by simplified least square procedure. 44(11):1906–1909, 1972.
- [261] Sander Kersten. Physiological regulation of lipoprotein lipase. Biochim. Biophys. Acta, 1841(7):919–33, 2014.
- [262] Ryan A Kellogg, Chengzhe Tian, Tomasz Lipniacki, Stephen R Quake, and Savas Tay. Digital signaling decouples activation probability and population heterogeneity. Elife, 4, 2015.
- [263] Andreja Jovic, Susan M Wade, Richard R Neubig, Jennifer J Linderman, and Shuichi Takayama. Microfluidic interrogation and mathematical modeling of multi-regime calcium signaling dynamics. Integr. Biol., 5(7):932, 2013.
- [264] Megan N. McClean, Pascal Hersen, and Sharad Ramanathan. In vivo measurement of signaling cascade dynamics. Cell Cycle, 8(3):373–376, feb 2009.
- [265] Amnon Amir, Shiri Meshner, Tsevi Beatus, and Joel Stavans. Damped oscillations in the adaptive response of the iron homeostasis network of *E. coli*. Mol. Microbiol., 76(2):428–436, 2010.
- [266] Carine Gubelmann, Sebastian M Waszak, Alina Isakova, Wiebke Holcombe, Korneel Hens, Antonina Iagovitina, Jean-Daniel Feuz, Sunil K Raghav, Jovan Simicevic, and Bart Deplancke. A yeast one-hybrid and microfluidics-based pipeline to map mammalian gene regulatory networks. Mol. Syst. Biol., 9(1):682, aug 2013.
- [267] Gregory Neveu, Rina Barouch-Bentov, Amotz Ziv-Av, Doron Gerber, Yves Jacob, and Shirin Einav. Identification and Targeting of an Interaction between a Tyrosine Motif within Hepatitis C Virus Core Protein and AP2M1 Essential for Viral Assembly. PLoS Pathog., 8(8):e1002845, aug 2012.

- [268] Marcel Geertz, David Shore, and Sebastian J Maerkl. Massively parallel measurements of molecular interaction kinetics on a microfluidic platform. Proc. Natl. Acad. Sci. U S A, 109(41):16540–16545, oct 2012.
- [269] Ya-Yu Chiang and Jonathan West. Ultrafast cell switching for recording cell surface transitions: new insights into epidermal growth factor receptor signalling. Lab Chip, 13(6):1031, 2013.
- [270] Roger Y Tsien. THE GREEN FLUORESCENT PROTEIN. Annual Review of Biochemistry, 67(1):509–544, jun 1998.
- [271] Wenshe Liu, Ansgar Brock, Shuo Chen, Shuibing Chen, and Peter G Schultz. Genetic incorporation of unnatural amino acids into proteins in mammalian cells. Nat. Methods, 4(3):239–244, mar 2007.
- [272] Adrian M. Schrell, Nikita Mukhitov, Lian Yi, Xue Wang, and Michael G. Roper. Microfluidic Devices for the Measurement of Cellular Secretion. Annual review of analytical chemistry (Palo Alto, Calif.), 9(1):249–69, 2016.
- [273] Joe F Lo, Yong Wang, Alexander Blake, Gene Yu, Tricia A Harvat, Hyojin Jeon, Jose Oberholzer, and David T Eddington. Islet preconditioning via multimodal microfluidic modulation of intermittent hypoxia. Anal. Chem., 84(4):1987–1993, feb 2012.
- [274] Dongyoung Lee, Yong Wang, Joshua E Mendoza-Elias, Adeola F Adewola, Tricia A Harvat, Katie Kinzer, Diana Gutierrez, Meirigeng Qi, David T Eddington, and José Oberholzer. Dual microfluidic perfusion networks for concurrent islet perfusion and optical imaging. Biomed. Microdevices, 14(1):7–16, feb 2012.
- [275] John F Dishinger and Robert T Kennedy. Serial Immunoassays in Parallel on a Microfluidic Chip for Monitoring Hormone Secretion from Living Cells. Anal. Chem., 79(3):947–954, feb 2007.
- [276] Jonathan G Shackman, Gabriella M Dahlgren, Jennifer L Peters, and Robert T Kennedy. Perfusion and chemical monitoring of living cells on a microfluidic chip. Lab Chip, 5(1):56–63, 2005.
- [277] Kendra R Reid and Robert T Kennedy. Continuous Operation of Microfabricated Electrophoresis Devices for 24 Hours and Application to Chemical Monitoring of Living Cells. Anal. Chem., 81(16):6837–6842, 2009.
- [278] Nikita Mukhitov, Lian Yi, Adrian M Schrell, and Michael G Roper. Optimization of a microfluidic electrophoretic immunoassay using a Peltier cooler. J. Chromatogr. A, 1367:154–160, 2014.
- [279] Anna R Lomasney, Lian Yi, and Michael G Roper. Simultaneous monitoring of insulin and islet amyloid polypeptide secretion from islets of Langerhans on a microfluidic device. Anal. Chem., 85(16):7919–7925, aug 2013.

- [280] Ewa Heyduk, Benjamin Dummit, Yie-Hwa Chang, and Tomasz Heyduk. Molecular Pincers: Antibody-Based Homogeneous Protein Sensors. Anal. Chem., 80(13):5152–5159, jul 2008.
- [281] Kennon S. Deal and Christopher J. Easley. Self-regulated, droplet-based sample chopper for microfluidic absorbance detection. Anal. Chem., 84(3):1510–1516, 2012.
- [282] Jonathan A. Vickers, Meghan M. Caulum, and Charles S. Henry. Generation of hydrophilic poly(dimethylsiloxane) for high-performance microchip electrophoresis. Anal. Chem., 78(21):7446–52, nov 2006.
- [283] Patrick Gilon, Magalie A Ravier, J.-C. Jonas, and J.-C. Henquin. Control Mechanisms of the Oscillations of Insulin Secretion In Vitro and In Vivo. Diabetes, 51(Supplement 1):S144–S151, feb 2002.
- [284] Martina Schifferer, Dmytro A. Yushchenko, Frank Stein, Andrey Bolbat, and Carsten Schultz. A Ratiometric Sensor for Imaging Insulin Secretion in Single  $\beta$  Cells. Cell Chem. Biol., 24(4):525–531.e4, apr 2017.
- [285] Takashi Tanaka, Kazuaki Nagashima, Nobuya Inagaki, Hidetaka Kioka, Seiji Takashima, Hajime Fukuoka, Hiroyuki Noji, Akira Kakizuka, and Hiromi Imamura. Glucose-stimulated Single Pancreatic Islets Sustain Increased Cytosolic ATP Levels during Initial  $\text{Ca}^{2+}$  Influx and Subsequent  $\text{Ca}^{2+}$  Oscillations. J. Biol. Chem., 289(4):2205–2216, jan 2014.
- [286] Matthew C. Cane, John Parrington, Patrik Rorsman, Antony Galione, and Guy A. Rutter. The two pore channel TPC2 is dispensable in pancreatic  $\beta$ -cells for normal  $\text{Ca}^{2+}$  dynamics and insulin secretion. Cell Calcium, 59(1):32–40, 2016.
- [287] Boah Lee, Taegeun Song, Kayoung Lee, Jaeyoon Kim, Seungmin Han, Per-Olof Berggren, Sung Ho Ryu, and Junghyo Jo. Phase modulation of insulin pulses enhances glucose regulation and enables inter-islet synchronization. Plos One, 12(2):e0172901, 2017.
- [288] Eric Glynn, Benjamin Thompson, Suryakiran Vadrevu, Shusheng Lu, Robert T. Kennedy, Joon Ha, Arthur Sherman, and Leslie S. Satin. Chronic glucose exposure systematically shifts the oscillatory threshold of mouse islets: Experimental evidence for an early intrinsic mechanism of compensation for hyperglycemia. Endocrinology, 157(2):611–623, 2016.
- [289] Maryam Mirzaei, Mateu Pla-Roca, Roozbeh Safavieh, Elena Nazarova, Mohammadali Safavieh, Huiyan Li, Jackie Vogel, and David Juncker. Microfluidic perfusion system for culturing and imaging yeast cell microarrays and rapidly exchanging media. Lab Chip, 10(18):2449, 2010.
- [290] Katarina Blagovic, Lily Y. Kim, and Joel Voldman. Microfluidic Perfusion for Regulating Diffusible Signaling in Stem Cells. PLoS One, 6(8):e22892, aug 2011.

- [291] Lily Kim, Yi-Chin Toh, Joel Voldman, and Hanry Yu. A practical guide to microfluidic perfusion culture of adherent mammalian cells. Lab Chip, 7(6):681, 2007.
- [292] Rocio J. Jimenez-Valdes, Roberto Rodriguez-Moncayo, Diana F. Cedillo-Alcantar, and Jose L. Garcia-Cordero. Massive Parallel Analysis of Single Cells in an Integrated Microfluidic Platform. Anal. Chem., 89(10):5210–5220, may 2017.
- [293] Pingan Zhu and Liqiu Wang. Passive and active droplet generation with microfluidics: a review. Lab Chip, 17(1):34–75, 2017.
- [294] Linas Mazutis, Jean-Christophe Baret, Patrick Treacy, Yousr Skhiri, Ali Fallah Araghi, Michael Ryckelynck, Valérie Taly, and Andrew D. Griffiths. Multi-step microfluidic droplet processing: kinetic analysis of an in vitro translated enzyme. Lab Chip, 9(20):2902, 2009.
- [295] Michele Zagnoni and Jonathan M. Cooper. A microdroplet-based shift register. Lab Chip, 10(22):3069, 2010.
- [296] Shia-Yen Teh, Robert Lin, Lung-Hsin Hung, and Abraham P Lee. Droplet microfluidics. Lab Chip, 8(2):198–220, 2008.
- [297] Philipp Gruner, Birte Riechers, Laura Andreina Chacòn Orellana, Quentin Brosseau, Florine Maes, Thomas Beneyton, Deniz Pekin, and Jean-Christophe Baret. Stabilisers for water-in-fluorinated-oil dispersions: Key properties for microfluidic applications. Curr. Opin. Colloid Interface Sci., 20(3):183–191, jun 2015.
- [298] Ilia Platzman, Jan-Willi Janiesch, and Joachim Pius Spatz. Synthesis of Nanostructured and Biofunctionalized Water-in-Oil Droplets as Tools for Homing T Cells. J. Am. Chem. Soc., 135(9):3339–3342, mar 2013.
- [299] N Michael Green. Avidin and streptavidin. Methods Enzymol., 184:51–67, 1990.
- [300] Edward A Bayer and Meir Wilchek. Biotin-binding proteins: Overview and prospects. Methods Enzymol., 184:49–51, 1990.
- [301] Meir Wilchek and Edward A Bayer. Isolation of biologically active compounds: A universal approach. Methods Enzymol., 184:243–244, 1990.
- [302] Meir Wilchek, Edward A Bayer, and Ehud Skutelsky. Affinity cytochemistry. Methods Enzymol., 184:340–342, 1990.
- [303] Walter Newman, L Dawson Beall, and Zafar I Randhawa. Biotinylation of peptide hormones: Structural analysis and application to flow cytometry. Methods Enzymol., 184:275–285, 1990.
- [304] Edward A Bayer, Haya Ben-Hur, and Meir Wilchek. Analysis of proteins and glycoproteins on blots. Methods Enzymol., 184:415–429, 1990.
- [305] Meir Wilchek and Edward A Bayer. Avidin-biotin mediated immunoassays: Overview. Methods Enzymol., 184:467–469, 1990.

- [306] Su-Ming Hsu. Immunohistochemistry. Methods Enzymol., 184:357–363, 1990.
- [307] Meir Wilchek and Edward A Bayer. Gene probes. Methods Enzymol., 184:560–561, 1990.
- [308] Chadron M. Friesen, Jon L. Howell, Ashley Jamieson, and Daryl A. Nyvall. Understanding the influence of hydrocarbon insulators in fluorinated amines: Reactivity of poly(hexafluoropropylene oxide) amine containing methylene spacers. J. Fluorine Chem., 129(3):193–203, mar 2008.
- [309] Calum S Neish, Ian L Martin, Robert M Henderson, and J Michael Edwardson. Direct visualization of ligand-protein interactions using atomic force microscopy. Br. J. Pharmacol., 135(8):1943–1950, apr 2002.
- [310] Chengli Zong, Andre Venot, Omkar Dhamale, and Geert-Jan Boons. Fluorous Supported Modular Synthesis of Heparan Sulfate Oligosaccharides. Org. Lett., 15(2):342–345, jan 2013.
- [311] Vincent M. Monnier, David R. Sell, Zhenyu Dai, Ina Nemet, Francois Collard, and Jianye Zhang. The Role of the Amadori Product in the Complications of Diabetes. Ann. N. Y. Acad. Sci., 1126(1):81–88, apr 2008.
- [312] Nessar Ahmed. Advanced glycation endproducts—role in pathology of diabetic complications. Diabetes Res. Clin. Pract., 67(1):3–21, jan 2005.
- [313] Sho-ichi Yamagishi, Shinjiro Amano, Yosuke Inagaki, Tamami Okamoto, Kohachiro Koga, Nobuyuki Sasaki, Hiroshi Yamamoto, Masayoshi Takeuchi, and Zenji Makita. Advanced Glycation End Products-Induced Apoptosis and Overexpression of Vascular Endothelial Growth Factor in Bovine Retinal Pericytes. Biochem. Biophys. Res. Commun., 290(3):973–978, jan 2002.
- [314] R E Perry, M S Swamy, and E C Abraham. Progressive changes in lens crystallin glycation and high-molecular-weight aggregate formation leading to cataract development in streptozotocin-diabetic rats. Exp. Eye Res., 44(2):269–282, feb 1987.
- [315] R Bucala. Lipoprotein Modification by Advanced Glycosylation Endproducts (AGEs): Role in Atherosclerosis. Trends Cardiovasc. Med., 7(2):39–47, feb 1997.
- [316] E. Y. Skolnik. Human and rat mesangial cell receptors for glucose-modified proteins: potential role in kidney tissue remodelling and diabetic nephropathy. J. Exp. Med., 174(4):931–939, oct 1991.
- [317] H Vlassara, M Brownlee, and A Cerami. Recognition and uptake of human diabetic peripheral nerve myelin by macrophages. Diabetes, 34(6):553–7, jun 1985.
- [318] U J Eriksson, P Wentzel, H S Minhas, and P J Thornalley. Teratogenicity of 3-deoxyglucosone and diabetic embryopathy. Diabetes, 47(12):1960–6, dec 1998.

- [319] David B. Sacks. Measurement of Hemoglobin A1c: A new twist on the path to harmony. Diabetes Care, 35(12):2674–2680, dec 2012.
- [320] H Vernon Roohk and Asad R Zaidi. A Review of Glycated Albumin as an Intermediate Glycation Index for Controlling Diabetes. J. Diabetes. Sci. Technol., 2(6):1114–1121, nov 2008.
- [321] United States Department of Health Statistics, Human Services. Centers for Disease Control, and Prevention. National Center for Health. National Health and Nutrition Examination Survey (NHANES), 2005-2006, 2012.

## APPENDICES

## Appendix A

### Statistical analysis of demographic information and health condition effects on glycohemoglobin levels

#### A.1 Introduction

Diabetes is characterized by chronic hyperglycemia with disturbances of carbohydrate, fat, and protein metabolism. In the short term, diabetes causes symptoms of increased thirst, increased urination, increased hunger, and weight loss. However, in the long term, it causes damages to eyes, kidney, and nerves, which eventually leads to blindness, renal failure, impotence, foot disorders, and other complications of diabetes [1]. Although the pathogenesis of diabetic complications is still less understood, accumulated evidence has emerged in recent years showing that advanced glycation of proteins is strongly associated with the development of diabetic complications [311].

Hyperglycemia induced non-enzymatic glycation is initiated by a fast and highly reversible nucleophilic addition between amino residues of proteins and the carbonyl group of reducing sugars. Once formed, over a period of weeks, the Schiff's base product rearranges to more stable Amadori products (Figure A.1). The spontaneous glycation reaction of protein is depending on the blood glucose level and duration, the half-life of the protein, and the permeability of the tissue to free glucose [312]. Further reactions of the glycated proteins leads to irreversible products called advanced glycation endproducts (AGEs). A major consequence of elevated blood glucose in diabetics is accumulation of AGEs, which is now known to be associated with diabetic retinopathy [313], diabetic cataract [314], diabetic atherosclerosis [315], diabetic nephropathy [316], diabetic neuropathy [317], diabetic embryopathy [318], and other diabetic complications.

Hemoglobin (Hb), the oxygen transporting protein in red blood cells, which carries oxygen

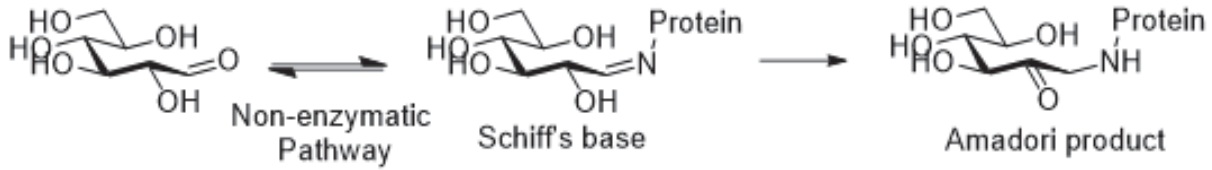


Figure A.1: Glycoation of Protein

from the lungs to other tissues, accounts for approximately 60% of the total protein content in serum and 90% of the dry weight of the red blood cells, and it is widely exposed to blood glucose. Normally, only 4% to 6% of Hb in the blood is glycated. However, people with elevated blood glucose caused by diabetes and other conditions have a higher percentage of glycohemoglobin, or HbA<sub>1c</sub>. As an indicator that reflects the average glucose level over the preceding 8-12 weeks, HbA<sub>1c</sub> provides an additional criterion other than glucose measurement for assessing glucose control in patient that is free of the wide diurnal fluctuations that occurs in blood glucose[319, 320].

Therefore, in order to study the effects of demographic information and health condition on the glycohemoglobin level, a 2092 case data set from United States Department of Health and Human Services was analyzed by multiple linear regression model herein. The prediction models for HbA<sub>1c</sub> level the effects of different variables were obtained by this study.

## A.2 Method and Analysis

### A.2.1 Data

The data was adopted from the United States Department of Health and Human Services, Centers for Disease Control and Prevention, National Center for Health Statistics, National Health and Nutrition Examination Survey (NHANES), 2005-2006. ICPSR25504-v5[321].

The data included a complete blood count (CBC) test results from laboratory and a follow-up questionnaire interview dataset. The two datasets were merged together by the respondent

Name	Description	Codes/values
<i>Seqn</i>	Respondent sequence	31131 to 41474
<i>Gh</i>	Glycohemoglobin (%)	3.8 to 12.8
<i>Wt</i>	Weight (kg)	29.1 to 371
<i>Ht</i>	Standing Height (cm)	138.6 to 204.1
<i>BMI</i>	Body Mass Index (kg/m**2)	14.39 to130.21
<i>Gendr</i>	gender	1: male; 0: female
<i>Ageex</i>	age at screening adjusted	144 to 1019
<i>Glu</i>	Fasting Glucose (mmol/L)	3.442 to 18.263
<i>Ins</i>	Insulin (pmol/L)	6 to 530.1
<i>Diabete</i>	have diabetes	1: Yes; 0: No
<i>Race</i>	race/ ethnicity	1: Mexican American; 2: Other Hispanic ; 3: White; 4: Black; 5: Others
<i>Health</i>	General health condition	1: excellent; 2: very good; 3: good; 4: fair; 5: poor
<i>FmInc</i>	Annual Family Income	1: 0-4999; 2: 5000-9999; 3:10000-14999; 4: 15000-19999; 5:20000-24999; 6: 25000-34999; 7: 35000-44999; 8: 45000-54999; 9: 55000-64999; 10: 65000-74999; 11: 75000 and over
<i>Prg</i>	Pregnancy Status at Exam	1: pregnant; 0: not pregnant
<i>Wtint2yr</i>	Weight of the data	

Table A.1: List of variables

sequence number of each case. The original data had 10430 cases and 63 variables. Any cases with empty values and the variable of non-interest were removed. 2092 cases and 14 variables remained. The description and codes are described in table A.1.

### A.2.2 Define dummy variables

As shown in Table A.1, among the 14 variables, 6 of them are categorical. *Gendr*, *Diabete* and *Prg* have two levels: 0 and 1, which were used in the model directly. Other categorical variables, *Race*, has 5 different levels, for which 4 dummy variables were created, and the level of ‘others’ was treated as reference. For the ordinal variables, *Health* and *Fminc*, the code of *Health* and the mid-rank of *Fminc* were used as continuous variables in the analysis.

Variable	DF	Parameter Estimate	Standard Error	t-value	Pr > t	Variance Inflation
<i>Intercept</i>	1	3.94524	0.54821	7.20	<.0001	0
<i>Ageex</i>	1	0.00040857	0.00004077	10.02	<.0001	1.21390
<i>BMI</i>	1	-0.01182	0.00960	-1.23	0.2180	75.00135
<i>Diabede</i>	1	0.18502	0.09502	1.95	0.0517	1.01655
<i>Inc</i>	1	-1.93759E-7	3.319134E-7	-0.58	0.5594	1.13648
<i>Glu</i>	1	0.40374	0.00966	41.81	<.0001	1.23141
<i>Gendr</i>	1	-0.04377	0.02246	-1.95	0.0515	2.01638
<i>Ht</i>	1	-0.00698	0.00327	-2.14	0.0328	17.60764
<i>Ins</i>	1	-0.00043038	0.00016745	-2.57	0.0102	1.48667
<i>Prg</i>	1	-0.06937	0.10936	-0.63	0.5260	1.01081
<i>race1</i>	1	0.02572	0.04561	0.56	0.5729	2.41070
<i>race2</i>	1	0.03988	0.05668	0.70	0.4818	1.62901
<i>race3</i>	1	-0.02792	0.03697	-0.76	0.4502	4.31576
<i>race4</i>	1	0.22382	0.04319	5.18	<.0001	2.87793
<i>Wt</i>	1	0.00550	0.00336	1.64	0.1013	93.73820
<i>Health</i>	1	0.01828	0.00961	1.90	0.0572	1.17690

Table A.2: Full model parameter estimates

### A.2.3 Multiple linear regression (Full model)

The 10 demographic information and general health condition predictors were fitted into the weighted least squares multiple linear regression model with the response variable, *Gh*, with *Wtint2yr* as the weight. The analysis of variance F-test  $p$  value is smaller than 0.0001 and the  $R^2$  is 56.46%, suggest there are linear relationship between the HbA<sub>1c</sub> level and the 10 predictors. In the parameter estimates, several variance inflation factors were greater than 10 (table A.2), which indicated serious problems with multicollinearity, and model selection was needed. The model assumption was checked with the diagnostics panel (Figure A.2). The residual showed no clear pattern, and the histogram of residual approximately followed a normal distribution. The  $R_{student}$ , leverage and Cook's D plot showed there are a few possible outliers. However, no outliers were removed because all the cases were plausible observations.

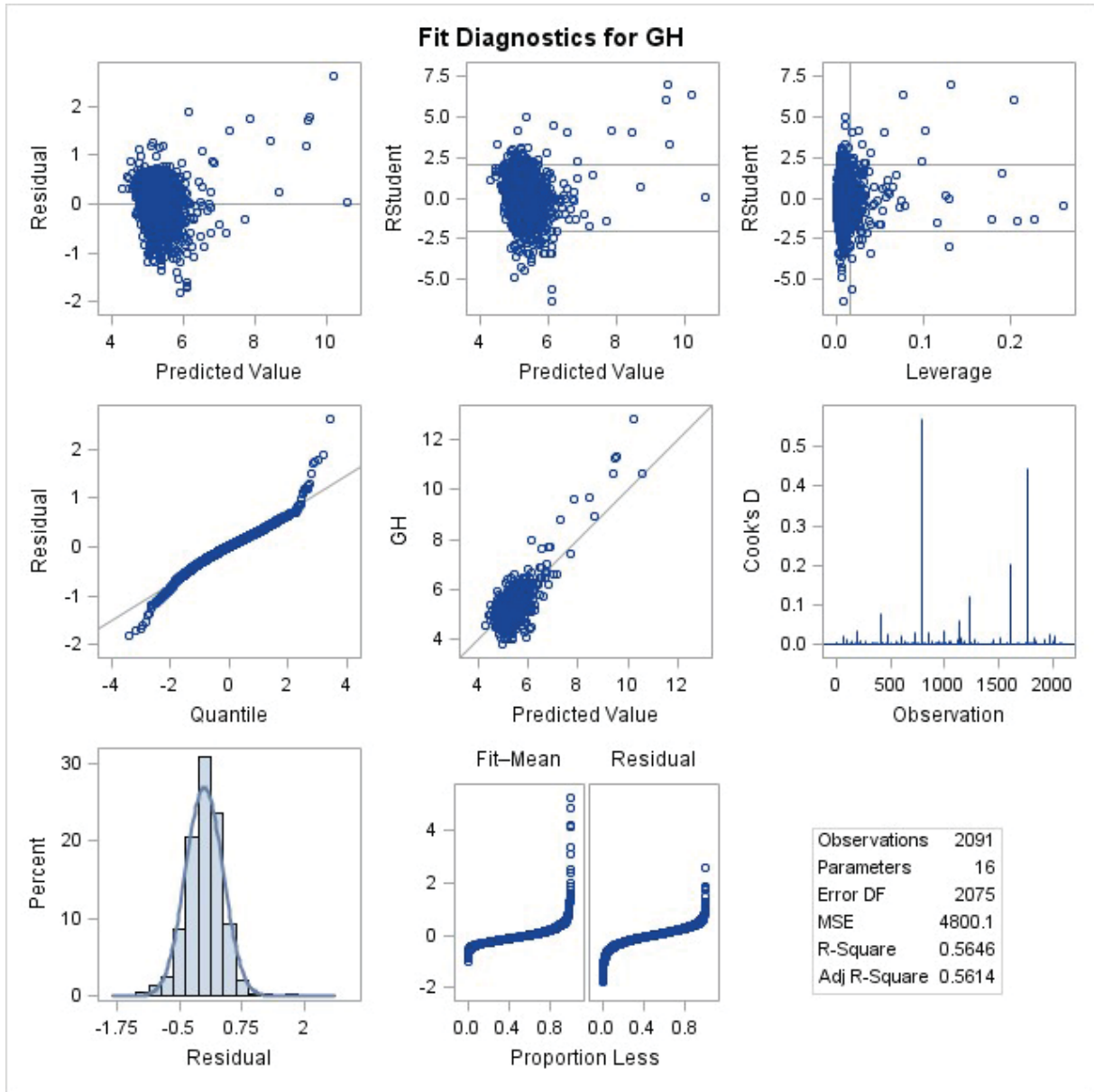


Figure A.2: Stepwise model parameter estimate

Variable	Parameter estimate	Standard error	Type II SS	F Value	Pr >F
<i>Intercept</i>	3.35567	0.19517	1462671	295.61	<.0001
<i>Ageex</i>	0.00040618	0.00004023	504414	101.94	<.0001
<i>Diabete</i>	0.18424	0.09519	18536	3.75	0.0531
<i>Glu</i>	0.40175	0.00967	8535629	1725.07	<.0001
<i>Gendr</i>	-0.03674	0.02217	13589	2.75	0.0976
<i>Ht</i>	-0.00341	0.0012	39671	8.02	0.0047
<i>Ins</i>	-0.00040932	0.00016625	29993	6.06	0.0139
<i>race3</i>	-0.05064	0.02292	24153	4.88	0.0273
<i>race4</i>	0.2016	0.03163	201015	40.63	<.0001
<i>Wt</i>	0.00141	0.00047681	43101	8.71	0.0032
<i>Health</i>	0.01951	0.00932	21676	4.38	0.0365

Table A.3: Backward elimination parameter estimates

#### A.2.4 Model selection (Backward)

Since the variance inflation factors of the full model suggest multicollinearity exists (Table A.2), the backward elimination method was first used for model selection with the default *slstay* value of 0.10. During the backward elimination steps, *Race1*, *Race2*, *Inc*, *Prg*, and *BMI* were removed sequentially. The selected model contains 10 variables (Table A.3), and the  $R^2$  is 56.12%.

#### A.2.5 Model selection (Stepwise)

In the stepwise selection with default *slentry* of 0.15 and *slstay* of 0.15, the variables of *Glu*, *Ageex*, *Race4*, *Ht*, *Wt*, *Ins*, *Health*, *Diabete*, *Race3*, and *Gendr* were entered into the model sequentially, and no variable were removed. The exactly same model was achieved as with the backward elimination method.

#### A.2.6 Model selection (Best subset)

After backward elimination and stepwise selection, the best subset selection method was attempted to improve the model. Since there were 10 variables in the model, 1023 different subsets were compared by Mallows' Cp. The Mallows' Cp was plotted against the number

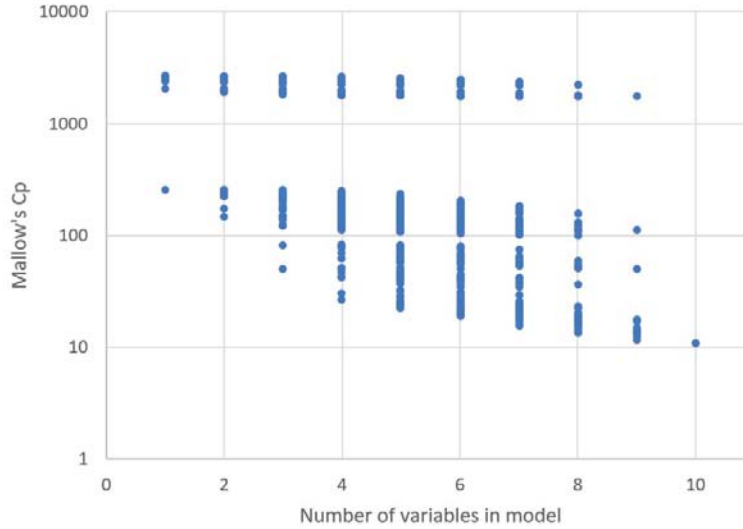


Figure A.3: Mallow's Cp

of variables in subset model (Figure A.3). The subset with all the 10 variables have the smallest Mallows Cp value (equals to 11). Thus, the final model includes all the 10 variables (Table A.2).

### A.3 Explanation, conclusion, and discussion

The final model selected is:

$$Gh = 3.3557 + 0.0004062Ageex + 0.1842Diabete + 0.4018Glu - 0.03674Gendr - 0.00341Ht - 0.0004093Ins - 0.0506Race3 + 0.2016Race4 + 0.00141Wt + 0.01951Health$$

As expected, diabetes and fasting blood glucose level have positive effects, and insulin level has a negative effect on the HbA<sub>1c</sub> level. Age also showed a positive effect, which could be explained by the decreased metabolism rate with aging. The half life of hemoglobin of elder people is longer and thus it is exposed for longer times to blood glucose. The body mass index was dropped in the model selection step. However, the body height has a negative effect and body weight has a positive effect, which still suggests that keeping fit will help decrease the level of HbA<sub>1c</sub>. Two race dummy variables and gender were left in the model. For white people, HbA<sub>1c</sub> level is lower, and for African American, the HbA<sub>1c</sub> level is higher.

The other race groups were not different. Male HbA<sub>1c</sub> was lower than female. General health condition also has a positive effect; the healthier people feel themselves, the lower level of HbA<sub>1c</sub> they have.

#### **A.4 Conclusion**

In conclusion, the effects of demographic information and health condition on Glycohemoglobin, (HbA<sub>1c</sub>) levels were studied by a multiple linear regression model. Age, diabetes, fasting glucose level, body weight, and general health condition have positive effects. Standing height and blood insulin level have negative effects. Family income, pregnancy, and body mass index have no effects on HbA<sub>1c</sub> level.

## A.5 SAS code

```
/*Load data set.*/  
PROC IMPORT OUT= WORK.GH DATAFILE=  
    "\\spirit.auburn.edu\xzl0034\HbA1c\all_data\gh_weight.xlsx"  
DBMS=xlsx REPLACE;  
SHEET="DATA";  
GETNAMES=YES;  
RUN;  
  
proc sort data= gh;  
by seqn;  
run;  
  
proc contents data=gh;  
run;  
  
/*Create dummy variable for the data set.*/  
data gh_1;  
set gh;  
if race=1 then race1 =1; else race1=0;  
if race=2 then race2=1; else race2=0;  
if race=3 then race3 =1; else race3=0;  
if race=4 then race4=1; else race4=0;  
if FMINC =1 then INC= 2500;  
if FMINC =2 then INC= 7500;  
if FMINC =3 then INC= 12500;  
if FMINC =4 then INC= 17500;  
if FMINC =5 then INC= 22500;
```

```

if FMINC =6 then INC= 30000;
if FMINC =7 then INC= 40000;
if FMINC =8 then INC= 50000;
if FMINC =9 then INC= 60000;
if FMINC =10 then INC= 70000;
if FMINC =11 then INC= 80000;
run;

```

```

/*FULL MODEL*/
proc reg data =gh_1;
model gh=Ageex bmi diabete inc glu gendr ht ins prg
  race1 race2 race3 race4 wt health/vif;
weight wtint2yr;
run;

```

```

/*FULL MODEL*/
proc reg data =gh_1;
model gh=ageex bmi diabede inc glu gendr ht ins prg race1
  race2 race3 race4 wt health;
weight wtint2yr;
run;

```

```

/*MODEL SELECTION WITHOUT REMOVE OUTLIERS*/
proc reg data =gh_1;
model gh=ageex bmi diabede inc glu gendr ht ins prg race1
  race2 race3 race4 wt health/ selection = backward ;
weight wtint2yr;

```

```
run;
```

```
/*MODEL SELECTION WITHOUT REMOVE OUTLIERS*/
```

```
proc reg data =gh_1;
```

```
model gh=ageex bmi diabede inc glu gendr ht ins prg race1
```

```
race2 race3 race4 wt health/SELECTION = STEPWISE;
```

```
weight wtint2yr;
```

```
run;
```

```
/*MODEL SELECTION BASED ON MALLOW'S CP*/
```

```
proc reg data = gh_1 outest = fitted;
```

```
model gh=ageex diabede glu gendr ht ins race3 race4 wt
```

```
health / selection = rsquare adjrsq Cp;
```

```
weight wtint2yr;
```

```
run;
```

Appendix B  
Spectra

**B.1 CD36 inhibitor spectrum**

**B.2 Kry-Biotin spectrum**

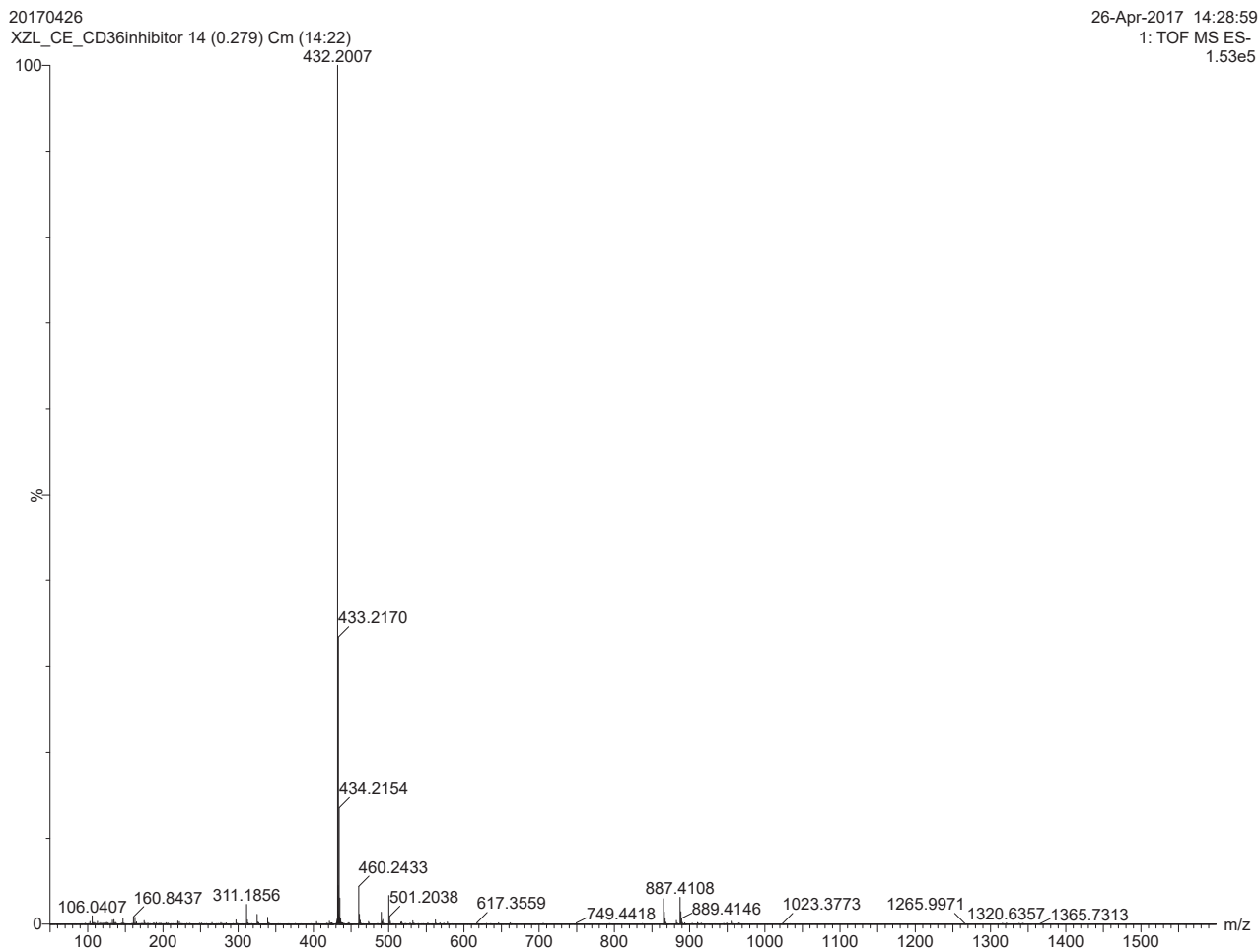


Figure B.1: Mass Spectrum of CD36 Inhibitor

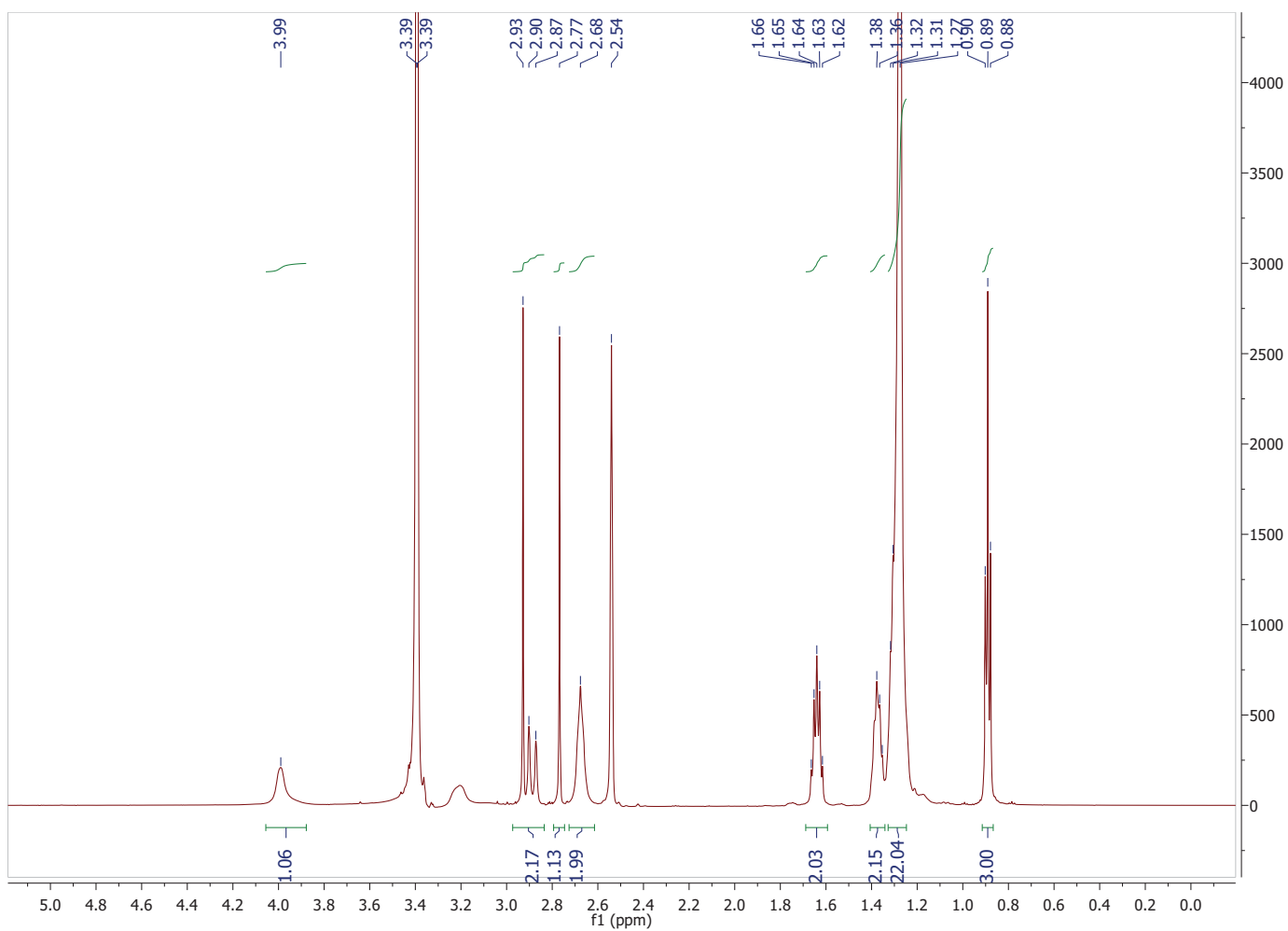


Figure B.2:  $^1\text{H-NMR}$  Spectrum of CD36 Inhibitor in  $\text{DMSO-}d_6$  at room temperature.

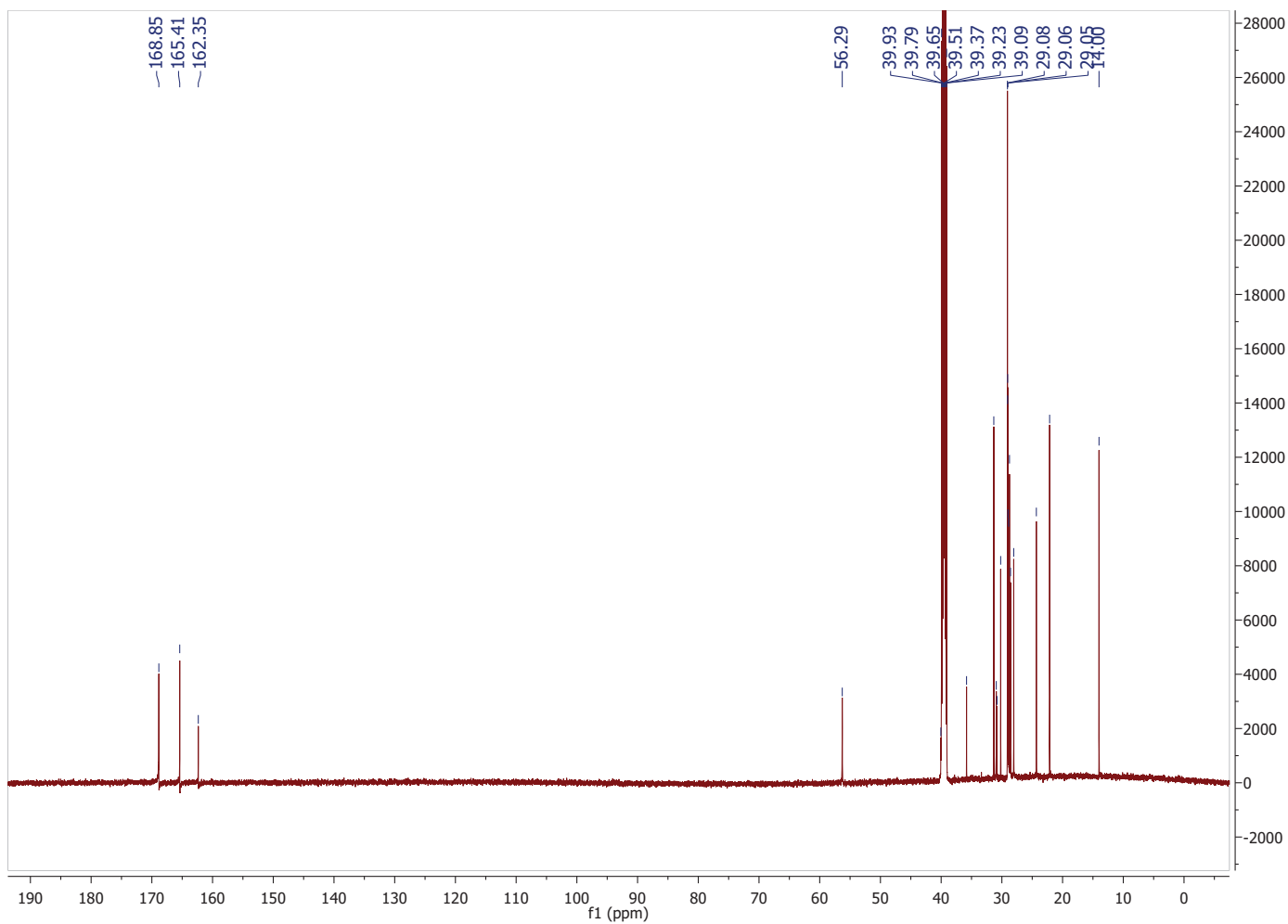


Figure B.3:  $^{13}\text{C}$ -NMR Spectrum of CD36 Inhibitor in  $\text{DMSO-}d_6$  at room temperature.

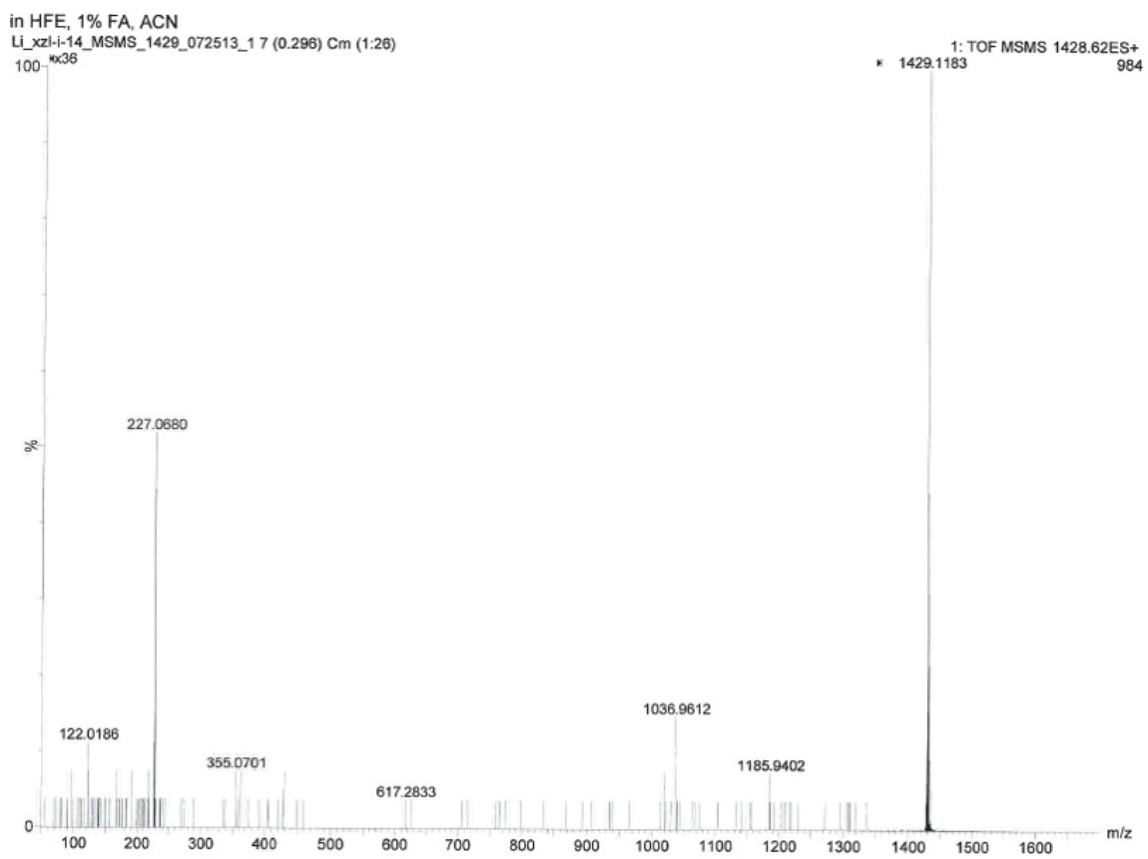


Figure B.4: Mass Spectrum of Kry-Biotin

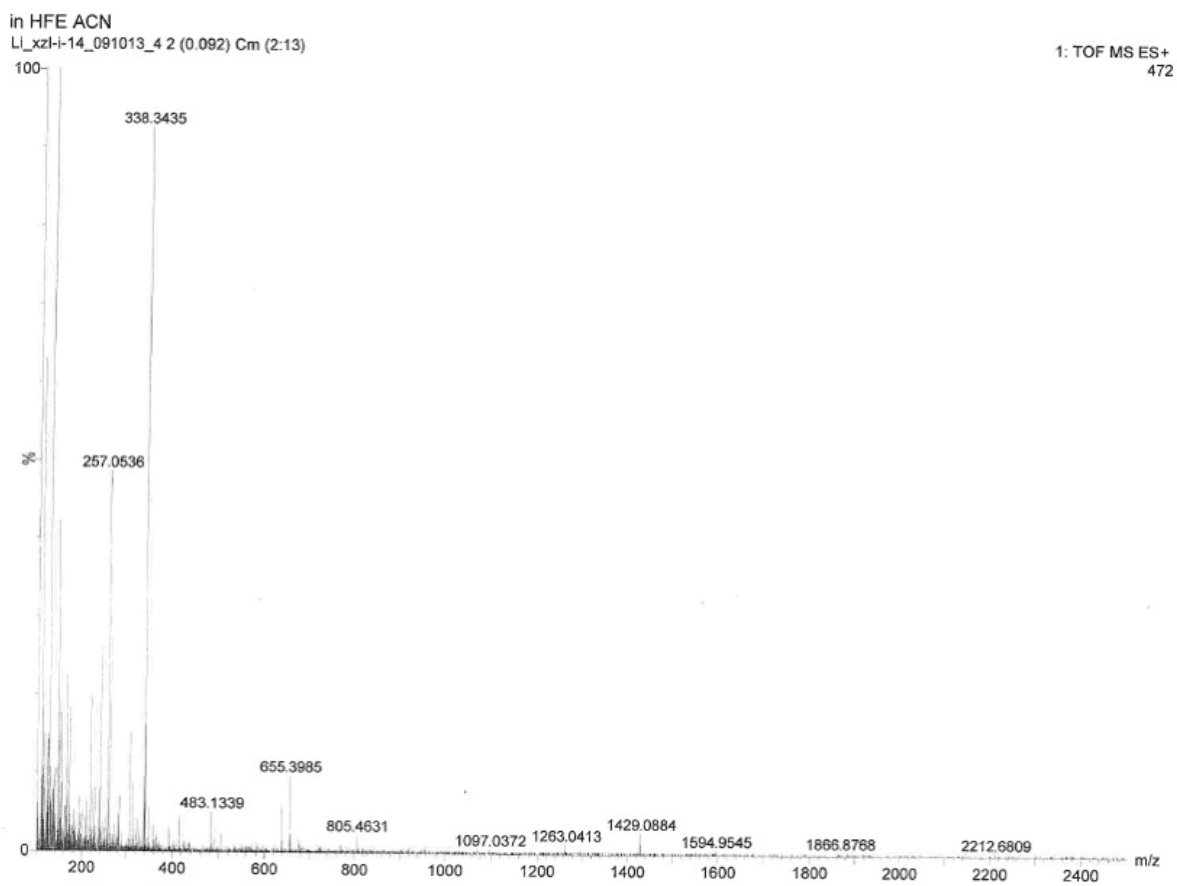


Figure B.5: Mass Spectrum of Kry-Biotin after one month storage at 4 °C

Appendix C  
LabVIEW Codes

**C.1 LabVIEW application for  $\mu$ MUX device**

(Figure C.1 to C.10)

**C.2 LabVIEW application for PumpDrop device**

(Figure C.11 to C.35)

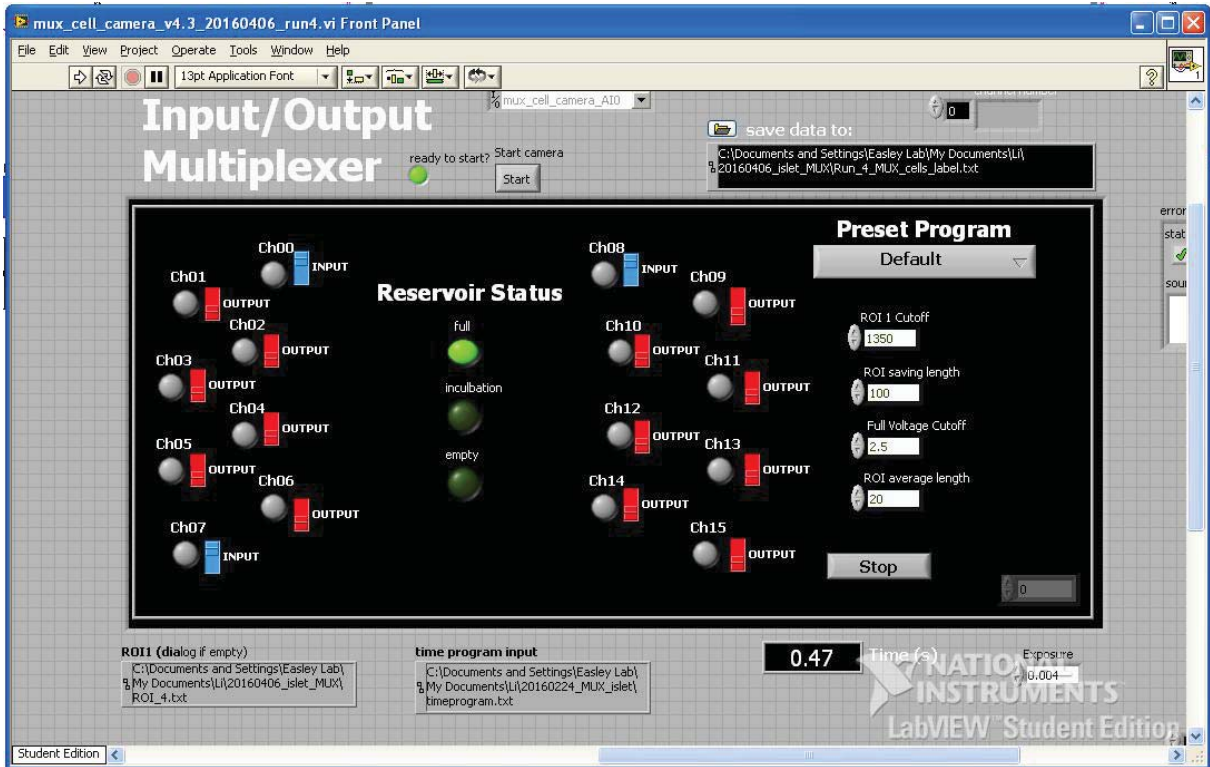


Figure C.1: Front panel of LabVIEW application for  $\mu$ MUX control

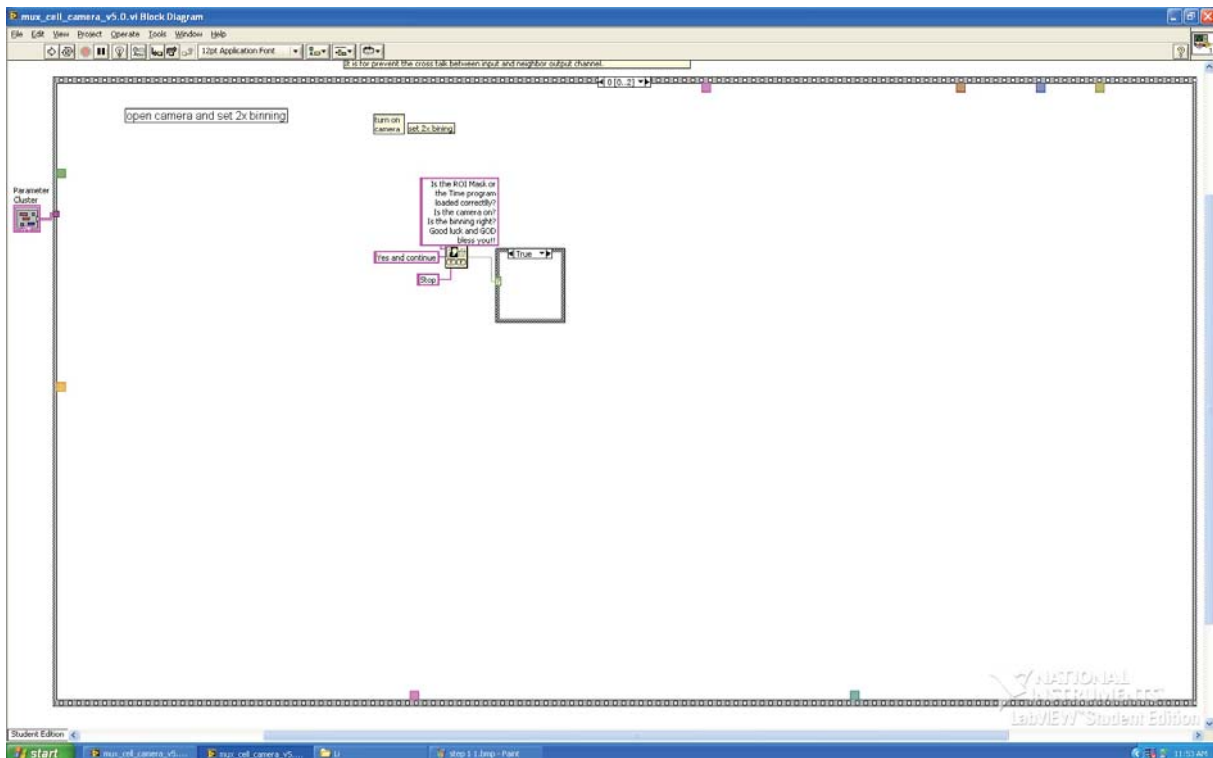


Figure C.2: Block diagram of LabVIEW application for  $\mu$ MUX control, (step 0)

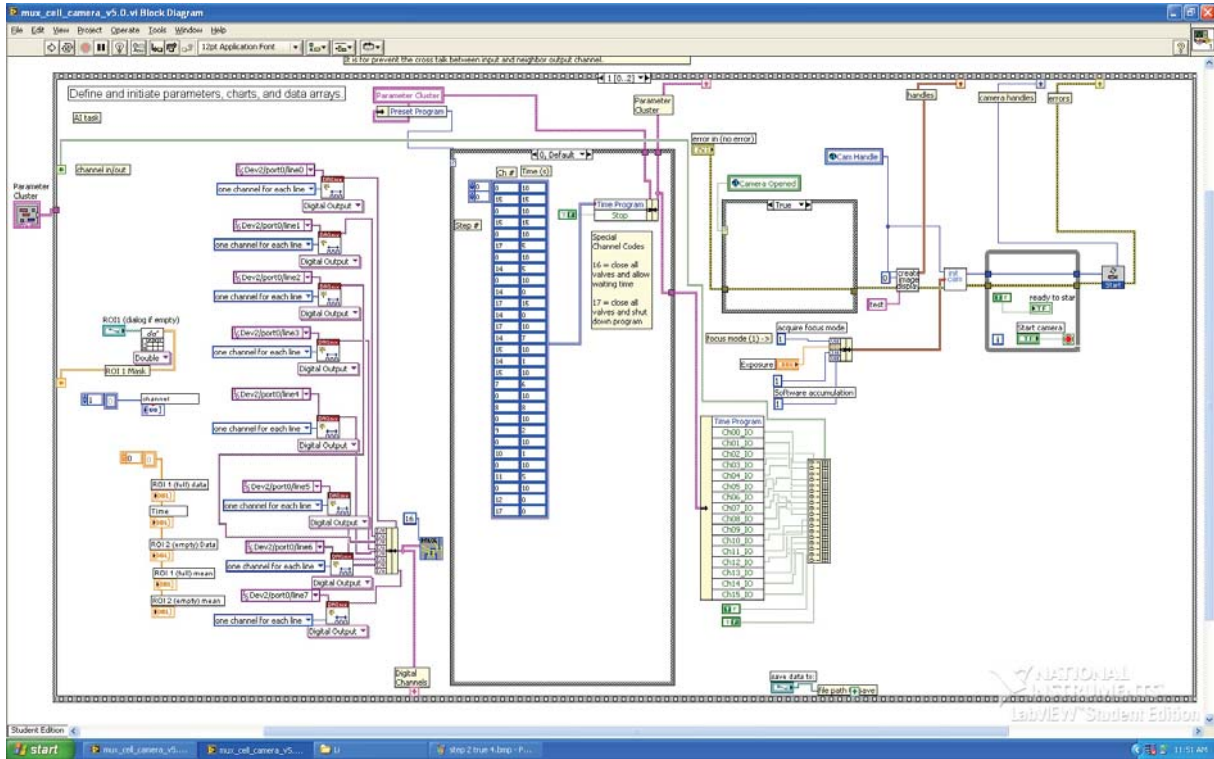


Figure C.3: Block diagram of LabVIEW application for  $\mu$ MUX control, (step 1 A)

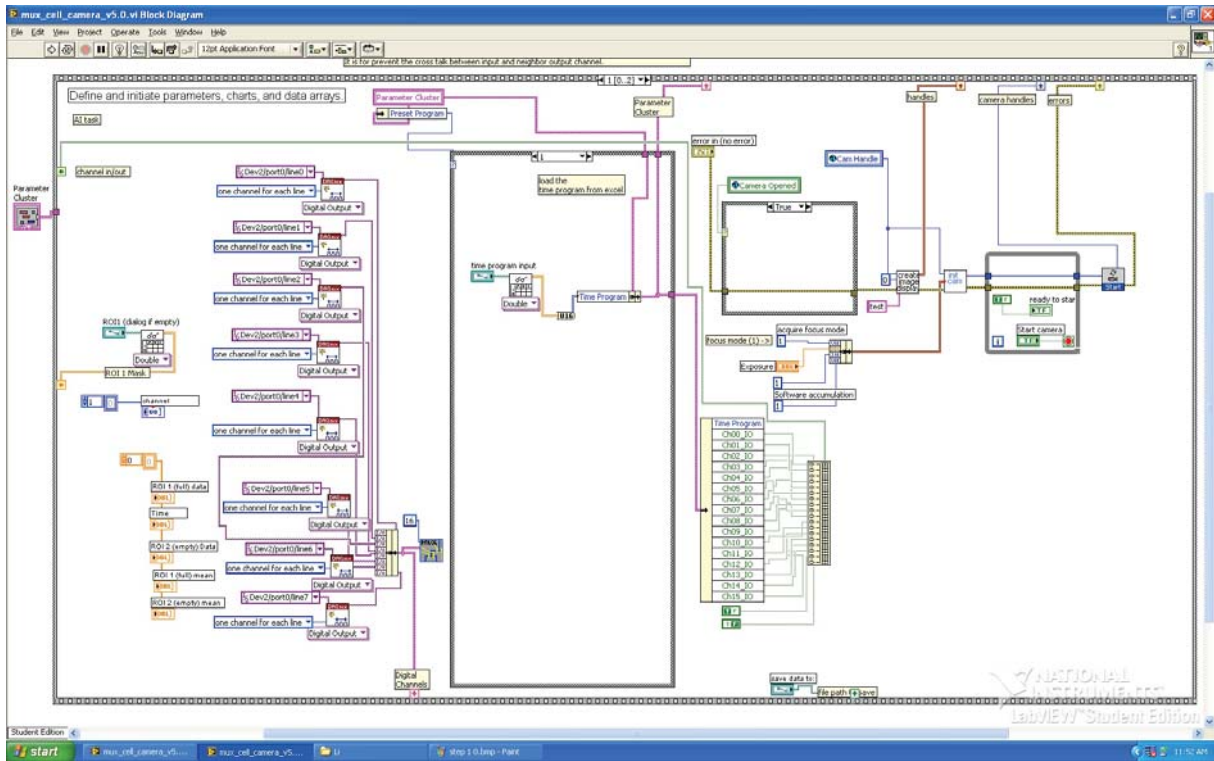


Figure C.4: Block diagram of LabVIEW application for  $\mu$ MUX control, (step 1 B)

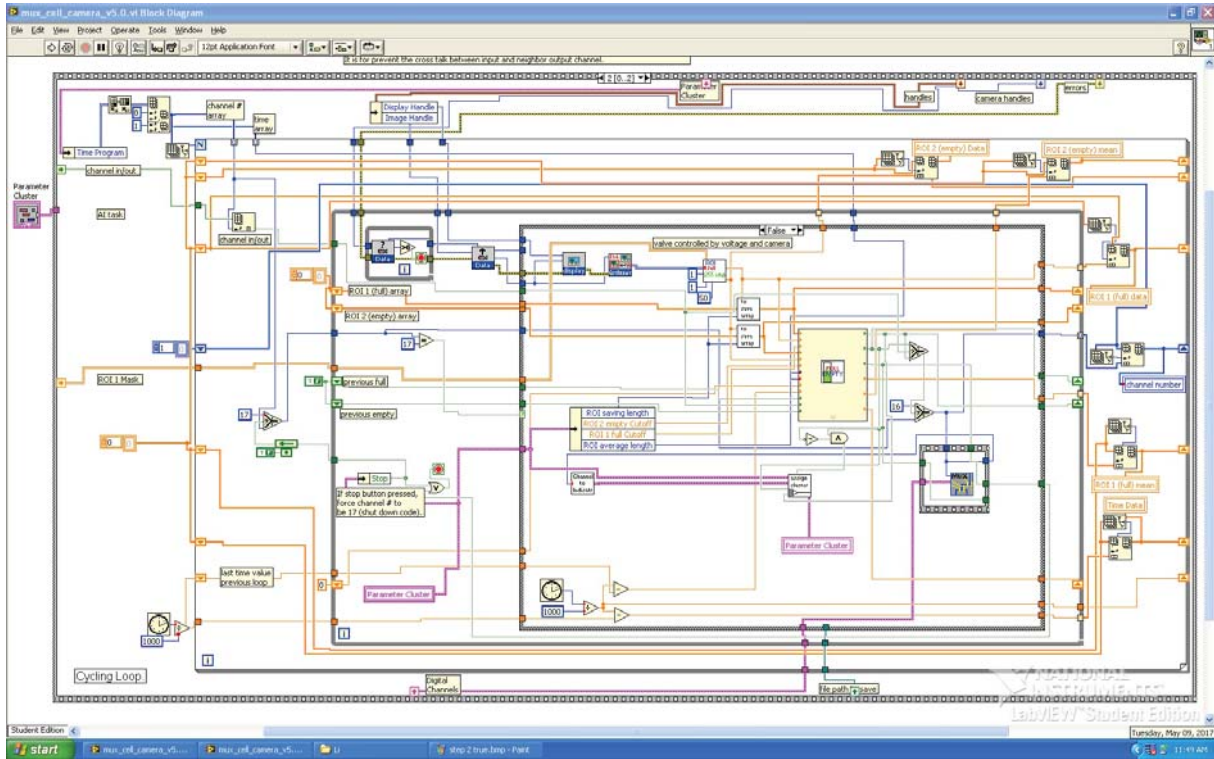


Figure C.5: Block diagram of LabVIEW application for  $\mu$ MUX control, (step 2 A)

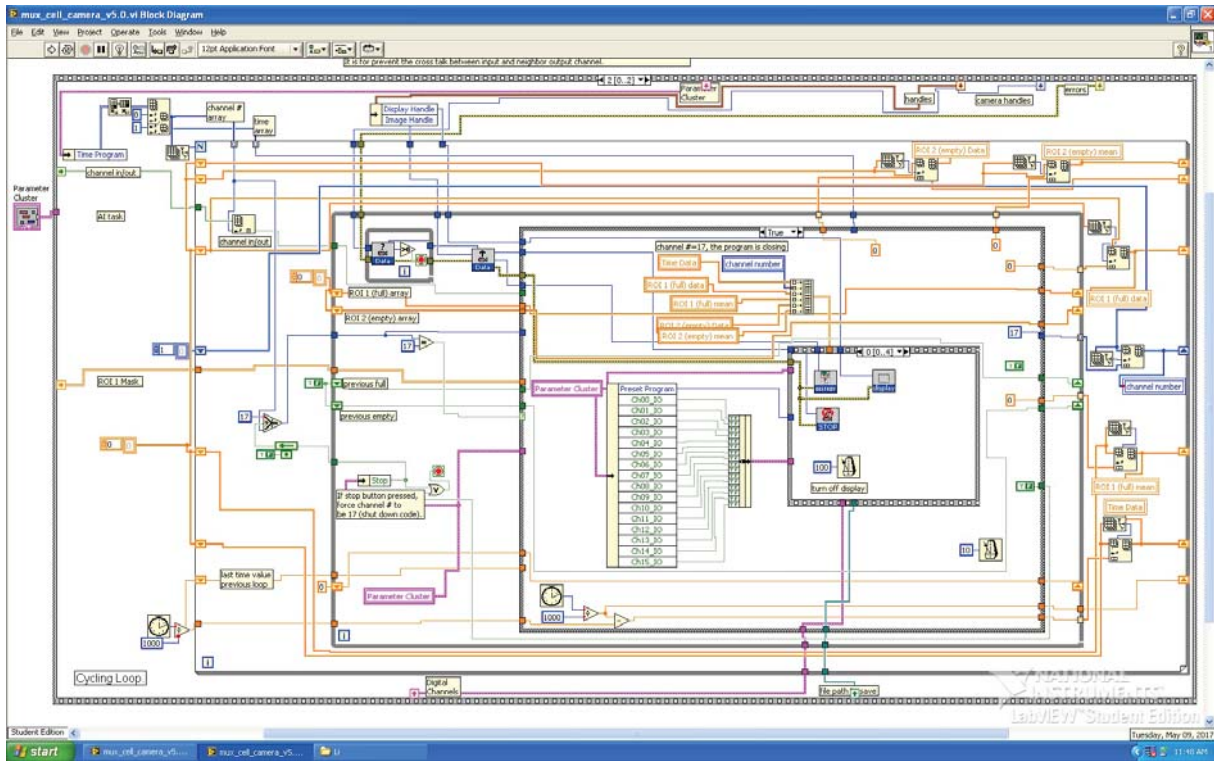


Figure C.6: Block diagram of LabVIEW application for  $\mu$ MUX control, (step 2 B)

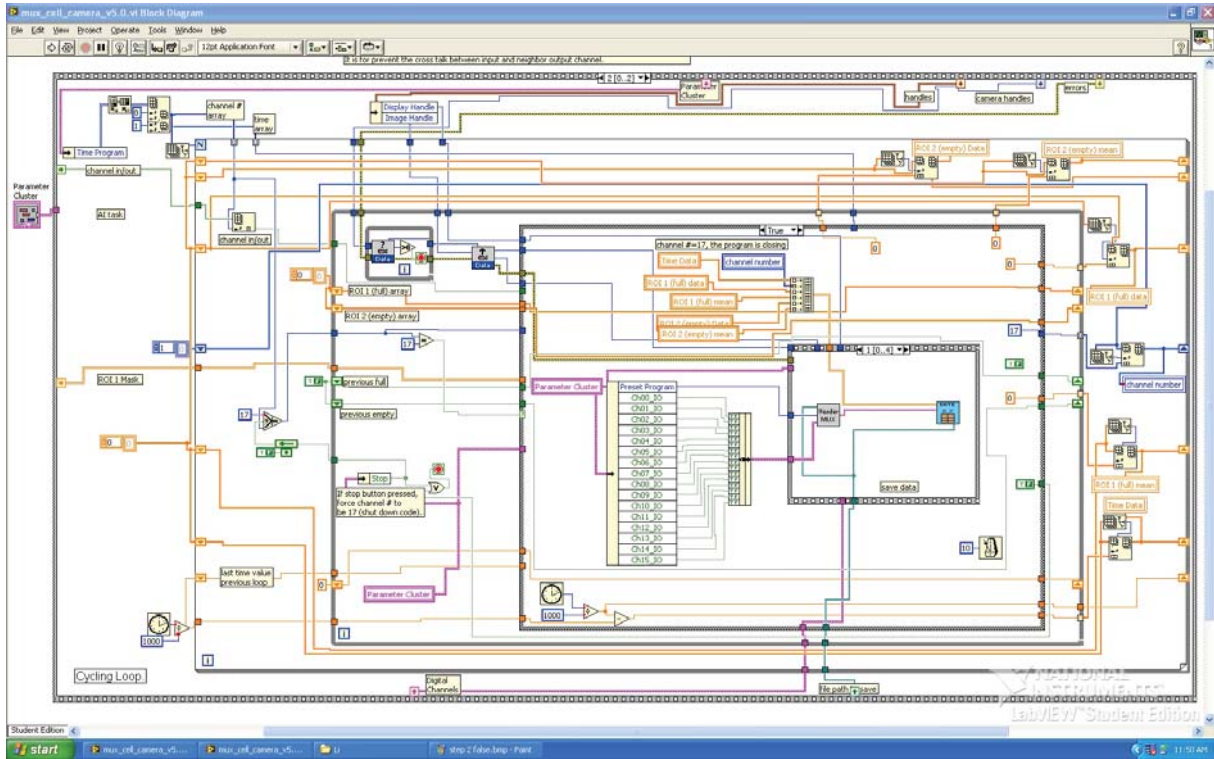


Figure C.7: Block diagram of LabVIEW application for  $\mu$ MUX control, (step 2 C)

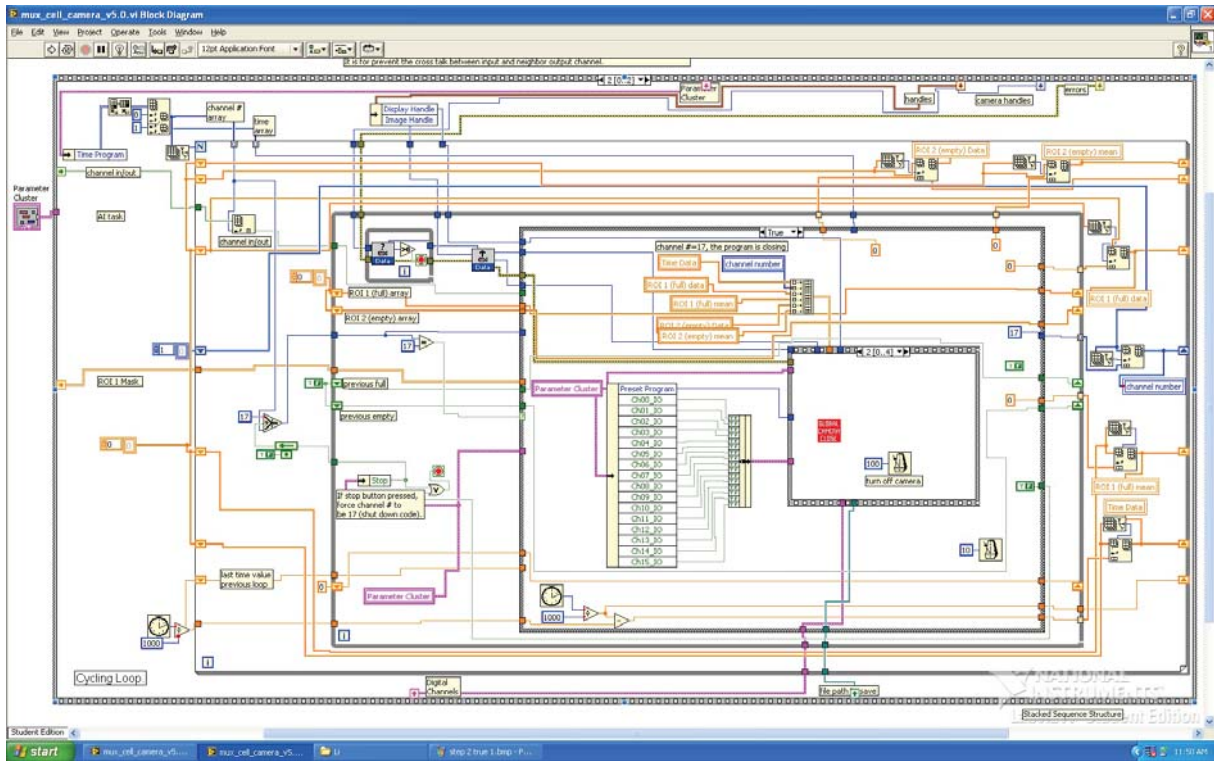


Figure C.8: Block diagram of LabVIEW application for  $\mu$ MUX control, (step 2 D)

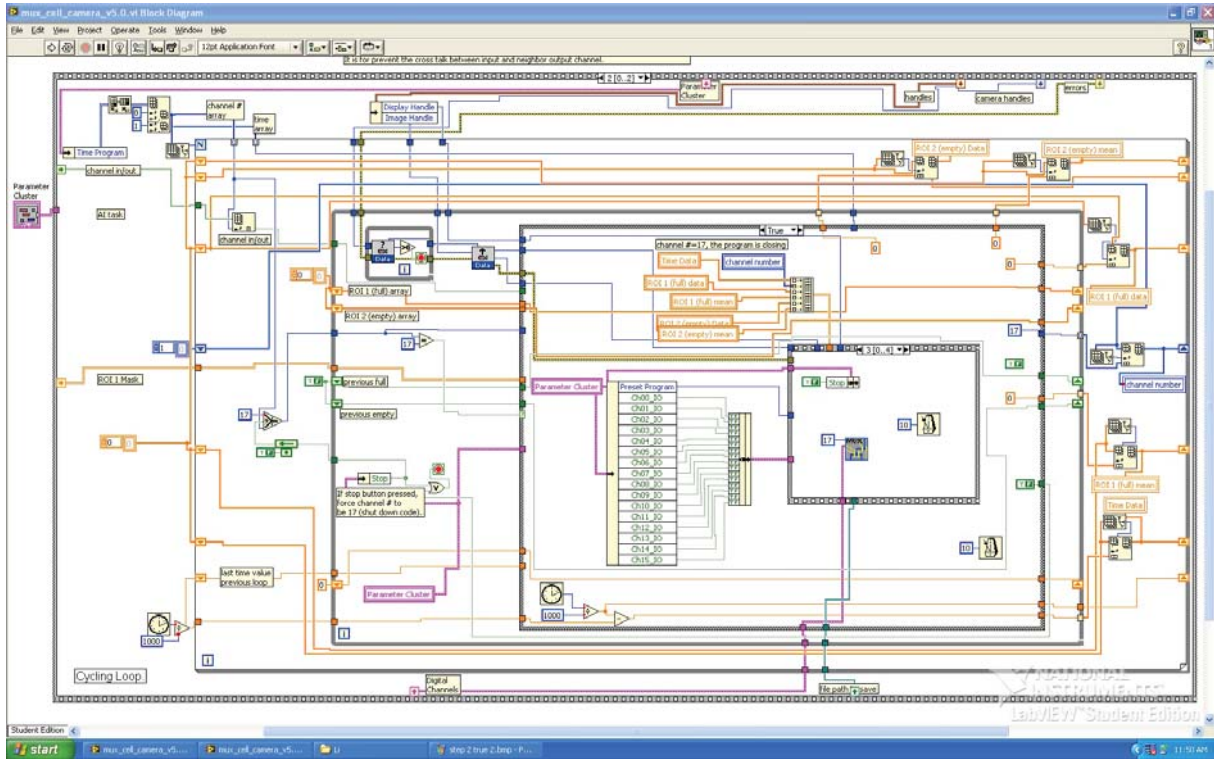


Figure C.9: Block diagram of LabVIEW application for  $\mu$ MUX control, (step 2 E)

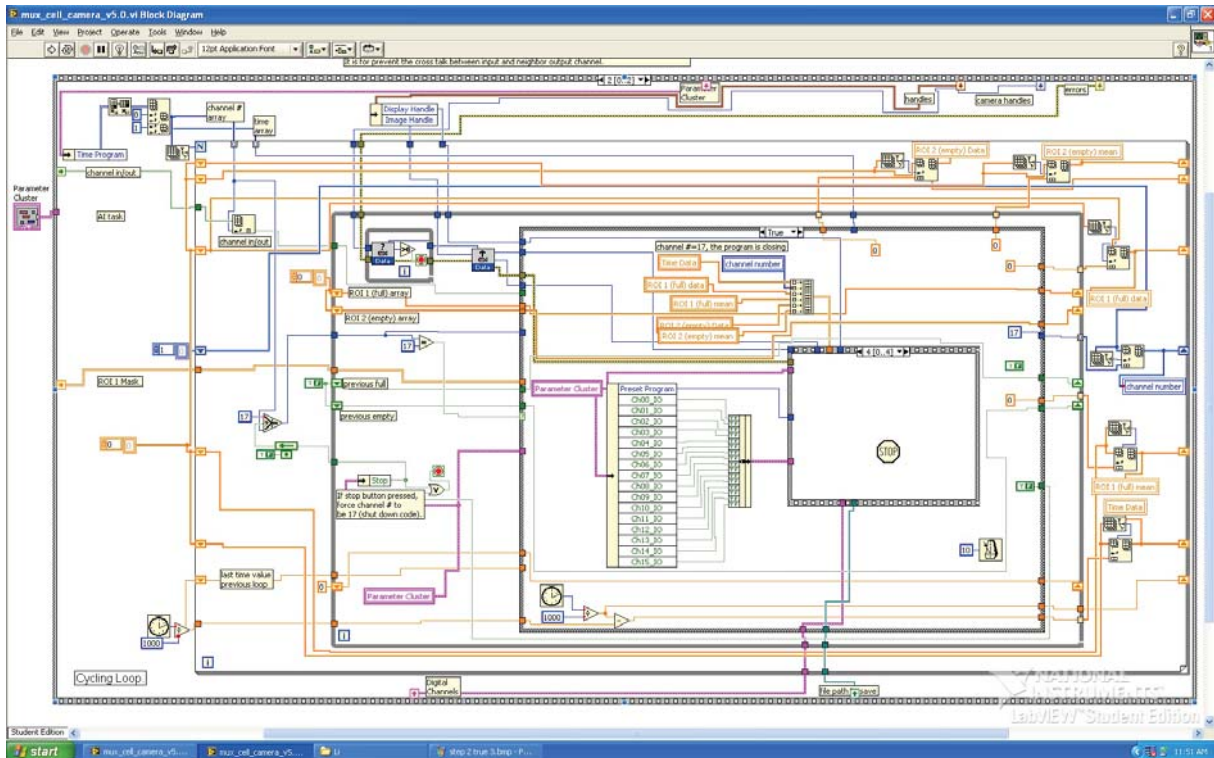


Figure C.10: Block diagram of LabVIEW application for  $\mu$ MUX control, (step 2 F)

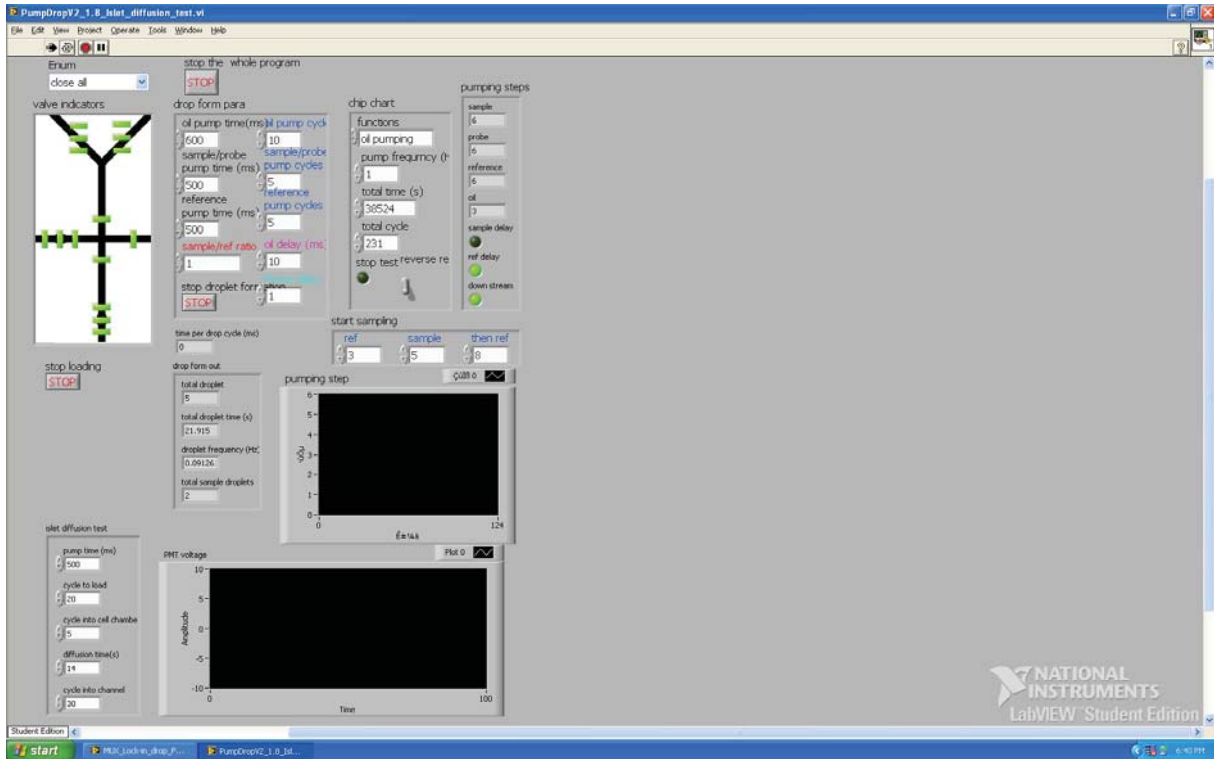


Figure C.11: Front panel of LabVIEW application for PumpDrop

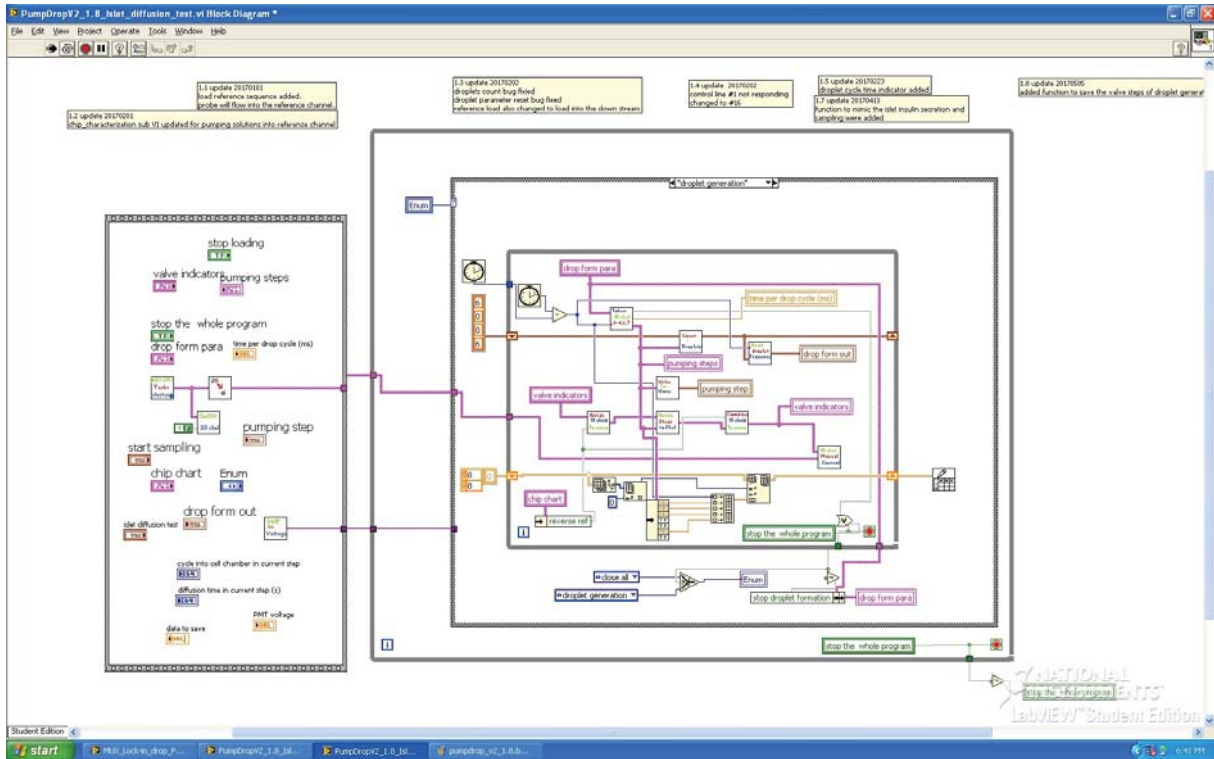


Figure C.12: Block diagram of LabVIEW application for PumpDrop

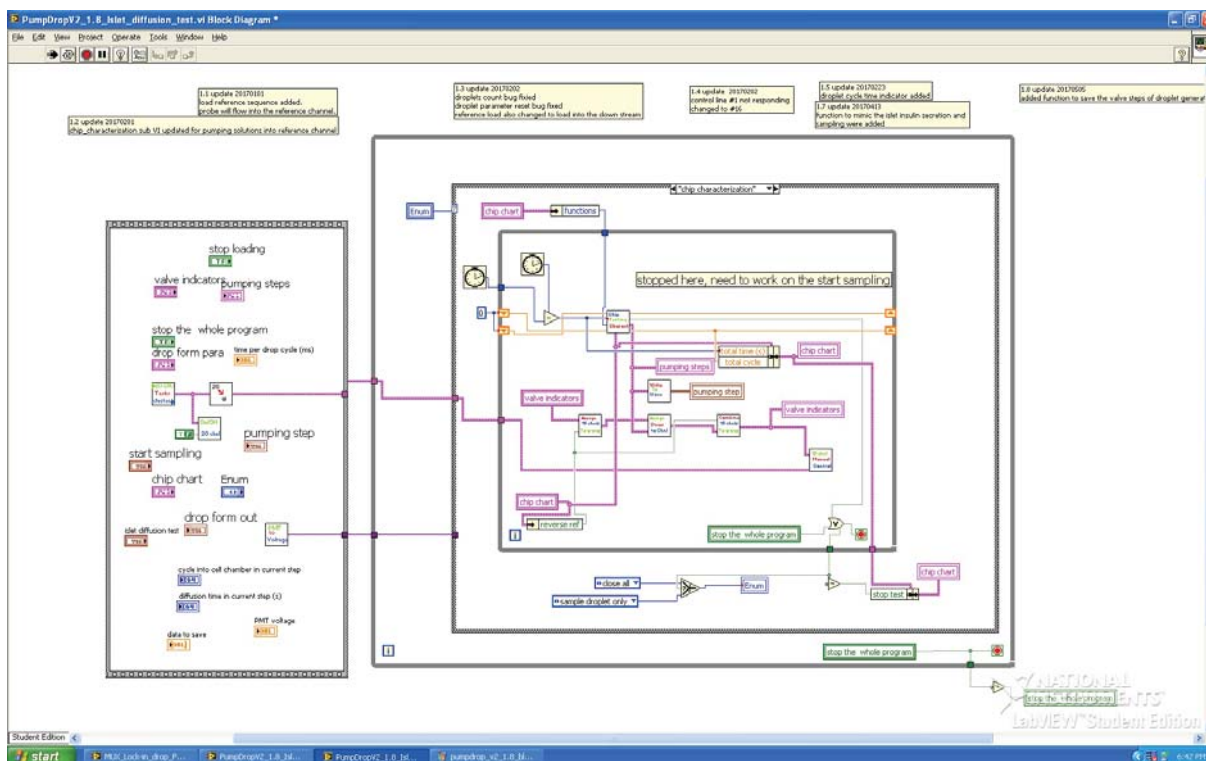


Figure C.13: Block diagram of LabVIEW application for PumpDrop (Characterization mode)

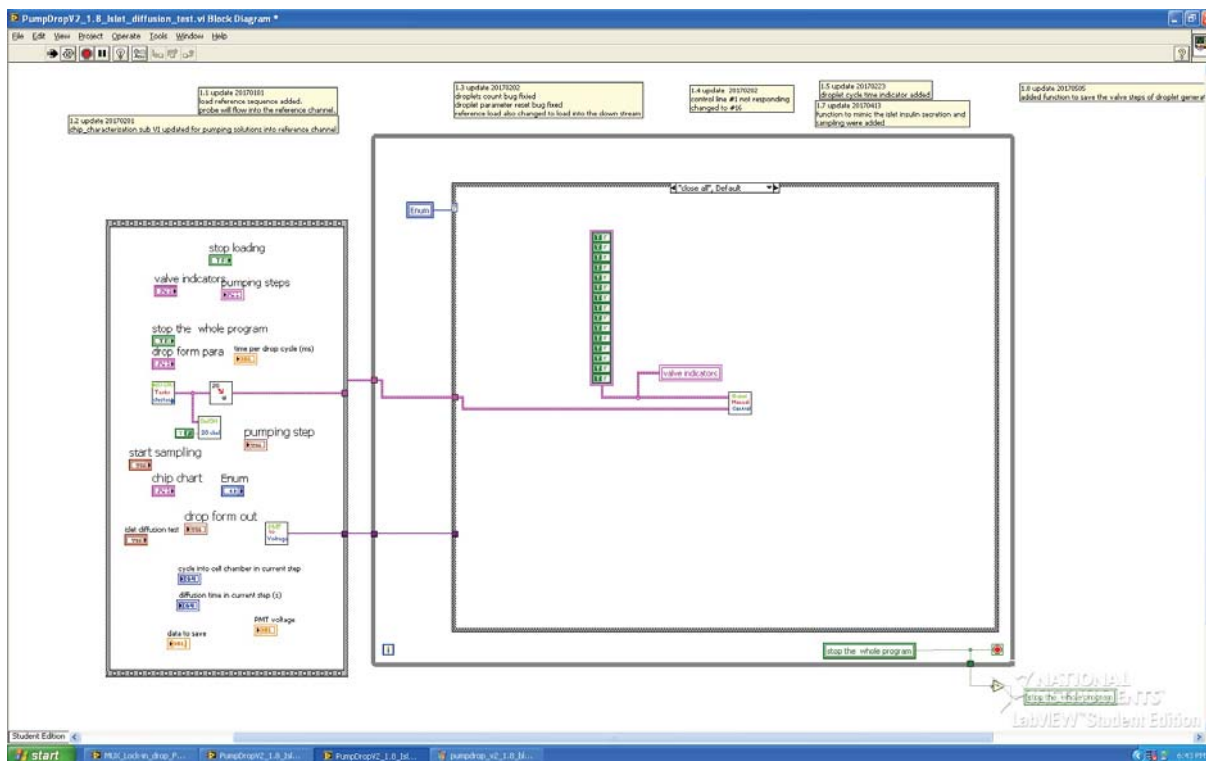


Figure C.14: Block diagram of LabVIEW application for PumpDrop (Close all valves)

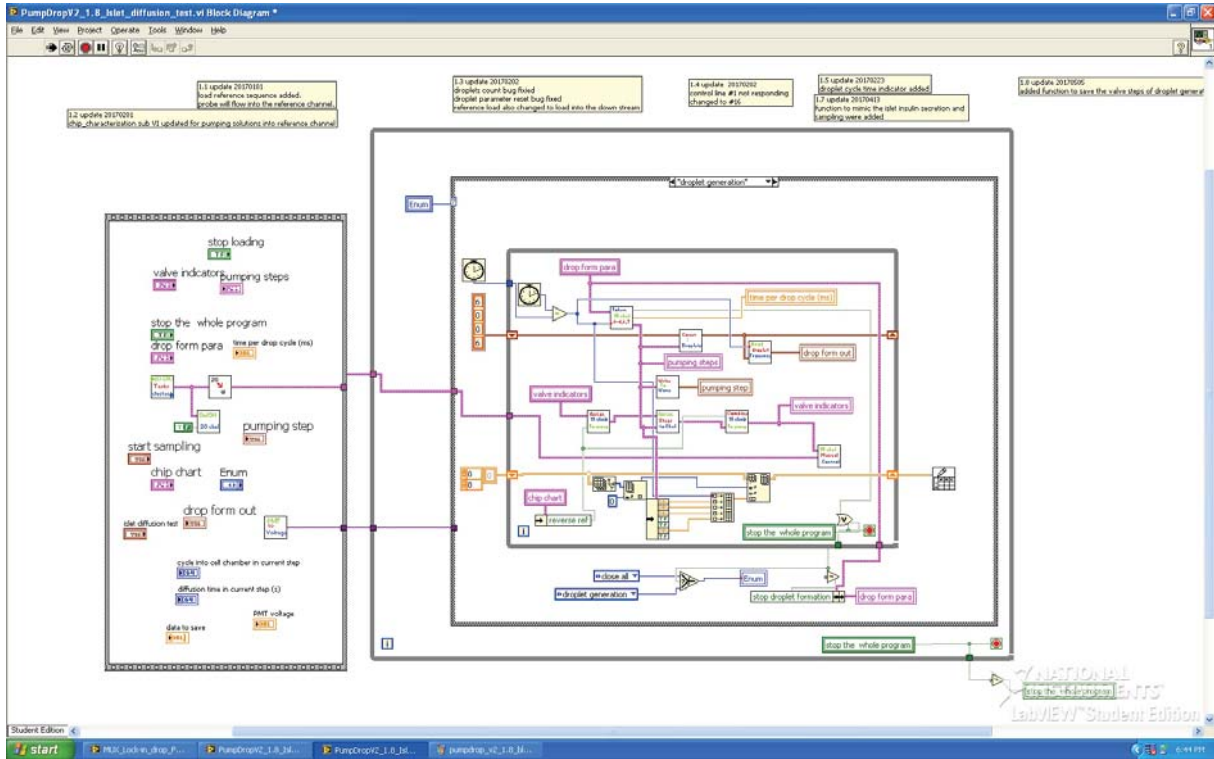


Figure C.15: Block diagram of LabVIEW application for PumpDrop (Droplet generation mode)

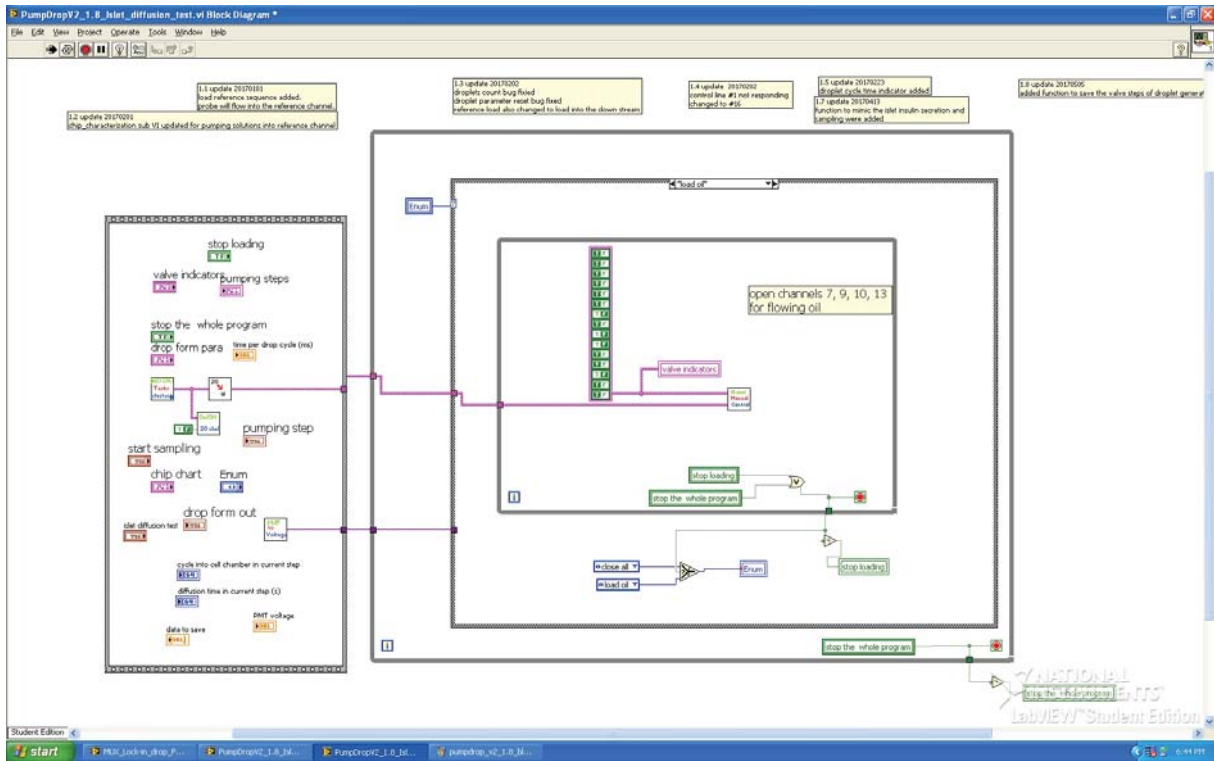


Figure C.16: Block diagram of LabVIEW application for PumpDrop (Load oil)

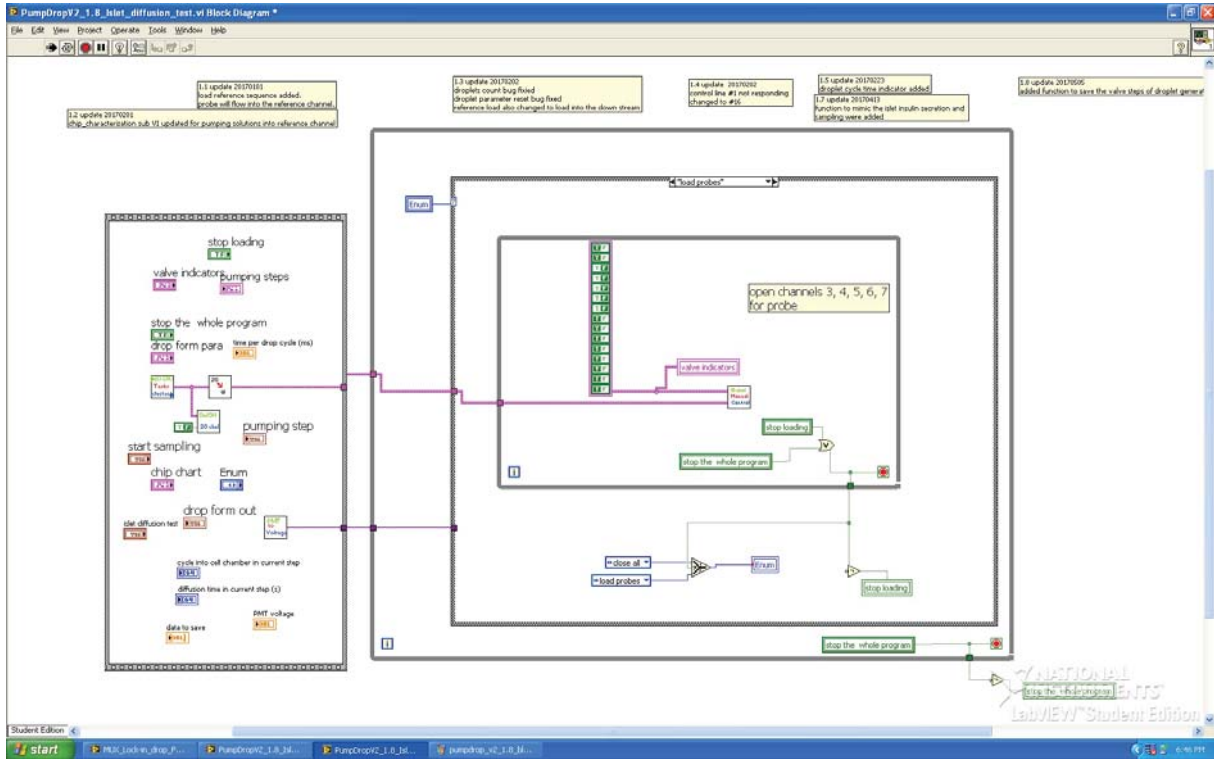


Figure C.17: Block diagram of LabVIEW application for PumpDrop (Load probes)

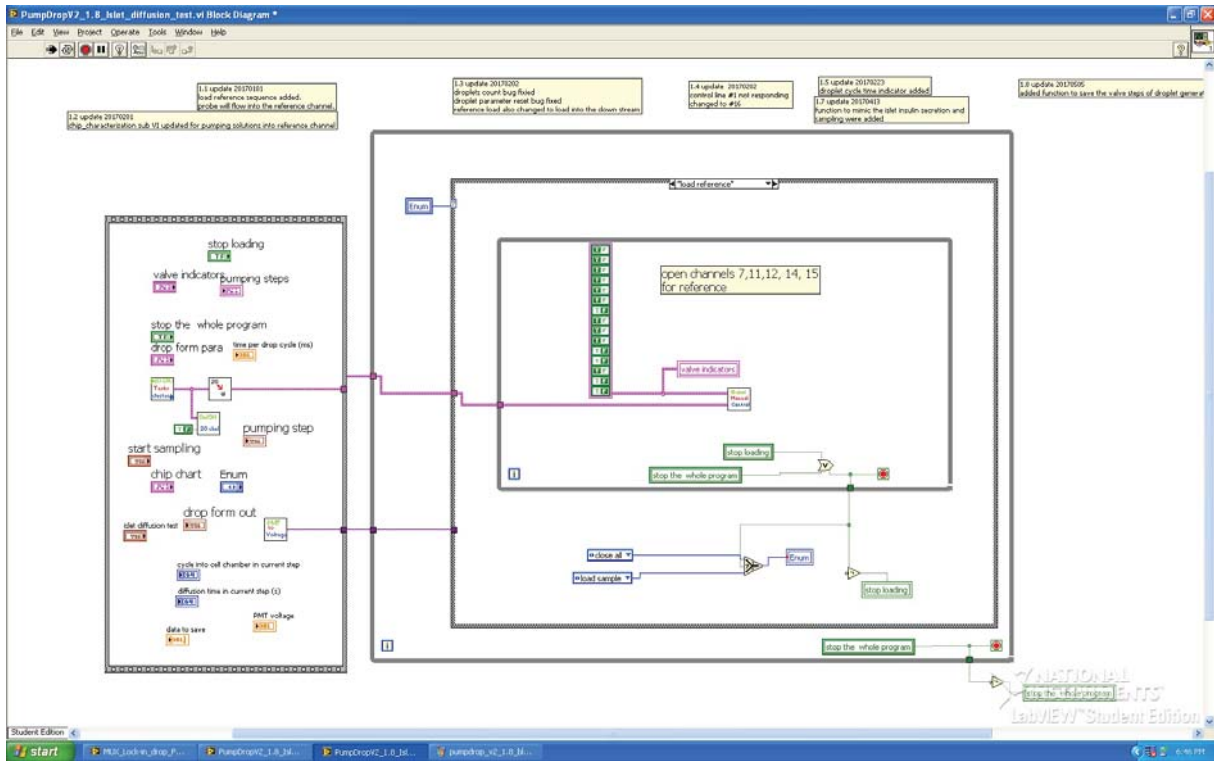


Figure C.18: Block diagram of LabVIEW application for PumpDrop (Load reference)

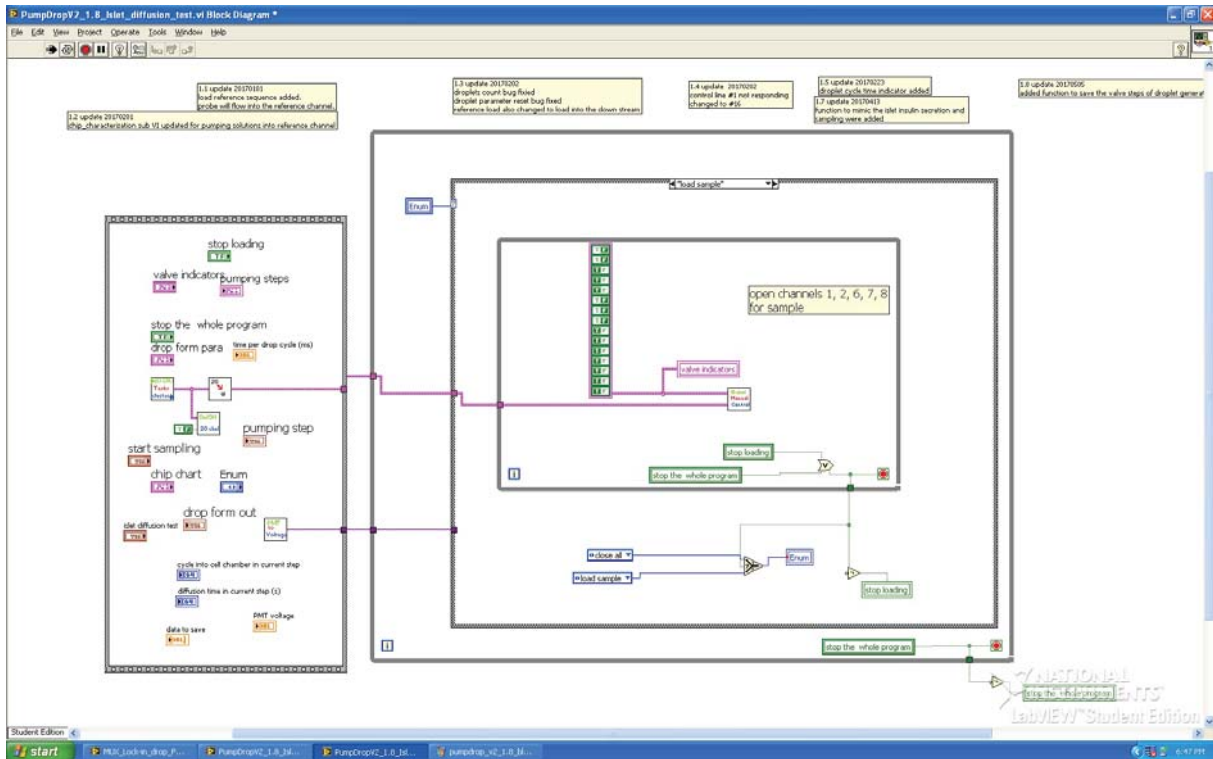


Figure C.19: Block diagram of LabVIEW application for PumpDrop (Load sample)

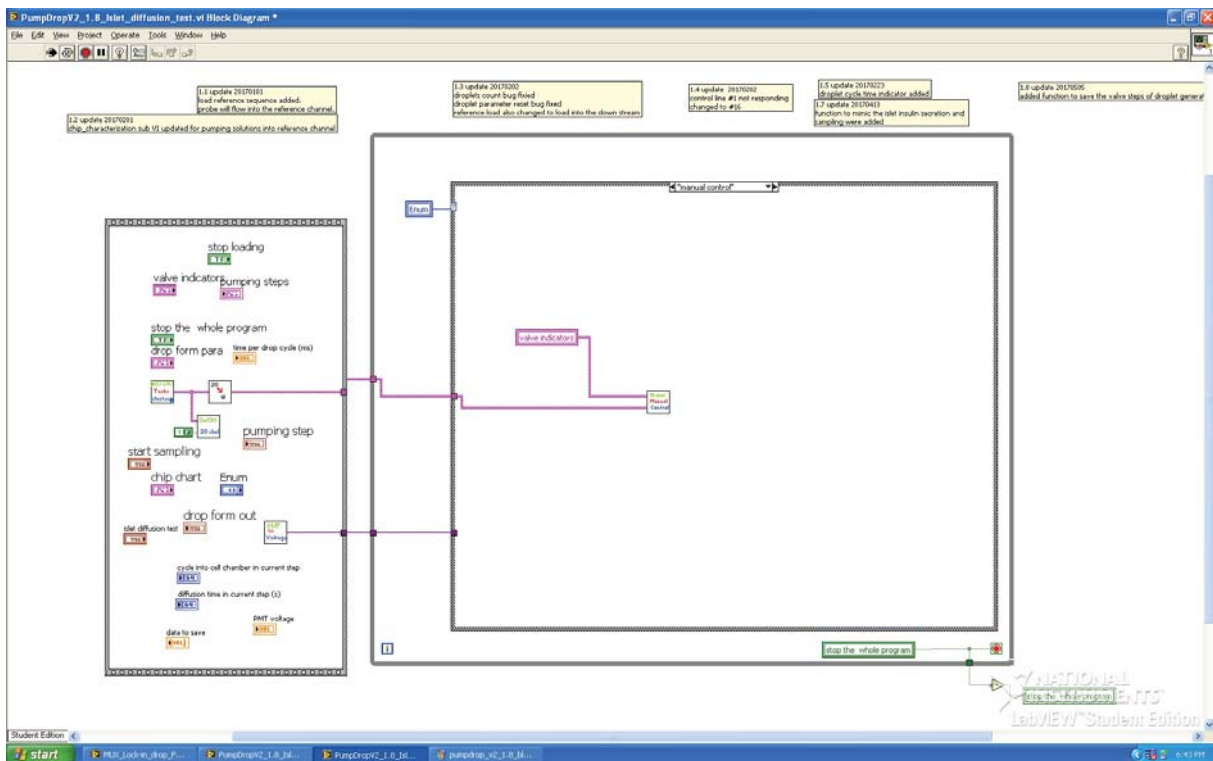


Figure C.20: Block diagram of LabVIEW application for PumpDrop (Manual control)

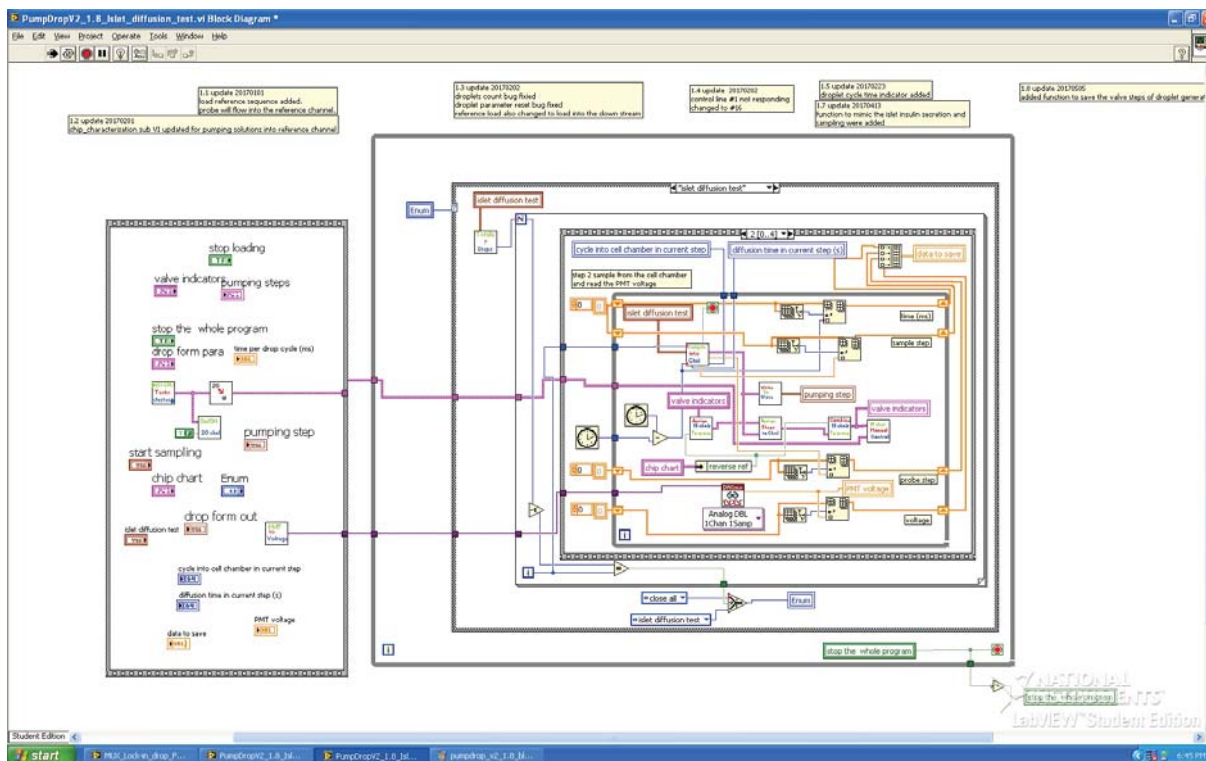


Figure C.21: Block diagram of LabVIEW application for PumpDrop (Islet mimic mode)

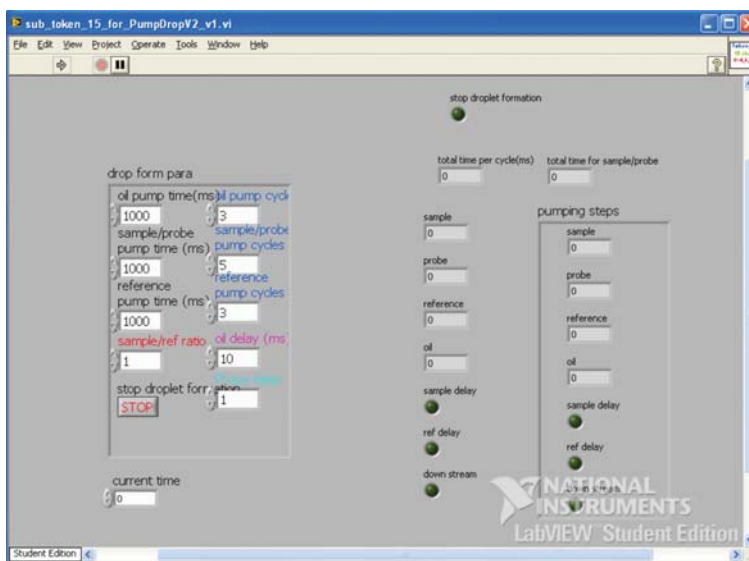


Figure C.22: SubVI front panel of LabVIEW application for PumpDrop (Calculate pumping step for droplet formation)

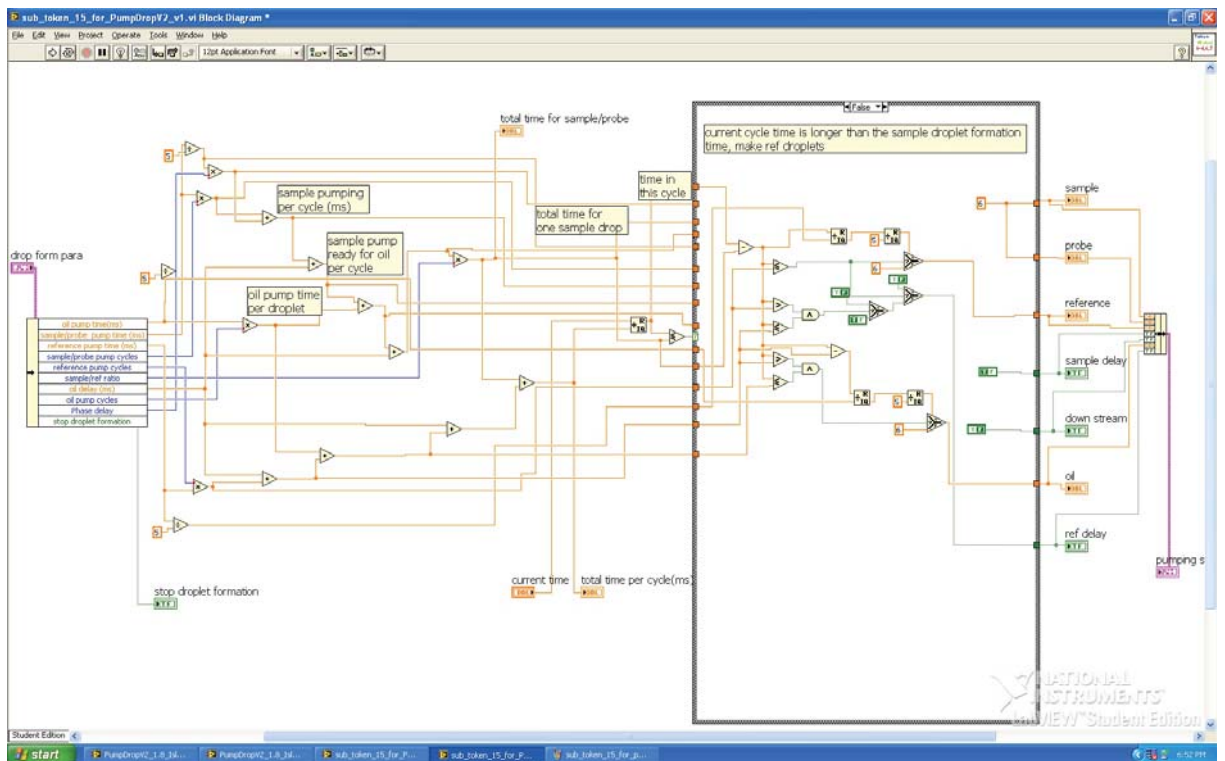


Figure C.23: SubVI block diagram of LabVIEW application for PumpDrop (Calculate pumping step for droplet formation mode)

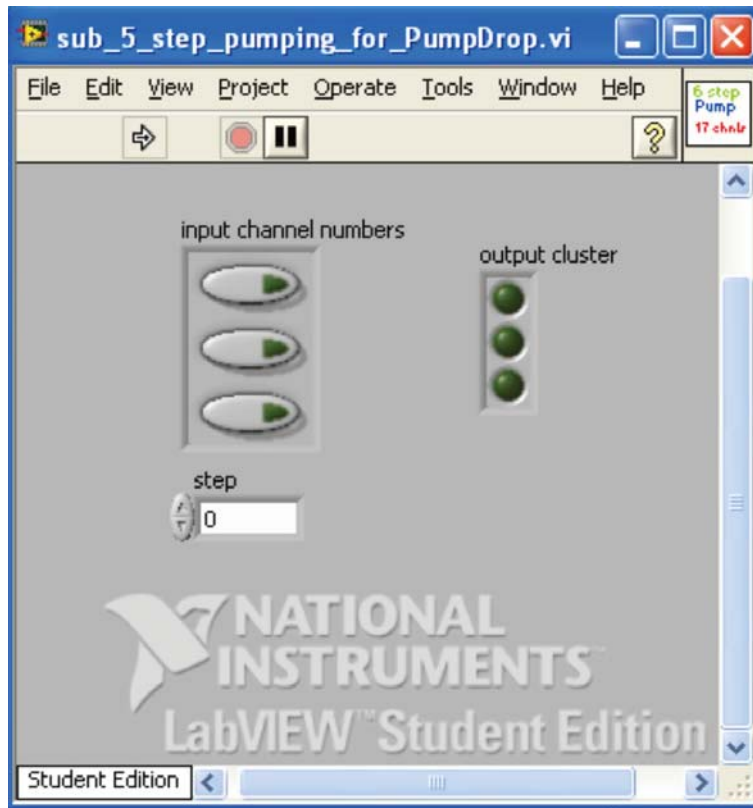


Figure C.24: SubVI front panel of LabVIEW application for PumpDrop (5 step pump)

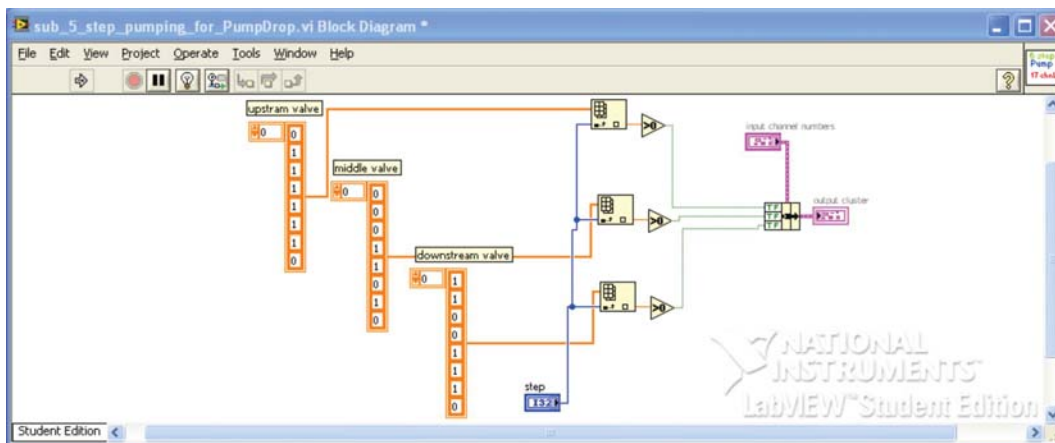


Figure C.25: SubVI block diagram of LabVIEW application for PumpDrop (5 step pump)

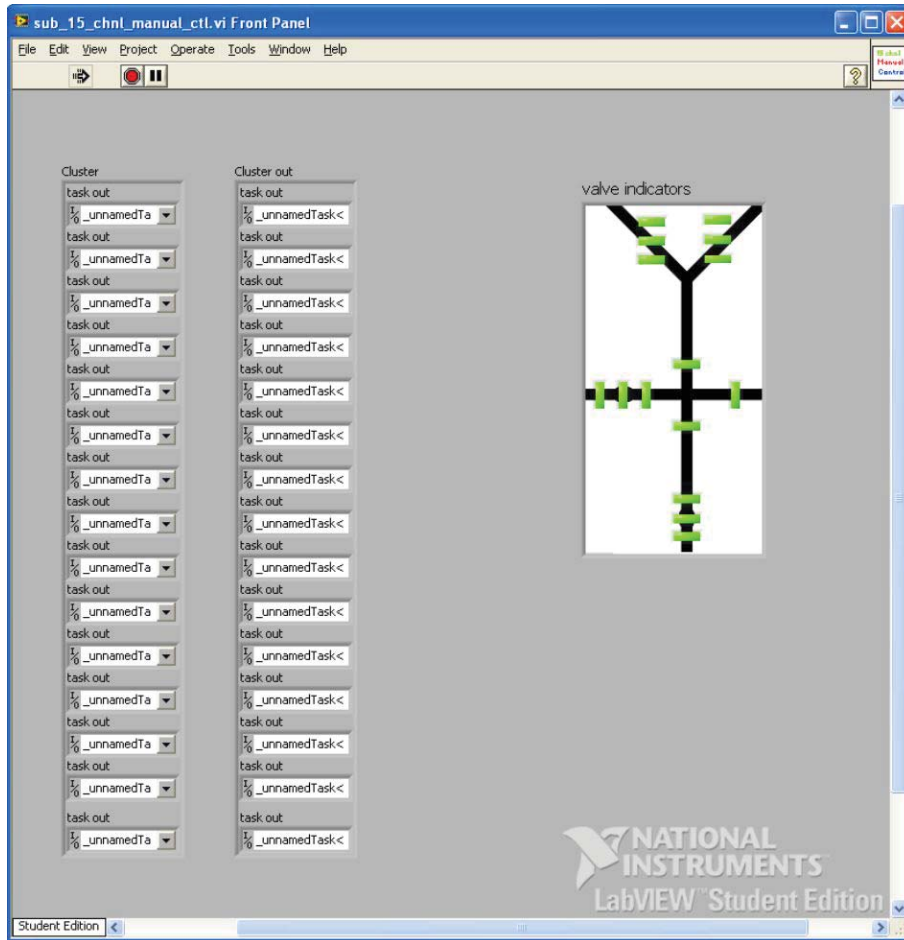


Figure C.26: SubVI front panel of LabVIEW application for PumpDrop (15 DIO channel control)

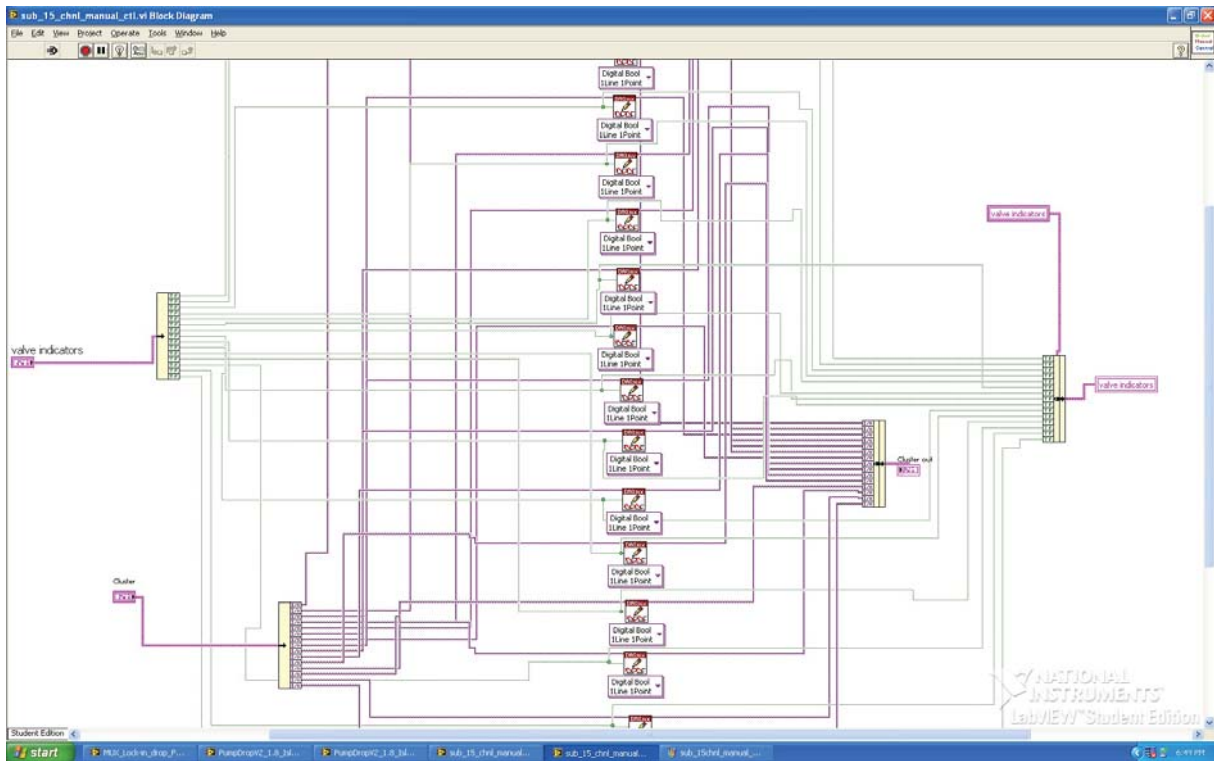


Figure C.27: SubVI block panel of LabVIEW application for PumpDrop (15 DIO channel control)

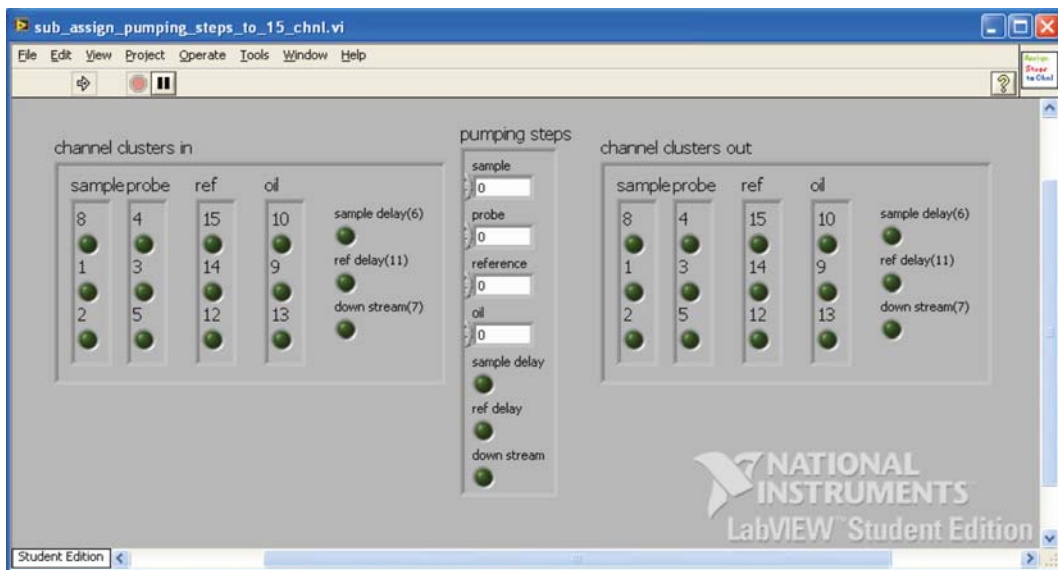


Figure C.28: SubVI front panel of LabVIEW application for PumpDrop (Assign pumping steps)

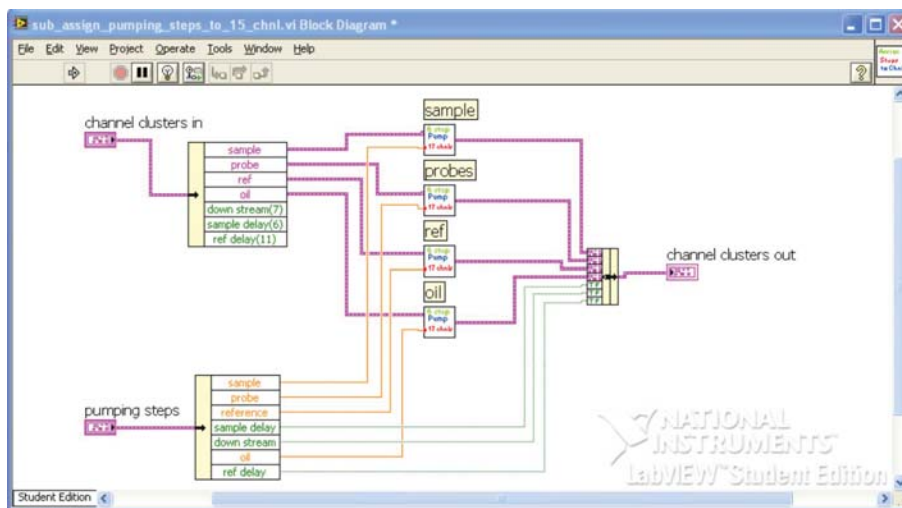


Figure C.29: SubVI block diagram of LabVIEW application for PumpDrop (Assign pumping steps)

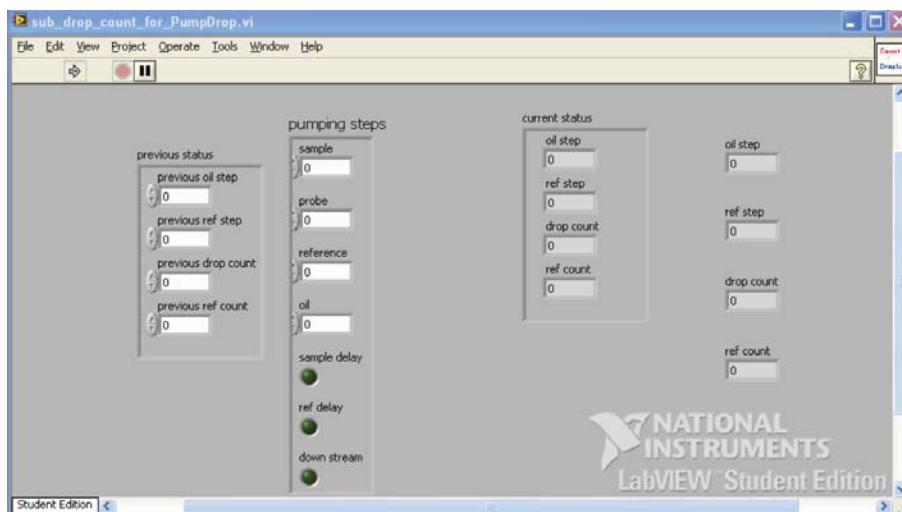


Figure C.30: SubVI front panel of LabVIEW application for PumpDrop (Count droplets)

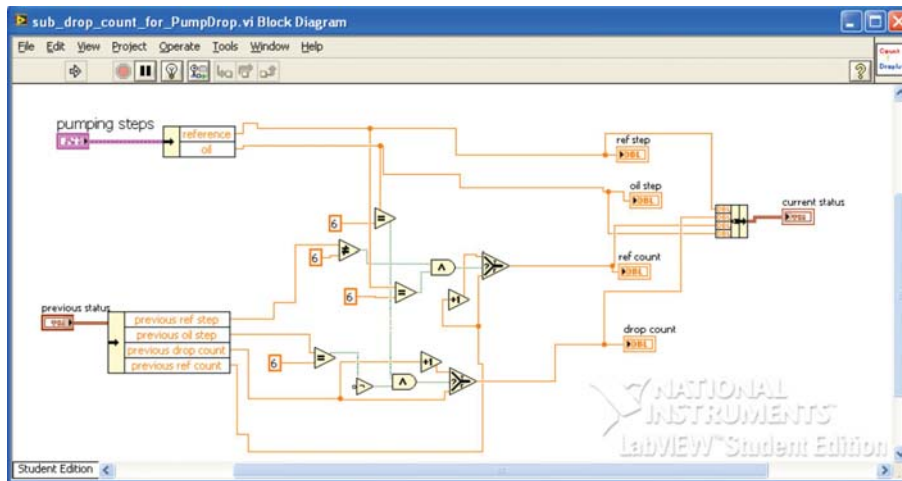


Figure C.31: SubVI block diagram of LabVIEW application for PumpDrop (Count droplets)

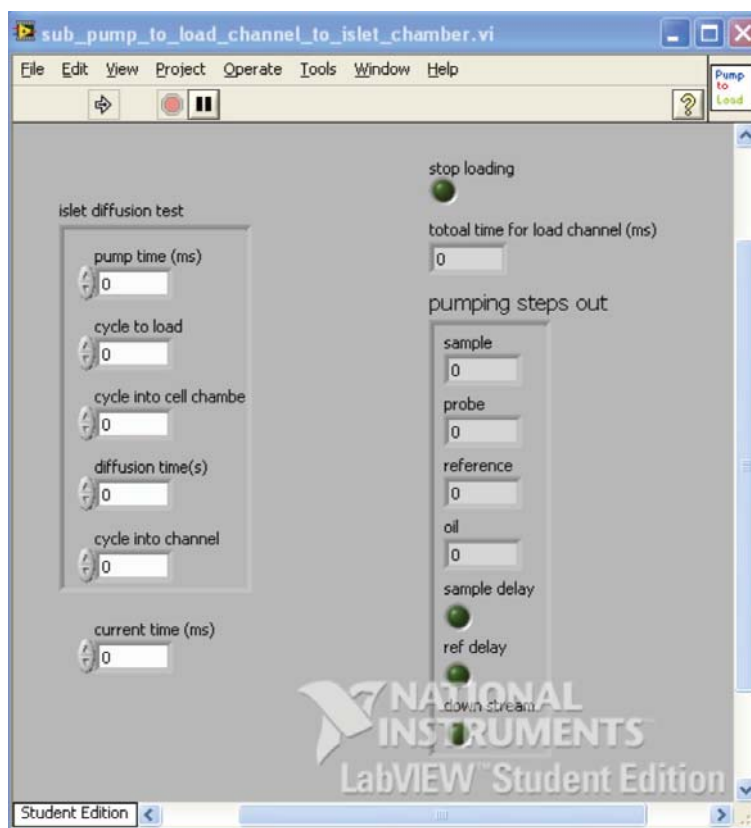


Figure C.32: SubVI front panel of LabVIEW application for PumpDrop (Load cell channel for islet mimicking)

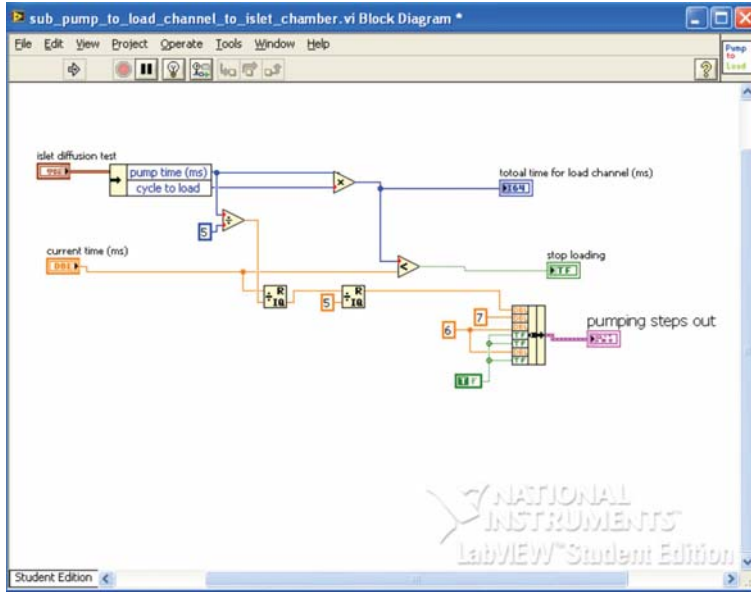


Figure C.33: SubVI block diagram of LabVIEW application for PumpDrop (Load cell channel for islet mimicking)

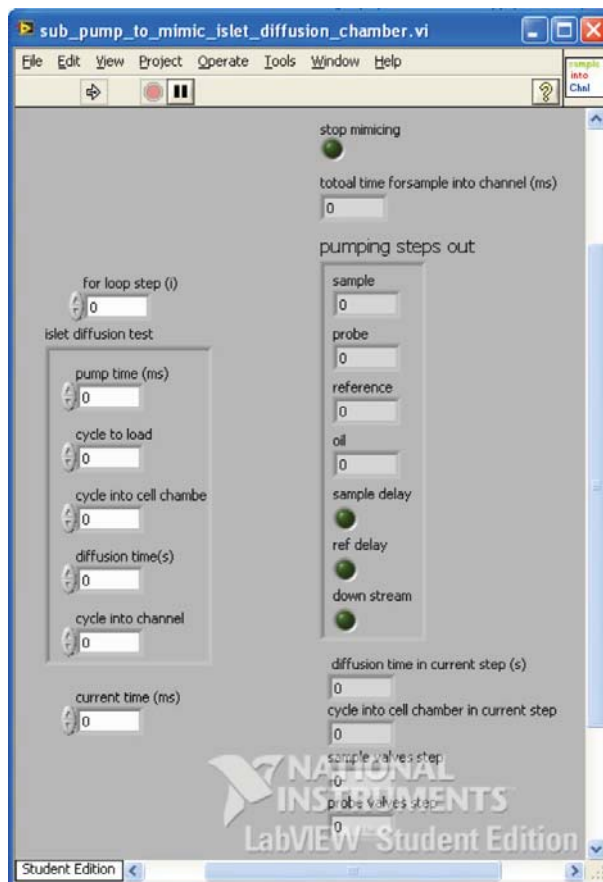


Figure C.34: SubVI front panel of LabVIEW application for PumpDrop (Incubation for islet mimicking)

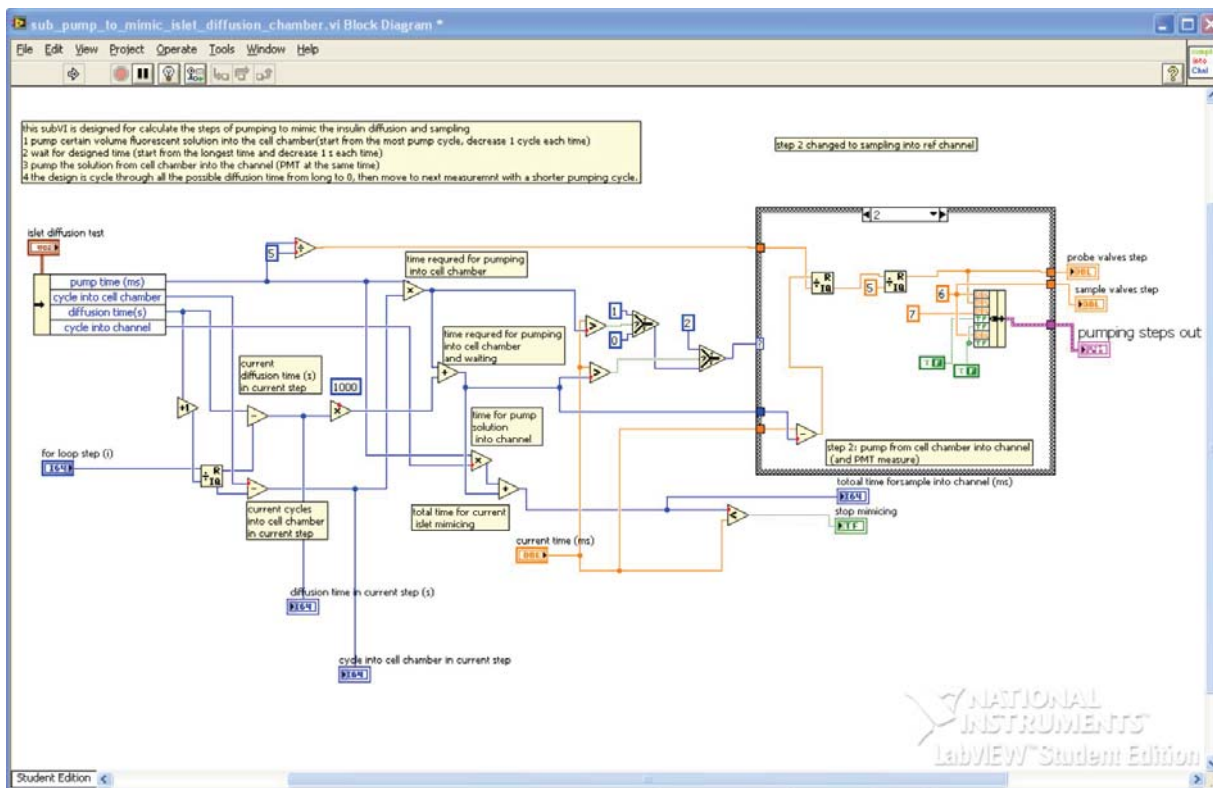


Figure C.35: SubVI block diagram of LabVIEW application for PumpDrop (Incubation for islet mimicking)

Appendix D  
Copyright Permissions

**RightsLink**®[Home](#)[Account Info](#)[Help](#)**ACS Publications**  
Most Trusted. Most Cited. Most Read.**Title:** K-Channel: A Multifunctional Architecture for Dynamically Reconfigurable Sample Processing in Droplet MicrofluidicsLogged in as:  
Xiangpeng Li  
Account #:  
3001138095**Author:** Steven R. Doonan, Ryan C. Bailey[LOGOUT](#)**Publication:** Analytical Chemistry**Publisher:** American Chemical Society**Date:** Apr 1, 2017

Copyright © 2017, American Chemical Society

**PERMISSION/LICENSE IS GRANTED FOR YOUR ORDER AT NO CHARGE**

This type of permission/license, instead of the standard Terms & Conditions, is sent to you because no fee is being charged for your order. Please note the following:

- Permission is granted for your request in both print and electronic formats, and translations.
- If figures and/or tables were requested, they may be adapted or used in part.
- Please print this page for your records and send a copy of it to your publisher/graduate school.
- Appropriate credit for the requested material should be given as follows: "Reprinted (adapted) with permission from (COMPLETE REFERENCE CITATION). Copyright (YEAR) American Chemical Society." Insert appropriate information in place of the capitalized words.
- One-time permission is granted only for the use specified in your request. No additional uses are granted (such as derivative works or other editions). For any other uses, please submit a new request.

If credit is given to another source for the material you requested, permission must be obtained from that source.

[BACK](#)[CLOSE WINDOW](#)

Copyright © 2017 [Copyright Clearance Center, Inc.](#) All Rights Reserved. [Privacy statement.](#) [Terms and Conditions.](#) Comments? We would like to hear from you. E-mail us at [customercare@copyright.com](mailto:customercare@copyright.com)



# RightsLink®

[Home](#)
[Account Info](#)
[Help](#)


**Title:** Microfluidics: reframing biological enquiry

**Author:** Todd A. Duncombe, Augusto M. Tentori, Amy E. Herr

**Publication:** Nature Reviews Molecular Cell Biology

**Publisher:** Nature Publishing Group

**Date:** Aug 21, 2015

Logged in as:  
Xiangpeng Li  
Account #:  
3001138095

[LOGOUT](#)

Copyright © 2015, Rights Managed by Nature Publishing Group

## Order Completed

Thank you for your order.

This Agreement between Xiangpeng Li ("You") and Nature Publishing Group ("Nature Publishing Group") consists of your license details and the terms and conditions provided by Nature Publishing Group and Copyright Clearance Center.

Your confirmation email will contain your order number for future reference.

### [Printable details.](#)

License Number	4092890961213
License date	Apr 20, 2017
Licensed Content Publisher	Nature Publishing Group
Licensed Content Publication	Nature Reviews Molecular Cell Biology
Licensed Content Title	Microfluidics: reframing biological enquiry
Licensed Content Author	Todd A. Duncombe, Augusto M. Tentori, Amy E. Herr
Licensed Content Date	Aug 21, 2015
Licensed Content Volume	16
Licensed Content Issue	9
Type of Use	reuse in a dissertation / thesis
Requestor type	academic/educational
Format	print and electronic
Portion	figures/tables/illustrations
Number of figures/tables/illustrations	1
High-res required	no
Figures	cell dynamics
Author of this NPG article	no
Your reference number	
Title of your thesis / dissertation	Automated microfluidic device development for metabolism, nutrient uptake, and hormone secretion analyses from primary endocrine tissues
Expected completion date	Jul 2017
Estimated size (number of pages)	200
Requestor Location	Xiangpeng Li 179 chemistry building
	AUBURN UNIVERSITY, AL 36849 United States Attn: Xiangpeng Li
Billing Type	Invoice
Billing address	Xiangpeng Li 179 chemistry building

223



# RightsLink®

[Home](#)
[Account Info](#)
[Help](#)


**Title:** Drop formation in a co-flowing ambient fluid

**Author:** Carsten Cramer, Peter Fischer, Erich J. Windhab

**Publication:** Chemical Engineering Science

**Publisher:** Elsevier

**Date:** August 2004

Copyright © 2004 Elsevier Ltd. All rights reserved.

Logged in as:  
Xiangpeng Li  
Account #:  
3001138095

[LOGOUT](#)

## Order Completed

Thank you for your order.

This Agreement between Xiangpeng Li ("You") and Elsevier ("Elsevier") consists of your license details and the terms and conditions provided by Elsevier and Copyright Clearance Center.

Your confirmation email will contain your order number for future reference.

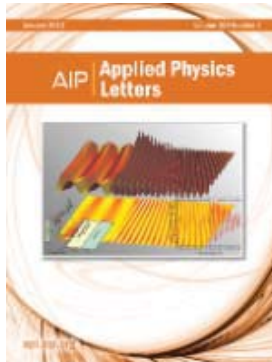
### [Printable details.](#)

License Number	4093760953120
License date	Apr 21, 2017
Licensed Content Publisher	Elsevier
Licensed Content Publication	Chemical Engineering Science
Licensed Content Title	Drop formation in a co-flowing ambient fluid
Licensed Content Author	Carsten Cramer, Peter Fischer, Erich J. Windhab
Licensed Content Date	August 2004
Licensed Content Volume	59
Licensed Content Issue	15
Licensed Content Pages	14
Type of Use	reuse in a thesis/dissertation
Portion	figures/tables/illustrations
Number of figures/tables/illustrations	1
Format	both print and electronic
Are you the author of this Elsevier article?	No
Will you be translating?	No
Order reference number	
Original figure numbers	co-flow
Title of your thesis/dissertation	Automated microfluidic device development for metabolism, nutrient uptake, and hormone secretion analyses from primary endocrine tissues
Expected completion date	Jul 2017
Estimated size (number of pages)	200
Elsevier VAT number	GB 494 6272 12
Requestor Location	Xiangpeng Li 179 chemistry building  AUBURN UNIVERSITY, AL 36849 United States Attn: Xiangpeng Li
Publisher Tax ID	98-0397604
Total	0.00 USD

[ORDER MORE](#)
[224  
CLOSE WINDOW](#)



# RightsLink®

[Home](#)
[Account Info](#)
[Help](#)


**Title:** Electrocoalescence of drops synchronized by size-dependent flow in microfluidic channels

**Author:** Keunho Ahn, Jeremy Agresti, Henry Chong, et al

**Publication:** Applied Physics Letters

**Volume/Issue:** 88/26

**Publisher:** AIP Publishing LLC

**Date:** Jun 26, 2006

**Page Count:** 3

Logged in as:  
Xiangpeng Li  
Account #:  
3001138095

[LOGOUT](#)

Rights managed by AIP Publishing LLC.

## Order Completed

Thank you for your order.

This Agreement between Xiangpeng Li ("You") and AIP Publishing LLC ("AIP Publishing LLC") consists of your license details and the terms and conditions provided by AIP Publishing LLC and Copyright Clearance Center.

Your confirmation email will contain your order number for future reference.

### [Printable details.](#)

License Number	4094971306845
License date	Apr 23, 2017
Licensed Content Publisher	AIP Publishing LLC
Licensed Content Publication	Applied Physics Letters
Licensed Content Title	Electrocoalescence of drops synchronized by size-dependent flow in microfluidic channels
Licensed Content Author	Keunho Ahn, Jeremy Agresti, Henry Chong, et al
Licensed Content Date	Jun 26, 2006
Licensed Content Volume	88
Licensed Content Issue	26
Requestor type	Student
Format	Print and electronic
Portion	Photograph/Image
Requestor Location	Xiangpeng Li 179 chemistry building
	AUBURN UNIVERSITY, AL 36849 United States Attn: Xiangpeng Li
Billing Type	Invoice
Billing address	Xiangpeng Li 179 chemistry building
	AUBURN UNIVERSITY, AL 36849 United States Attn: Xiangpeng Li
Total	0.00 USD

[ORDER MORE](#)
[CLOSE WINDOW](#)

Copyright © 2017 [Copyright Clearance Center, Inc.](#) All Rights Reserved. [Privacy statement.](#) [Terms and Conditions.](#)  
Comments? We would like to hear from you. E-mail us at [customercare@copyright.com](mailto:customercare@copyright.com)



# RightsLink®

[Home](#)
[Account Info](#)
[Help](#)


**Title:** Fluorescence-activated droplet sorting (FADS): efficient microfluidic cell sorting based on enzymatic activity

**Author:** Jean-Christophe Baret, Oliver J. Miller, Valerie Taly, Michaël Ryckelynck, Abdeslam El-Harrak, Lucas Frenz, Christian Rick, Michael L. Samuels, J. Brian Hutchison, Jeremy J. Agresti, Darren R. Link, David A. Weitz, Andrew D. Griffiths

Logged in as:  
Xiangpeng Li  
Account #:  
3001138095

[LOGOUT](#)

**Publication:** Lab on a Chip

**Publisher:** Royal Society of Chemistry

**Date:** Apr 23, 2009

Copyright © 2009, Royal Society of Chemistry

## Order Completed

Thank you for your order.

This Agreement between Xiangpeng Li ("You") and Royal Society of Chemistry ("Royal Society of Chemistry") consists of your license details and the terms and conditions provided by Royal Society of Chemistry and Copyright Clearance Center.

Your confirmation email will contain your order number for future reference.

### [Printable details.](#)

License Number	4094580793121
License date	Apr 23, 2017
Licensed Content Publisher	Royal Society of Chemistry
Licensed Content Publication	Lab on a Chip
Licensed Content Title	Fluorescence-activated droplet sorting (FADS): efficient microfluidic cell sorting based on enzymatic activity
Licensed Content Author	Jean-Christophe Baret, Oliver J. Miller, Valerie Taly, Michaël Ryckelynck, Abdeslam El-Harrak, Lucas Frenz, Christian Rick, Michael L. Samuels, J. Brian Hutchison, Jeremy J. Agresti, Darren R. Link, David A. Weitz, Andrew D. Griffiths
Licensed Content Date	Apr 23, 2009
Licensed Content Volume	9
Licensed Content Issue	13
Type of Use	Thesis/Dissertation
Requestor type	non-commercial (non-profit)
Portion	figures/tables/images
Number of figures/tables/images	1
Distribution quantity	10
Format	print and electronic
Will you be translating?	no
Order reference number	
Title of the thesis/dissertation	Automated microfluidic device development for metabolism, nutrient uptake, and hormone secretion analyses from primary endocrine tissues
Expected completion date	Jul 2017
Estimated size	200
Requestor Location	Xiangpeng Li

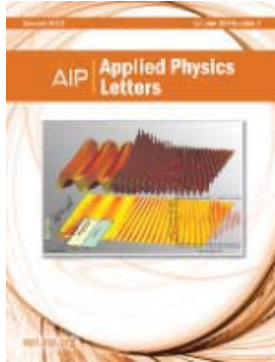
226



Home

Account Info

Help



**Title:** Microfluidic sorting with high-speed single-layer membrane valves

**Author:** Adam R. Abate,Jeremy J. Agresti,David A. Weitz

**Publication:** Applied Physics Letters

**Volume/Issue** 96/20

**Publisher:** AIP Publishing LLC

**Date:** May 17, 2010

**Page Count:** 3

Rights managed by AIP Publishing LLC.

Logged in as:  
Xiangpeng Li  
Account #:  
3001138095

LOGOUT

### Order Completed

Thank you for your order.

This Agreement between Xiangpeng Li ("You") and AIP Publishing LLC ("AIP Publishing LLC") consists of your license details and the terms and conditions provided by AIP Publishing LLC and Copyright Clearance Center.

Your confirmation email will contain your order number for future reference.

#### Printable details.

License Number	4094580860775
License date	Apr 23, 2017
Licensed Content Publisher	AIP Publishing LLC
Licensed Content Publication	Applied Physics Letters
Licensed Content Title	Microfluidic sorting with high-speed single-layer membrane valves
Licensed Content Author	Adam R. Abate,Jeremy J. Agresti,David A. Weitz
Licensed Content Date	May 17, 2010
Licensed Content Volume	96
Licensed Content Issue	20
Requestor type	Student
Format	Print and electronic
Portion	Figure/Table
Number of figures/tables	1
Requestor Location	Xiangpeng Li 179 chemistry building  AUBURN UNIVERSITY, AL 36849 United States Attn: Xiangpeng Li
Billing Type	Invoice
Billing address	Xiangpeng Li 179 chemistry building  AUBURN UNIVERSITY, AL 36849 United States Attn: Xiangpeng Li
Total	0.00 USD

ORDER MORE

CLOSE WINDOW



# RightsLink®

[Home](#)
[Account Info](#)
[Help](#)


**Title:** Culture and Sampling of Primary Adipose Tissue in Practical Microfluidic Systems

**Author:** Jessica C. Brooks

**Publication:** Springer eBook

**Publisher:** Springer

**Date:** Jan 1, 2017

Logged in as:  
Xiangpeng Li  
Account #:  
3001138095

[LOGOUT](#)

Copyright © 2017, Springer Science+Business Media LLC

## Order Completed

Thank you for your order.

This Agreement between Xiangpeng Li ("You") and Springer ("Springer") consists of your license details and the terms and conditions provided by Springer and Copyright Clearance Center.

Your confirmation email will contain your order number for future reference.

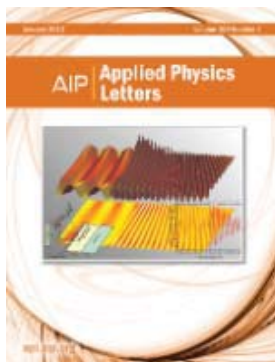
### [Printable details.](#)

License Number	4094550784749
License date	Apr 22, 2017
Licensed Content Publisher	Springer
Licensed Content Publication	Springer eBook
Licensed Content Title	Culture and Sampling of Primary Adipose Tissue in Practical Microfluidic Systems
Licensed Content Author	Jessica C. Brooks
Licensed Content Date	Jan 1, 2017
Type of Use	Thesis/Dissertation
Portion	Figures/tables/illustrations
Number of figures/tables/illustrations	1
Author of this Springer article	No
Order reference number	
Original figure numbers	fat on chip
Title of your thesis / dissertation	Automated microfluidic device development for metabolism, nutrient uptake, and hormone secretion analyses from primary endocrine tissues
Expected completion date	Jul 2017
Estimated size(pages)	200
Requestor Location	Xiangpeng Li 179 chemistry building
	AUBURN UNIVERSITY, AL 36849 United States Attn: Xiangpeng Li
Billing Type	Invoice
Billing address	Xiangpeng Li 179 chemistry building
	AUBURN UNIVERSITY, AL 36849 United States Attn: Xiangpeng Li
Total	0.00 USD

[ORDER MORE](#)
[CLOSE WINDOW](#)



# RightsLink®

[Home](#)
[Account Info](#)
[Help](#)


**Title:** Formation of dispersions using "flow focusing" in microchannels

**Author:** Shelley L. Anna, Nathalie Bontoux, Howard A. Stone

**Publication:** Applied Physics Letters

**Volume/Issue** 82/3

**Publisher:** AIP Publishing LLC

**Date:** Jan 20, 2003

**Page Count:** 3

Rights managed by AIP Publishing LLC.

Logged in as:  
Xiangpeng Li  
Account #:  
3001138095

[LOGOUT](#)

## Order Completed

Thank you for your order.

This Agreement between Xiangpeng Li ("You") and AIP Publishing LLC ("AIP Publishing LLC") consists of your license details and the terms and conditions provided by AIP Publishing LLC and Copyright Clearance Center.

Your confirmation email will contain your order number for future reference.

### [Printable details.](#)

License Number	4093760516428
License date	Apr 21, 2017
Licensed Content Publisher	AIP Publishing LLC
Licensed Content Publication	Applied Physics Letters
Licensed Content Title	Formation of dispersions using "flow focusing" in microchannels
Licensed Content Author	Shelley L. Anna, Nathalie Bontoux, Howard A. Stone
Licensed Content Date	Jan 20, 2003
Licensed Content Volume	82
Licensed Content Issue	3
Requestor type	Student
Format	Print and electronic
Portion	Figure/Table
Number of figures/tables	2
Requestor Location	Xiangpeng Li 179 chemistry building  AUBURN UNIVERSITY, AL 36849 United States Attn: Xiangpeng Li
Billing Type	Invoice
Billing address	Xiangpeng Li 179 chemistry building  AUBURN UNIVERSITY, AL 36849 United States Attn: Xiangpeng Li
Total	0.00 USD

[ORDER MORE](#)
[CLOSE WINDOW](#)

229



# RightsLink®

Home

Create Account

Help



**Title:** Rapid detection of single bacteria in unprocessed blood using Integrated Comprehensive Droplet Digital Detection

**Author:** Dong-Ku Kang, M. Monsur Ali, Kaixiang Zhang, Susan S. Huang, Ellena Peterson et al.

**Publication:** Nature Communications

**Publisher:** Nature Publishing Group

**Date:** Nov 13, 2014

Copyright © 2014, Rights Managed by Nature Publishing Group

**LOGIN**

**If you're a copyright.com user,** you can login to RightsLink using your copyright.com credentials. Already a **RightsLink user** or want to [learn more?](#)

### Creative Commons

**The article for which you have requested permission has been distributed under a Creative Commons CC-BY license (please see the article itself for the license version number). You may reuse this material without obtaining permission from Nature Publishing Group, providing that the author and the original source of publication are fully acknowledged, as per the terms of the license.**

**For license terms, please see <http://creativecommons.org/>**

**CLOSE WINDOW**

Are you the [author](#) of this NPG article?

To order reprints of this content, please contact the Nature Publishing Group reprint office by e-mail: [reprints@nature.com](mailto:reprints@nature.com).

Copyright © 2017 [Copyright Clearance Center, Inc.](#) All Rights Reserved. [Privacy statement.](#) [Terms and Conditions.](#) Comments? We would like to hear from you. E-mail us at [customercare@copyright.com](mailto:customercare@copyright.com)

# NATURE PUBLISHING GROUP LICENSE TERMS AND CONDITIONS

Apr 11, 2017

This Agreement between Xiangpeng Li ("You") and Nature Publishing Group ("Nature Publishing Group") consists of your license details and the terms and conditions provided by Nature Publishing Group and Copyright Clearance Center.

License Number	4086141316133
License date	Apr 11, 2017
Licensed Content Publisher	Nature Publishing Group
Licensed Content Publication	Nature Reviews Molecular Cell Biology
Licensed Content Title	Regulation of glucose transport by insulin: traffic control of GLUT4
Licensed Content Author	Dara Leto and Alan R. Saltiel
Licensed Content Date	May 23, 2012
Licensed Content Volume	13
Licensed Content Issue	6
Type of Use	reuse in a dissertation / thesis
Requestor type	academic/educational
Format	print and electronic
Portion	figures/tables/illustrations
Number of figures/tables/illustrations	1
High-res required	no
Figures	figure in box1
Author of this NPG article	no
Your reference number	
Title of your thesis / dissertation	Automated microfluidic device development for metabolism, nutrient uptake, and hormone secretion analyses from primary endocrine tissues
Expected completion date	Jul 2017
Estimated size (number of pages)	200
Requestor Location	Xiangpeng Li 179 chemistry building  AUBURN UNIVERSITY, AL 36849 United States Attn: Xiangpeng Li
Billing Type	Invoice
Billing Address	Xiangpeng Li 179 chemistry building  AUBURN UNIVERSITY, AL 36849 United States Attn: Xiangpeng Li
Total	<b>0.00 USD</b>
Terms and Conditions	



[My Orders](#) [My Library](#) [My Profile](#)

Welcome xzi0034@auburn.edu [Log out](#) | [Help](#)

[My Orders](#) > [Orders](#) > [All Orders](#)

## License Details

This Agreement between Xiangpeng Li ("You") and Nature Publishing Group ("Nature Publishing Group") consists of your license details and the terms and conditions provided by Nature Publishing Group and Copyright Clearance Center.

[printable details](#)

<a href="#">License Number</a>	4086510469300
<a href="#">License date</a>	Apr 12, 2017
<a href="#">Licensed Content Publisher</a>	Nature Publishing Group
<a href="#">Licensed Content Publication</a>	Nature Reviews Endocrinology
<a href="#">Licensed Content Title</a>	Importance of oestrogen receptors to preserve functional [beta]-cell mass in diabetes
<a href="#">Licensed Content Author</a>	Joseph P. Tiano and Franck Mauvais-Jarvis
<a href="#">Licensed Content Date</a>	Feb 14, 2012
<a href="#">Licensed Content Volume</a>	8
<a href="#">Licensed Content Issue</a>	6
<a href="#">Type of Use</a>	reuse in a dissertation / thesis
<a href="#">Requestor type</a>	academic/educational
<a href="#">Format</a>	print and electronic
<a href="#">Portion</a>	figures/tables/illustrations
<a href="#">Number of figures/tables/illustrations</a>	1
<a href="#">High-res required</a>	no
<a href="#">Figures</a>	insulin network v2
<a href="#">Author of this NPG article</a>	no
<a href="#">Your reference number</a>	
<a href="#">Title of your thesis / dissertation</a>	Automated microfluidic device development for metabolism, nutrient uptake, and hormone secretion analyses from primary endocrine tissues
<a href="#">Expected completion date</a>	Jul 2017
<a href="#">Estimated size (number of pages)</a>	200
<a href="#">Requestor Location</a>	Xiangpeng Li 179 chemistry building
<a href="#">Billing Type</a>	AUBURN UNIVERSITY, AL 36849 United States Attn: Xiangpeng Li Invoice
<a href="#">Billing address</a>	Xiangpeng Li 179 chemistry building
<a href="#">Total</a>	AUBURN UNIVERSITY, AL 36849 United States Attn: Xiangpeng Li <b>0.00 USD</b>

[BACK](#)

**NATURE PUBLISHING GROUP LICENSE  
TERMS AND CONDITIONS**

Apr 12, 2017

This Agreement between Xiangpeng Li ("You") and Nature Publishing Group ("Nature Publishing Group") consists of your license details and the terms and conditions provided by Nature Publishing Group and Copyright Clearance Center.

License Number	4086670473907
License date	Apr 12, 2017
Licensed Content Publisher	Nature Publishing Group
Licensed Content Publication	Nature Reviews Molecular Cell Biology
Licensed Content Title	Adipocyte dysfunctions linking obesity to insulin resistance and type 2 diabetes
Licensed Content Author	Adilson Guilherme, Joseph V. Virbasius, Vishwajeet Puri and Michael P. Czech
Licensed Content Date	May 1, 2008
Licensed Content Volume	9
Licensed Content Issue	5
Type of Use	reuse in a dissertation / thesis
Requestor type	academic/educational
Format	print and electronic
Portion	figures/tables/illustrations
Number of figures/tables/illustrations	1
High-res required	no
Figures	insulin resistance
Author of this NPG article	no
Your reference number	
Title of your thesis / dissertation	Automated microfluidic device development for metabolism, nutrient uptake, and hormone secretion analyses from primary endocrine tissues
Expected completion date	Jul 2017
Estimated size (number of pages)	200
Requestor Location	Xiangpeng Li 179 chemistry building  AUBURN UNIVERSITY, AL 36849 United States Attn: Xiangpeng Li

[Print This Page](#)

**NATURE PUBLISHING GROUP LICENSE  
TERMS AND CONDITIONS**

Apr 11, 2017

This Agreement between Xiangpeng Li ("You") and Nature Publishing Group ("Nature Publishing Group") consists of your license details and the terms and conditions provided by Nature Publishing Group and Copyright Clearance Center.

License Number	4086161236081
License date	Apr 11, 2017
Licensed Content Publisher	Nature Publishing Group
Licensed Content Publication	Nature Reviews Drug Discovery
Licensed Content Title	G protein-coupled receptors for energy metabolites as new therapeutic targets
Licensed Content Author	Clara C. Blad, Cong Tang and Stefan Offermanns
Licensed Content Date	Jul 13, 2012
Licensed Content Volume	11
Licensed Content Issue	8
Type of Use	reuse in a dissertation / thesis
Requestor type	academic/educational
Format	print and electronic
Portion	figures/tables/illustrations
Number of figures/tables/illustrations	1
High-res required	no
Figures	figure insulin secretion
Author of this NPG article	no
Your reference number	
Title of your thesis / dissertation	Automated microfluidic device development for metabolism, nutrient uptake, and hormone secretion analyses from primary endocrine tissues
Expected completion date	Jul 2017
Estimated size (number of pages)	200
Requestor Location	Xiangpeng Li 179 chemistry building  AUBURN UNIVERSITY, AL 36849 United States Attn: Xiangpeng Li
Billing Type	Invoice

[Print This Page](#)



# RightsLink®

[Home](#)
[Account Info](#)
[Help](#)


**Title:** Biocompatible surfactants for water-in-fluorocarbon emulsions

**Author:** C. Holtze, A. C. Rowat, J. J. Agresti, J. B. Hutchison, F. E. Angilè, C. H. J. Schmitz, S. Köster, H. Duan, K. J. Humphry, R. A. Scanga, J. S. Johnson, D. Pisignano, D. A. Weitz

Logged in as:  
Xiangpeng Li  
Account #:  
3001138095

[LOGOUT](#)

**Publication:** Lab on a Chip  
**Publisher:** Royal Society of Chemistry  
**Date:** Sep 2, 2008

Copyright © 2008, Royal Society of Chemistry

## Order Completed

Thank you for your order.

This Agreement between Xiangpeng Li ("You") and Royal Society of Chemistry ("Royal Society of Chemistry") consists of your license details and the terms and conditions provided by Royal Society of Chemistry and Copyright Clearance Center.

Your confirmation email will contain your order number for future reference.

### [Printable details.](#)

License Number	4093860506519
License date	Apr 21, 2017
Licensed Content Publisher	Royal Society of Chemistry
Licensed Content Publication	Lab on a Chip
Licensed Content Title	Biocompatible surfactants for water-in-fluorocarbon emulsions
Licensed Content Author	C. Holtze, A. C. Rowat, J. J. Agresti, J. B. Hutchison, F. E. Angilè, C. H. J. Schmitz, S. Köster, H. Duan, K. J. Humphry, R. A. Scanga, J. S. Johnson, D. Pisignano, D. A. Weitz
Licensed Content Date	Sep 2, 2008
Licensed Content Volume	8
Licensed Content Issue	10
Type of Use	Thesis/Dissertation
Requestor type	academic/educational
Portion	figures/tables/images
Number of figures/tables/images	1
Distribution quantity	10
Format	print and electronic
Will you be translating?	no
Order reference number	
Title of the thesis/dissertation	Automated microfluidic device development for metabolism, nutrient uptake, and hormone secretion analyses from primary endocrine tissues
Expected completion date	Jul 2017
Estimated size	200
Requestor Location	Xiangpeng Li 179 chemistry building

AUBURN UNIVERSITY, AL 36849  
United States  
Attn: Xiangpeng Li

235



# RightsLink®

[Home](#)[Create Account](#)[Help](#)

**ACS Publications**  
Most Trusted. Most Cited. Most Read.

**Title:** Lab-on-a-Disc for Fully Integrated Multiplex Immunoassays  
**Author:** Jiwoon Park, Vijaya Sunkara, Tae-Hyeong Kim, et al  
**Publication:** Analytical Chemistry  
**Publisher:** American Chemical Society  
**Date:** Mar 1, 2012

Copyright © 2012, American Chemical Society

[LOGIN](#)

If you're a **copyright.com user**, you can login to RightsLink using your copyright.com credentials. Already a **RightsLink user** or want to [learn more?](#)

## PERMISSION/LICENSE IS GRANTED FOR YOUR ORDER AT NO CHARGE

This type of permission/license, instead of the standard Terms & Conditions, is sent to you because no fee is being charged for your order. Please note the following:

- Permission is granted for your request in both print and electronic formats, and translations.
- If figures and/or tables were requested, they may be adapted or used in part.
- Please print this page for your records and send a copy of it to your publisher/graduate school.
- Appropriate credit for the requested material should be given as follows: "Reprinted (adapted) with permission from (COMPLETE REFERENCE CITATION). Copyright (YEAR) American Chemical Society." Insert appropriate information in place of the capitalized words.
- One-time permission is granted only for the use specified in your request. No additional uses are granted (such as derivative works or other editions). For any other uses, please submit a new request.

If credit is given to another source for the material you requested, permission must be obtained from that source.

[BACK](#)[CLOSE WINDOW](#)

Copyright © 2017 [Copyright Clearance Center, Inc.](#) All Rights Reserved. [Privacy statement.](#) [Terms and Conditions.](#) Comments? We would like to hear from you. E-mail us at [customercare@copyright.com](mailto:customercare@copyright.com)

**NATURE PUBLISHING GROUP LICENSE  
TERMS AND CONDITIONS**

Apr 17, 2017

This Agreement between Xiangpeng Li ("You") and Nature Publishing Group ("Nature Publishing Group") consists of your license details and the terms and conditions provided by Nature Publishing Group and Copyright Clearance Center.

License Number	4091631071362
License date	Apr 17, 2017
Licensed Content Publisher	Nature Publishing Group
Licensed Content Publication	Nature Methods
Licensed Content Title	Laminar flow cells for single-molecule studies of DNA-protein interactions
Licensed Content Author	Laurence R Brewer and Piero R Bianco
Licensed Content Date	Jun 1, 2008
Licensed Content Volume	5
Licensed Content Issue	6
Type of Use	reuse in a dissertation / thesis
Requestor type	academic/educational
Format	print and electronic
Portion	figures/tables/illustrations
Number of figures/tables/illustrations	1
High-res required	no
Figures	lamina flow
Author of this NPG article	no
Your reference number	
Title of your thesis / dissertation	Automated microfluidic device development for metabolism, nutrient uptake, and hormone secretion analyses from primary endocrine tissues
Expected completion date	Jul 2017
Estimated size (number of pages)	200
Requestor Location	Xiangpeng Li 179 chemistry building  AUBURN UNIVERSITY, AL 36849 United States Attn: Xiangpeng Li
Billing Type	Invoice



# RightsLink®

[Home](#)
[Account Info](#)
[Help](#)


**Title:** Microfluidic Large-Scale Integration  
**Author:** Todd Thorsen, Sebastian J. Maerkl, Stephen R. Quake  
**Publication:** Science  
**Publisher:** The American Association for the Advancement of Science  
**Date:** Oct 18, 2002

Logged in as:  
 Xiangpeng Li  
 Account #:  
 3001138095

[LOGOUT](#)

Copyright © 2002, The American Association for the Advancement of Science

## Order Completed

Thank you for your order.

This Agreement between Xiangpeng Li ("You") and The American Association for the Advancement of Science ("The American Association for the Advancement of Science") consists of your license details and the terms and conditions provided by The American Association for the Advancement of Science and Copyright Clearance Center.

Your confirmation email will contain your order number for future reference.

### [Printable details.](#)

License Number	4092681217609
License date	Apr 19, 2017
Licensed Content Publisher	The American Association for the Advancement of Science
Licensed Content Publication	Science
Licensed Content Title	Microfluidic Large-Scale Integration
Licensed Content Author	Todd Thorsen, Sebastian J. Maerkl, Stephen R. Quake
Licensed Content Date	Oct 18, 2002
Licensed Content Volume	298
Licensed Content Issue	5593
Volume number	298
Issue number	5593
Type of Use	Thesis / Dissertation
Requestor type	Scientist/individual at a research institution
Format	Print and electronic
Portion	Figure
Number of figures/tables	1
Order reference number	
Title of your thesis / dissertation	Automated microfluidic device development for metabolism, nutrient uptake, and hormone secretion analyses from primary endocrine tissues
Expected completion date	Jul 2017
Estimated size(pages)	200
Requestor Location	Xiangpeng Li 179 chemistry building
	AUBURN UNIVERSITY, AL 36849 United States Attn: Xiangpeng Li
Billing Type	Invoice
Billing address	Xiangpeng Li

238

**RightsLink**®[Home](#)[Account Info](#)[Help](#)**ACS Publications**  
Most Trusted. Most Cited. Most Read.**Title:** Passively Operated Microfluidic Device for Stimulation and Secretion Sampling of Single Pancreatic Islets**Author:** Leah A. Godwin, Meagan E. Pilkerton, Kennon S. Deal, et al**Publication:** Analytical Chemistry**Publisher:** American Chemical Society**Date:** Sep 1, 2011

Copyright © 2011, American Chemical Society

Logged in as:  
Xiangpeng Li  
Account #:  
3001138095[LOGOUT](#)**PERMISSION/LICENSE IS GRANTED FOR YOUR ORDER AT NO CHARGE**

This type of permission/license, instead of the standard Terms & Conditions, is sent to you because no fee is being charged for your order. Please note the following:

- Permission is granted for your request in both print and electronic formats, and translations.
- If figures and/or tables were requested, they may be adapted or used in part.
- Please print this page for your records and send a copy of it to your publisher/graduate school.
- Appropriate credit for the requested material should be given as follows: "Reprinted (adapted) with permission from (COMPLETE REFERENCE CITATION). Copyright (YEAR) American Chemical Society." Insert appropriate information in place of the capitalized words.
- One-time permission is granted only for the use specified in your request. No additional uses are granted (such as derivative works or other editions). For any other uses, please submit a new request.

If credit is given to another source for the material you requested, permission must be obtained from that source.

[BACK](#)[CLOSE WINDOW](#)

Copyright © 2017 [Copyright Clearance Center, Inc.](#) All Rights Reserved. [Privacy statement.](#) [Terms and Conditions.](#) Comments? We would like to hear from you. E-mail us at [customercare@copyright.com](mailto:customercare@copyright.com)

**RightsLink**®[Home](#)[Account Info](#)[Help](#)**ACS Publications**  
Most Trusted. Most Cited. Most Read.

**Title:** Diagnostics for the Developing World: Microfluidic Paper-Based Analytical Devices

**Author:** Andres W. Martinez, Scott T. Phillips, George M. Whitesides, et al

Logged in as:  
Xiangpeng Li  
Account #:  
3001138095

[LOGOUT](#)

**Publication:** Analytical Chemistry  
**Publisher:** American Chemical Society  
**Date:** Jan 1, 2010

Copyright © 2010, American Chemical Society

### PERMISSION/LICENSE IS GRANTED FOR YOUR ORDER AT NO CHARGE

This type of permission/license, instead of the standard Terms & Conditions, is sent to you because no fee is being charged for your order. Please note the following:

- Permission is granted for your request in both print and electronic formats, and translations.
- If figures and/or tables were requested, they may be adapted or used in part.
- Please print this page for your records and send a copy of it to your publisher/graduate school.
- Appropriate credit for the requested material should be given as follows: "Reprinted (adapted) with permission from (COMPLETE REFERENCE CITATION). Copyright (YEAR) American Chemical Society." Insert appropriate information in place of the capitalized words.
- One-time permission is granted only for the use specified in your request. No additional uses are granted (such as derivative works or other editions). For any other uses, please submit a new request.

If credit is given to another source for the material you requested, permission must be obtained from that source.

[BACK](#)[CLOSE WINDOW](#)

Copyright © 2017 [Copyright Clearance Center, Inc.](#) All Rights Reserved. [Privacy statement.](#) [Terms and Conditions.](#) Comments? We would like to hear from you. E-mail us at [customercare@copyright.com](mailto:customercare@copyright.com)



# RightsLink®

[Home](#)
[Account Info](#)
[Help](#)


**Title:** Reconstituting Organ-Level Lung Functions on a Chip

**Author:** Dongeun Huh, Benjamin D. Matthews, Akiko Mammoto, Martín Montoya-Zavala, Hong Yuan Hsin, Donald E. Ingber

Logged in as:  
Xiangpeng Li  
Account #:  
3001138095

[LOGOUT](#)

**Publication:** Science

**Publisher:** The American Association for the Advancement of Science

**Date:** Jun 25, 2010

Copyright © 2010, Copyright © 2010, American Association for the Advancement of Science

## Order Completed

Thank you for your order.

This Agreement between Xiangpeng Li ("You") and The American Association for the Advancement of Science ("The American Association for the Advancement of Science") consists of your license details and the terms and conditions provided by The American Association for the Advancement of Science and Copyright Clearance Center.

Your confirmation email will contain your order number for future reference.

### [Printable details.](#)

License Number	4093150504084
License date	Apr 20, 2017
Licensed Content Publisher	The American Association for the Advancement of Science
Licensed Content Publication	Science
Licensed Content Title	Reconstituting Organ-Level Lung Functions on a Chip
Licensed Content Author	Dongeun Huh, Benjamin D. Matthews, Akiko Mammoto, Martín Montoya-Zavala, Hong Yuan Hsin, Donald E. Ingber
Licensed Content Date	Jun 25, 2010
Licensed Content Volume	328
Licensed Content Issue	5986
Volume number	328
Issue number	5986
Type of Use	Thesis / Dissertation
Requestor type	Scientist/individual at a research institution
Format	Print and electronic
Portion	Figure
Number of figures/tables	1
Order reference number	
Title of your thesis / dissertation	Automated microfluidic device development for metabolism, nutrient uptake, and hormone secretion analyses from primary endocrine tissues
Expected completion date	Jul 2017
Estimated size(pages)	200
Requestor Location	Xiangpeng Li 179 chemistry building

AUBURN UNIVERSITY, AL 36849  
United States  
Attn: Xiangpeng Li

241



# RightsLink®

[Home](#)
[Account Info](#)
[Help](#)


**Title:** Integrated nanoliter systems  
**Author:** Jong Wook HongandStephen R Quake  
**Publication:** Nature Biotechnology  
**Publisher:** Nature Publishing Group  
**Date:** Oct 1, 2003

Logged in as:  
 Xiangpeng Li  
 Account #:  
 3001138095

[LOGOUT](#)

Copyright © 2003, Rights Managed by Nature Publishing Group

## Order Completed

Thank you for your order.

This Agreement between Xiangpeng Li ("You") and Nature Publishing Group ("Nature Publishing Group") consists of your license details and the terms and conditions provided by Nature Publishing Group and Copyright Clearance Center.

Your confirmation email will contain your order number for future reference.

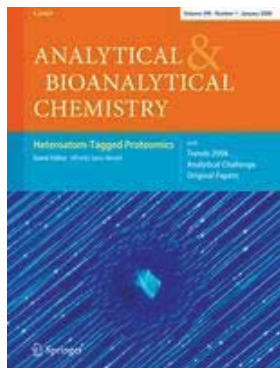
### [Printable details.](#)

License Number	4093200598912
License date	Apr 20, 2017
Licensed Content Publisher	Nature Publishing Group
Licensed Content Publication	Nature Biotechnology
Licensed Content Title	Integrated nanoliter systems
Licensed Content Author	Jong Wook HongandStephen R Quake
Licensed Content Date	Oct 1, 2003
Licensed Content Volume	21
Licensed Content Issue	10
Type of Use	reuse in a dissertation / thesis
Requestor type	academic/educational
Format	print and electronic
Portion	figures/tables/illustrations
Number of figures/tables/illustrations	1
High-res required	no
Figures	moore's law
Author of this NPG article	no
Your reference number	
Title of your thesis / dissertation	Automated microfluidic device development for metabolism, nutrient uptake, and hormone secretion analyses from primary endocrine tissues
Expected completion date	Jul 2017
Estimated size (number of pages)	200
Requestor Location	Xiangpeng Li 179 chemistry building
	AUBURN UNIVERSITY, AL 36849 United States Attn: Xiangpeng Li
Billing Type	Invoice
Billing address	Xiangpeng Li 179 chemistry building

AUBURN UNIVERSITY, AL 36849



# RightsLink®

[Home](#)
[Account Info](#)
[Help](#)


**Title:** Monitoring cell secretions on microfluidic chips using solid-phase extraction with mass spectrometry

**Author:** Colleen E. Dugan

**Publication:** Analytical and Bioanalytical Chemistry

**Publisher:** Springer

**Date:** Jan 1, 2016

Copyright © 2016, Springer-Verlag Berlin Heidelberg

Logged in as:  
Xiangpeng Li  
Account #:  
3001138095

[LOGOUT](#)

## Order Completed

Thank you for your order.

This Agreement between Xiangpeng Li ("You") and Springer ("Springer") consists of your license details and the terms and conditions provided by Springer and Copyright Clearance Center.

Your confirmation email will contain your order number for future reference.

### [Printable details.](#)

License Number	4094531292275
License date	Apr 22, 2017
Licensed Content Publisher	Springer
Licensed Content Publication	Analytical and Bioanalytical Chemistry
Licensed Content Title	Monitoring cell secretions on microfluidic chips using solid-phase extraction with mass spectrometry
Licensed Content Author	Colleen E. Dugan
Licensed Content Date	Jan 1, 2016
Licensed Content Volume	409
Licensed Content Issue	1
Type of Use	Thesis/Dissertation
Portion	Figures/tables/illustrations
Number of figures/tables/illustrations	2
Author of this Springer article	No
Order reference number	
Original figure numbers	SPE MS NEFA detection
Title of your thesis / dissertation	Automated microfluidic device development for metabolism, nutrient uptake, and hormone secretion analyses from primary endocrine tissues
Expected completion date	Jul 2017
Estimated size(pages)	200
Requestor Location	Xiangpeng Li 179 chemistry building
	AUBURN UNIVERSITY, AL 36849 United States Attn: Xiangpeng Li
Billing Type	Invoice
Billing address	Xiangpeng Li 179 chemistry building

**RightsLink**®[Home](#)[Account Info](#)[Help](#)**ACS Publications**  
Most Trusted. Most Cited. Most Read.**Title:**

Label Free Screening of Enzyme Inhibitors at Femtomole Scale Using Segmented Flow Electrospray Ionization Mass Spectrometry

Logged in as:

Xiangpeng Li

Account #:

3001138095

[LOGOUT](#)**Author:**

Shuwen Sun, Thomas R. Slaney, Robert T. Kennedy

**Publication:** Analytical Chemistry**Publisher:** American Chemical Society**Date:** Jul 1, 2012

Copyright © 2012, American Chemical Society

**PERMISSION/LICENSE IS GRANTED FOR YOUR ORDER AT NO CHARGE**

This type of permission/license, instead of the standard Terms & Conditions, is sent to you because no fee is being charged for your order. Please note the following:

- Permission is granted for your request in both print and electronic formats, and translations.
- If figures and/or tables were requested, they may be adapted or used in part.
- Please print this page for your records and send a copy of it to your publisher/graduate school.
- Appropriate credit for the requested material should be given as follows: "Reprinted (adapted) with permission from (COMPLETE REFERENCE CITATION). Copyright (YEAR) American Chemical Society." Insert appropriate information in place of the capitalized words.
- One-time permission is granted only for the use specified in your request. No additional uses are granted (such as derivative works or other editions). For any other uses, please submit a new request.

If credit is given to another source for the material you requested, permission must be obtained from that source.

[BACK](#)[CLOSE WINDOW](#)

Copyright © 2017 [Copyright Clearance Center, Inc.](#) All Rights Reserved. [Privacy statement.](#) [Terms and Conditions.](#) Comments? We would like to hear from you. E-mail us at [customercare@copyright.com](mailto:customercare@copyright.com)

## NATURE PUBLISHING GROUP LICENSE TERMS AND CONDITIONS

Apr 11, 2017

---

This Agreement between Xiangpeng Li ("You") and Nature Publishing Group ("Nature Publishing Group") consists of your license details and the terms and conditions provided by Nature Publishing Group and Copyright Clearance Center.

License Number	4086150725435
License date	Apr 11, 2017
Licensed Content Publisher	Nature Publishing Group
Licensed Content Publication	Nature Reviews Genetics
Licensed Content Title	Pancreatic organogenesis [mdash] developmental mechanisms and implications for therapy
Licensed Content Author	Helena Edlund
Licensed Content Date	Jul 1, 2002
Licensed Content Volume	3
Licensed Content Issue	7
Type of Use	reuse in a dissertation / thesis
Requestor type	academic/educational
Format	print and electronic
Portion	figures/tables/illustrations
Number of figures/tables/illustrations	1
High-res required	no
Figures	figure of pancreas
Author of this NPG article	no
Your reference number	
Title of your thesis / dissertation	Automated microfluidic device development for metabolism, nutrient uptake, and hormone secretion analyses from primary endocrine tissues
Expected completion date	Jul 2017
Estimated size (number of pages)	200
Requestor Location	Xiangpeng Li 179 chemistry building  AUBURN UNIVERSITY, AL 36849 United States Attn: Xiangpeng Li
Billing Type	Invoice
Billing Address	Xiangpeng Li 179 chemistry building

245  
AUBURN UNIVERSITY, AL 36849

**RightsLink**®[Home](#)[Account Info](#)[Help](#)**ACS Publications**  
Most Trusted. Most Cited. Most Read.

**Title:** Replication and Compression of Surface Structures with Polydimethylsiloxane Elastomer

**Author:** George C. Lisensky, Dean J. Campbell, Katie J. Beckman, et al

Logged in as:  
Xiangpeng Li  
Account #:  
3001138095

[LOGOUT](#)

**Publication:** Journal of Chemical Education

**Publisher:** American Chemical Society

**Date:** Apr 1, 1999

Copyright © 1999, American Chemical Society

### PERMISSION/LICENSE IS GRANTED FOR YOUR ORDER AT NO CHARGE

This type of permission/license, instead of the standard Terms & Conditions, is sent to you because no fee is being charged for your order. Please note the following:

- Permission is granted for your request in both print and electronic formats, and translations.
- If figures and/or tables were requested, they may be adapted or used in part.
- Please print this page for your records and send a copy of it to your publisher/graduate school.
- Appropriate credit for the requested material should be given as follows: "Reprinted (adapted) with permission from (COMPLETE REFERENCE CITATION). Copyright (YEAR) American Chemical Society." Insert appropriate information in place of the capitalized words.
- One-time permission is granted only for the use specified in your request. No additional uses are granted (such as derivative works or other editions). For any other uses, please submit a new request.

If credit is given to another source for the material you requested, permission must be obtained from that source.

[BACK](#)[CLOSE WINDOW](#)

Copyright © 2017 [Copyright Clearance Center, Inc.](#) All Rights Reserved. [Privacy statement.](#) [Terms and Conditions.](#) Comments? We would like to hear from you. E-mail us at [customercare@copyright.com](mailto:customercare@copyright.com)

PNAS

## Rights and Permissions

### About PNAS

(/site/aboutpnas/index.xhtml#PNAS\_Online)

#### Free Content

(/site/aboutpnas/index.xhtml#free)

#### Special Features

(/site/aboutpnas/special.xhtml)

#### Colloquium Papers

(/site/aboutpnas/colloquia.xhtml)

#### Article and Journal Metrics

(/site/aboutpnas/metrics.xhtml)

#### Developing Countries With Free Access to PNAS Online

(/site/aboutpnas/developingcountries.xhtml)

#### Marketing Brochure

(/site/misc/pnasmarketingbrochure.pdf)

#### RSS Feeds

(/site/aboutpnas/rss.xhtml)

#### About Direct Submission

(/site/aboutpnas/submiss.xhtml)

#### Reprints

(/site/aboutpnas/reprints.xhtml)

#### Rights and Permissions

(/site/aboutpnas/rightperm.xhtml)

#### Author Rights and Permissions

(/site/aboutpnas/rightpermfaq.xhtml)

#### Frequently Asked Questions

(/site/aboutpnas/rightpermfaq.xhtml)

#### Frequently Asked Questions

(/site/aboutpnas/faq.xhtml)

#### PNAS Portals

(/site/misc/pnas\_portals.xhtml)

#### PNAS Full-Text App

(/site/misc/pnas\_mobile.xhtml)

#### Android App Permissions

(/site/misc/androidfaq.xhtml)

#### PNAS Alerts

(/site/misc/PNASAlerts.xhtml)

### Editorial Board

(/site/misc/masthead.xhtml)

### News & Multimedia

(/multimedia)

### Subscriptions

(/site/subscriptions/index.xhtml)

### Contact

(/site/misc/contact.xhtml)

Beginning with articles submitted in Volume 106 (2009) the author(s) retains copyright to individual articles, and the National Academy of Sciences of the United States of America retains an exclusive License to Publish

(/site/misc/authorlicense.pdf) these articles and holds copyright to the collective work. Volumes 90–105 (1993–2008) copyright © National Academy of

Sciences. For volumes 1–89 (1915–1992), the author(s) retains copyright to individual articles, and the National Academy of Sciences holds copyright to collective work.

The PNAS listing on the Sherpa RoMEO publisher copyright policies and self-archiving detail pages can be found here

(http://www.sherpa.ac.uk/romeo/search.php?id=94&la=en&flDnum=).

### Requests for Permission to Reprint Material Published in PNAS

Anyone may, without requesting permission, use original figures or tables published in PNAS for noncommercial and educational use (i.e., in a review article, in a book that is not for sale), provided that the full journal reference is cited and, for articles published in volumes 90–105 (1993–2008), "Copyright (copyright year) National Academy of Sciences." Commercial reuse of figures and tables (i.e., in promotional materials, in a textbook for sale) requires permission from PNAS.

PNAS authors need not obtain permission for the following cases: 1) to use their original figures or tables in their future works; 2) to make copies of their papers for their own personal use, including classroom use, or for the personal use of colleagues, provided those copies are not for sale and are not distributed in a systematic way; 3) to include their papers as part of their dissertations; or 4) to use all or part of their articles in printed compilations of their own works. The full journal reference must be cited and, for articles published in volumes 90–105 (1993–2008), "Copyright (copyright year) National Academy of Sciences."

For permission to reprint material in volumes 1–89 (1915–1992), requests should be sent to the original authors, who hold the copyright. The full journal reference must be cited.

For permission to reprint material in volumes 90–present (1993–present), requests should be sent via email to PNASPermissions@nas.edu

(mailto:PNASPermissions@nas.edu) and must include the following information:

1. Your full name, affiliation, and title
2. Your complete mailing address, phone number, and email
3. PNAS volume number, issue number, and issue date
4. PNAS article title
5. PNAS authors' names
6. Page numbers of items to be reprinted
7. Figure/table number or portion of text to be reprinted

Requests must also include the following information about the intended use of the material:

1. Title of work in which PNAS material will appear
2. Authors/editors of work
3. Publisher of work
4. Retail price of work
5. Number of copies of work to be produced
6. Intended audience
7. Whether work is for nonprofit or commercial use

Authors whose work will be reused should be notified. PNAS cannot supply original artwork. Use of PNAS material must not imply any endorsement by



(/content/current)

Current Issue  
(/content/current)

Email Alerts  
(/site/misc/PNASAlerts.xhtml)

Subscribe  
(/site/subscriptions/index.xhtml)

RSS  
(/site/aboutpnas/rss.xhtml)

### Don't Miss

PNAS is excited to announce our latest LaTeX template (<https://www.overleaf.com/latex/templates/template-for-preparing-your-research-report-submission-to-pnas-using-overleaf/fzcbzjvpxn>) is available on Overleaf (<https://www.overleaf.com/>). Overleaf allows authors to easily create their submissions using a PNAS-formatted LaTeX template.

### Other PNAS Media

Image Gallery  
(/site/media/imagegallery.xhtml)

Video Library  
(/site/media/videolibrary.xhtml)

Follow Us on Twitter  
(<https://twitter.com/PNASNews>)

Find Us on Facebook  
(<http://www.facebook.com/pages/PNAS/1826>)

### MOST READ MOST CITED

1. Overcoming catastrophic forgetting in neural networks  
(/cgi/content/short/pnas;114/13/3521?rss=1&source=mfr)
2. Quon 3D language for quantum information  
(/cgi/content/short/pnas;114/10/2497?rss=1&source=mfr)
3. New Middle Pleistocene hominin cranium from Gruta da Aroeira (Portugal)  
(/cgi/content/short/pnas;114/13/3397?rss=1&source=mfr)
4. Anatomy of news consumption on Facebook  
(/cgi/content/short/pnas;114/12/3035?rss=1&source=mfr)
5. Opinion: Gender diversity leads to better science  
(/cgi/content/short/pnas;114/8/1740?rss=1&source=mfr)

50 Most-Read Articles »  
(/reports/most-read)



# RightsLink®

[Home](#)[Account Info](#)[Help](#)

**Title:** Microfluidic Large-Scale Integration: The Evolution of Design Rules for Biological Automation

**Author:** Jessica Melin, Stephen R. Quake

**Publication:** Annual Review of Biophysics and Biomolecular Structure

**Publisher:** Annual Reviews

**Date:** Jun 1, 2007

Copyright © 2007, Annual Reviews

Logged in as:

Xiangpeng Li

Account #:

3001138095

[LOGOUT](#)

### Permission Not Required

Material may be republished in a thesis / dissertation without obtaining additional permission from Annual Reviews, providing that the author and the original source of publication are fully acknowledged.

[BACK](#)[CLOSE WINDOW](#)

Copyright © 2017 [Copyright Clearance Center, Inc.](#) All Rights Reserved. [Privacy statement.](#) [Terms and Conditions.](#) Comments? We would like to hear from you. E-mail us at [customercare@copyright.com](mailto:customercare@copyright.com)



# RightsLink®

[Home](#)
[Account Info](#)
[Help](#)


**Title:** Scaling by shrinking: empowering single-cell 'omics' with microfluidic devices

**Author:** Sanjay M. Prakadan, Alex K. Shalek, David A. Weitz

**Publication:** Nature Reviews Genetics

**Publisher:** Nature Publishing Group

**Date:** Apr 10, 2017

Logged in as:  
Xiangpeng Li  
Account #:  
3001138095

[LOGOUT](#)

Copyright © 2017, Rights Managed by Nature Publishing Group

## Order Completed

Thank you for your order.

This Agreement between Xiangpeng Li ("You") and Nature Publishing Group ("Nature Publishing Group") consists of your license details and the terms and conditions provided by Nature Publishing Group and Copyright Clearance Center.

Your confirmation email will contain your order number for future reference.

### [Printable details.](#)

License Number	4092760305428
License date	Apr 19, 2017
Licensed Content Publisher	Nature Publishing Group
Licensed Content Publication	Nature Reviews Genetics
Licensed Content Title	Scaling by shrinking: empowering single-cell 'omics' with microfluidic devices
Licensed Content Author	Sanjay M. Prakadan, Alex K. Shalek, David A. Weitz
Licensed Content Date	Apr 10, 2017
Type of Use	reuse in a dissertation / thesis
Requestor type	academic/educational
Format	print and electronic
Portion	figures/tables/illustrations
Number of figures/tables/illustrations	1
High-res required	no
Figures	single cell trapping
Author of this NPG article	no
Your reference number	
Title of your thesis / dissertation	Automated microfluidic device development for metabolism, nutrient uptake, and hormone secretion analyses from primary endocrine tissues
Expected completion date	Jul 2017
Estimated size (number of pages)	200
Requestor Location	Xiangpeng Li 179 chemistry building
	AUBURN UNIVERSITY, AL 36849 United States Attn: Xiangpeng Li
Billing Type	Invoice
Billing address	Xiangpeng Li 179 chemistry building

AUBURN UNIVERSITY, AL 36849



# RightsLink®

[Home](#)
[Account Info](#)
[Help](#)


**Title:** Cell-phone-based measurement of TSH using Mie scatter optimized lateral flow assays

**Author:** David J. You, Tu San Park, Jeong-Yeol Yoon

**Publication:** Biosensors and Bioelectronics

**Publisher:** Elsevier

**Date:** 15 February 2013

Copyright © 2012 Elsevier B.V. All rights reserved.

Logged in as:  
Xiangpeng Li  
Account #:  
3001138095

[LOGOUT](#)

## Order Completed

Thank you for your order.

This Agreement between Xiangpeng Li ("You") and Elsevier ("Elsevier") consists of your license details and the terms and conditions provided by Elsevier and Copyright Clearance Center.

Your confirmation email will contain your order number for future reference.

### [Printable details.](#)

License Number	4092681108470
License date	Apr 19, 2017
Licensed Content Publisher	Elsevier
Licensed Content Publication	Biosensors and Bioelectronics
Licensed Content Title	Cell-phone-based measurement of TSH using Mie scatter optimized lateral flow assays
Licensed Content Author	David J. You, Tu San Park, Jeong-Yeol Yoon
Licensed Content Date	15 February 2013
Licensed Content Volume	40
Licensed Content Issue	1
Licensed Content Pages	6
Type of Use	reuse in a thesis/dissertation
Portion	figures/tables/illustrations
Number of figures/tables/illustrations	1
Format	both print and electronic
Are you the author of this Elsevier article?	No
Will you be translating?	No
Order reference number	
Original figure numbers	1
Title of your thesis/dissertation	Automated microfluidic device development for metabolism, nutrient uptake, and hormone secretion analyses from primary endocrine tissues
Expected completion date	Jul 2017
Estimated size (number of pages)	200
Elsevier VAT number	GB 494 6272 12
Requestor Location	Xiangpeng Li 179 chemistry building
	AUBURN UNIVERSITY, AL 36849 United States Attn: Xiangpeng Li
Publisher Tax ID	98-0397604
Total	0.00 USD

250



# RightsLink®

[Home](#)
[Account Info](#)
[Help](#)


**Title:** Microfabrication meets microbiology  
**Author:** Douglas B. Weibel, Willow R. DiLuzio and George M. Whitesides  
**Publication:** Nature Reviews Microbiology  
**Publisher:** Nature Publishing Group  
**Date:** Mar 1, 2007

Logged in as:  
 Xiangpeng Li  
 Account #:  
 3001138095

[LOGOUT](#)

Copyright © 2007, Rights Managed by Nature Publishing Group

## Order Completed

Thank you for your order.

This Agreement between Xiangpeng Li ("You") and Nature Publishing Group ("Nature Publishing Group") consists of your license details and the terms and conditions provided by Nature Publishing Group and Copyright Clearance Center.

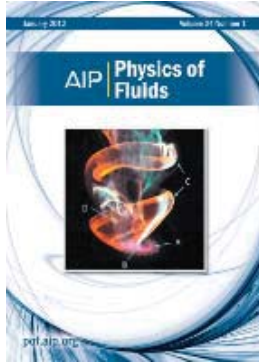
Your confirmation email will contain your order number for future reference.

### [Printable details.](#)

License Number	4092080626513
License date	Apr 18, 2017
Licensed Content Publisher	Nature Publishing Group
Licensed Content Publication	Nature Reviews Microbiology
Licensed Content Title	Microfabrication meets microbiology
Licensed Content Author	Douglas B. Weibel, Willow R. DiLuzio and George M. Whitesides
Licensed Content Date	Mar 1, 2007
Licensed Content Volume	5
Licensed Content Issue	3
Type of Use	reuse in a dissertation / thesis
Requestor type	academic/educational
Format	print and electronic
Portion	figures/tables/illustrations
Number of figures/tables/illustrations	1
High-res required	no
Figures	soft lithography
Author of this NPG article	no
Your reference number	
Title of your thesis / dissertation	Automated microfluidic device development for metabolism, nutrient uptake, and hormone secretion analyses from primary endocrine tissues
Expected completion date	Jul 2017
Estimated size (number of pages)	200
Requestor Location	Xiangpeng Li 179 chemistry building  AUBURN UNIVERSITY, AL 36849 United States Attn: Xiangpeng Li
Billing Type	Invoice
Billing address	Xiangpeng Li 179 chemistry building



# RightsLink®

[Home](#)
[Account Info](#)
[Help](#)


**Title:** Dynamics of step-emulsification: From a single to a collection of emulsion droplet generators

**Author:** Nitesh Mittal, Céline Cohen, Jérôme Bibette, et al.

**Publication:** Physics of Fluids

**Volume/Issue:** 26/8

**Publisher:** AIP Publishing LLC

**Date:** Aug 1, 2014

**Page Count:** 14

Logged in as:  
Xiangpeng Li  
Account #:  
3001138095

[LOGOUT](#)

Rights managed by AIP Publishing LLC.

## Order Completed

Thank you for your order.

This Agreement between Xiangpeng Li ("You") and AIP Publishing LLC ("AIP Publishing LLC") consists of your license details and the terms and conditions provided by AIP Publishing LLC and Copyright Clearance Center.

Your confirmation email will contain your order number for future reference.

### [Printable details.](#)

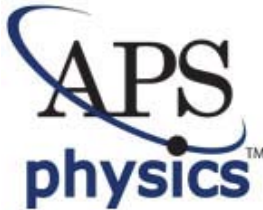
License Number	4093761432731
License date	Apr 21, 2017
Licensed Content Publisher	AIP Publishing LLC
Licensed Content Publication	Physics of Fluids
Licensed Content Title	Dynamics of step-emulsification: From a single to a collection of emulsion droplet generators
Licensed Content Author	Nitesh Mittal, Céline Cohen, Jérôme Bibette, et al.
Licensed Content Date	Aug 1, 2014
Licensed Content Volume	26
Licensed Content Issue	8
Requestor type	Student
Format	Print and electronic
Portion	Photograph/Image
Requestor Location	Xiangpeng Li 179 chemistry building
	AUBURN UNIVERSITY, AL 36849 United States Attn: Xiangpeng Li
Billing Type	Invoice
Billing address	Xiangpeng Li 179 chemistry building
	AUBURN UNIVERSITY, AL 36849 United States Attn: Xiangpeng Li
Total	0.00 USD

[ORDER MORE](#)
[CLOSE WINDOW](#)

Copyright © 2017 [Copyright Clearance Center, Inc.](#) All Rights Reserved. [Privacy statement.](#) [Terms and Conditions.](#)  
Comments? We would like to hear from you. E-mail us at [customercare@copyright.com](mailto:customercare@copyright.com)



# RightsLink®

[Home](#)
[Account Info](#)
[Help](#)


**Title:** Dynamic Pattern Formation in a Vesicle-Generating Microfluidic Device

**Author:** Todd Thorsen et al.

**Publication:** Physical Review Letters

**Publisher:** American Physical Society

**Date:** Apr 30, 2001

Copyright © 2001, American Physical Society

Logged in as:  
Xiangpeng Li  
Account #:  
3001138095

[LOGOUT](#)

## Order Completed

Thank you for your order.

This Agreement between Xiangpeng Li ("You") and American Physical Society ("American Physical Society") consists of your license details and the terms and conditions provided by American Physical Society and Copyright Clearance Center.

Your confirmation email will contain your order number for future reference.

### [Printable details.](#)

License Number	4093751336546
License date	Apr 21, 2017
Licensed Content Publisher	American Physical Society
Licensed Content Publication	Physical Review Letters
Licensed Content Title	Dynamic Pattern Formation in a Vesicle-Generating Microfluidic Device
Licensed Content Author	Todd Thorsen et al.
Licensed Content Date	Apr 30, 2001
Licensed Content Volume	86
Type of use	Presentation/Slides
Requestor type	Student
Format	Print, Electronic
Portion	image/photo
Number of images/photos requested	1
Portion description	T-junction droplet formation
Rights for	Main product
Duration of use	Life of Current Edition
Creation of copies for the disabled	no
With minor editing privileges	no
For distribution to	Worldwide
In the following language(s)	Original language of publication
With incidental promotional use	no
Lifetime unit quantity of new product	0 to 499
The requesting person/organization	Xiangpeng Li
Order reference number	
Title of the presentation	Automated microfluidic device development for metabolism, nutrient uptake, and hormone secretion analyses from primary endocrine tissues
Name of the sponsor	Xiangpeng LI



# RightsLink®

[Home](#)
[Account Info](#)
[Help](#)


**Title:** A Systems Approach to Measuring the Binding Energy Landscapes of Transcription Factors

**Author:** Sebastian J. Maerkl, Stephen R. Quake

**Publication:** Science

**Publisher:** The American Association for the Advancement of Science

**Date:** Jan 12, 2007

Copyright © 2007, American Association for the Advancement of Science

Logged in as:  
Xiangpeng Li  
Account #:  
3001138095

[LOGOUT](#)

## Order Completed

Thank you for your order.

This Agreement between Xiangpeng Li ("You") and The American Association for the Advancement of Science ("The American Association for the Advancement of Science") consists of your license details and the terms and conditions provided by The American Association for the Advancement of Science and Copyright Clearance Center.

Your confirmation email will contain your order number for future reference.

### [Printable details.](#)

License Number	4093120347683
License date	Apr 20, 2017
Licensed Content Publisher	The American Association for the Advancement of Science
Licensed Content Publication	Science
Licensed Content Title	A Systems Approach to Measuring the Binding Energy Landscapes of Transcription Factors
Licensed Content Author	Sebastian J. Maerkl, Stephen R. Quake
Licensed Content Date	Jan 12, 2007
Licensed Content Volume	315
Licensed Content Issue	5809
Volume number	315
Issue number	5809
Type of Use	Thesis / Dissertation
Requestor type	Scientist/individual at a research institution
Format	Print and electronic
Portion	Figure
Number of figures/tables	1
Order reference number	
Title of your thesis / dissertation	Automated microfluidic device development for metabolism, nutrient uptake, and hormone secretion analyses from primary endocrine tissues
Expected completion date	Jul 2017
Estimated size(pages)	200
Requestor Location	Xiangpeng Li 179 chemistry building

AUBURN UNIVERSITY, AL 36849  
United States  
Attn: Xiangpeng Li

254